Doctoral Dissertation
博士論文

The behavior of the chromospheric lines of helium at 10830Å in late-type stars and the measurement of helium abundance

(晩期型星におけるヘリウム彩層吸収線の観測とヘリウム組成の測定)

A Dissertation Submitted for the Degree of Doctor of Philosophy
July 2022
令和 4 年 7 月博士（理学）申請

Department of Astronomy, Graduate School of Science,
The University of Tokyo
東京大学大学院理学系研究科
天文学専攻

Mingjie Jian
简 明杰

Doctoral Dissertation
博士論文

The behavior of the chromospheric lines of helium at 10830Å in late-type stars and the measurement of helium abundance

(晩期型星におけるヘリウム彩層吸収線の観測とヘリウム組成の測定)

A Dissertation Submitted for the Degree of Doctor of Philosophy
July 2022
令和 4 年 7 月博士（理学）申請

Department of Astronomy, Graduate School of Science,
The University of Tokyo
東京大学大学院理学系研究科
天文学専攻

Mingjie Jian
简 明杰

To my family.

Acknowledgements

I would like to express my deepest appreciation to my supervisor, Professor Noriyuki Matsunaga, for being his group member from my master's course. You have given me ample space and time to find and research on the question which is truly interesting to me, and have provided tremendous help in the process, including the comments and suggestions for research, access to the WINERED data, and opportunities to seek collaborations. The route of research is not always smooth, but what I have learned these years have been, and will remain, valuable experiences. I am also thankful to my official supervisor, Professor Motohide Tamura, for his kind support of my IRD proposals, and his patience in handling all the paperwork. Many thanks to Scarlet S. Elgueta for your support, including the help on the WINERED observation in 2017, and the encouragement over the past few months, which helped me a lot. I would like to thank Daisuke Taniguchi. Your expertise makes our discussions efficient and stimulating.

Thanks should also go to those who have supported this thesis mainly from the observational side. This thesis would not be complete if I miss the contribution of the whole WINERED team, including but not limited to Professor Naoto Kobayashi, Yuji Ikeda, Sohei Kondo, Hiroaki Sameshima, Satoshi Hamano and Shogo Otsubo. Thank you very much for building, testing and maintaining such a fantastic instrument, and I believe WINERED will play an important role in near-infrared spectroscopic. I would like to express my sincere gratitude to Xiaoting Fu, who kindly shared the Stock-2 dataset, encouraged me to go on and helped me realize what I have achieved at the end of my PhD course. I am also grateful to Angela Bragaglia and Giuseppe Bono, who helped me and inspired me in the analysis of Stock-2 and X-SHOOTER Library data. Thanks should also go to Brian Thorsbro, who provided so much help on my application and thesis.

I would like to mention the other members of the VECTOR collaboration, Yudong Luo, Lizhi Xie, Zhiyu Zhang and Jingjing Shi. You have enlarged my vision from stellar spectroscopic to other fields in Astronomy, and it is a great pleasure to collaborate with all of you.

To my friends in Japan and in other places who helped me balance my time between academics and life. It was grateful to share an apartment with my former roommate, Minxi He. I enjoyed our discussion and living time, especially during the pandemic period. Huanyu Teng from Tokyo Tech, you can always inspire me with some new ideas during our conversation. I am also thankful to Yingci Ye, Haoxiang Lin, Chang Liu, Zhongdao Chen, Yuchen Wu, Rongyu Hu and Lichen Luo. You have helped me solve issues from technical problems to troubles in daily life, accompanied me when I struggled, and made me feel at home. I would be remiss in not mentioning my family. It is a pity that we could only be connected by the Internet for the past two years, but I know you are always there, supporting me.

Lastly, I would like to acknowledge the financial support from the Japan Society for the Promotion of Science (JSPS), and the Grant-in-Aid for JSPS Fellows 21J11301.

Abstract

The aim of Galactic archaeology, like traditional archaeology, is to reveal the evolutionary history of the Milky Way or other galaxies through the "remnant" observed today. The kinematics and chemical compositions of the "remnant" stars provide us with information about the environment where the stars were formed. Abundances of various elements can be measured with medium- or high-resolution spectra, and these abundances imprint the nucleosynthesis process in the former generation stars. However, one main product of stellar nucleosynthesis, helium, has been missing from galactic archaeology. Spectral synthesis shows that the helium spectral lines formed in the photosphere are weak or undetectable at effective temperature $T_{\rm eff} < 7000\,{\rm K}$. Measuring the helium abundance of low-temperature stars spectroscopically has to rely on other features, if any, that appear in the spectra.

Here we focus on one of the helium absorption features that are often detected in low-temperature stars, the triplet lines at 10 830 Å. Unlike most atomic lines formed in the photosphere, this feature (He 10 830, hereinafter) is formed in a higher layer of the stellar atmosphere, i.e., the chromosphere. The lower state of this triplet, 2s, is metastable. It can be populated by the photoionization-recombination (PR) or collisional excitation (CE) mechanism that ionizes or excites the helium atoms at the ground state. However, our knowledge of He 10 830 is limited, mainly for two reasons: (1) The sensitivity of the line strength to the helium abundance depends on the dominant excitation mechanism (PR or CE), and main formation mechanism for stars other than the sun is not clear. (2) Previous observations on He 10 830 were limited in precision and did not sample stars with different stellar parameters, e.g., $T_{\rm eff}$ and metallicity, well. We aim to determine the dominant formation mechanism of He 10 830 over a wide range of the HR diagram occupied by dwarf and giant stars. Such information is crucial toward our ultimate goal to use He 10 830 as a helium abundance indicator for low-temperature stars.

Combining our own data and publicly available spectra, we have collected a large sample of medium- and high-resolution spectra covering the wavelength range of He 10 830 for over 700 stars, including dwarfs, giants and supergiants over the metallicity range of $-2 < [\mathrm{Fe/H}] < 0.2$. The empirical relations between the line strength and stellar parameters can be examined in detail. We then discuss the formation mechanisms that work in our sample stars and whether the helium abundance can be determined based on He 10830.

The main steps of this study are:

1. determining how He 10 830 and other chromosphere lines varies under different formation mechanisms and helium abundance (Chapter 2).
2. calibrating the oscillator strengths of blending lines and evaluating their contamination using synthetic spectra (Chapter 4);
3. measuring the helium line strength and profile, as well as the Ca indices and X-ray luminosity (Chapter 5);
4. studying the relationships between the parameters we obtain in step 3 and determining the dominant formation mechanism varying with stellar parameters, mainly temperature (Chapter 6);

We used the non-local thermodynamic equilibrium (NLTE) radiative transfer calculation to study the behavior of He 10 830 under the PR or CE mechanism. We adopted the commonly-used 1D solar model with chromosphere and its variants to perform the synthesis of Hα, Hβ, Ca II H&K lines and He 10 830. When the PR mechanism dominates the formation of the He 10 830, the line strength is correlated with the number of high-energy photons illuminated into the chromosphere, but it is not sensitive to helium abundance. The amount of atoms being excited to the lower state of He 10 830 is determined by the amount of high-energy radiation. In this case, the number density of helium atoms, or the helium abundance, has very little effect, if any, on the line strength. On the other hand, the collisional process in the CE formation mechanism always depends on the number density of helium atoms. The He 10 830 strength, in this case, is correlated with chromosphere density, helium abundance and metallicity. We confirmed these behaviors in our calculation although we

have used a limited set of chromosphere models, and more comprehensive calculations should be done in the future.

The He 10 830 absorption is weak in many of our sample stars, and thus it is necessary to estimate the strengths of the lines that blend with the helium feature and subtract the contaminating absorption. We first calibrated the oscillator strengths of the blending lines using the high-quality spectra of stars in the open cluster Stock-2. The synthesized spectra with the expected parameters indicate that the blending line strengths could be overestimated if the oscillator strengths in a standard line list (Vienna Atomic Line Database) were used. Therefore, we determined the oscillator strengths of the blending lines with which we find better fits to the observed spectra. We then used the revised oscillator strengths to estimate the total blending line strength around He 10 830. According to the spectral synthesis using the calibrated oscillator strengths, the blending is expected to be smaller than 40 mÅ in the equivalent width (EW) for most of our sample stars.

The measurement of EW of He 10 830, corrected for the blending EW, was then performed by skew-Gaussian profile fitting or summing up the pixel-by-pixel absorption directly. These two methods are suited for strong and weak helium lines, respectively, but the profile fitting provides information about the line profile, too. We then found the trends of the He 10830 absorption against the effective temperature as illustrated in Figure 1. The main trend rightward of the blue dashed line in Figure 1 (dwarf) peaks at $T_{\rm eff} \sim 4000$ K, and decreases toward lower or higher temperature. The distribution shows a clear lower envelope, which is similar to that in the Ca II H&K index–$T_{\rm eff}$ relation, while a large scatter is found towards the higher EW. The second trend showing an increasing sequence from 7500 K to 5500 K has not been found before. We discuss this newly found trend in Chapter 7 although stars in this group are not good targets for helium abundance measurements. For giants, the He 10 830 strength tends to be weaker towards low metallicity, with EW $\sim$ 50 mÅ on the higher temperature side and decreases to 0 as $T_{\rm eff}$ decreases. Metal-rich giants tend to show stronger helium absorption and a larger scatter, and the line strength seems to show dependency on the evolutionary stage, too.

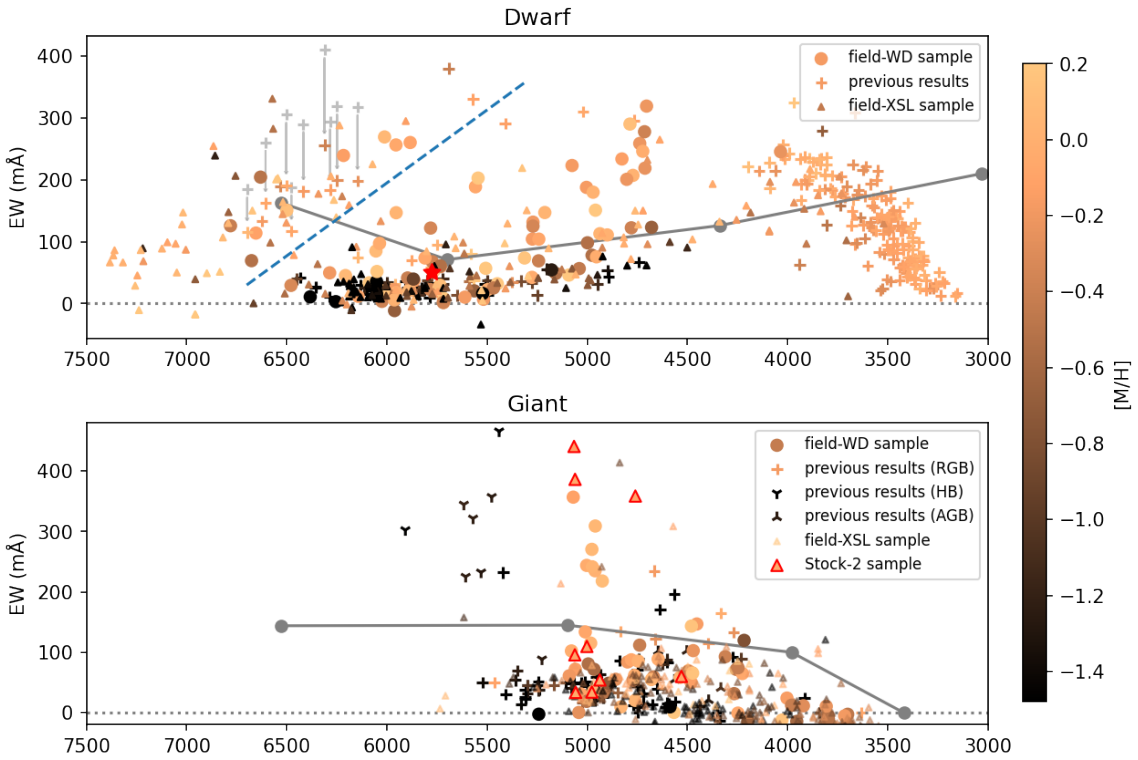


Figure 1: The equivalent width of He 10 830 versus $T_{\rm eff}$ for our dwarf and giant samples. In the upper panel for swarfs, the dashed line divides two trends. The trends from Zirin (1982) are plotted in gray for dwarfs (upper) and giants (lower).

We then measured or searched the literature for the key parameters, i.e., the Ca II H&K indices and the fractional X-ray luminosity, related to the formation mechanisms of He 10 830. Roughly speaking, the helium line strengths are correlated with both parameters. The Ca II H&K indices show the trend as a function of $T_{\rm eff}$ that resembles the lower envelope of the main $T_{\rm eff}$–EW(He) trend in dwarfs mentioned before. On the other hand, the X-ray luminosity normalized by the bolometric luminosity seems responsible for the scatter above the lower envelope of the trend in dwarfs in Figure 1. These indicate that the PR and CE mechanisms are both present in the formation of He 10 830 in dwarfs, and the PR mechanism is required to explain a large EW, e.g., around 150 mÅ or more.

Based on these results, we infer what kind of stars should be observed for measuring the helium abundance using He 10 830. The correlations between EW(He) and $\log R'_{\rm HK}$ as well as the fractional X-ray luminosity seen in our dataset indicate that the PR and CE formation mechanisms are present in dwarfs and giants with $T_{\rm eff} > 4500$ K. Their He 10 830 strength is not sensitive to the helium abundance, according to our NLTE line synthetic calculation. In contrast, He 10 830 in cool giants, separated by the coronal dividing line, is expected to be dominated by the CE machanism and sensitive to helium abundance. Our conclusion is supported by the relation between the He 10 830 strength and metallicity in the cool giants of our sample. Such correlation is caused by the metal-dependent change in the chromosphere structure, and/or the helium abundance difference. Our conclusion provides information of formation mechanisms and constraints on the chromosphere model. How to determine the chromosphere structure of such stars and how to measure the helium abundance remain to be established. The spectral lines formed sufficiently near the line-forming layer of He 10 830, e.g., the hydrogen Lyman-α line (though not available now), would allow us to model the chromosphere including the upper layers in which the CE-triggered He 10 830 is formed.

Contents

1 Introduction **1**

1.1 Chemical evolution of the Milky Way 1

1.2 Stellar helium abundance 4

1.2.1 Indirect evidence of helium enrichment in the Milky Way . . . 5

1.3 Target line: the He 10 830 feature 6

1.3.1 Formation mechanism of He 10 830 9

1.4 Previous observations on He 10 830 13

1.4.1 Previous observations of the field stars 13

1.4.1.1 Observations from 1960s to 1980s 15

1.4.1.2 Observations after 1980s 18

1.4.2 Previous observations of globular cluster stars 22

1.5 Aims and structure of the thesis 26

2 Formation and synthesis of He 10 830 **29**

2.1 Process and code for NLTE spectral synthesis 30

2.2 The solar and stellar chromosphere models 31

2.3 Formation of He 10 830 in solar atmosphere model 33

2.3.1 External radiation variation 38

2.3.2 Chromosphere density variation 38

2.4 Sensitivity of the He 10 830 strength to the helium abundance 46

3 Targets and Observations **49**

3.1 The Stock-2 sample 49

3.2 The field-WD sample 53

3.3 The field-XSL sample 55

4 Data reduction and calibration of blending line parameters 59
4.1 Data reduction . . . 59
4.1.1 Reduction of the Stock-2 spectra . . . 60
4.1.2 Reduction of the field-WD spectra . . . 66
4.1.3 Reduction of the field-XSL spectra . . . 66
4.2 Contamination on He 10 830 . . . 67
4.2.1 Microturbulence, metallicity and broadening velocity measurement of the Stock-2 sample . . . 70
4.2.2 $\log gf$ calibration of contaminating lines and blending situation 72
4.2.3 Contamination situation around He 10 830 . . . 78

5 Measurement of the line strengths and indices 81
5.1 Measurement of He 10 830 . . . 81
5.2 Measurement of stellar Ca II and X-ray indices . . . 86
5.2.1 Measurement of the Ca II index . . . 89
5.2.2 Measurement of fractional X-ray luminosity . . . 95

6 Empirical trends toward stellar parameters 99
6.1 Empirical relation with $T_{\rm eff}$ and metallicity . . . 99
6.1.1 Dwarf . . . 100
6.1.2 Giant . . . 101
6.1.3 Supergiant . . . 101
6.2 Empirical relation with chromosphere indices . . . 102
6.3 Empirical relation with X-ray luminosity . . . 107

7 Discussion 113
7.1 The secondary trend in dwarf . . . 113
7.2 The EW lower boundary in dwarfs . . . 115
7.3 CE dominated He 10 830 in a simple model for giants . . . 119
7.4 The usage of helium 10 830 Å line as a helium abundance tracer . . . 122
7.5 Relations between EW(He) and metallicity for cool giants . . . 124

8 Conclusions 129

A Stellar parameters and He 10 830 measurement for previous studies 133

B List of parameters and measurements on the field-WD sample 151

C Spectral atlas of the helium line in field-WD stars **163**

D The He 10 830 and Ca II line atlas of Stock-2 sample **173**

E List of parameters and measurements on the field-XSL sample **187**

Bibliography **210**

List of Figures

1 The equivalent width of He 10 830 versus $T_{\rm eff}$ for our dwarf and giant samples. In the upper panel for swarfs, the dashed line divides two trends. The trends from Zirin (1982) are plotted in gray for dwarfs (upper) and giants (lower). . . . . .

1.1 The all-sky view of the Milky Way, with the main components labeled. This picture is created using the data in the second data release of Gaia mission (Gaia Collaboration et al., 2018). Adopted from ESA/Gaia/DPAC. 2

1.2 The time evolution of elements creation calculated from galactic evolution model. Horizontal axes represent the age of the universe, and vertical axes represent the abundance of each element. The vertical dotted lines indicate the time when the sun is born, and horizontal dotted lines indicate solar initial abundances. Adopted from Kobayashi et al. (2020) 3

1.3 Schematic explanation of the MSP formation scenario in globular clusters. The later generation stars are depleted in O, enriched in Na and He. The detail description of this scenario is in section 1.2.1. Adopted from Kim & Lee (2018). 7

1.4 The helium enrichment law calibrated from the dwarfs observed by Verma et al. (2019). Adopted from Verma et al. (2019) 8

1.5 The Grotrian diagram of He I, with main transitions in the optical and NIR. The transition of our target feature, He 10 830 is marked by a red square. The black arrows indicate the radiative decay pathways of He atom, while the blue solid and dotted arrays indicate the pathways of PR and CE formation mechanism. Adopted from Kulkarni (2021; `https://sites.astro.caltech.edu/\protect\unhbox\voidb@x\protect\penalty\@M\{}srk/Ay126/Lectures/Lecture4/Helium.pdf`). 10

1.6 Example spectra around 10 830 Å with three resolutions from our sample (Chapter 3). The three values in the legend after resolution (R) are $T_{\rm eff}$, $\log g$ and [Fe/H] of the star. The gray arrows indicate the blending lines with oscillator strength calibrated in Chapter 3, and the red shaded area indicates the wavelength region used for measuring the line strength in Chapter 5. 11
1.7 The temperature stratification and line forming regions of the VAL-C model. The model is divided into three parts: lower chromosphere (Height h from 0 to 500 km), upper chromosphere (0–2000 km) and transition region ($>$ 2000 km). Adopted from Vernazza et al. (1981). . 14
1.8 The average He 10 830 EW versus spectral type from the Zirin (1982) sample. Trends of stars with different luminosity types are separated and labeled by their types. Adopted from Zirin (1982) 15
1.9 The HR-diagram with the stars observed in Obrien & Lambert (1986). The solid line is the coronal dividing line from Linsky & Haisch (1979). Adopted from Obrien & Lambert (1986) 17
1.10 The average He 10 830 EW from the Zirin (1982) sample versus $T_{\rm eff}$. Zirin's trends with luminosity type V and III are converted to $T_{\rm eff}$ and overplotted for comparison. 19
1.11 The Kiel diagram for the observations from the 1960s to 1980s, color coded by the He 10 830 EW. The stars with EW $\leq$ 0 are in gray. The vertical dashed line indicates the boundary of stars showing clear absorption proposed by Smith et al. (2004). 20
1.12 The He 10 830 EW versus fractional X-ray luminosity (left panel) and $\log R'_{\rm HK}$ index (right panel) for dwarfs. Adopted from Smith (2016). . 22
1.13 The He 10 830 EW versus $T_{\rm eff}$ for the stars observed after the 1980s. . 24
1.14 The [Fe/H] histogram of the sample summarized in section 1.4, divided to those observed in the 1960s–1980s, after the 1980s (including globular cluster member stars) and the M-dwarfs from Fuhrmeister et al. (2019). The area of the histograms are normalized to better present their distribution, and the number of the samples are written in the legend. 25

2.1 Temperature and electron number density structure of the VAL-C model. The horizontal axes, $\log \rho x$ is the logarithm of column density in $\mathrm{g\,cm^{-2}}$, and this value increases from the outer part (transition region on the left side) of the model to the inner part (photosphere on the right side). 32
2.2 The external radiation model from Tobiska (1991) used in the following line synthesis. The vertical dashed line at $\lambda = 504\,\text{Å}$ indicates the threshold of the photon which can ionize helium atom. 34
2.3 Synthetic spectra of chromospheric lines generated using the VAL-C model and external radiation of I_T. The observed spectra of these lines are overplotted in orange for comparison. 36
2.4 The synthetic spectra (left panel) a weak Cr line calculated by `pymoog`. The stellar and line parameters used for generating the synthetic spectra are written in the title. The contribution function of this line is plotted in the right panel, with the solid gray curve indicating the contribution of the continuum, and the blue curve indicating the contribution of line absorption. Only the photosphere is included in this synthesis. 37
2.5 Same as Figure 2.4 but for a strong Si line. 37
2.6 Left panels: the synthetic spectra of chromosphere lines (rotated 90 degrees counter-clockwise) in VAL-C model with $I = I_\mathrm{T}$. Right panels: the contribution functions of the lines in different optical depths and wavelengths, indicated by the colors. The temperature profile is overplotted for comparison. 39
2.7 Synthetic spectra generated using the VAL-C model with $I = 0, 10, 20$ and $30 I_\mathrm{T}$. 40
2.8 Left panels: the synthetic spectra of chromosphere lines (rotated 90 degrees counter-clockwise) in VAL-C model with $I = 0, 10, 20$ and $30 I_\mathrm{T}$. Right panels: the contribution functions of the lines in different optical depths and wavelengths, indicated by the colors. The temperature profile is overplotted for comparison. 41
2.9 Population of the ionized He atom ($N_{\mathrm{He\,II}}$) in ground state of the VAL-C model with $I = 0, 10, 20$ and $30 I_\mathrm{T}$. The temperature profile is plotted as a reference. 42

2.10 Population of the neutral He atom in 2^3S state of the VAL-C model with $I = 0, 10, 20$ and $30I_{\rm T}$. The temperature profile is plotted as a reference. 42
2.11 Temperature stratification of the VAL-C model and the two modified models with varying chromosphere density. 43
2.12 Synthetic spectra generated using the models with solar, low and high chromosphere density. 44
2.13 Left panels: the synthetic spectra of chromosphere lines (rotated 90 degrees counter-clockwise) in models with solar, low and high chromosphere density. Right panels: the contribution functions of the lines in different optical depths and wavelengths, indicated by the colors. The temperature profile is overplotted for comparison. 45
2.14 The synthetic He 10 830 with different helium abundances with a PR mechanism dominated model (the model with $20I_{\rm T}$ in section 2.3.1). . 47
2.15 The synthetic He 10 830 with different helium abundances with CE mechanism dominated model (the high density model in section 2.3.2). 48

3.1 The HR diagram of Stock-2 member stars. The isochrone with the age and metallicity of the cluster are drawn as the cyan curve, and the red squares label the giants with GIANO-B observation. 51
3.2 The Kiel and [Fe/H]–$T_{\rm eff}$ diagram for the field-WD sample. 54
3.3 The classification for the field-XSL sample, in HR diagram (upper panel) and Kiel diagram (lower panel). The stars in area-D, G and S are classified as dwarf, giant and supergiant respectively, and those in area-M are classified as giant or supergiant if their metallicity is smaller or larger than -0.25. 57
3.4 The Kiel and [Fe/H]–$T_{\rm eff}$ diagram for field-XS sample. 58

4.1 The model telluric spectra for orders 57–61 in WINERED-WIDE mode. The spectra, generated by `telfit`, are separated into four main species (H_2O, CO_2, CH_4 and O_2) contributing to the telluric absorption in these wavelengths. 61
4.2 Same as Figure 4.1, but for orders 52–56. The position of He 10 830 is indicated by the vertical dashed line in the panel of order 52. 62
4.3 Same as Figure 4.1, but for orders 47–51. 63
4.4 Same as Figure 4.1, but for orders 42–46. 64

4.5 The spectra of Stock-2 g4 star in He 10 830, Hα, Hβ and Ca II H&K wavelength range. The dotted squares and triangles are the wavelength bands for measuring the S-index. The spectra of other Stock-2 stars are in gray. 65
4.6 The He 10 830 spectra of field-WD sample, divided into dwarfs, giants and supergiants. The He 10 830 appear in most of the late-type stars in this sample. The atlas of all the spectra is presented in Appendix C. 67
4.7 The He 10 830, Hα, Hβ and Ca II H&K spectra for HD 17072 in the field-XSL sample. The chromosphere lines are clearly seen under a resolution of 10 000. 68
4.8 The blending lines around He 10 830. The spectra in blue is synthesized using the stellar parameters in the title with a resolution of 28 000, and the orange spectra is a giant star with similar stellar parameters observed by WINERED. Black arrows indicate the location of relatively strong atomic lines other than the He 10 830. 68
4.9 Curve of growth for a spectral line with different ξ values. In a fixed line EW, ξ and abundance ($\log A$) degenerate when the line is saturated. The MPFIT algorithm use this feature to determine ξ and metallicity by matching the observed and synthesized spectra of multiple Fe lines. Adopted from Gray (2005) 71
4.10 The [M/H]–ξ diagram (upper panel), [M/H]–X (middle panels) in three ξ values and the histogram of ξ and [M/H] of the 1000 times repeated MPFIT algorithm. These panels are used to determine ξ and [Fe/H] for Stock-2 g2 star, shown as an example (for the detail of MPFIT algorithm, please refer to the text in section 4.2.1). 73
4.11 Comparison of the MPFIT determined ξ with the trend for giants from Holtzman et al. (2018) (right panel), and [Fe/H] with those from Alonso-Santiago et al. (2021). 73
4.12 Example spectra (the g1 star) for the $\log gf$ calibration. The vertical dashed lines indicate the wavelengths of the lines being calibrated, while the lines with red crosses are excluded from the calibration for this star. The spectra for all stars are presented in Appendix D. . . 75
4.13 The $\log gf$ calibration result is plotted with the spectra of star Stock-g7. 76

4.14 Comparison between the observed Arcturus spectra and the synthetic spectra before and after the $\log gf$ calibration. The spectra after $\log gf$ calibration are more consistent with the observed one. 77
4.15 The contamination situation of the blending lines in different metallicity and resolutions. The black contours show contamination EW in various stellar parameters, and the gray points are the grid points used to calculate the contours. The field-WD sample stars are labeled by orange circles. 79

5.1 Definition of the line parameters to be measured. The blue curve shows a fabricated line with asymmetry, and the gray dashed curve shows a line with a Gaussian profile for comparison. The definition of line parameters are described in section 5.1. 82
5.2 The observed spectra (gray) of Stock2-g1, and the spectra after the removal of Si and telluric lines (blue). The measurement of He 10 830 is done by skew-Gaussian fitting shown as the orange dashed curve, and the fitting parameters are listed in the title. 85
5.3 The FWHM, $\log \mathrm{R/B}$ and λ_{min} for the field-WD sample stars. The vertical dashed line in the FWHM, $\log \mathrm{R/B}$ and λ_{min} panels indicate the median value of FWHM, $\log \mathrm{R/B} = 0$ and $\lambda = 10\,830.336$ Å (the rest wavelength of the strongest component of He 10 830), respectively . 87
5.4 The He 10 830, Hα, Hβ and Ca II H&K spectra of HD188262 from the field-XSL sample. 88
5.5 Same as Figure 5.4, but for Cl* NGC 5139 SAW V1 88
5.6 The Grotrian diagram of Ca II with the transition of H and K lines labeled. Adopted from Linsky & Avrett (1970). 90
5.7 The Ca II H&K spectra for Stock-2 g3 star scaled to the PHOENIX scale. The shaded areas are used for measuring the $\log R'_{\mathrm{HK}}$ index described in section 5.2.1. The spectra for other stars in the Stock-2 sample are plotted in Appendix D. 91
5.8 S-index versus T_{eff} for field-XSL sample stars, color-coded by their metallicity. 93
5.9 $\log R'_{\mathrm{HK}}$ index versus T_{eff} for field-XSL sample stars, color-coded by their metallicity. 94

6.1 The He 10 830 EW versus $T_{\rm eff}$, for dwarf, giant and supergiant and color-coded by their [Fe/H]. The gray plus signs are the stars from Andretta et al. (2017), and they are scaled down by a factor of 5/8 to exclude the absorption from the weak component. The gray dotted lines are those reported in Zirin (1982), with luminosity types V, III and I (also see Figure 1.8). 103
6.2 EW(He) versus $\log R'_{\rm HK}$ and S-index for stars in field-XSL and Stock-2 sample. The dwarfs are separated by the main and secondary trends. 104
6.3 $\log R'_{\rm HK}$ versus $(B-V)$ color for dwarf stars. An increase in $\log R'_{\rm HK}$ is seen in $1 < B-V < 1.4$, similar to that in the EW(He)–$T_{\rm eff}$ relation. Adopted from Mittag et al. (2013). 105
6.4 Similar to Figure 6.1, but color-coded by $\log R'_{\rm HK}$. 106
6.5 The He 10 830 EW versus the fractional X-ray luminosity from XMM-Newton bands. 108
6.6 The He 10 830 EW versus the fractional X-ray luminosity from ROSAT bands. The labels are the same as those in Figure 6.5 109
6.7 Similar to Figure 6.1, but color-coded by ROSAT fractional X-ray luminosity. Note that no X-ray measurement is available for supergiants, thus the panel for supergiant is omitted. 110

7.1 The [Fe/H] histogram of dwarfs, divided into the main and secondary trends. Most of the stars in the secondary trend are around solar. The histograms are normalized to better show their distribution in [Fe/H]. 114
7.2 EW(He) versus ROSAT X-ray luminosity for the dwarfs in main and secondary trends. 116
7.3 Fractional X-ray luminosity from XMM-Newton measurement versus $T_{\rm eff}$ distribution for field stars. The two blue dashed vertical lines indicate the $T_{\rm eff}$ range where the secondary trend appears, and the main component of the stars in the two areas with low $\log(F_{\rm X}/F_{\rm Gaia})$ are labeled. Adopted from Freund et al. (2018). 117
7.4 The lower boundary for the main trend dwarfs. Blue points are the dwarfs in the main trend, and those with ROSAT X-ray luminosity measurement are color coded. Orange points are the lower boundary EWs in each $T_{\rm eff}$ bin determined in section 7.2, and the orange solid (dashed) curve is the fitted lower boundary (the boundary shiftred by 27 mÅ). 118

7.5 The giant model used for generating the synthetic spectra in section 7.3, similar to Figure 2.1. The two vertical dashed lines indicate the separation of the transition region and chromosphere, and that of the chromosphere and photosphere parts, from left to right. 120
7.6 Synthetic spectra of chromospheric lines generated using the giant model in Figure 7.5. 121
7.7 The He 10 830 with two helium abundances, generated using the giant model in Figure 7.5. 122
7.8 The He 10 830 EW from previous GC observations are plotted against $T_{\rm eff}$ (left) and [Na/Fe] (right). Stars rightward of the CDL (with $T_{\rm eff} <$ 4500 K) are emphasized with black circle. 124
7.9 EW(He) versus $\log R'_{\rm HK}$ for field-XSL giants separated in $T_{\rm eff}$ bins. The title of each panel indicates the $T_{\rm eff}$ range. 125
7.10 EW(He) versus [Fe/H] for field-XSL giants separated in $T_{\rm eff}$ bins. The title of each panel indicates the $T_{\rm eff}$ range, Pearson correlation coefficient ρ and slope s of the linear fitting. 126
7.11 The slope and correlation relation of the linear fits in Figure 7.10. The orange shaded area highlights the $T_{\rm eff}$ range with larger slopes and correlation coefficients. 126

C.1 The atlas of He 10 830 line of field-WD sample, with the measurement result in the title. 164
C.2 The atlas of He 10 830 line of field-WD sample, with the measurement result in the title. 165
C.3 The atlas of He 10 830 line of field-WD sample, with the measurement result in the title. 166
C.4 The atlas of He 10 830 line of field-WD sample, with the measurement result in the title. 167
C.5 The atlas of He 10 830 line of field-WD sample, with the measurement result in the title. 168
C.6 The atlas of He 10 830 line of field-WD sample, with the measurement result in the title. 169
C.7 The atlas of He 10 830 line of field-WD sample, with the measurement result in the title. 170
C.8 The atlas of He 10 830 line of field-WD sample, with the measurement result in the title. 171

D.1 The spectra around He 10 830 of Stock-2 g1 star, with the synthetic spectra for $\log gf$ calibration. 174
D.2 The spectra around He 10 830 of Stock-2 g2 star, with the synthetic spectra for $\log gf$ calibration. 174
D.3 The spectra around He 10 830 of Stock-2 g3 star, with the synthetic spectra for $\log gf$ calibration. 175
D.4 The spectra around He 10 830 of Stock-2 g4 star, with the synthetic spectra for $\log gf$ calibration. 175
D.5 The spectra around He 10 830 of Stock-2 g5 star, with the synthetic spectra for $\log gf$ calibration. 176
D.6 The spectra around He 10 830 of Stock-2 g6 star, with the synthetic spectra for $\log gf$ calibration. 176
D.7 The spectra around He 10 830 of Stock-2 g7 star, with the synthetic spectra for $\log gf$ calibration. 177
D.8 The spectra around He 10 830 of Stock-2 g9 star, with the synthetic spectra for $\log gf$ calibration. 177
D.9 The spectra around He 10 830 of Stock-2 g10 star, with the synthetic spectra for $\log gf$ calibration. 178
D.10 The He 10 830 line spectra of Stock-2 g1 star, with the measurement result in the title. 178
D.11 The He 10 830 line spectra of Stock-2 g2 star, with the measurement result in the title. 179
D.12 The He 10 830 line spectra of Stock-2 g3 star, with the measurement result in the title. 179
D.13 The He 10 830 line spectra of Stock-2 g4 star, with the measurement result in the title. 180
D.14 The He 10 830 line spectra of Stock-2 g5 star, with the measurement result in the title. 180
D.15 The He 10 830 line spectra of Stock-2 g6 star, with the measurement result in the title. 181
D.16 The He 10 830 line spectra of Stock-2 g7 star, with the measurement result in the title. 181
D.17 The He 10 830 line spectra of Stock-2 g9 star, with the measurement result in the title. 182
D.18 The He 10 830 line spectra of Stock-2 g10 star, with the measurement result in the title. 182

D.19 The Ca II H&K line spectra of Stock-2 g1 star, with the measurement result of $\log R'_{\mathrm{HK}}$ in the title. 183
D.20 The Ca II H&K line spectra of Stock-2 g2 star, with the measurement result of $\log R'_{\mathrm{HK}}$ in the title. 183
D.21 The Ca II H&K line spectra of Stock-2 g3 star, with the measurement result of $\log R'_{\mathrm{HK}}$ in the title. 183
D.22 The Ca II H&K line spectra of Stock-2 g4 star, with the measurement result of $\log R'_{\mathrm{HK}}$ in the title. 184
D.23 The Ca II H&K line spectra of Stock-2 g5 star, with the measurement result of $\log R'_{\mathrm{HK}}$ in the title. 184
D.24 The Ca II H&K line spectra of Stock-2 g6 star, with the measurement result of $\log R'_{\mathrm{HK}}$ in the title. 184
D.25 The Ca II H&K line spectra of Stock-2 g7 star, with the measurement result of $\log R'_{\mathrm{HK}}$ in the title. 185
D.26 The Ca II H&K line spectra of Stock-2 g9 star, with the measurement result of $\log R'_{\mathrm{HK}}$ in the title. 185
D.27 The Ca II H&K line spectra of Stock-2 g10 star, with the measurement result of $\log R'_{\mathrm{HK}}$ in the title. 185

Chapter 1

Introduction

This thesis is focused on the behavior of the helium spectral absorption at 10 830 Å (hereinafter He 10 830), its formation mechanisms, and the possibility of using it as a helium abundance tracer. We introduce the background and motivation for studying He 10 830 in this chapter, starting from the chemical evolution of the Milky Way, and solar and stellar helium abundance. The introduction to the He 10 830 and previous observation in this frature is then presented.

1.1 Chemical evolution of the Milky Way

The galaxy where our solar system is located, the Milky Way, is a typical disk galaxy with a mass of $\sim 5 \times 10^{10}\,M_{\odot}$ (Bland-Hawthorn & Gerhard, 2016). We now know that the Milky Way has several components or substructures, as shown in Figure 1.1. These components include:

- Thin disk: The most prominent disk-like structure with a scale height of $\sim$ 300 pc (Bland-Hawthorn & Gerhard, 2016). Most of the ongoing star formation happens in the thin disk, and the stars in thin disk are relatively young.
- Thick disk: A thicker and more diffuse disk-like structure hosting older stars compared to the thin disk. The stars in the thick disk tend to be less enhanced in metal (all the elements heavier than Helium) than those in the thin disk.
- Halo: The most extended structure traced, e.g., by globular clusters. The rotational speed of halo stars is close to zero, and they are considered to be formed by disrupted dwarf galaxies that have been accreted into the Milky Way.

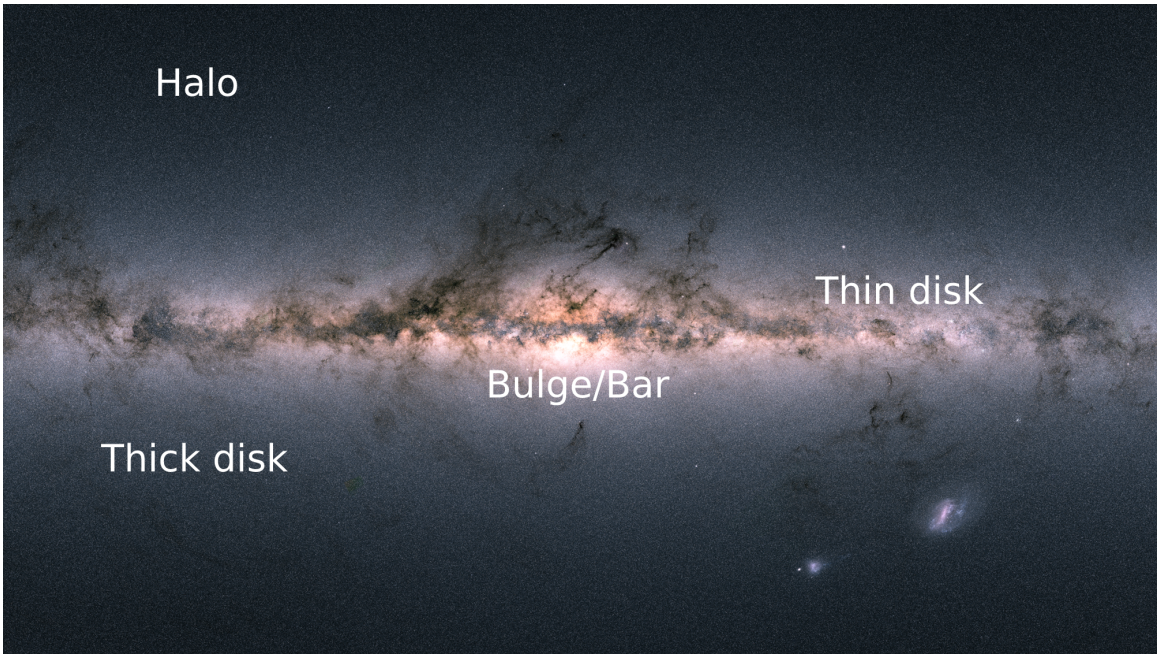


Figure 1.1: The all-sky view of the Milky Way, with the main components labeled. This picture is created using the data in the second data release of Gaia mission (Gaia Collaboration et al., 2018). Adopted from ESA/Gaia/DPAC.

- Bulge (or bar): The concentrated component within a few kpc at around the Galactic center, viewed as a bump at the center of Figure 1.1. This is the highly obscured region since we need to penetrate a large amount of dust in the disk to reach the bulge.

Stars in different components show differences in spatial distributions, kinematic behaviors, and chemical compositions (see, e.g., Helmi 2020). The chemical compositions of each star reflect the stellar nucleosynthesis history of the interstellar environment where the star was born.

Stellar nucleosynthesis refers to the nuclear reaction inside the stars. All the stars fuse hydrogen to helium during their main-sequence stage (Bethe, 1939), and sustain their structure using the energy emitted from these reactions. Later when the star leaves the main sequence, helium changes from the product to the fuel, and heavier elements are synthesized until they reach iron (Hoyle, 1946), the one with the largest binding energy per nucleon. The theory of stellar nucleosynthesis from hydrogen to iron was summarized in the famous review paper referred to as B^2FH (Burbidge et al., 1957). The elements heavier than iron, on the other hand, cannot be produced from nuclear fusion. Instead, they are created from proton processes where a "seed" (for example, an iron nucleus) is placed in a neutron flow. The seed has a chance to

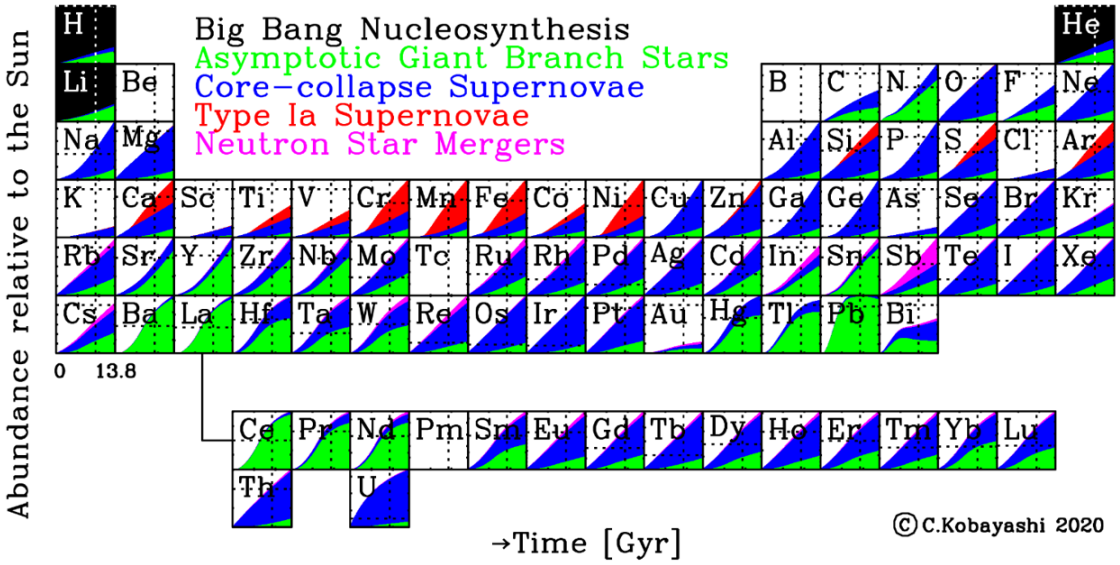


Figure 1.2: The time evolution of elements creation calculated from galactic evolution model. Horizontal axes represent the age of the universe, and vertical axes represent the abundance of each element. The vertical dotted lines indicate the time when the sun is born, and horizontal dotted lines indicate solar initial abundances. Adopted from Kobayashi et al. (2020)

merge with a neutron, increasing its mass number and possibly decaying into another element. If the density of neutron is low, e.g., in the interior of asymptotic giant branch (AGB) stars, the seed will have enough time to β decay before interacting with another neutron. This is called the s(low)-process (Clayton et al., 1961) and it is responsible for the creation of the s-process elements (Cr, Y, Zr, etc). If the neutron density is high, e.g., in the case of an explosion of massive stars or binary neutron star merger, the seed will absorb more neutrons before being able to decay, thus the elements created during this r(apid)-process (Seeger et al., 1965) will be heavier than that from s-process. The s- and r-process elements include all the elements up to Pu (Z=94), except Tc and Pm.

The element synthesized from nuclear fusion and s-process is kept in the interior of the star. They are then emitted into the interstellar medium along with the r-process elements when the star ends its life by supernova, nova explosion, etc. A "cycle" of the material is completed, with the hydrogen as input to the star, and heavier elements as the output back to the environment. Figure 1.2 summarized these processes in the form of the periodic table.

Detecting the appearance of elements, when being in the interstellar material, would be hard. The formation of spectral lines of an element requires the atoms to

be in the excitation stage, or there is a light source shining on the material. The environment of the interstellar medium does not meet the conditions for the spectral lines in the optical or infrared wavelength ranges. The surface of the star, or the stellar atmosphere, is usually with a temperature of a few thousand Kelvin and a pressure ranging from, e.g., 10^6 to 10^{-1} dyne cm^{-2} (Linsky, 2017). Such an environment is hot and dense enough to provide radiation for exciting the atom. Spectral lines are usually imprinted in their spectra, and the process for measuring the abundances using these lines is mature (see, e.g., Jofré et al. 2019 and Hubeny & Mihalas 2014).

Further, the temperature in the stellar photosphere is not high enough to trigger the nuclear reaction, so the amount of atoms in the stellar atmosphere is considered the same as, or at least, related to that in the interstellar medium when the star is born, as stated in Helmi (2020): "stars have memory of their origin". We can use the spectral lines formed on the surface of the next-generation stars to probe the element synthesized from the previous populations. The stellar elemental abundance can be then used to verify the galactic chemical evolution models and trace the evolutionary history of galaxies.

The study using the elemental abundances of stars to probe the evolution of the Milky Way or other galaxies is called chemical tagging in the field of Galactic Archaeology. Thanks to the observation from recent large-scale spectroscopic surveys, e.g., APOGEE (Majewski et al., 2017), LAMOST (Deng et al., 2012), GALAH (Buder et al., 2021), the precise stellar elemental abundances of millions of stars can be measured. Such a sample makes the comparison between galactic chemical evolution models and observation possible, and deepens our understanding of the evolutionary history of our Milky Way.

In short, the measurement of stellar abundances can provide essential constraints on the evolution history of the Milky Way. However, one element, helium, is missing in the spectroscopic observation of present-day chemical tagging. We will discuss the necessity and difficulties in measuring helium abundance in section 1.2.

1.2 Stellar helium abundance

The helium abundance, Y, is defined as the mass fraction of the helium of a star. Similarly, the hydrogen and metal abundances are denoted as X and Z. Here the solar surface helium abundance of $Y_{\odot\mathrm{s}} = 0.2423 \pm 0.0054$ is adopted from Asplund et al. (2021). The initial solar helium abundance, $Y_{\odot\mathrm{i}} = 0.2725$, is larger than $Y_{\odot\mathrm{s}}$ since atomic diffusion happens in the solar atmosphere. It is clear that $Y_{\odot\mathrm{i}}$ is larger

than the primordial helium abundance, $Y_{\rm p} = 0.24705 \pm 0.00019$ (Pitrou et al., 2018), since our sun does not belong to the first generation stars and there is an imprint from the older generation of enriched helium.

1.2.1 Indirect evidence of helium enrichment in the Milky Way

The need to measure stellar helium abundance comes from the indirect evidence of helium enrichment, from the globular clusters (GCs) and the galaxy as a whole.

According to the traditional view of the globular clusters, they represent a single stellar population, i.e., all the stars in each cluster were born at the same time with similar chemical compositions. However, this view has been proven to be incorrect at least 10 years ago (Bastian & Lardo, 2018). Various photometric studies (e.g., Piotto et al. 2007) revealed that there are more than one main-sequences (MSs) and/or red giant branches (RGBs) in globular clusters. The presence of multiple stellar populations (MSPs) is obvious in the UV bands, such as the F275W, F336W and F438W bands in Hubble Space Telescope (Piotto et al., 2015). Moreover, spectroscopic observations of stars in different populations reveal the variation of chemical abundances. For example, nearly all the clusters with MSPs in Carretta et al. (2009) show some extent of anticorrelation in their Na and O abundances (see their Figure 6).

One of the scenarios which can explain the origin of MSPs is the multi-epoch star formation in GCs, summarized in Figure 1.3 from Kim & Lee (2018). The first generation (G1) stars are formed in the giant molecular cloud with initial chemical compositions. These stars then generate stellar winds and ejecta in their main-sequence and later evolution stages. These ejecta are at slow speed, thus they cannot escape from the cluster and are mixed with the leftover from the initial molecular cloud. When the massive G1 stars explode as SN, the SN ejecta are with higher speed and escaped from the cluster. The second-generation (G2) stars are nurtured by the leftover gas polluted by the slow ejecta, thus their chemical abundances are altered. Similar procedures happen for the later generations, and the difference in their abundance compared to that of the first generation is gradually enlarged. Helium, nitrogen, sodium and aluminum abundances are enriched, while oxygen and magnesium abundances are depleted in this process. The enrichment of helium abundance in the later generations is responsible for altering the position of their MS and RGB (e.g., Piotto et al. 2007 and Lee et al. 1999), thus creating the MSP phenomenon in the color-magnitude diagram. Anticorrelations between the above elements have been well detected, except for helium. Since helium is the key element that alters the

position of the MS and RGB, the lack of helium abundance measurement for late-type stars means we lack the most direct evidence supporting this formation scenario.

A similar concern also exists when we consider the evolution of the Milky Way or other galaxies as a whole. The enrichment of helium is usually correlated with that of metallicity. The metallicity and initial helium abundance of our sun are higher than their primordial values. The helium enrichment law,

$$Y = Y_{\rm p} + \frac{\Delta Y}{\Delta Z} Z \tag{1.1}$$

is widely adopted to describe the enrichment history of helium at a given Z. The slope of this equation is determined by the helium abundance and metallicity of the sun. While most of the studies involving stellar models, e.g., Yonsei-Yale models (Yi et al., 2001), The Dartmouth Stellar Evolution Program (Dotter et al., 2008), and Modules for Experiments in Stellar Astrophysics (Paxton et al., 2011) have incorporated helium enrichment law in their calculation, their laws are slightly different due to the different solar helium abundances they adopted. Also, whether other stars follow this law calibrated by the sun is not clear due to the lack of stellar helium abundance measurement. Recently, Verma et al. (2019) derived the helium enrichment law using a set of dwarfs with helium abundance measured with asteroseismology observation. Their slope $\frac{\Delta Y}{\Delta Z}$ is smaller than those adopted in the stellar models. Also, there is a large scatter around the relation, indicating that a fixed relation may not be a good choice for describing the helium enrichment law in different environments. A method that can measure the stellar helium abundance precisely is required for a better characterization of the helium enrichment law.

In short, determining the helium abundance of late-type stars can provide essential constraints on the formation history of globular clusters and the Milky Way. However, the method to measure the helium abundance for late-type stars are limited. The surface Y from asteroseismology measurements are limited to dwarfs, and it requires years of continuous high-precision photometry. Current photometry satellites, such as the Kepler-K2 mission (Howell et al., 2014) and TESS satellite (Ricker et al., 2015) cannot provide data with such a long-time coverage. Determining the stellar helium abundance using helium spectral lines seems to be the most plausible method.

1.3 Target line: the He 10 830 feature

Here we focus on a special helium feature at 10 830 Å. Measurement of the helium abundance using spectral lines is with high difficulty since the excitation potential of

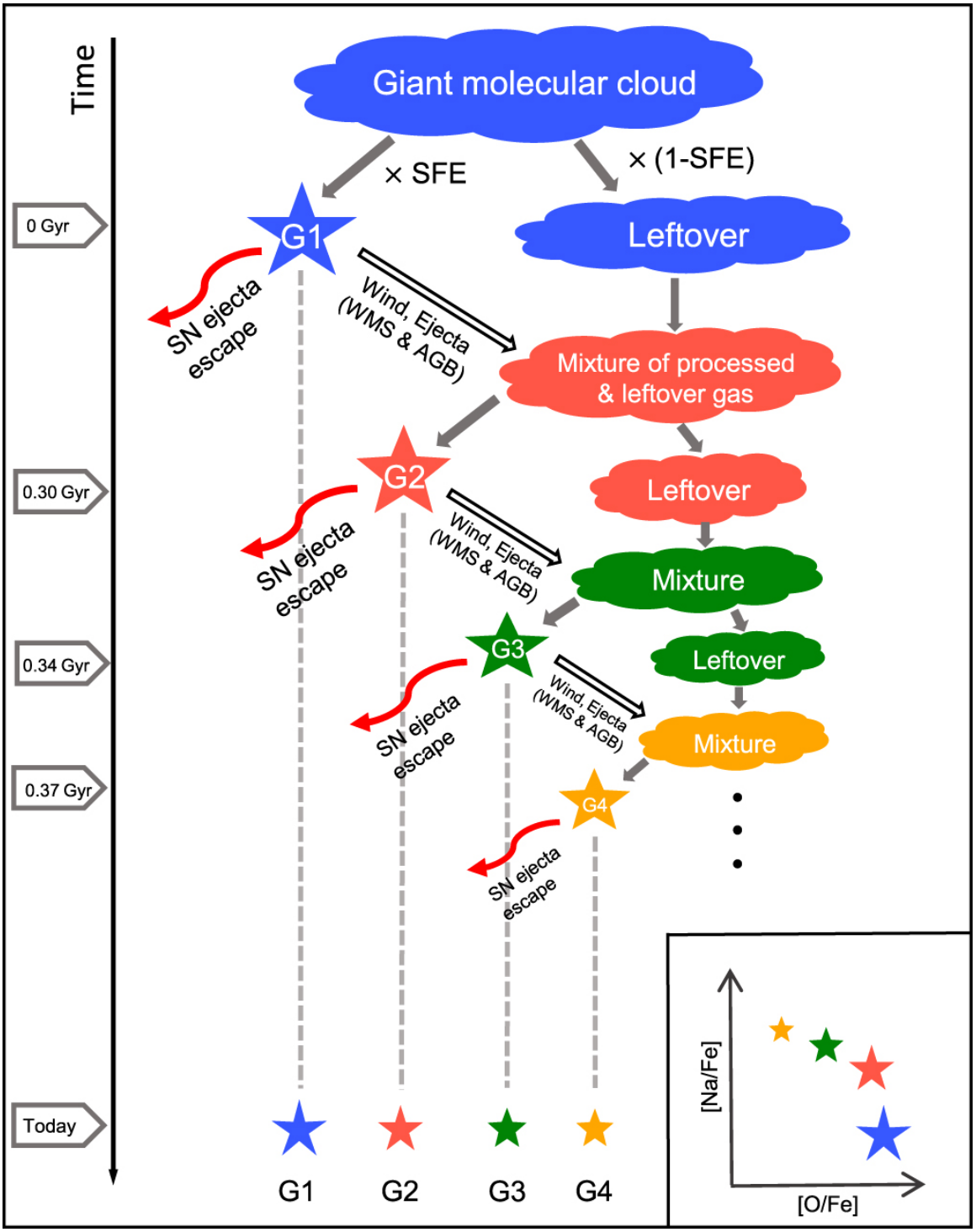


Figure 1.3: Schematic explanation of the MSP formation scenario in globular clusters. The later generation stars are depleted in O, enriched in Na and He. The detail description of this scenario is in section 1.2.1. Adopted from Kim & Lee (2018).

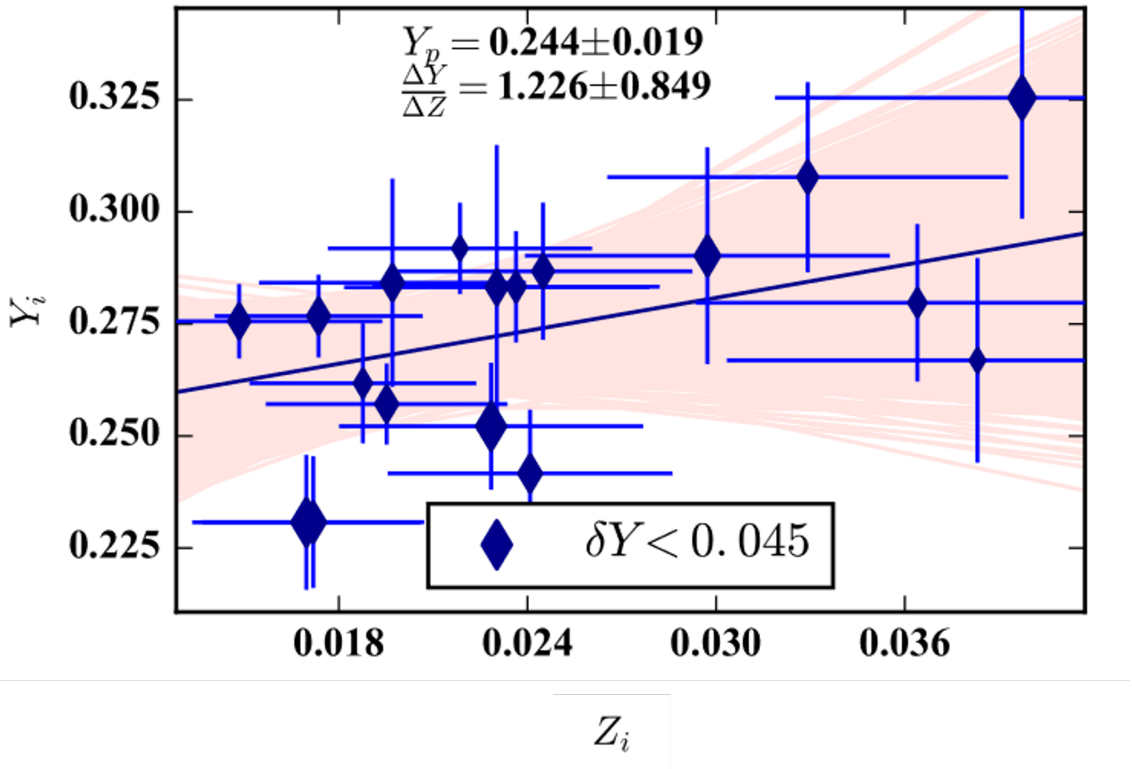


Figure 1.4: The helium enrichment law calibrated from the dwarfs observed by Verma et al. (2019). Adopted from Verma et al. (2019)

Table 1.1: The parameters of the helium line from Vienna Atomic Line Database linelist (Ryabchikova et al., 2015).

Wavelength (Å)	$\log gf$	$E_{\rm low}$ ($\rm cm^{-1}$)	$E_{\rm up}$ ($\rm cm^{-1}$)	$J_{\rm low}$	$J_{\rm up}$
10829.0880	-0.745	159855.9726	169087.8290	1	0
10830.2470	-0.268	159855.9726	169086.8410	1	1
10830.3360	-0.047	159855.9726	169086.7640	1	2

the resonance lines is large, so they do not appear in the late-type stars. Figure 1.5 shows the Grotrian diagram of He I atom with most of the transitions in the optical and near-infrared. The energy of the ground state is located 19.8 eV lower than the next one, 2s triplet level. Such a large energy gap decreases the population of the excited levels, e.g., the singlet and triplet 2s and 2p levels, where most of the absorption lines in the optical and near-infrared region are dependent on. Thus, most of these transitions are not observable in cool stars, i.e., their depth is smaller than 0.01 for the dwarfs with $T_{\rm eff} \lesssim 8000$ K, or for the giants with $T_{\rm eff} \lesssim 7000$ K. One exception is the 2s triplet level. Since the transitions involving the change in multiplicity are forbidden, the 1s helium atom cannot be exited directly by a photon to the 2s triplet state, and vice versa. If there are some other mechanisms that can populate the 2s triplet state, then most of the helium atom will stay at this level, and the transitions related to this level will be strengthened. Such mechanisms exist, and this is the reason why the helium 10 830 Å lines appear in most of the late-type stars.

Since the upper level of the feature is triplets, there are three components around the line wavelength (Table 1.1). Two of the components around 10 830.3 Å have larger oscillator strength ($\log gf$) values and form a strong feature. The third component at 10 829.0880 Å has a smaller $\log gf$ value and is usually weaker. As shown in Figure 1.6, it is a helium line that appears in the spectra of most of the late-type stars (also refer to section 1.4). Here we first explain why He 10 830 is usually stronger than other helium lines by introducing its formation mechanism, and summarize the necessity of studying this feature.

1.3.1 Formation mechanism of He 10 830

As mentioned above, the population of the helium 2s state cannot be populated directly from the ground state by radiation. Other mechanisms, if not one, are then required to exicte the helium atom from the ground state to the 2s state. Some studies

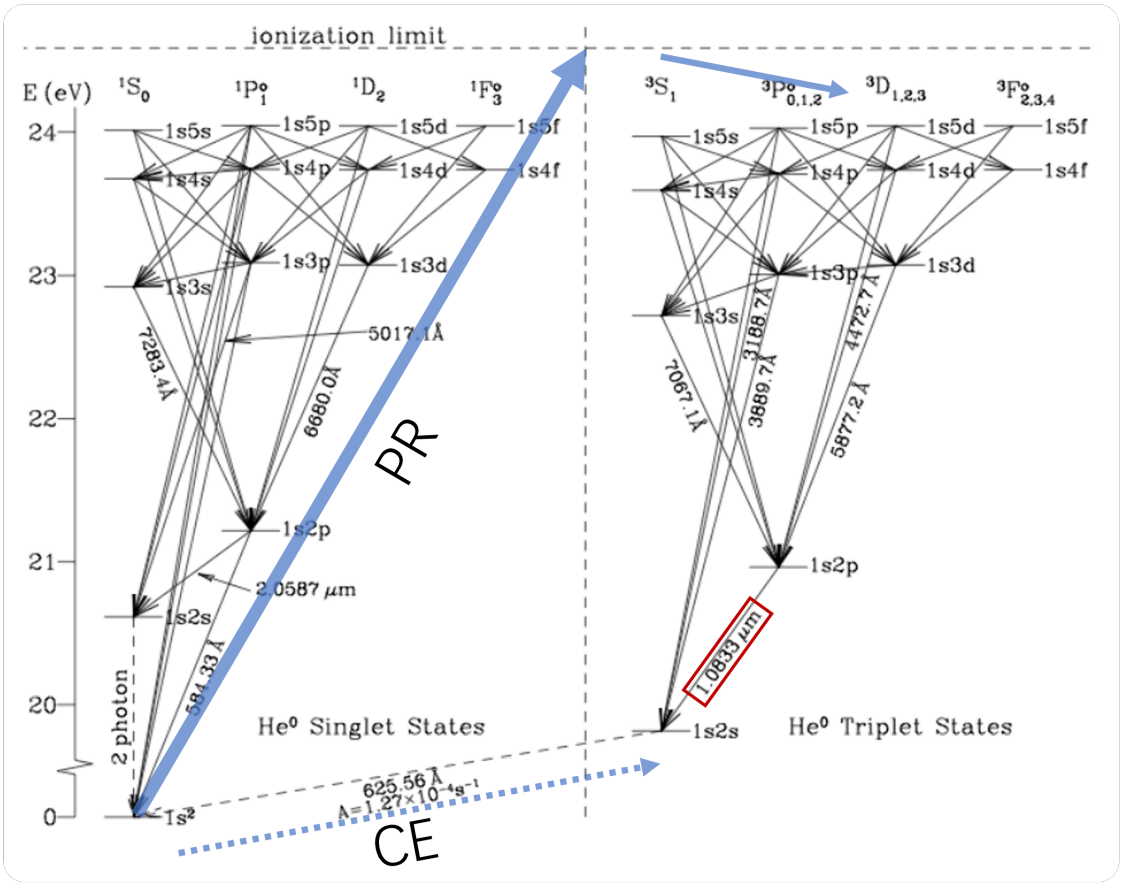


Figure 1.5: The Grotrian diagram of He I, with main transitions in the optical and NIR. The transition of our target feature, He 10 830 is marked by a red square. The black arrows indicate the radiative decay pathways of He atom, while the blue solid and dotted arrays indicate the pathways of PR and CE formation mechanism. Adopted from Kulkarni (2021; https://sites.astro.caltech.edu/~srk/Ay126/Lectures/Lecture4/Helium.pdf).

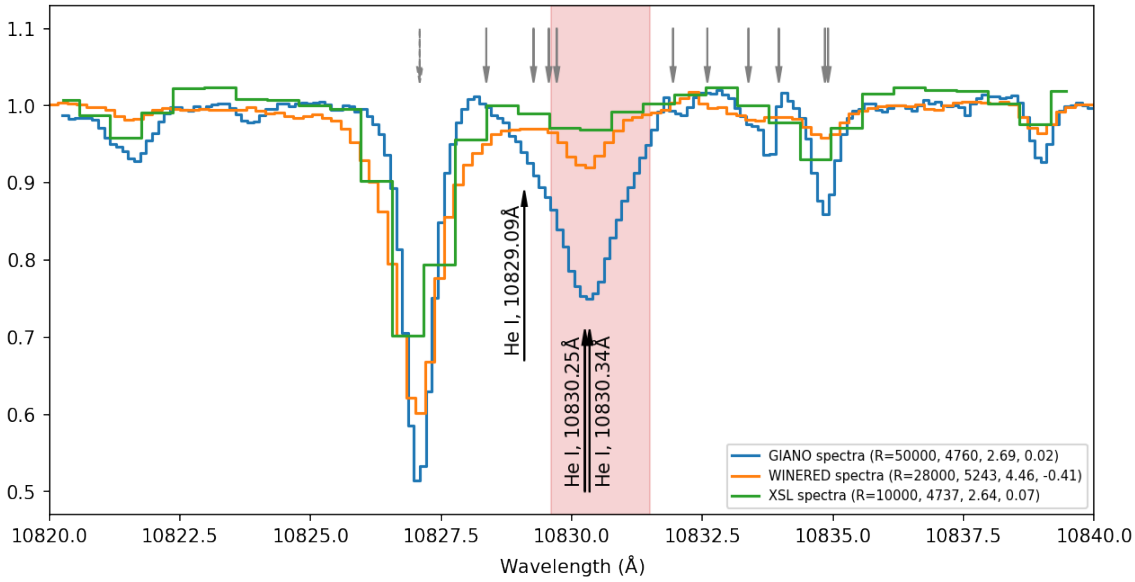


Figure 1.6: Example spectra around 10 830 Å with three resolutions from our sample (Chapter 3). The three values in the legend after resolution (R) are $T_{\rm eff}$, $\log g$ and [Fe/H] of the star. The gray arrows indicate the blending lines with oscillator strength calibrated in Chapter 3, and the red shaded area indicates the wavelength region used for measuring the line strength in Chapter 5.

(Hirayama 1971, Zirin 1975 and Avrett et al. 1994) suggested the photoionization-recombination (PR) mechanism can populate the 2s state. The helium atom can be ionized by the photons with a wavelength shorter than its photoionization threshold, 504 Å. The ionized atom then recombines with a free electron, emits photons and transits to singlet or triplet levels. The recombined atoms in the triplet levels then transit downward, and finally reach to the 2s state. Since the 2s state is the one with the lowest energy in the triplet levels, and the transit to the ground level violates the transition rule, the atoms accumulate at this level. The ionizing high-energy photons are mainly emitted in the corona. They penetrate into the chromosphere and ionize the helium atoms. Thus, the absorption of the photons by the 2s state helium atom occurs in the upper chromosphere.

Collisional transitions, on the other hand, can move atoms from singlet levels to triplet levels directly (Athay & Menzel 1956) if the electron temperature ($T_{\rm e}$) is higher than 20 000 K (in the solar case; Andretta & Jones 1997). This is called the collisional excitation (CE) mechanism. The line formation region when the CE mechanism dominates, roughly in the formation region for the Lyman-α line, is slightly higher than that when the PR mechanism dominates.

The PR and CE mechanisms may both appear in the solar and stellar atmosphere

(see, e.g., Milkey et al. 1973 and Obrien & Lambert 1986), and contribute to the 2s state population as well as the helium line absorption. In the case of the sun, the PR mechanism seems to be dominant. Avrett et al. (1994) and Andretta & Jones (1997) synthesized the He 10 830 in various conditions. The stratification of the solar atmosphere model is varied to simulate the change of chromosphere density and the CE mechanism, and various X-ray and UV radiation (usually called external radiation) is imposed at the top of the atmosphere to account for the PR mechanism. They found that the variation of external radiation can distinctly enhance or diminish the strength of He 10 830, thus the PR mechanism is dominant at least in the solar case. The existence of CE mechanism in the sun cannot be completely ruled out, though. Variation of the chromosphere model also affects the strength of the feature, though usually smaller than that caused by external radiation (Andretta & Jones, 1997).

Whether PR or CE mechanism dominates the formation of He 10 830 for other stars are not clear. Linear relations between the equivalent width (EW) of He 10 830 and the amount of core emission in Ca II H&K lines (quantified by $\log R'_{\rm HK}$) as well as X-ray luminosity for dwarfs are reported in Smith (2016) (see also Figure 1.12). However, $\log R'_{\rm HK}$ and X-ray luminosity are also correlated in this sample, so the change in chromosphere structure may also increases the high-energy radiation. Sanz-Forcada & Dupree (2008) measured the EW of He 10 830 and X-ray luminosity for 9 active dwarfs and 5 active giants. Relations between these two parameters are found in the active giants only, and the authors concluded that the dominant formation mechanism for the dwarfs may be CE mechanism, and that for the giants is PR mechanism. While this may be true for their sample, most of their samples are RS CVn stars and with high activity (e.g., relative large X-ray luminosity). As our targets are non-active stars, the conclusions from these studies may not apply to our sample. Determining the presence of the two formation mechanisms is important for using the helium line as a helium abundance tracer, since the sensitivity of the line strength on the abundance is different when PR or CE is dominant (Chapter 2).

Observing and measuring the He 10 830 can also provide constraints on the stellar chromosphere model. The stellar atmosphere model is the basis of chemical abundance measurement using spectral lines. The strength and profile of the spectral absorption lines (the one we are focusing on in this thesis) are controlled by the physical conditions of the region where the absorption is formed. The conditions include temperature, density, the extent of turbulence and chemical composition. Only when temperature, density and the extent of turbulence are determined for a star, can we

determine the chemical abundance by fitting the synthetic spectra with the observed ones. Thus, a good stellar atmosphere model is usually required in industrial spectral analysis. Most of the lines used in measuring the abundances are formed in the middle or bottom of the photosphere. The density in this region is higher than that in the upper layers, thus the radiation and materials are well coupled. They are in local thermodynamic Equilibrium (LTE), and the construction of such atmopshere model is well established. For example, the model with $3500 \leq T_{\rm eff} \leq 10000\,{\rm K}$, $0 \leq \log g \leq 5$ and $-5 \leq {\rm [M/H]} \leq 1$ are availabe in the ATLAS9 model collections (Kurucz, 2005). The model of upper layers, i.e., chromosphere, transition region and corona, is not well determined yet. The density in these layers are lower than that of the photosphere, thus the LTE assumption is not valid. The usual way to determine the atmosphere model is then assume a temperature stratification in the chromosphere and calculate the synthetic spectra of chromosphere lines. They are then compared with the observed spectra, and the temperature profile is modified to produce a good match between the observed and synthetic spectra. This is called empirical modeling. Such an approach requires observing multiple lines formed in various layers to provide enough information for constructing the temperature profile. The most widely used solar chromosphere model is the one developed in Vernazza et al. (1981), or the VAL models. Figure 1.7 presents the temperature profile of their model C, with the formation region of chromosphere lines labeled. He 10 830 is not included in the lines used to determine this temperature, thus if observation of the He 10 830 is available for the sun and other stars, then it can better constrain their temperature profile.

In summary, observation of a large sample of stars, a consistent method for measuring its strength, and discussion on its reaction to the variation of helium abundance are necessary. We then discuss whether the previous observation can achieve this goal.

1.4 Previous observations on He 10 830

1.4.1 Previous observations of the field stars

This section introduces and summarizes the previous results on He 10 830. The first observation on this line for stars other than the sun was reported in 1968. The observations later on until the 1980s gathered a large sample of solar-metal field stars. However, their measurement precision was limited for various reasons: the spectral resolution, the instruments and measurement methods available then. The measurements in the 1990s and later are significantly better, and the measurement methods got established enough for comparing the values in different studies with

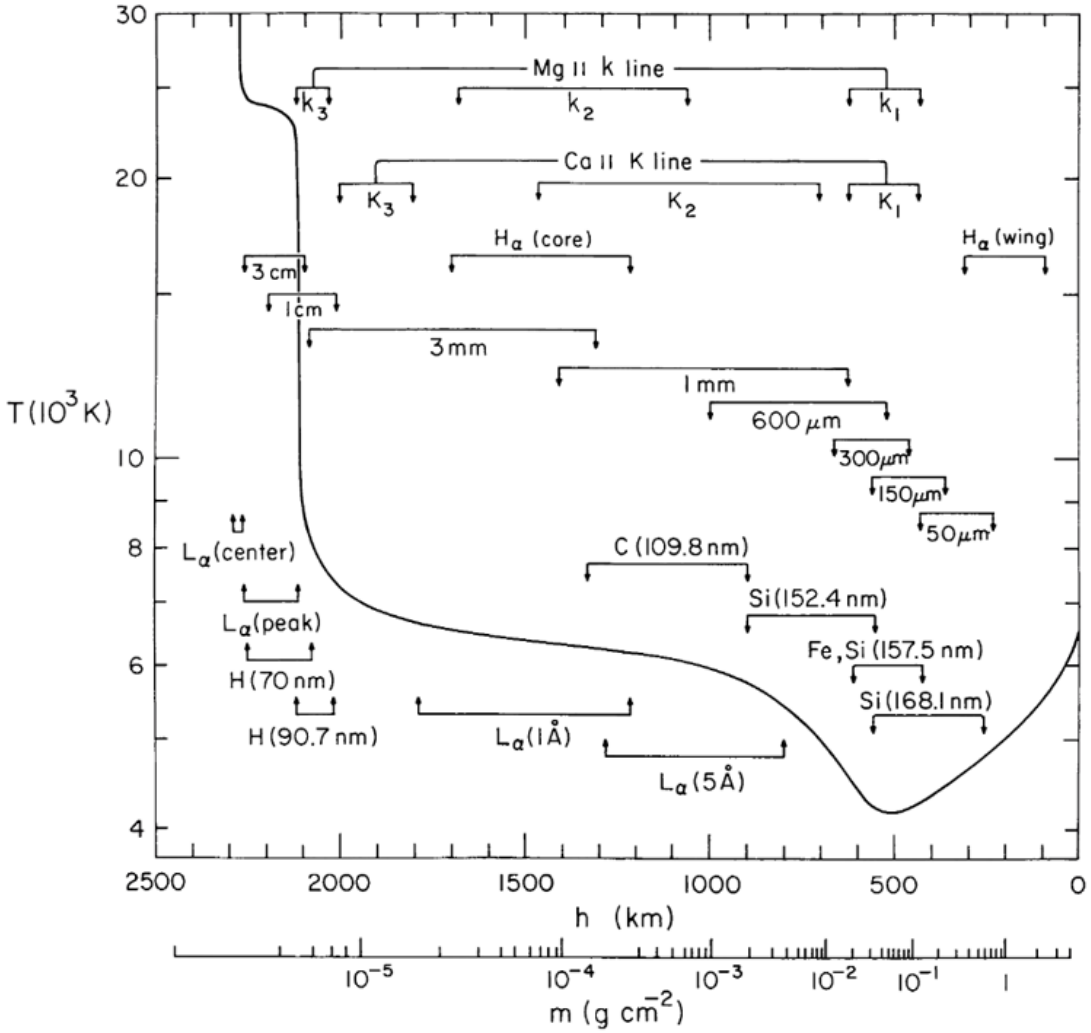


Figure 1.7: The temperature stratification and line forming regions of the VAL-C model. The model is divided into three parts: lower chromosphere (Height h from 0 to 500 km), upper chromosphere (0–2000 km) and transition region ($>$ 2000 km). Adopted from Vernazza et al. (1981).

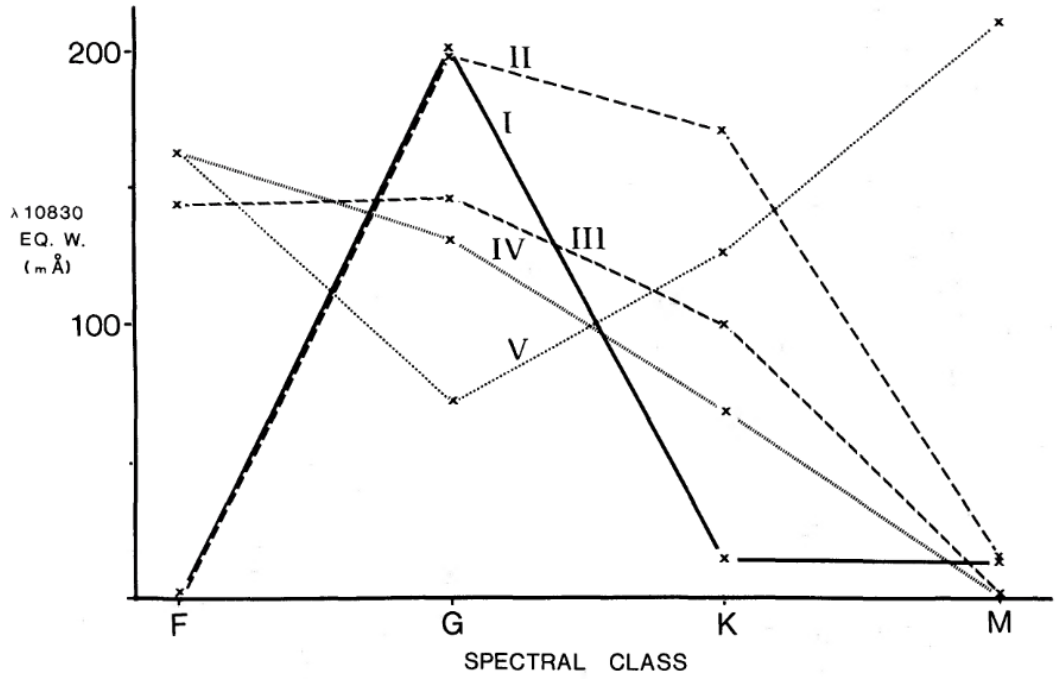


Figure 1.8: The average He 10 830 EW versus spectral type from the Zirin (1982) sample. Trends of stars with different luminosity types are separated and labeled by their types. Adopted from Zirin (1982)

each other. Most of the targets in the 1990s and later are metal-poor stars, thus they form a good sample to compare with our sample stars which are around solar metallicity.

1.4.1.1 Observations from 1960s to 1980s

The observation of He 10 830 in late-type stars was initiated by Vaughan & Zirin (1968). The line strengths of 86 stars with spectral types from F0–M5 were measured using image-tube spectrographs and a spectrum scanner. The line equivalent widths (EWs) for the M- and F-type stars are smaller than that for the K-type stars. The author also tried to correlate the EW with some other parameters, such as the Ca II K emission intensity. Similar results were also obtained by Zirin (1976) with a larger sample. Later Zirin (1982) greatly enlarged the sample by providing the EWs of 455 F–M type stars, with their luminosity type ranging from I to V. Such a large sample allowed them to derive the first empirical trend between EW and some other parameters (Figure 1.8). He also found that the width (line broadening, not the EW) of the helium line is larger in giants than in dwarfs.

Smith (1983) found a relation between the X-ray luminosity (L_X) and the He 10 830 strength using F–K dwarfs and G–K giants. Despite some scatters, the increase of the EW for dwarfs and giants is accompanied by the increase of the X-ray luminosity. The dependency on the X-ray luminosity was later confirmed by Zarro & Zirin (1986), where the authors also state that the dependency was unclear in the dwarfs with spectral type earlier than F7. The L_X–EW correlation was also discovered in supergiants, though only three stars (β Dra, 56 Peg and β Cam) show extremely large EW and X-ray luminosity. The appearance of these relations indicates that the photoionization-recombination (PR) mechanism plays an important role in the He 10 830 formation of these stars.

The He 10 830 strengths of 60 F, G and K type giants were measured by Obrien & Lambert (1986). These values are, for the first time, plotted in the HR diagram and compared with the coronal dividing line (CDL). The CDL is a line separating stars with and without obvious high-temperature corona. Linsky & Haisch (1979) acquired the UV spectra of 22 bright field stars, and inspected lines presented in the spectra. The presence of Hydrogen Lyman-α and some other single or doubly ionized lines indicate that there is plasma present with temperatures less than 20 000 K in this wavelength region, while those with higher ionization state indicate plasma with $T > 20\,000$ K. These two groups of lines approximately correspond to the temperature of the chromosphere and corona, thus the occurrences of these lines in the spectra can reveal the possible presence of either a chromosphere or a corona or both. Linsky & Haisch (1979) divided their sample into two groups by a coronal dividing line (CDL), with one showing both the chromospheric and coronal lines, and another showing only the chromospheric lines. The first group consists of all the observed dwarfs including the Sun, and a part of giants with $T_{\rm eff} < 4500$ K, while the second group consists of the lower-temperature giants. The authors suspected that the energy input to the corona of low-temperature giants is smaller, and most of them are in the form of stellar wind and being carried away from the star. Thus, all the dwarfs and giants with $T_{\rm eff} > 4500$ K are expected to have at least some extent of corona, and they are not the ideal target for measuring the helium abundance using the helium 10 830 Å line.

As shown in Figure 1.9, the stars located on the different sides of the CDL show different behaviors: those on the left always show absorption, and those on the right show both absorption and emission. The relation between He 10 830 EW and the flux in the C IV line at 1550 Å reported in Obrien & Lambert (1986) indicates that there

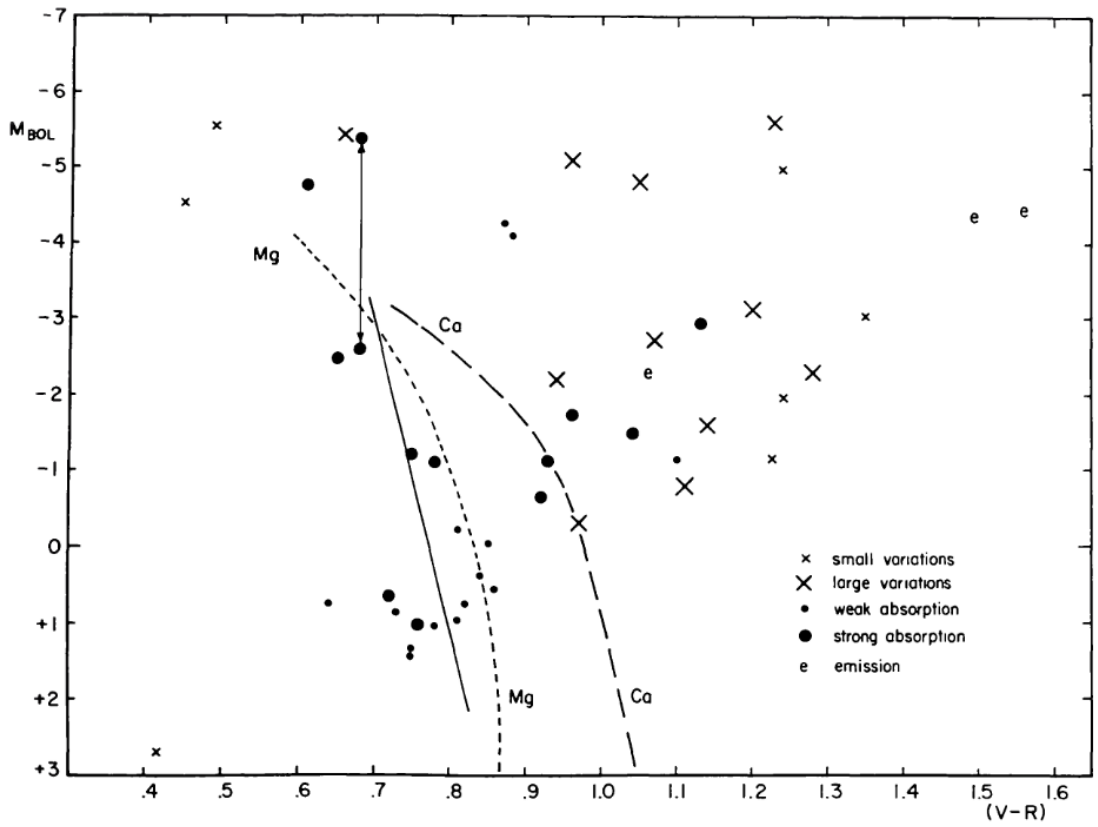


Figure 1.9: The HR-diagram with the stars observed in Obrien & Lambert (1986). The solid line is the coronal dividing line from Linsky & Haisch (1979). Adopted from Obrien & Lambert (1986)

is another mechanism of forming the He line, by populating the lower state of the transition through collision, since the C IV line is sensitive to the collision.

Lambert (1987) performed a long-term observation of He 10 830 in 19 late-type stars. The observation of Arcturus from 1978 to 1987 reveals the time variability of the He line in this star. The EW is varied throughout the 10 years, with a period of 78 days (or a multiple). They concluded that this period should be related to the rotation period of Arcturus, since the variation on the helium line EW is caused by the inhomogeneity of the absorption on the surface of the star.

It is worth mentioning that the above measurement of the line strength is not precise and the targets may be biased. Zirin (1982) states that the measurement below 100 mÅ is not precise and the sample is "somewhat biased in favor of more active stars". The reason for the limited precision may include the relatively low spectral resolution of the spectra, systematics of the measurements with different spectrographs, and the method for line strength measurement. The detection limits in

many previous studies were higher than 20 or 30 mÅ, and stars without the detection could still have weak but significant absorption of the He line. Detecting stars with large He 10 830 EW, i.e., active stars, was thus favored under this condition. We include the previous measurement of helium line strength described in this section in the catalog we compile, but they will not be compared quantitatively with newer measurements including our own.

Table A.1 lists the compiled line EW from the above studies, cross-matched with the stellar parameters from SIMBAD Astronomical Database. For the stars with multi-epoch measurements, they are excluded from the comparison if the scatter of the EWs is larger than 50 mÅ. For those with a scatter smaller than 50 mÅ, their mean values are adopted as the EW. Those with emissions in the helium line, i.e., the negative EW, are also excluded.

We divided the He 10 830 EW measurements from Zirin (1982) into two groups with $\log g$ larger and smaller than 3.3, approximately corresponding to the luminosity types V and III. They are plotted against $T_{\rm eff}$ in Figure 1.10, with the type V and III trends from Figure 1.8. The average EW of dwarfs is roughly consistent with the trends, but the numbers of stars in the low $T_{\rm eff}$ end are limited. The scatter in the EW of giants is large, so the comparison with the trend barely yields consistency.

Figure 1.11 presents the Kiel diagram of the samples summarized above, with their He 10 830 EWs indicated by color. No clear trend can be seen in this plot, mainly because the measurement of the EW is not precise, with some measurements rounded into 50 mÅ. Smith et al. (2004) concluded from a sample of metal-poor giants that the stars with $T_{\rm eff} < 4600$ K shows weak absorption. However, some low-temperature giants still have large EWs, indicating that the metal-rich stars may show different behavior compared to the metal-poor stars.

1.4.1.2 Observations after 1980s

Observations of He 10 830 for field stars after the 1980s are with higher precision, mainly because of the increase in spectral resolution and the use of modern spectrographs. The helium line of HD 6833 was observed in Dupree et al. (1992), and the authors were focused on the line profile. The line wing for this star extends to the position of the strong Si line on its left, corresponding to a radial velocity of -90 km/s. This value is comparable to, or larger than the escape velocity from the photosphere of the star. Later Smith et al. (2004) performed a similar study for 10 metal-poor giants, with 4 in the field and 6 in the globular cluster M13. They found that the stars with obvious He absorption have chromospheric outflow velocities ranging from

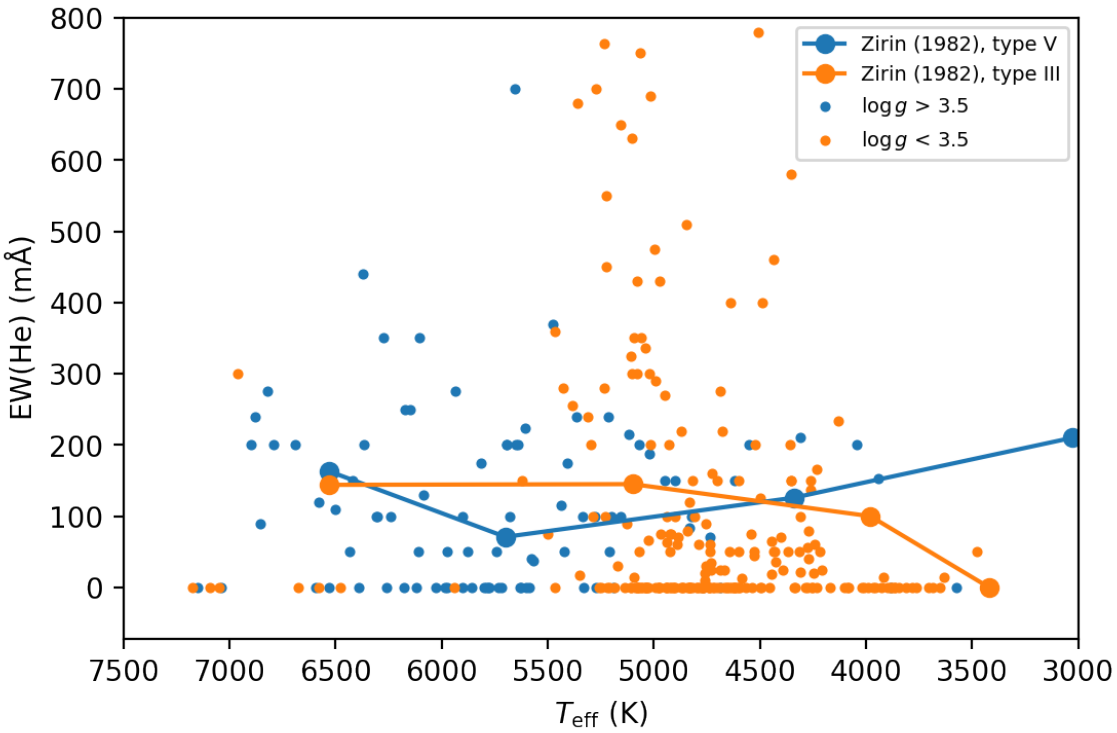


Figure 1.10: The average He 10 830 EW from the Zirin (1982) sample versus $T_{\rm eff}$. Zirin's trends with luminosity type V and III are converted to $T_{\rm eff}$ and overplotted for comparison.

Table 1.2: Summary of previous observations on He 10 830 for field stars. Note that no table is given in Smith (1983), and the helium line strength measurement in Smith (2016) are adopted from Zarro & Zirin (1986).

Study	Main targets	Number of stars
Vaughan & Zirin (1968)	FGK giants	86
Zirin (1976)	GK dwarfs & giants	122
Zirin (1982)	FGK dwarfs & giants	455
Smith (1983)	FGK dwarfs & giants	-
Zarro & Zirin (1986)	FGK dwarfs & giants	113
Obrien & Lambert (1986)	GK giants	60
Lambert (1987)	GK giants	19
Dupree et al. (1992)	HD6833	1
Smith et al. (2004)	Red giants	4
Sanz-Forcada & Dupree (2008)	Active stars	7
Dupree et al. (2009)	Metal-poor giants	41
Takeda & Takada-Hidai (2011)	Metal-poor dwarfs & giants	33
Smith et al. (2012)	Metal-poor subdwarfs	23
Smith (2016)	Metal-poor dwarfs	-
Fuhrmeister et al. (2019)	M-type dwarfs	319

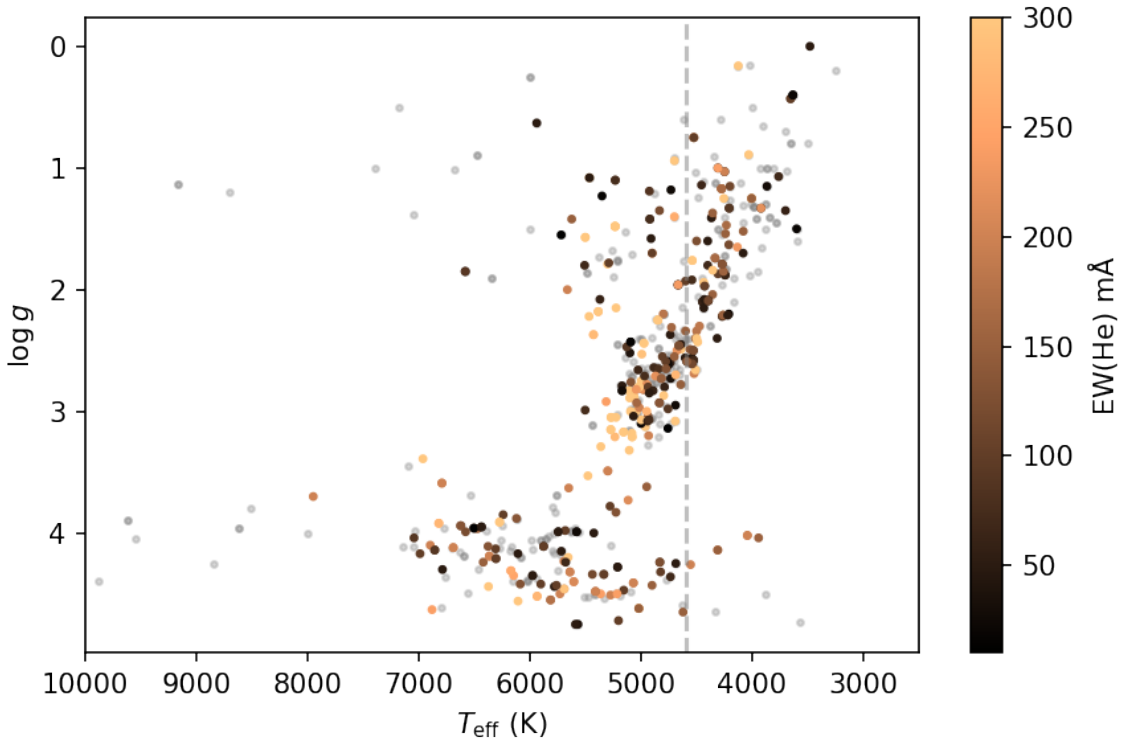


Figure 1.11: The Kiel diagram for the observations from the 1960s to 1980s, color coded by the He 10 830 EW. The stars with EW ≤ 0 are in gray. The vertical dashed line indicates the boundary of stars showing clear absorption proposed by Smith et al. (2004).

30 to 140 km/s. Such velocities are comparable to the escape velocity of the cluster core, and suggest that the stellar wind could clear out the interstellar medium of the globular cluster.

The observation reported in Sanz-Forcada & Dupree (2008) filled the blank of the relation between He 10 830 EW and X-ray luminosity for very active stars. They obtained the spectra of 7 dwarfs and 7 giants with an unprecedented resolution of R∼170 000, and correlated their line strength with extreme ultraviolet (EUV) and X-ray luminosity from Extreme Ultraviolet Explorer. The EW of dwarfs is saturated in $L_{\rm x}/L_{\rm bol} > -4$, with a maximum EW of ∼300 mÅ. This value is consistent with the result in Andretta & Giampapa (1995), which states that the line will be in emission if the activity level is higher. On the other hand, the linear relation between $L_{\rm x}/L_{\rm bol}$ and EW for giants extends up to 1000 mÅ, with no evidence of saturation. The two competing mechanisms, PR and CE mechanisms, are both important in the formation of the line in this sample, while the PR mechanism is dominant for giants, judging from the tight relation with X-ray luminosity.

Dupree et al. (2009) extended the empirical relation between the He 10 830 EW and $T_{\rm eff}$ to horizontal branch stars. Their sample of metal-poor giants consists of the red giant branch (RGB), asymptotic giant branch (AGB), and red horizontal branch (RHB) stars. Their EWs are systematically weaker than metal-rich stars (or "POP-I" stars in their paper). The EW for RHB stars is strongly correlated with $T_{\rm eff}$, possibly related to the development of a hotter chromosphere. The effect of the helium abundance on the line strength was discussed for the first time, and the idea of detecting the variation of line strength using member stars belonging to the different stellar populations in globular clusters was proposed.

The two subsequent studies on He 10 830 focus on the metal-poor dwarf. Takeda & Takada-Hidai (2011) and Smith et al. (2012) stated that there is no clear correlation between the line strength and metallicity, at least for the dwarfs with $-3.5 < [{\rm Fe/H}] < -0.5$. Stars with solar metallicity in Takeda & Takada-Hidai (2011) show a large scatter in EW, which is consistent with the conclusion of previous studies, e.g., Zarro & Zirin (1986).

Smith (2016) combined the He 10 830 EW measured in Zarro & Zirin (1986) with modern chromospheric activities (including X-ray luminosity from ROSAT and Ca II $R'_{\rm HK}$ index from Mount Wilson observation) and reported the tight relation between EW–$L_{\rm x}$ and EW–$\log R'_{\rm HK}$ for dwarfs (Figure 1.12). This is the first study that correlates the He 10 830 EW with the $R'_{\rm HK}$ index, and the relation is tighter than those using K band intensity (e.g., Vaughan & Zirin 1968).

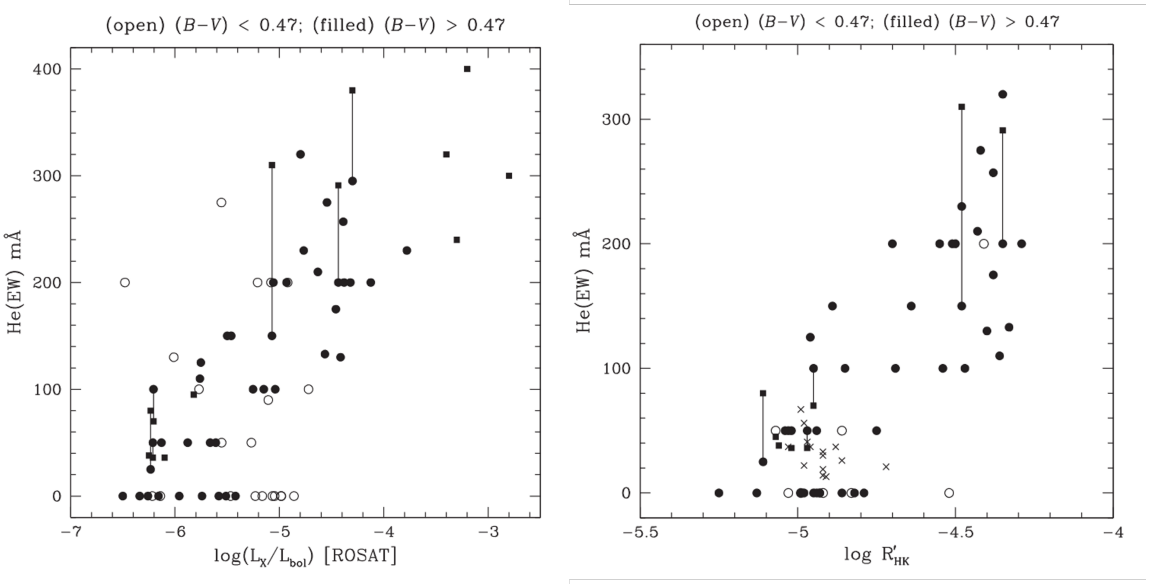


Figure 1.12: The He 10 830 EW versus fractional X-ray luminosity (left panel) and $\log R'_{\rm HK}$ index (right panel) for dwarfs. Adopted from Smith (2016).

Recently, the He 10 830 EW and variability of more than 300 M-type dwarfs are reported by Fuhrmeister et al. (2019). They are observed by the high-resolution spectrograph CARMENES (Seifert et al., 2012) and be used as an activity indicator. Systematic variations with the effective temperature, i.e., the decrease of the EW towards lower temperature are found (Figure 1.13).

The observations of the He 10 830 EW in this section (sec:obs-1980s-) are compiled together with those introduced in section 1.4.2. The sample size in the studies is mainly around a dozen, with a preference for active stars or metal-poor stars. Their precision, ~ 10 mÅ, is small enough to compare the values in different studies. However, the relations from Zirin (1982, Figure 1.8) is still the most complete sample showing variation of the He 10 830 EW against $T_{\rm eff}$. The measurement from such ambiguous relations is not precise enough for planning future observation (e.g., the required signal-to-noise ratio) on He 10 830. A homogeneous sample covering wide ranges of $T_{\rm eff}$, $\log g$ and metallicity is required for filling this gap, and would provide constraints on the formation mechanism of the feature.

1.4.2 Previous observations of globular cluster stars

As described in section 1.4.1.2, the first observation for globular cluster members on He 10 830 is Smith et al. (2004) for M13. The main focus of this study is the mass outflow of the stars, thus the line strength was not correlated with the indices

Table 1.3: Summary of previous observations on He 10 830 for globular cluster stars

Study	GC	Number of stars
Smith et al. (2004)	M13	6
Pasquini et al. (2011)	NGC2808	2
Dupree & Avrett (2013)	ω Cen	2
Smith et al. (2014)	M13	6
Navarrete et al. (2015)	ω Cen	24
Strader et al. (2015)	M4	16

related to stellar populations. Later Dupree et al. (2011) observed 12 stars in ω Cen, and found a bimodal distribution in EW. The EWs of these stars is correlated with Na and Al abundances, i.e., those with strong helium line absorption are also with large [Na/Fe] and [Al/Fe], and vice versa. As introduced in section 1.2.1, the Na-Al correlation is believed to be one of the indicators for multiple stellar populations in globular clusters. The Na and Al enriched stars are expected to have a larger He 10 830 EW, thus the bimodal distribution detected in Dupree et al. (2011) may infer the difference in helium abundance among the stars.

More detailed studies on smaller size samples were performed later by Pasquini et al. (2011) and Dupree & Avrett (2013), for two giant stars with different Na and O/Al abundances, respectively. These studies obtained the near-infrared and optical spectra covering He 10 830 and Ca II H&K lines or Hα/β line. The Ca or H lines were used to derive the empirical atmosphere model of the giants, and the helium abundance is determined by varying the input abundance of the model to fit the observed He 10 830 feature. A helium abundance difference, $\Delta Y \geq 0.17$, between the stars was reported in both of the studies.

Deriving helium abundance using the empirical model from chromospheric lines, as done in the two studies described above, would be difficult and time-consuming. The NLTE calculation on the radiative transfer in the photosphere and chromosphere for H, He and Ca atom is necessary, and the whole process needs to be repeated a few ten or hundred times to get the chromosphere model matches the observation. Thus later observation on GCs adopted another approach: assuming that the structure of chromosphere is similar for stars located in a small region on the Kiel diagram, a large sample of stars from different stellar populations are expected to show systematic differences in the He 10 830 strength. Smith et al. (2014), Navarrete et al. (2015) and Strader et al. (2015) observed such stars in M13, ω Cen and M4, respectively. However, the evidence of He 10 830 EW difference is not obvious in all these stars. For example, the M13 stars with different CN indices all have EWs around 50 mÅ

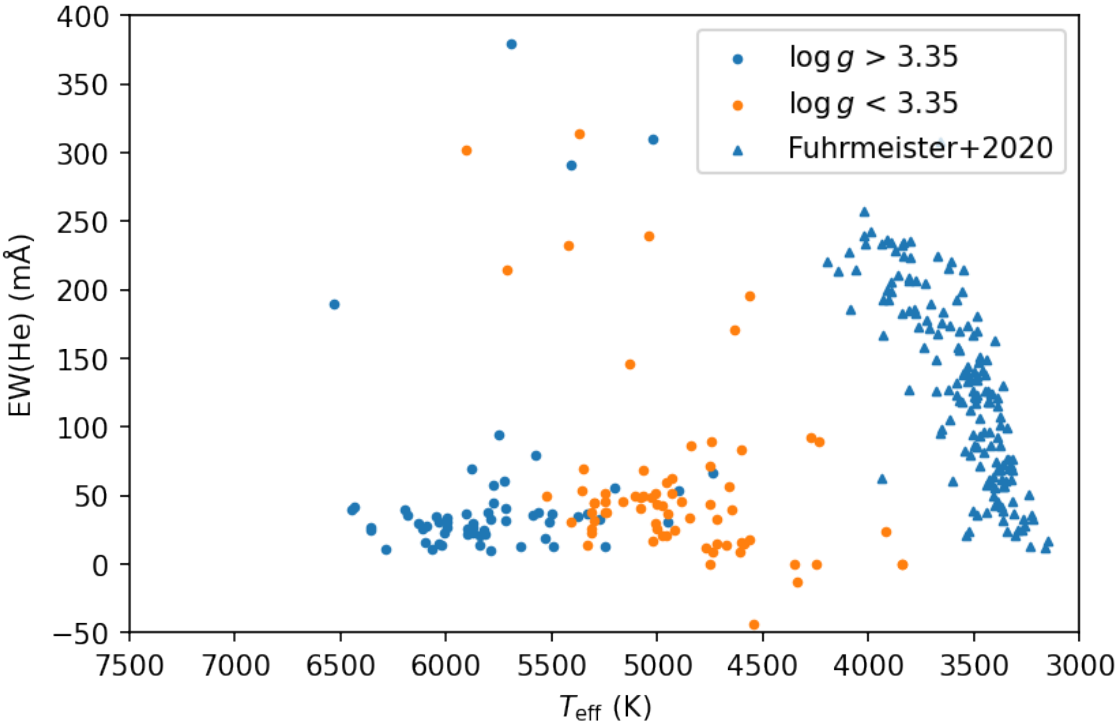


Figure 1.13: The He 10 830 EW versus $T_{\rm eff}$ for the stars observed after the 1980s.

(Figure 3 of Smith et al. 2014), and stars showing strong and weak helium absorption are not separated to either end of the Na-Al correlation (Figure 6 of Strader et al. 2015).

The EW of He 10 830 in section 1.4.1.2 and those in this section are compiled and listed in Table A.1. Figure 1.13 presents the empirical trend towards $T_{\rm eff}$, similar to those shown in Zirin (1982). The line strength of FGK-type dwarfs and giants are weaker than those in Figure 1.10, except for the M-dwarfs from Fuhrmeister et al. (2019).

Such difference may be explained by the difference in metallicity between the samples. Figure 1.14 presents the histogram of the samples described in this section. The older, less accurate observations are concentrated around solar metallicity, while those observed later, are with lower metallicity. As described in section 1.4.1.1, the blue sample in this figure will not be used to compare with our new observation in this thesis. Though the comparison of the line strengths between the samples indicates that metal-poor stars would have a weaker helium line, whether this is a solid trend, and the reason for such a difference in EW is still unclear. A new sample with dwarfs, giants and supergiants covering solar metallicity is necessary.

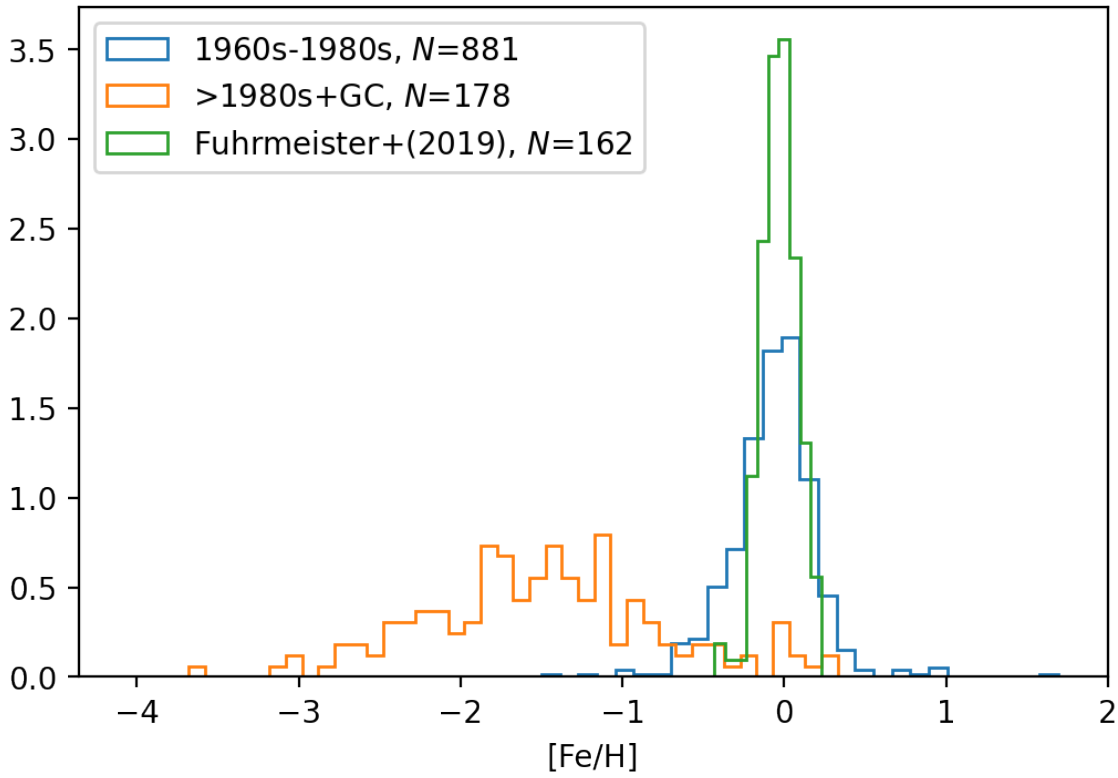


Figure 1.14: The [Fe/H] histogram of the sample summarized in section 1.4, divided to those observed in the 1960s–1980s, after the 1980s (including globular cluster member stars) and the M-dwarfs from Fuhrmeister et al. (2019). The area of the histograms are normalized to better present their distribution, and the number of the samples are written in the legend.

1.5 Aims and structure of the thesis

This thesis aims to provide the measurement of the helium line strengths, X-ray radiation and the Ca II H&K index for a large sample of stars, use them to discuss the formation mechanism for different kind of stars and the possibility of using the helium line as an abundance tracer.

The solar atmosphere model with chromosphere was firstly used to synthesize the chromosphere lines. The behavior of these lines under the PR and CE dominant case for the He 10 830 is then characterized, and we discuss the behavior of the helium line in the PR or CE dominant cases with different conditions, such as high-energy radiation, density and helium abundances.

We then collected three groups of stars with their He 10 830 observed with resolutions ranging from 10 000 to 50 000. As shown in Figure 1.6, the helium absorption is wider than other atomic lines. Thus its strength may be blended with other weak atomic lines. The spectra with the highest resolution are used to estimate the blending around the helium line. We calibrate the oscillator strengths of 10 atomic lines around 10 830 Å by matching the synthetic spectra with the observed ones. The blending equivalent width is then calculated from the synthetic spectra using the linelist with calibrated oscillator strengths and subtracted from the helium line equivalent width.

A method to fit the profile of the helium line is then derived, and used to measure its strength. The continuum is corrected before the strong lines on both side is removed by profile fitting, and we fit the pixels with a skewed-Gaussian profile in a specified wavelength. For those with a weak absorption feature or in a low resolution, we directly sum up all the pixels in that region and set the result as the line strength. Then for those with Ca II H&K line and X-ray photometric observation, we measured their S-index, $\log R'_{\rm HK}$ index and fractional X-ray luminosity.

These values are then compared with the stellar parameters ($T_{\rm eff}$, $\log g$ and [Fe/H]) to discuss whether the PR or CE mechanism is dominant for dwarfs and giants in various temperatures. Such comparisons also provide a rough estimate of the helium line strength when the stellar parameters are given. We then discuss the feature we found in the empirical trends and its possible explanation. A simple giant model is then used to generate the synthetic spectra to probe that CE formation mechanism can also create an obvious He 10 830 feature. We also discuss the parameter ranges of the stars whose helium line is expected to be used as abundance tracer, and compare them with previous globular clusters observation.

The structure of the thesis is as follows: We make use of NLTE spectral synthesis to explore the formation of the He 10 830 and its sensitivity to $\log R'_{\rm HK}$ index, fractional X-ray luminosity and helium abundance in Chapter 2. We then describe the targets and observations of our sample in Chapter 3. Their data reduction and the calibration of the blending line follow in Chapter 4. Chapter 5 describes the measurement of He 10 830 and chromosphere lines. The empirical trend with stellar parameters is discussed in Chapter 6. Finally, in Chapter 7, we discuss the new trends found in our observation, their possible reason, and what kind of stars should be used if we want to use the helium line as an abundance indicator.

We note that the author and collaborators contribute to the observation and data reduction of the spectra used in this thesis. The Stock-2 spectra are observed and reduced by the stellar population astrophysics group in ESO, and the field-XSL data are observed and reduced by the XSL group. The WINERED group members handle the WINERED spectral data, and the author is also involved in the observation and reduction. The author then performed the data analysis after the 1D spectra for our sample are reduced. The situatoin of the target and data is also described in Chapter 3 and 4.

Chapter 2

Formation and synthesis of He 10 830

This chapter discusses how He 10 830 is formed and its behavior under various conditions. In order to understand the underlying physics, we perform the theoretical synthesis of He 10 830 using the solar atmosphere model. The formation region of the helium and other chromospheric lines derived from the radiative transfer calculation can be used to confirm whether they are overlapped, and the experiment with varying input models can reveal the dominant formation mechanism in various conditions, and the sensitivity to the helium abundance.

The helium 10 830 Å line is formed in the chromosphere, where non-local thermodynamic equilibrium (NLTE) is important in the radiative transfer. Local thermodynamic equilibrium, or LTE, refers to the situation that the properties of the atmosphere, e.g., the population of states for an element and the amount of radiation at each wavelength, can be described by the local physical conditions, along with the thermodynamic equilibrium formulae. The source function becomes the Planck function and the population of atoms in each state follows the Saha-Boltzmann distribution. They can be calculated independently from the local temperature, pressure and chemical composition, thus the radiative transfer calculation is simple. The photosphere is the region that can be well described by LTE, and where most of the stellar atomic lines form.

However, the LTE hypothesis is not applicable to the helium 10 830 Å line. The density in the upper chromosphere is at least three orders lower than that in the photosphere (see, e.g., Linsky 2017). The mean free path of the photon is then longer, so the photons can travel for a long distance in the atmosphere. The "information" stored in the photon would be brought to the place where it is destroyed, and alter the local physical parameters in that place. That said, the local physical parameters

are not only determined by the local radiation and material, but also by the non-local radiation emitted from other locations. The source function is biased from the Planck function in the NLTE, and the state populations also do not follow the Saha-Boltzmann distribution.

We note that the NLTE radiative transfer calculation used in this study is limited to the 1D model and under the trace element assumption. The use of trace element assumes that except for hydrogen, the NLTE populations of all other elements do not affect the atmosphere structure, atom level, or the NLTE population of other elements. This assumption allows us to calculate the NLTE population of the elements interested separately, after the NLTE population of hydrogen is determined, thus it simplifies the calculation. Here helium and calcium are treated as trace elements. The observed spectra of our sample stars are integrated flux spectra, which reflect the averaged fluctuation of physical parameters in each depth point. Also, the computational cost for the 3D NLTE model is much higher than its 1D counterpart. Thus, using the 1D NLTE model is feasible for this study.

2.1 Process and code for NLTE spectral synthesis

The most important part of NLTE spectral synthesis is to determine the NLTE state population of the atom(s) of interest. This is achieved by solving the multiple equations involved in the radiative transfer numerically. An initial population is first assumed and put into the equations. The absorption and emission coefficients, thus the source function can be calculated from the population. Then the radiative transfer equation is solved, deriving the intensity of the light transported in the atmosphere. The intensity then alters the population through scattering, thus the population is corrected by the calculated intensity. The change of population then in turn changes the absorption/emission coefficients, source function, and finally the intensity. State populations are thus iterated in each round of the radiative transfer calculation, until they reach the convergence criteria. The detail of the process for establishing an NLTE stellar atmosphere is described, e.g., in chapter 18 of Hubeny & Mihalas (2014).

The NLTE radiative transfer code used in this study is MULTI (Carlsson, 1986). The advantage of using MULTI compared to other NLTE codes is the switch of external radiation. The presence of the PR formation mechanism of the He 10 830 is connected with the high-energy EUV or X-ray photons with a wavelength smaller than 504 Å to ionize the helium atom. This radiation is usually generated in the corona,

which is the further upper part of the stellar atmosphere. The stellar atmosphere models mentioned and used in this chapter are optimized to fit the spectral features formed in the chromosphere, but the corona is not included. MULTI can include a spectral external radiation emitting from the top of the atmosphere in the radiative transfer process. This radiation can simulate the high-energy radiation from the corona illuminating the chromosphere.

The process of the NLTE spectral synthesis includes:

1. Determine the atmosphere structure: setting a list of column mass, temperature, electron number density, radial velocity and turbulent velocity.

2. Generate the atom model file. This file stores the data of the levels and transitions of the atom. We use 6-level hydrogen, 6-level ionized calcium and 18-level helium in this study.

3. Perform the hydrogen run: run the code to calculate the NLTE population of hydrogen and the electron density, and store them in the atmosphere file. The Hα and Hβ lines are also synthesized in this step.

4. Perform the calcium run: calculate the NLTE population of the ionized calcium, and synthesize the Ca II H&K line. Note that the population is only used for line synthesis but not stored for later use.

5. Perform the helium run: calculate the NLTE population for helium, and synthesize the helium 10 830 Å line.

The synthesized absorption is then compared with the observed one when available.

2.2 The solar and stellar chromosphere models

We adopt the VAL-C model from Vernazza et al. (1981, model C) as the solar model used in this chapter. The VAL-C model is one of the commonly-used solar models with a detailed chromosphere structure. The model is set to provide a good agreement between synthetic and observed intensities in several wavelength ranges, including the EUV wavelength range from 400-1400 Å, hydrogen Lyman-α, Lyman-β and Ca/Mg II resonance lines. This model is widely used for the discussion in the formation of helium 10 830 Å line, such as Andretta & Jones (1997). Figure 2.1 presents the radial profile of the VAL-C model. The two most conspicuous features in the temperature

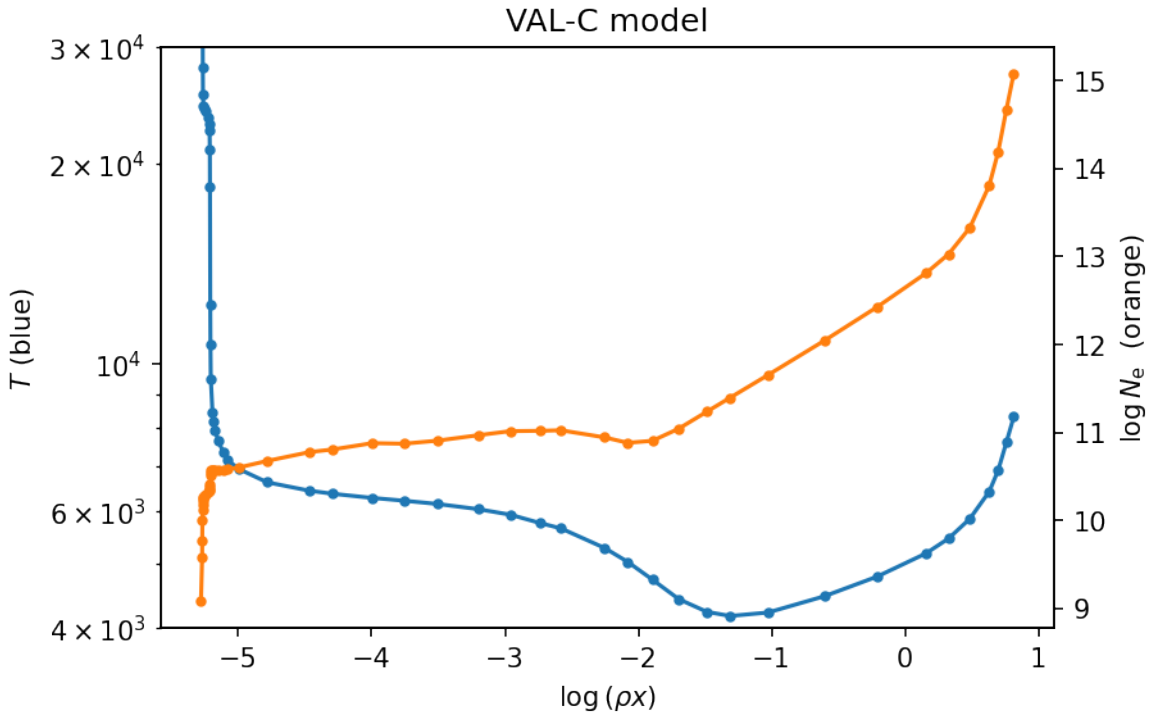


Figure 2.1: Temperature and electron number density structure of the VAL-C model. The horizontal axes, $\log \rho x$ is the logarithm of column density in $\mathrm{g\,cm^{-2}}$, and this value increases from the outer part (transition region on the left side) of the model to the inner part (photosphere on the right side).

profile is the temperature rise in the upper chromosphere ($-5 < \log \rho x < -2$, where ρx represents the column density) and a small plateau with $T \sim 24000\,\mathrm{K}$. The temperature rise is required to explain the core emission of the Ca II H&K lines (Linsky & Avrett, 1970), and the small plateau is for matching the observed emission in the Lyman series (the Layman plateau). Later a new series of models were developed in Fontenla et al. (1990, 1991) and Fontenla et al. (1993) (FAL models). More physical processes are included in these models, and the Lyman plateau is no longer needed. However, Andretta & Jones (1997) stated that the match between the synthetic spectra from FAL models and the observed one for He 10 830 was not good. Considering that the model calculation in this chapter only serves as a qualitative explanation for the formation of He 10 830, we chose the VAL-C model instead of the FAL ones to keep the consistency with Andretta & Jones (1997).

The chromosphere models for stars other than the sun are summarized in Linsky (2017, Table 4 and 5). Though models for dwarfs and giants are available, they are derived using different spectral diagnostics, atomic models and techniques. Further, since the availability and accuracy of the observation for stars other than the sun

is limited, most of the stellar chromosphere models, if available, are sparse in the depth grid point. The formation of He 10 830 may be only poorly reproduced with the low-resolution grid points. Further, determining the chromosphere model based on the observed spectra requires the line core of the chromosphere lines are well resolved. The spectra in our sample are medium-resolution (except for the Stock-2 spectra), and they are not feasible to provide detailed constraints to the chromosphere structure. Therefore, future high-resolution spectral observation of most of the stars in our samples is required to determine their chromosphere structure, and we limit the model used here to the solar one.

2.3 Formation of He 10 830 in solar atmosphere model

This section presents some details of the NLTE calculation process, their result and the behavior of chromosphere lines under PR and CE formation mechanisms. We have described the atmosphere model we use in the last section. The atom models are extracted from the HAOS-DIPER IDL package[1] (Judge & Meisner, 1994). This package stores the level and transition information (e.g., those from CHIANTI, Dere et al. 2001, and The Atomic Data and Analysis Structure[2]), and provides handy programs to manipulate the data and convert them to the MULTI format.

External radiation, as stated in the former sections, is also important for the synthesis of He 10 830. Tobiska (1991) derived the solar extreme ultraviolet irradiance model using the technique of empirical modeling. The model was adjusted to provide a good fit to the observations in EUV wavelengths and a few chromosphere lines. Figure 2.2 presents the external radiation (I_{T}) model with the ionization cross-section of the ground state of He I. The largest contribution of the external radiation comes from the peak at around 300 Å.

All the data for the NLTE calculation, i.e., the VAL-C atmosphere model, atom model and external radiation were input into MULTI along with the chemical composition setting, and the code derives the synthetic spectra for the chromosphere lines and supplementary data such as the state population and contribution functions. We developed the python wrapper of the MULTI code, `pymulti`[3], to handle the input and output data.

[1] https://www.hao.ucar.edu/modeling/haos-diper/
[2] https://open.adas.ac.uk/about-adas
[3] Developed by the author. Available at https://github.com/MingjieJian/pymulti

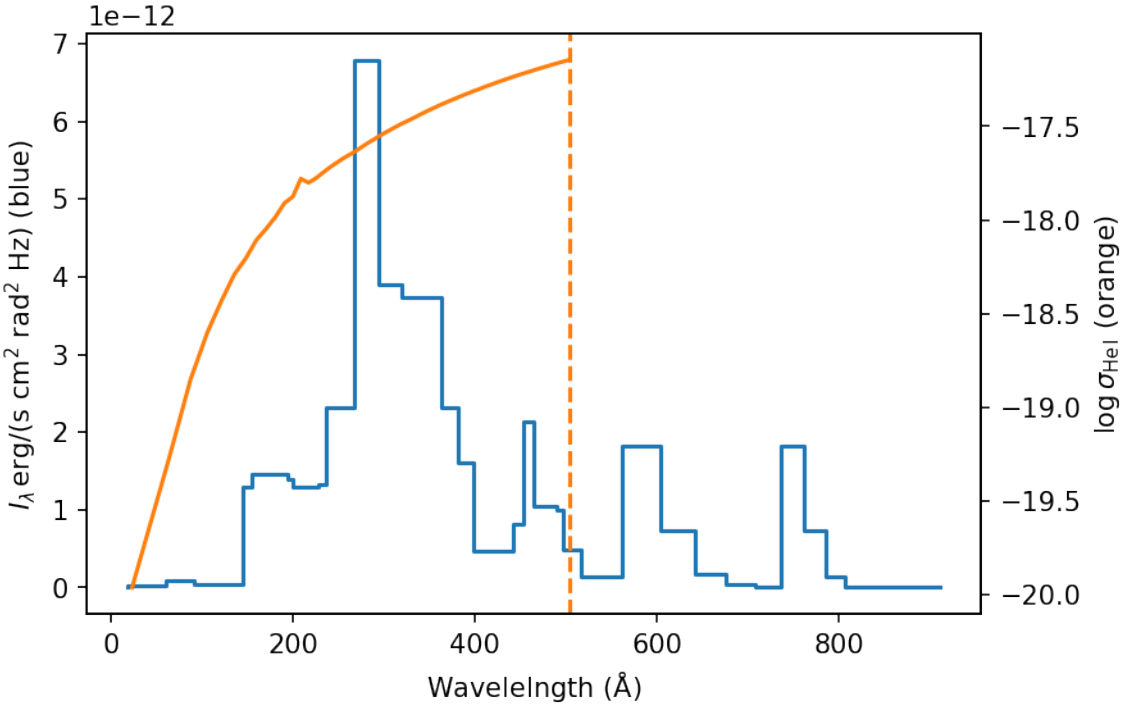


Figure 2.2: The external radiation model from Tobiska (1991) used in the following line synthesis. The vertical dashed line at $\lambda = 504\,\text{Å}$ indicates the threshold of the photon which can ionize helium atom.

We first compared the synthesized and observed profile for the chromosphere lines using the VAL-C model. Figure 2.3 shows the comparison between synthetic and observed spectra for the sun. The observed spectra of hydrogen and calcium lines are from the BASS2000 project[4], and the profiles of the hydrogen lines were scaled to match the wing part of the synthesized ones. We adopted the WINERED observation of the solar reflection spectra from the moon as the integrated solar spectra for He 10 830. The spectra synthesized by the VAL-C model are consistent with the observed Hα and Hβ profile, with only a small difference in the line depth. The Ca II line cores are, however, slightly in emission while the observed ones show the absorption only. The synthesized He 10 830 is weaker than the observed one.

The discrepancies seen between the observed and synthetic spectra may be due to the variation of the atmosphere structure along the solar cycle. The goal of this chapter is to discuss the formation mechanism of He 10 830, so modifying the model to derive a better fit is beyond our scope. Nevertheless, the modification to the VAL-C model in the following analysis may provide some hints for explaining this discrepancy.

Here we introduce a useful tool for visualizing line formation, the contribution function (CF). The contribution function describes the contribution of line intensity, flux or depression in these two quantities in each depth point. If the value of the contribution function is higher at a specific point, it means that there is more intensity or flux is emitted, or there is more absorption in this place. In the case of the absorption line, the CF of line depression is commonly used to trace the formation region of the line (Magain 1986 and Albrow & Cottrell 1996). The distribution of the CFs describes the formation region of a spectra line. For example, Figure 2.4 and 2.5 shows the contribution functions in the line core of a weak and strong line, respectively, calculated using `pymoog`. The I_c and D_l curves represent the contribution function of the continuum and the line depression. The emission of the continuum is located at the bottom of the atmosphere, with the optical depth $\tau_{\rm ref}$ close to 1. The depression appears at higher layers, reaching the peak and then decreasing slowly towards the outer part of the photosphere. The formation area of the stronger lines is usually higher than that of the weaker lines, since the core of the stronger line reflects the lower local temperature, hence the upper part of the photosphere. Since the line wing of the chromosphere lines is wide (e.g., that in the Ca II H&K lines), presenting the contribution function in the wavelengths from the line core to the wing parts is

[4] https://bass2000.obspm.fr/solar_spect.php

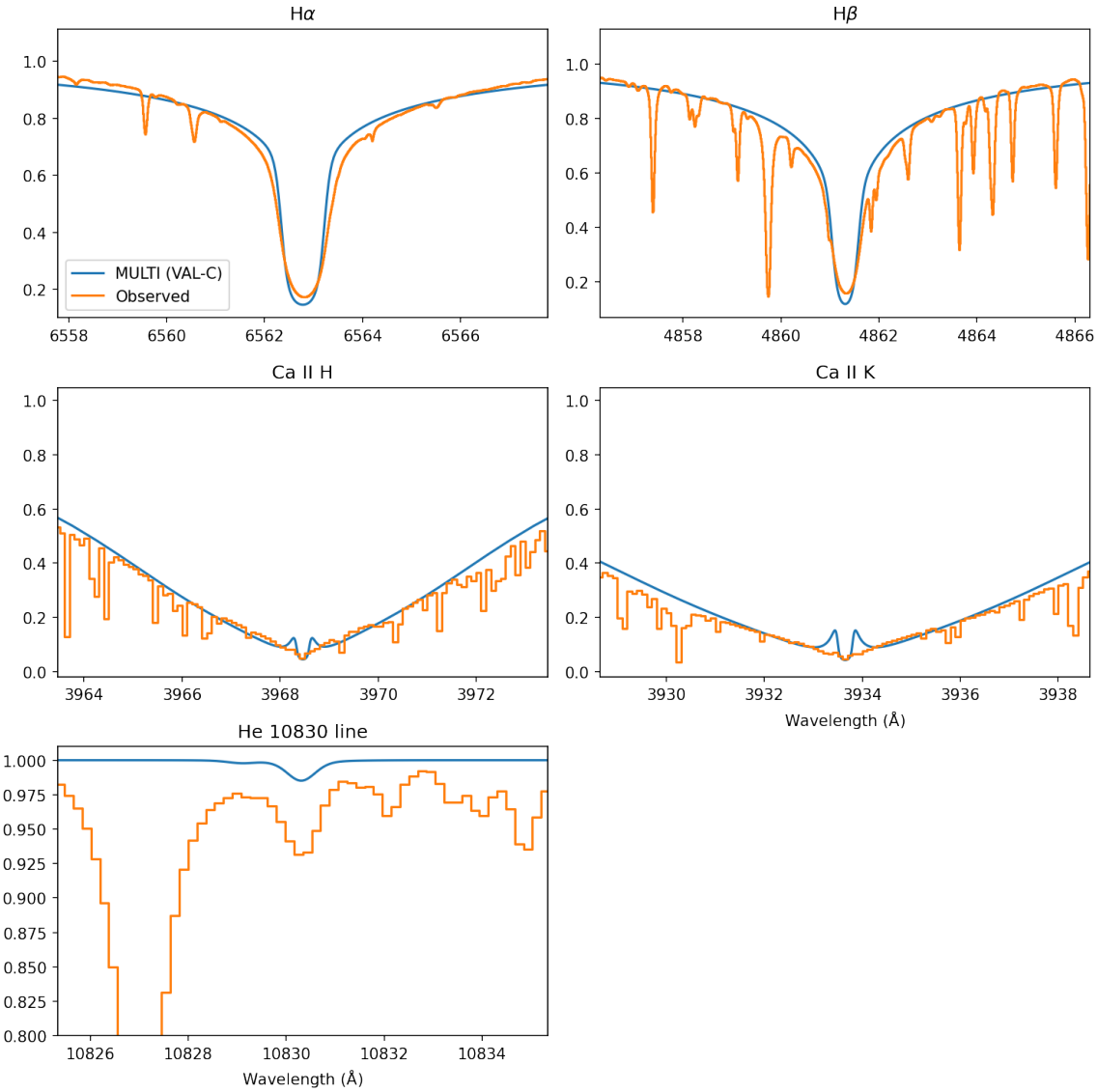


Figure 2.3: Synthetic spectra of chromospheric lines generated using the VAL-C model and external radiation of I_{T}. The observed spectra of these lines are overplotted in orange for comparison.

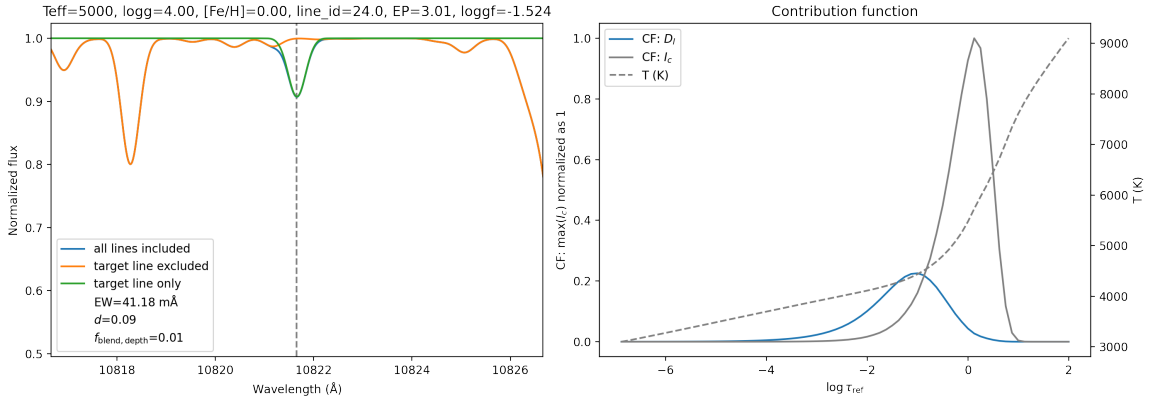


Figure 2.4: The synthetic spectra (left panel) a weak Cr line calculated by `pymoog`. The stellar and line parameters used for generating the synthetic spectra are written in the title. The contribution function of this line is plotted in the right panel, with the solid gray curve indicating the contribution of the continuum, and the blue curve indicating the contribution of line absorption. Only the photosphere is included in this synthesis.

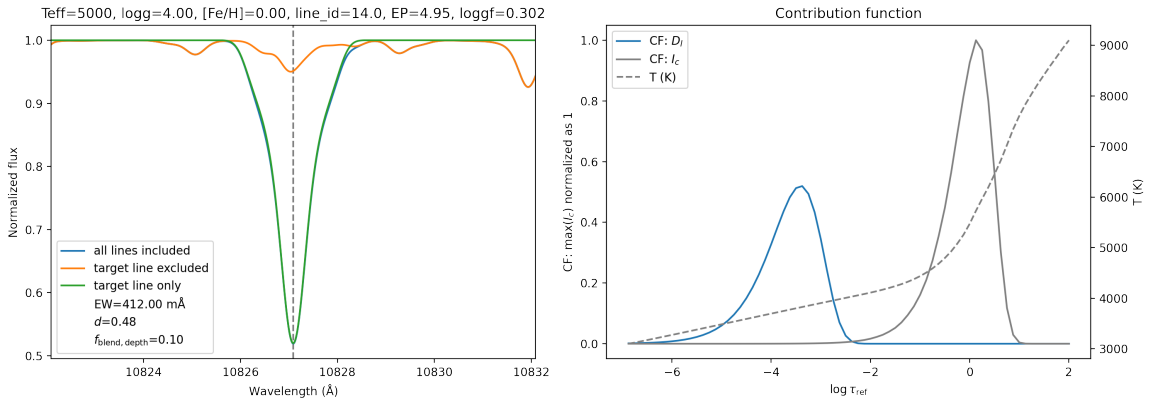


Figure 2.5: Same as Figure 2.4 but for a strong Si line.

necessary. MULTI calculates the CFs in each depth and wavelength grid point, thus the formation region of the line wings can also be revealed.

Figure 2.6 shows the contribution function of the chromosphere lines synthesized using the VAL-C model. The left panels present the synthesized spectra, rotated 90° counter clock-wised. Such configuration ensures that the y-axis for the spectra in the left panel and that for the CFs in the right panel are on the same scale. The temperature profile is plotted in white in the right panels, and the CFs are labeled in blocks by color. The black dots indicate the median value of the CF in each row (i.e., in each wavelength), thus the line formation region. For all the strong chromosphere lines, the line cores are formed in the chromosphere, while their line wings are formed

in the deeper layers. The core of Ca II H&K lines are formed in the upper part of the chromosphere, and the hydrogen line cores are formed in slightly deeper layers. He 10 830 is formed in a slightly upper layer, in the transition region. We note that only the strongest component of He 10 830 is presented in the last row, since MULTI synthesized the components separately and their contribution functions are similar. We then modify the VAL-C model to see how these lines react to the changes in external radiation and chromosphere density.

2.3.1 External radiation variation

The synthetic spectra and He 10 830 contribution function of VAL-C model with several configuration of external radiation (0, 1, 10, 20 and 30 times I_{T}) are presented in Figure 2.7 and 2.8. The variation of external radiation only affects the strength of He 10 830. When there is no external radiation, the absorption is weak. As the radiation increase, the line strength increases subsequently. Also, the formation range of He 10 830 revealed by the contribution function moves inside as the external radiation increase, from the transition region to the upper chromosphere.

The behavior of He 10 830 with different external radiation can be explained by the PR forming mechanism. As shown in Figure 2.1, the density of the corona and transition region is low, so the high-energy radiation generated there can transport down to the chromosphere, which contains more neutral helium atoms. The high-energy photon then ionizes the neutral helium to He II, then populate the 2^3S state. This explanation is consistent with the population of ionized helium and 2^3S state extracted from the calculation shown in Figure 2.9 and 2.10. The populations in the photosphere and lower chromosphere with different external radiation are same, but those in $-5 < \log \rho x < -4$ show differences. The larger amount of radiation does increase the He II population, suggesting that more helium atoms are ionized due to external radiation. The 2^3S state population also increases, and He 10 830 becomes stronger. The region of the model showing such a population enhancement is also consistent with the formation region seen in the CF. As a result, when external radiation is present in the VAL-C model, the dominant formation mechanism is PR mechanism.

2.3.2 Chromosphere density variation

The change in chromosphere density is also expected to affect the strength of He 10 830. Since the column density, or ρx, of the model represents the density of each grid

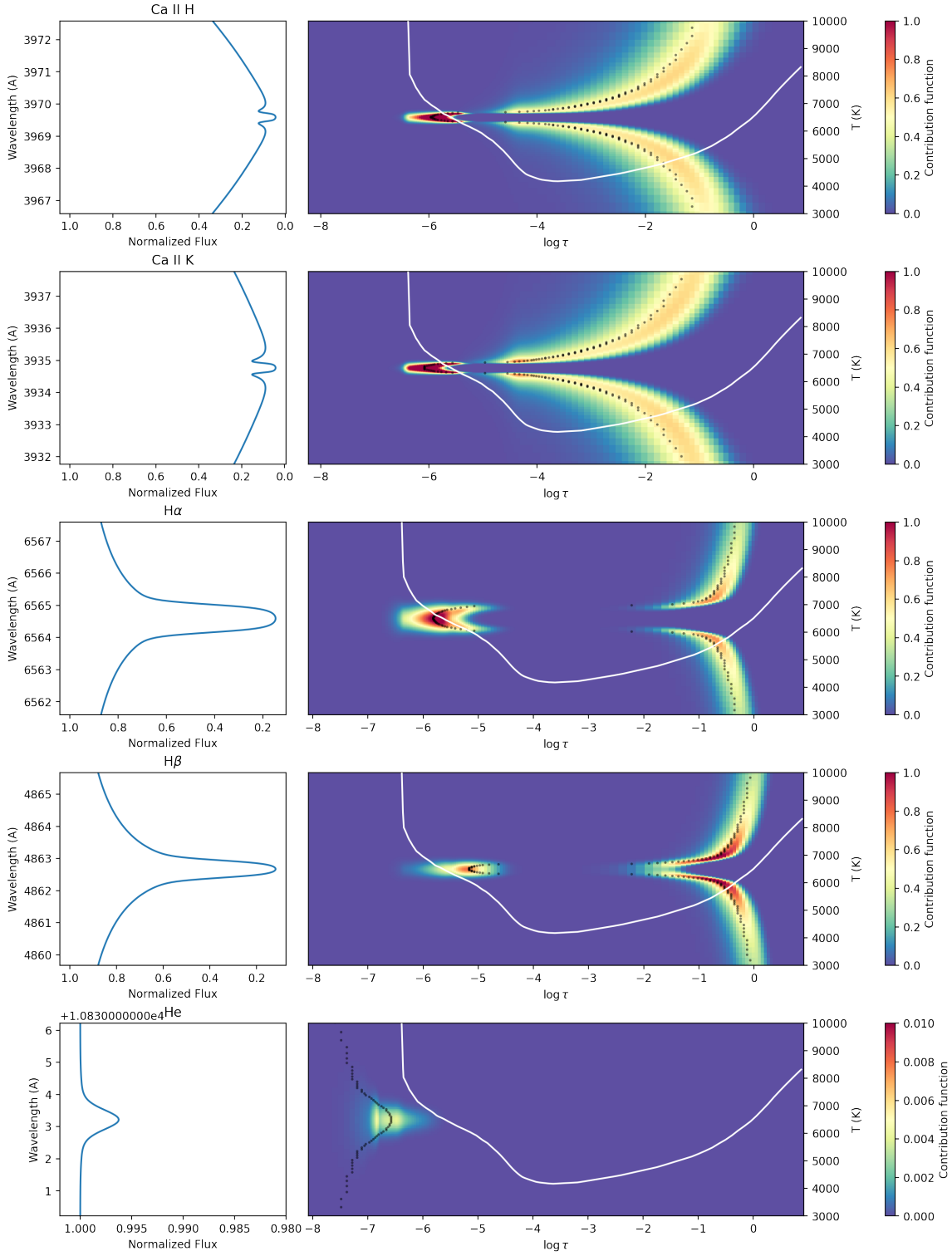


Figure 2.6: Left panels: the synthetic spectra of chromosphere lines (rotated 90 degrees counter-clockwise) in VAL-C model with $I = I_{\mathrm{T}}$. Right panels: the contribution functions of the lines in different optical depths and wavelengths, indicated by the colors. The temperature profile is overplotted for comparison.

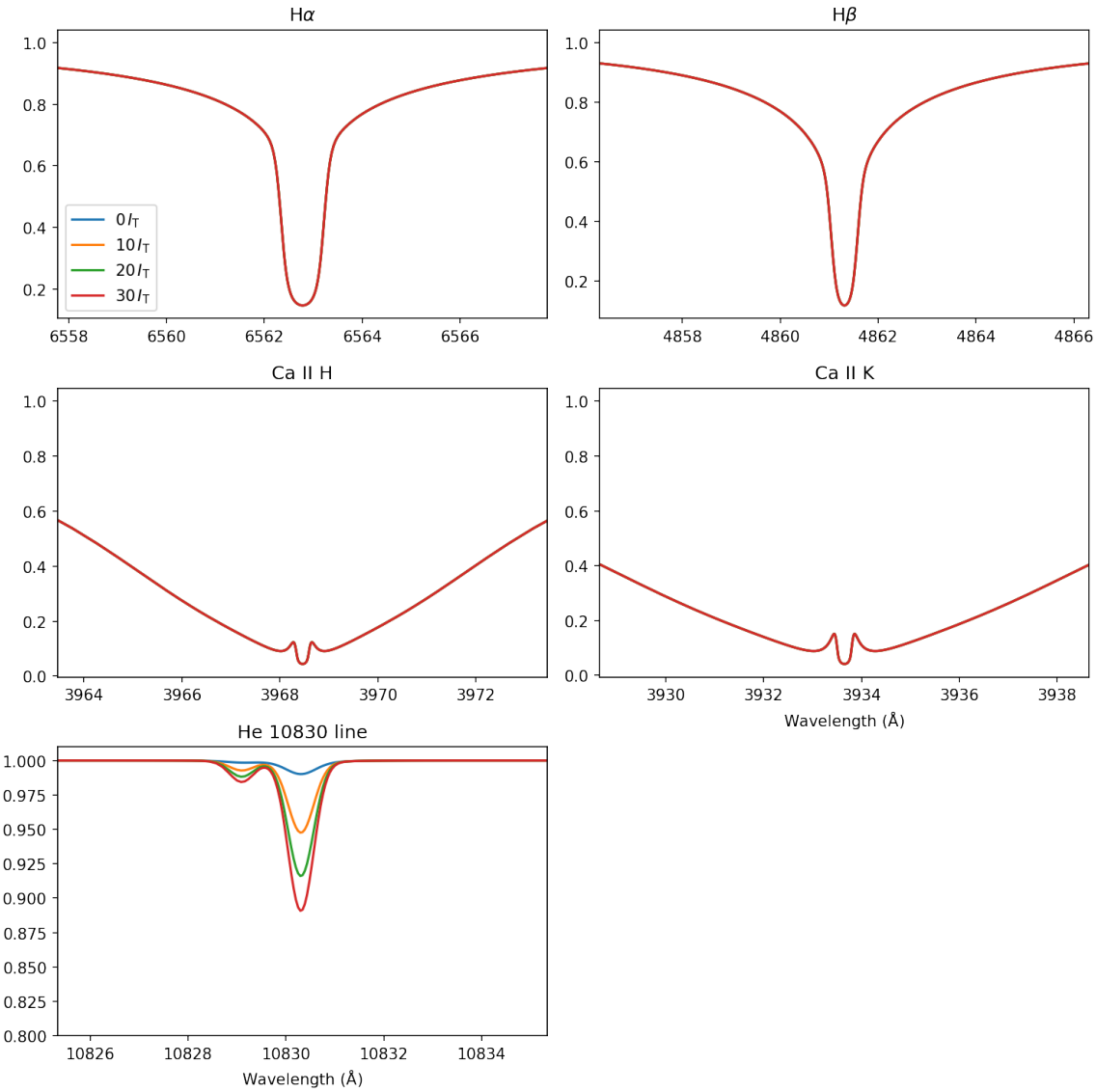


Figure 2.7: Synthetic spectra generated using the VAL-C model with $I = 0, 10, 20$ and $30 I_{\mathrm{T}}$.

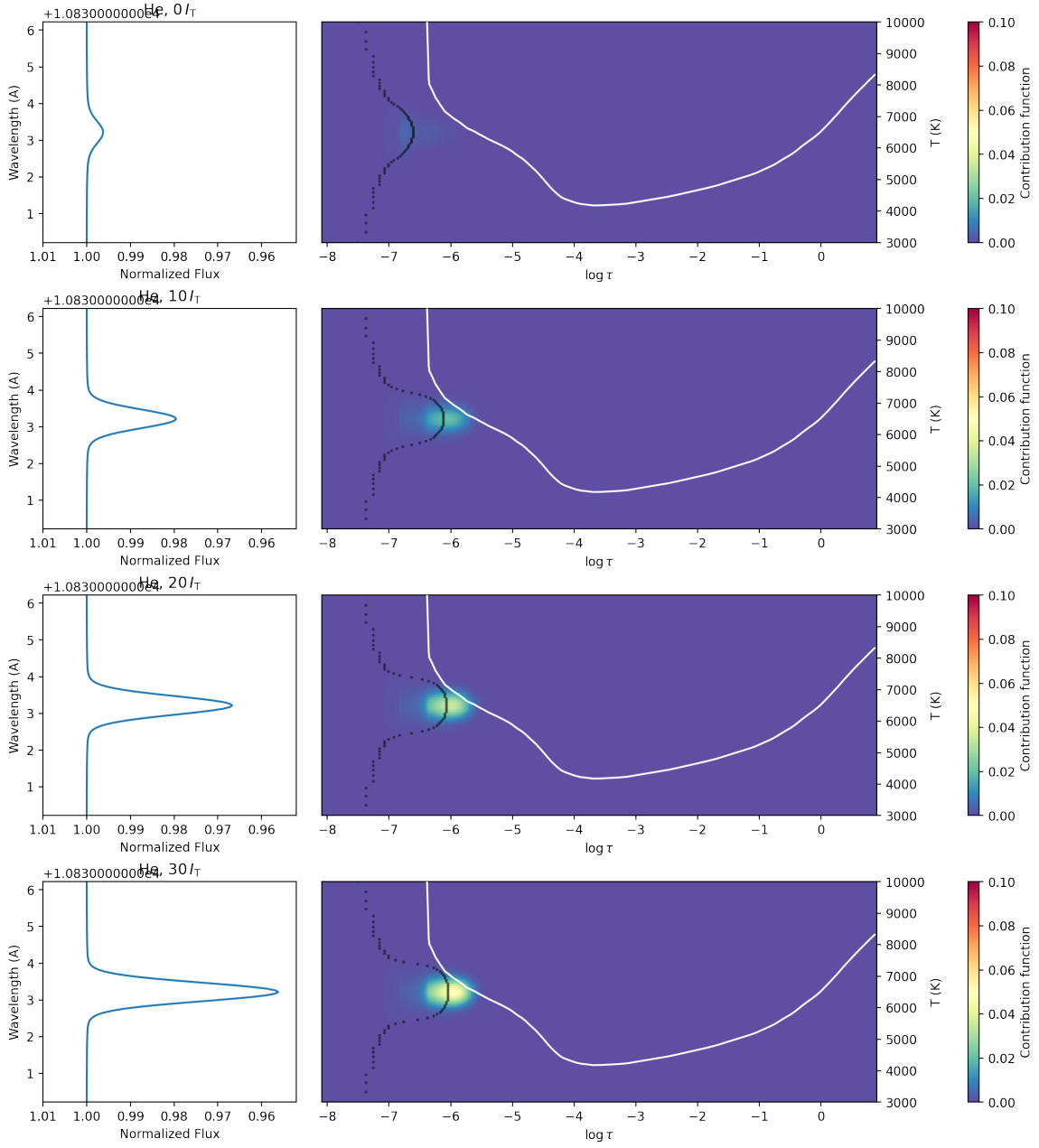


Figure 2.8: Left panels: the synthetic spectra of chromosphere lines (rotated 90 degrees counter-clockwise) in VAL-C model with $I = 0, 10, 20$ and $30 I_{\mathrm{T}}$. Right panels: the contribution functions of the lines in different optical depths and wavelengths, indicated by the colors. The temperature profile is overplotted for comparison.

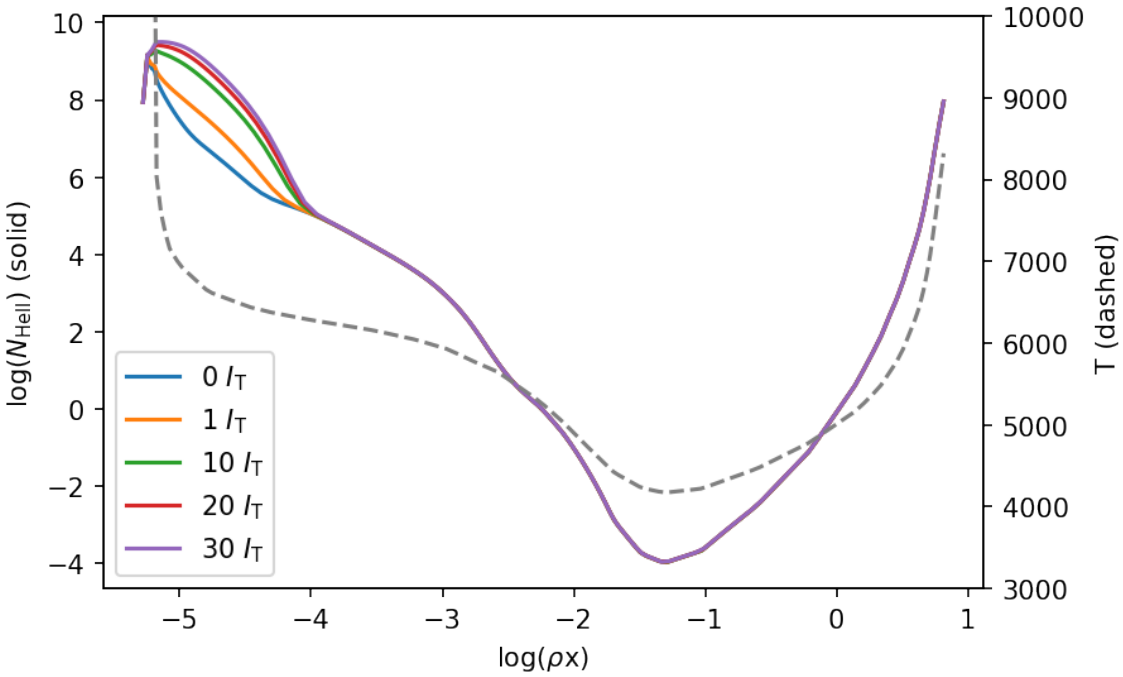


Figure 2.9: Population of the ionized He atom ($N_{\mathrm{He\,II}}$) in ground state of the VAL-C model with $I = 0, 10, 20$ and $30 I_{\mathrm{T}}$. The temperature profile is plotted as a reference.

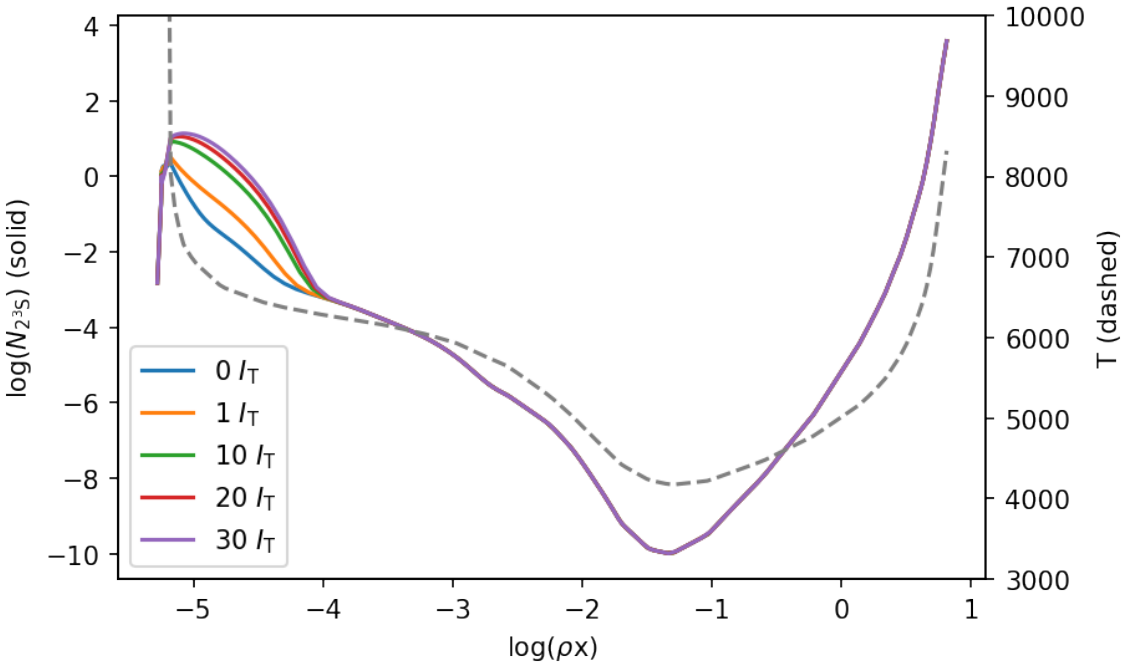


Figure 2.10: Population of the neutral He atom in 2^3S state of the VAL-C model with $I = 0, 10, 20$ and $30 I_{\mathrm{T}}$. The temperature profile is plotted as a reference.

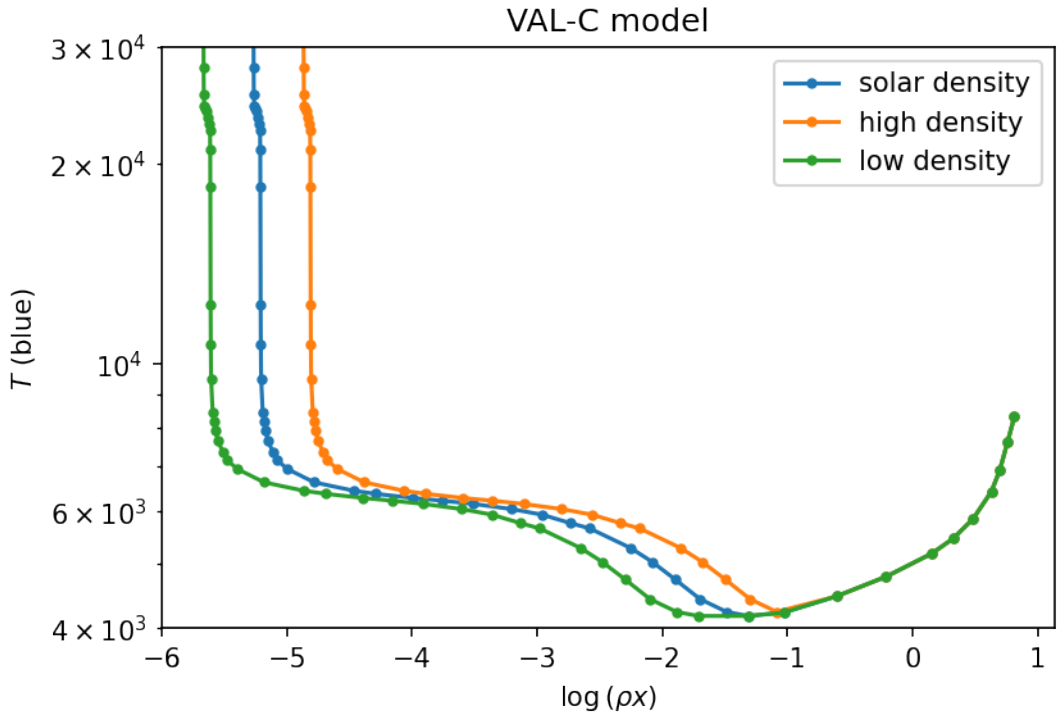


Figure 2.11: Temperature stratification of the VAL-C model and the two modified models with varying chromosphere density.

point, changing the position of the chromosphere and the transition region in Figure 2.1 varies their density. Two models with the transition region shifted horizontally compared with the initial VAL-C model are presented in Figure 2.11. The external radiation is switched off for the models present in this section.

Similar to the previous section, the synthesized lines and the CFs of He 10 830 are plotted Figure 2.12 and 2.13. The He 10 830 EW and width are also correlated with the density: the stronger, wider lines appear with the model having higher chromosphere density, and vice versa. The strength of Ca II H&K line is also stronger, while the change in the Hydrogen lines is small and negligible. The contribution function of He 10 830 shows that the line is always formed in the transition region, higher than the case where the line formation is dominated by the PR mechanism.

When the chromospheric density is high, the number density of particles is increased. The collisional transition rate from the ground state to the 2^3S is then enhanced, leading to more helium atoms being populated to the 2^3S state directly from the ground state. The formation of He 10 830 is then dominated by the CE mechanism. Such formation scenario is consistent with that in Andretta & Jones (1997).

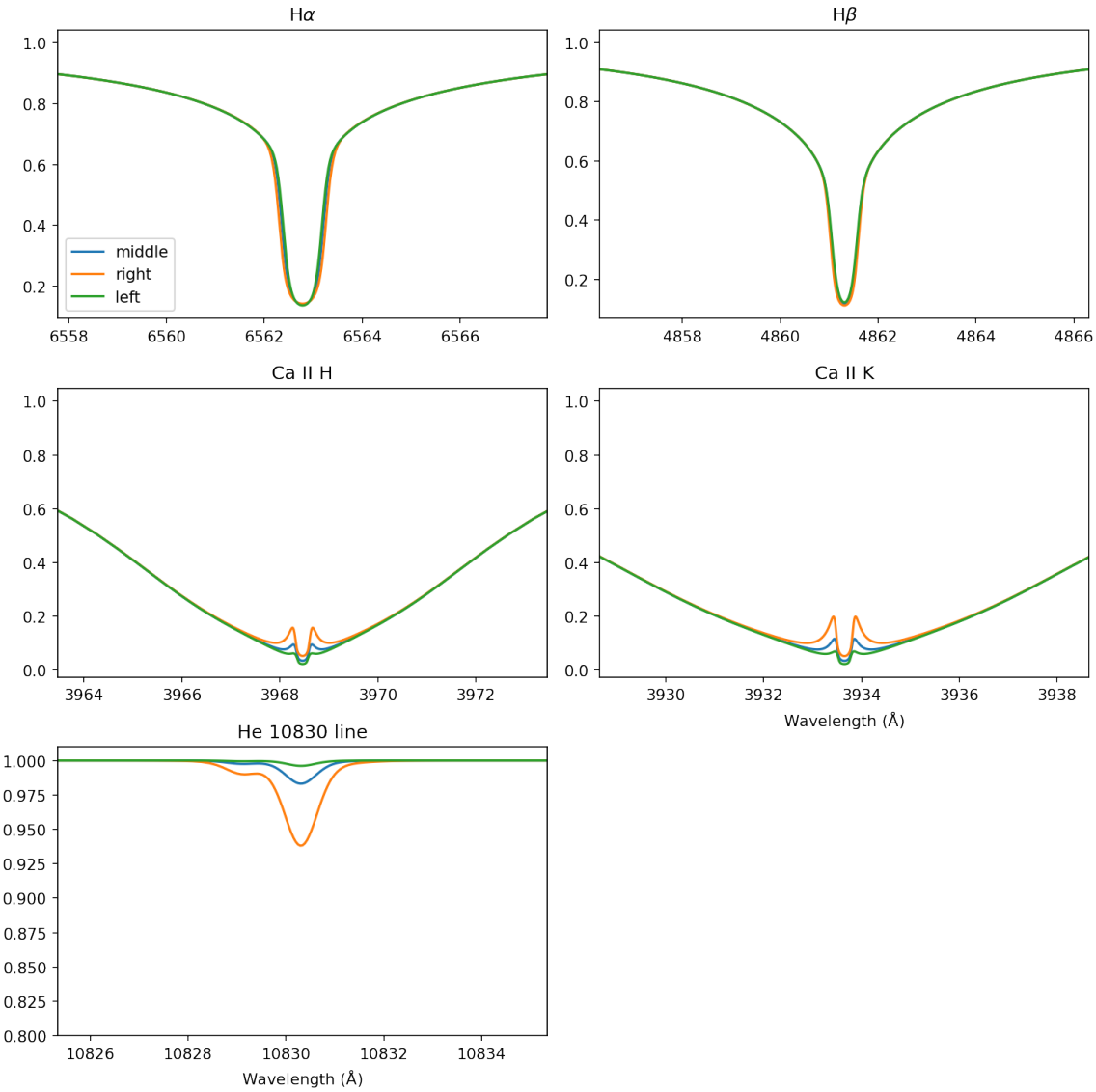


Figure 2.12: Synthetic spectra generated using the models with solar, low and high chromosphere density.

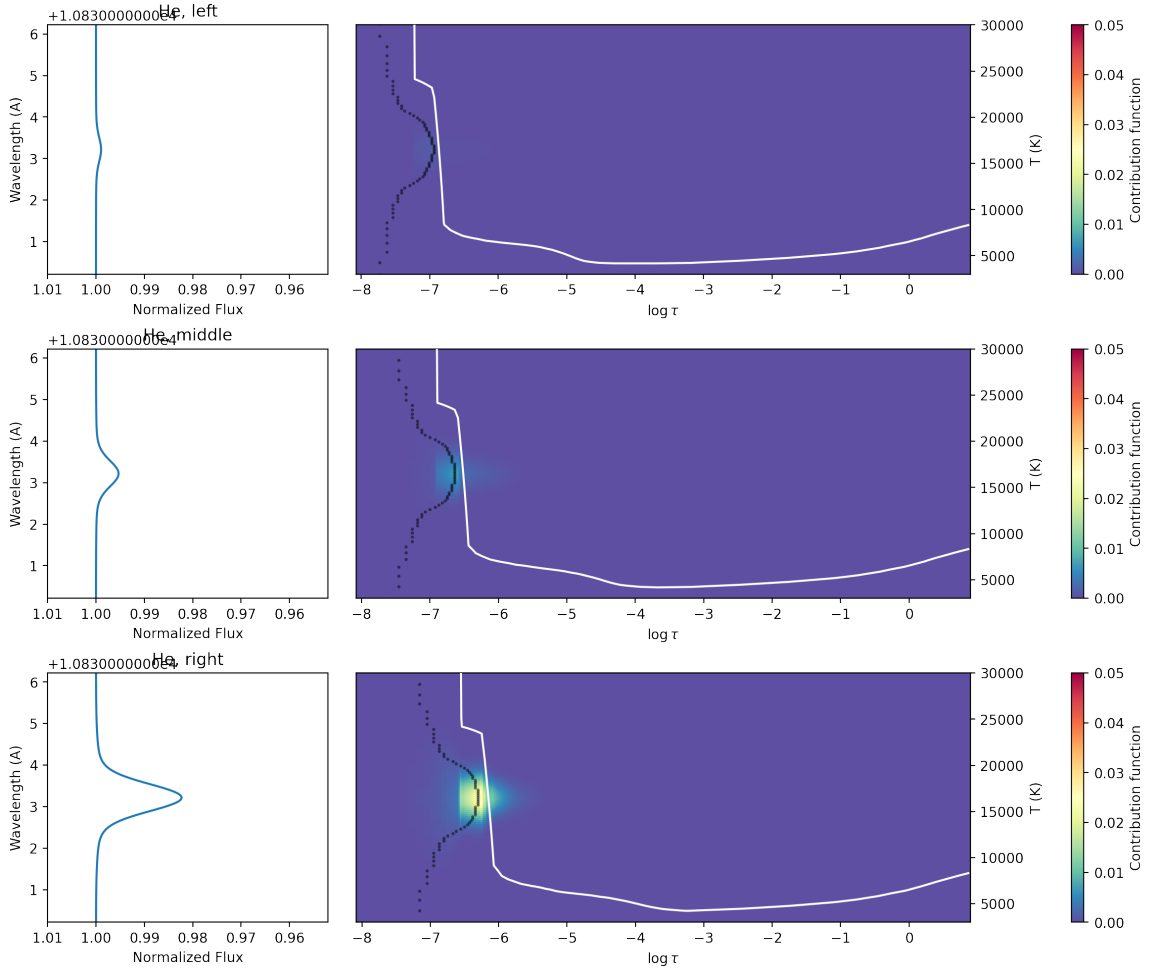


Figure 2.13: Left panels: the synthetic spectra of chromosphere lines (rotated 90 degrees counter-clockwise) in models with solar, low and high chromosphere density. Right panels: the contribution functions of the lines in different optical depths and wavelengths, indicated by the colors. The temperature profile is overplotted for comparison.

Both the PR and CE mechanisms can strengthen the absorption of He 10 830 in late-type stars, as shown by our observation and the synthetic spectra presented above. How the feature would react to the change of helium abundance under these two mechanisms, therefore should be discussed. We study the variation of He 10 830 strength by changing the helium abundance in models dominated by the PR and CE mechanisms in the next section.

2.4 Sensitivity of the He 10 830 strength to the helium abundance

Although the two formation mechanisms of He 10 830 may exist simultaneously in the stellar chromosphere, it is instructive to study the sensitivity of the He 10 830 strength on the helium abundance using two modified solar models, with PR or CE mechanism dominants, respectively. The adopted models are VAL-C model with a relative strong external radiation, $20I_{\rm T}$, in section 2.3.1, and the "right" model in section 2.3.2. The helium abundance are varied from solar abundance, $Y = 0.24$, to 0.17 and 0.34.

Figure 2.14 and 2.15 present the synthetic spectra of the two models with the different helium abundances, and the EWs of the synthesized line. The difference in EW(He) for the PR dominate model with $Y = 0.17$ and 0.34 is 12 mÅ. Note that the contribution from the CE mechanism also exists since there is a weak absorption for the VAL-C model without external radiation. The CE mechanism contribution to the difference in EW(He) is 5 mÅ. When the CE mechanism dominates, the change in He(EW) introduced by helium abundance variation is larger, around 20 mÅ. Such behavior differences between the PR and CE mechanisms can be explained by the dominant mechanisms themselves. The line strength in the model dominated by the PR mechanism is related to the amount of external radiation. If the amount of external radiation is large, and the number of neutral helium atoms is small, then the external radiation will ionize at least a large number of the helium atom, and the population of 2^3S state is limited by the number of the helium atom, or the helium abundance. Examples of this kind of star would be the active dwarfs reported in Sanz-Forcada & Dupree (2008). Those stars seems to be saturated with the fractional X-ray luminosity, when $\log L_{\rm X}/L_{\rm bol} > -4$. When the external radiation is small and the number of neutral helium atom is large, only a few helium atoms can be ionized and the external radiation decreases as it transports into the chromosphere, until all the radiation have been used to ionize helium atoms. The population of 2^3S

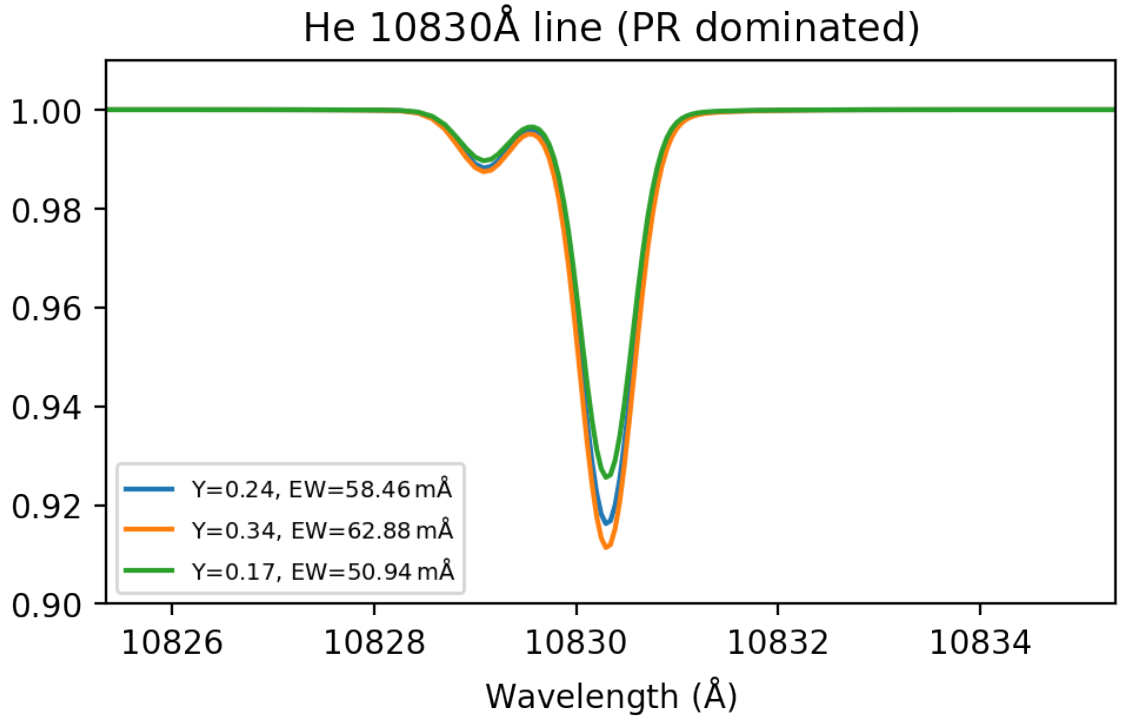


Figure 2.14: The synthetic He 10 830 with different helium abundances with a PR mechanism dominated model (the model with $20I_{\mathrm{T}}$ in section 2.3.1).

state is then determined by the amount of external radiation rather than the helium abundance. The "inactive" dwarfs, e.g., those with $\log L_{\mathrm{X}}/L_{\mathrm{bol}} < -4$ in Sanz-Forcada & Dupree (2008) and forms a tight He(EW)–$\log L_{\mathrm{X}}/L_{\mathrm{bol}}$ relation are considered to be in this case. The strength of the helium 10 830 Å line is then not sensitive to the helium abundance when the PR mechanism is dominated. On the other hand, collisional excitation from the ground state to the 2^3S state is correlated with the number density of the helium atom through the collisional rate formula (see, e.g., equation 9.51 of Hubeny & Mihalas 2014). Thus the sensitivity of the He 10 830 EW to the helium abundance is larger than that when the PR mechanism dominates as seen in Figure 2.15.

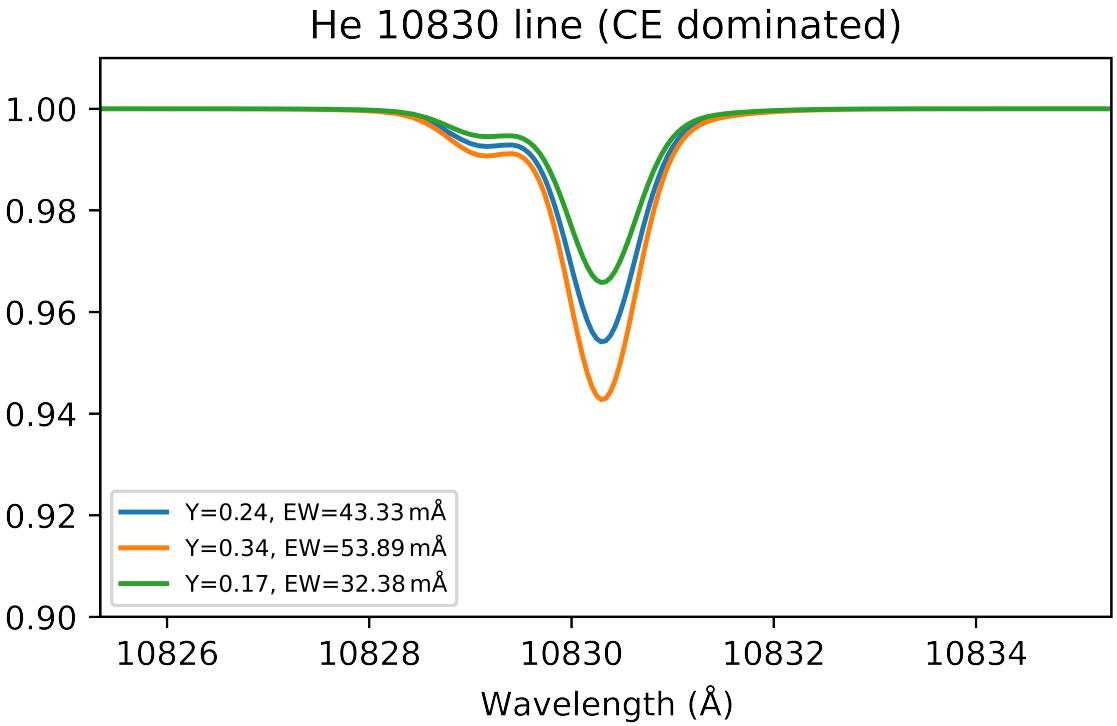


Figure 2.15: The synthetic He 10 830 with different helium abundances with CE mechanism dominated model (the high density model in section 2.3.2).

Chapter 3

Targets and Observations

As mentioned in Chapter 1, new observations on He 10 830 are necessary for calibrating empirical trends with the stellar parameter more precisely. Further, the blending due to the surrounding lines also needs to be accounted for. This chapter describes the targets and observations used in this study. They are divided into three groups, namely the Stock-2 sample, field-WD sample and field-XSL sample. Table 3.1 summarized the situation of the samples.

3.1 The Stock-2 sample

The Stock-2 sample consists of the optical and near-infrared (NIR) spectra of the giants in the open cluster Stock-2. Stock-2 is a nearby open cluster discovered by Stock (1956), with a distance of 400 pc (Dib et al., 2018). Despite its closeness, its age or chemical composition was not yet well known. The first detailed spectroscopic analysis for this cluster is Reddy & Lambert (2019). With a sample of three giants, they estimated the metallicity of the cluster is -0.06 ± 0.03. Later Ye et al. (2021) obtained a similar value of -0.04 ± 0.15 from LAMOST medium-resolution spectra of around 300 member stars. The high-resolution observation with the largest sample is those reported by Alonso-Santiago et al. (2021), as a part of the project Stellar

Table 3.1: Summary of our samples with the instrument, resolution (R) and numbers of dwarfs, giants and supergiants.

Sample	Instrument	R	N_{Dwarf}	N_{Giant}	$N_{\mathrm{Supegiant}}$
Stock-2	GIANO-B&HARPS-N	50 000&115 000	0	9	0
field-WD	WINERED	28 000	93	70	29
field-XSL	X-SHOOTER	10 000	225	265	58

population astrophysics Large Programme (see, e.g., Origlia et al. 2019). They obtained the spectra of 32 dwarfs, 14 main-sequence turnoff stars and 10 giants. The dwarfs and giants were observed in GIARPS mode (Claudi et al., 2017) of the Telescopio Nazionale Galileo in the Canarian Island of San Miguel de La Palma, with the near-infrared spectra from GIANO-B (Oliva et al., 2006) and optical spectra from HARPS (Cosentino et al., 2012) obtained simultaneously. 9 giants among the 10 from this study are included in the Stock-2 sample. The member stars in this cluster share similar age and chemical abundances, which is an ideal sample for testing the behavior of the He line in stars born in a homogeneous environment. The GIANO-B NIR spectra cover 0.9–2.45 µm with a resolution of 50000, and the HARPS spectra cover 0.383–0.690 µm with a resolution of 115000. The simultaneous observation of Hα, Hβ and Ca II H&K lines by HARPS and He 10 830 by GIANO-B enable a direct comparison between the behaviors of these lines.

Alonso-Santiago et al. (2021) derived the stellar parameters and chemical abundances of our target giants using HARPS-N spectra. Here we adopt the 'g' stars from their Table 1 as the name of our sample stars, and use the stellar parameters in this work. These stars are plotted in Fig. 3.1, and the stellar parameters are list in Table 3.2. They are concentrated on the bottom part of the red giant branch, and their metallicities are consistent with that of Stock-2, i.e., around 0.

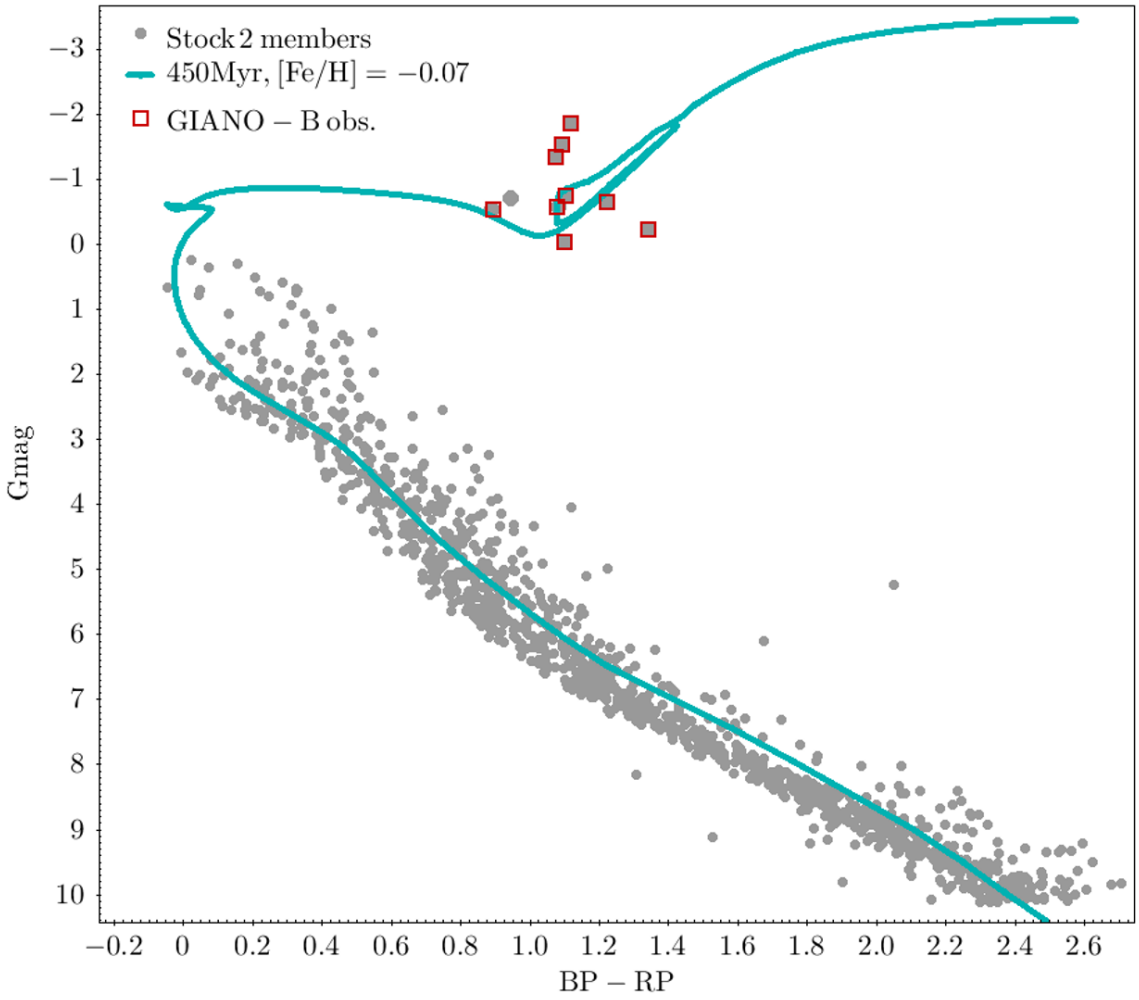


Figure 3.1: The HR diagram of Stock-2 member stars. The isochrone with the age and metallicity of the cluster are drawn as the cyan curve, and the red squares label the giants with GIANO-B observation.

Star	$T_{\rm eff}$ (HARPS) (K)	$\log g$ (HARPS)	[Fe/H] (HARPS)	[Na/Fe] (HARPS)	[Si/Fe] (HARPS)
g1	4530 ± 86	2.14 ± 0.1	0.01 ± 0.09	0.14 ± 0.15	0.12 ± 0.09
g2	4760 ± 111	2.69 ± 0.14	0.02 ± 0.1	0.11 ± 0.06	0.07 ± 0.12
g3	4937 ± 114	2.51 ± 0.35	0.04 ± 0.08	0.32 ± 0.13	0.09 ± 0.12
g4	4977 ± 117	2.82 ± 0.18	0.04 ± 0.08	0.26 ± 0.1	0.06 ± 0.13
g5	5061 ± 56	2.99 ± 0.19	0.04 ± 0.07	0.22 ± 0.13	0.03 ± 0.09
g6	5002 ± 110	2.96 ± 0.2	0.03 ± 0.07	0.25 ± 0.13	0.07 ± 0.11
g7	5058 ± 56	2.97 ± 0.2	0.03 ± 0.07	0.11 ± 0.08	0.06 ± 0.12
g9	5062 ± 56	3.0 ± 0.19	0.0 ± 0.09	0.15 ± 0.1	0.06 ± 0.11
g10	5066 ± 56	3.01 ± 0.19	-0.03 ± 0.09	0.32 ± 0.15	0.03 ± 0.13

Star	[Ca/Fe] (HARPS)	[Ti/Fe] (HARPS)	ξ (GIANO-B) (km/s)	[Fe/H] (GIANO-B)	$V_{\rm broad}$ (GIANO-B) (km/s)
g1	-0.10 ± 0.15	-1.56 ± 0.15	1.57 ± 0.20	-0.12 ± 0.05	4.6 ± 1.1
g2	-0.14 ± 0.15	-1.57 ± 0.15	1.10 ± 0.24	-0.04 ± 0.05	6.3 ± 1.6
g3	-0.06 ± 0.15	-1.40 ± 0.15	1.32 ± 0.26	-0.01 ± 0.06	6.3 ± 1.5
g4	-0.04 ± 0.15	-1.44 ± 0.1	1.21 ± 0.19	0.03 ± 0.04	4.7 ± 1.4
g5	-0.04 ± 0.14	-1.48 ± 0.13	1.07 ± 0.24	0.02 ± 0.05	5.8 ± 1.2
g6	-0.09 ± 0.1	-1.40 ± 0.15	0.87 ± 0.20	0.09 ± 0.04	4.7 ± 1.2
g7	-0.13 ± 0.12	-1.47 ± 0.11	1.39 ± 0.31	0.02 ± 0.06	6.3 ± 1.0
g9	-0.14 ± 0.15	-1.50 ± 0.14	1.18 ± 0.24	-0.01 ± 0.05	5.6 ± 1.2
g10	-0.23 ± 0.15	-1.55 ± 0.15	0.97 ± 0.29	-0.02 ± 0.05	5.6 ± 1.3

Table 3.2: Stellar parameters of Stock-2 sample. The parameters from HARPS are adopted from Alonso-Santiago et al. (2021), and those from GIANO-B are measured in Chapter 4.

3.2 The field-WD sample

The field-WD sample is a collection of observations on 192 field stars, including dwarfs, giants and supergiants. The observation was performed using the Warm INfrared Echelle spectrograph to Realize Extreme Dispersion and sensitivity[5] (WINERED, Ikeda et al. 2022). WINERED is a high-throughput NIR spectrograph covering the YJ-band (0.9–1.3 µm) with a resolution of 28 000 (WIDE mode) or 70 000 (HIRES mode). It was mounted in the Araki telescope at the Koyama observatory in the Kyoto Sangyo University, Japan, and then moved to the New Technology Telescope (NTT) at the La Silla Observatory in Chile. Starting from 2022, it will be operated with the Magellan Telescope at Las Campanas Observatory.

This dataset is collected from the WINERED observations in the WIDE mode of FGK type stars with reliable stellar parameters, e.g., from ESO observation of Gaia benchmark stars, Adibekyan et al. (2012) and the APOGEE survey (Ahumada et al., 2020). Among the 192 stars in the field-WD sample, 67 (41 dwarfs and 26 giants) are observed by the author under the proposal 0100.D-0852 using WINERED mounted in the ESO New Technology Telescope in December 2017. The rest stars are observed by other WINERED team members using the Araki telescope in Kyoto Sangyo University before 2017. Part of these stars have been used for several NIR spectral studies, including the calibration of relations between line-depth-ratio and $T_{\rm eff}$ (Jian et al. 2020 and Matsunaga et al. 2021), and the detection of new heavy-element lines (Matsunaga et al., 2020).

Fig. 3.2 shows the distribution of stellar parameters of the field-WD sample. A part of the dwarfs and giants in this sample is selected to cover the metallicity from -0.7 to 0.5 dex. Thus it is a good sample to examine how He 10 830 in dwarfs and giants behaves in different metallicities. The stellar parameters are adopted from, e.g., Adibekyan et al. (2012); Ahumada et al. (2020); Kovtyukh et al. (2003, 2004) and Jofré et al. (2014), and a few other sources (see Table B.1). Most of the stars are classified as dwarf, giant or supergiant by the studies we adopted for their stellar parameter. Only dwarfs and giants appear in those with no classification in the source study, so we use $\log g = 3.5$ to divide them into dwarf and giant.

This sample provides a set of high-resolution spectra observed in a similar instrumental configuration. The wide coverages in $T_{\rm eff}$, metallicity and $\log g$ ensure the variation of He 10 830 EW can be detected, if there is any. Finally, the resolution of 28 000 is sufficient for measuring its profile.

[5] http://lihweb.kyoto-su.ac.jp/WINERED/overview_winered.html

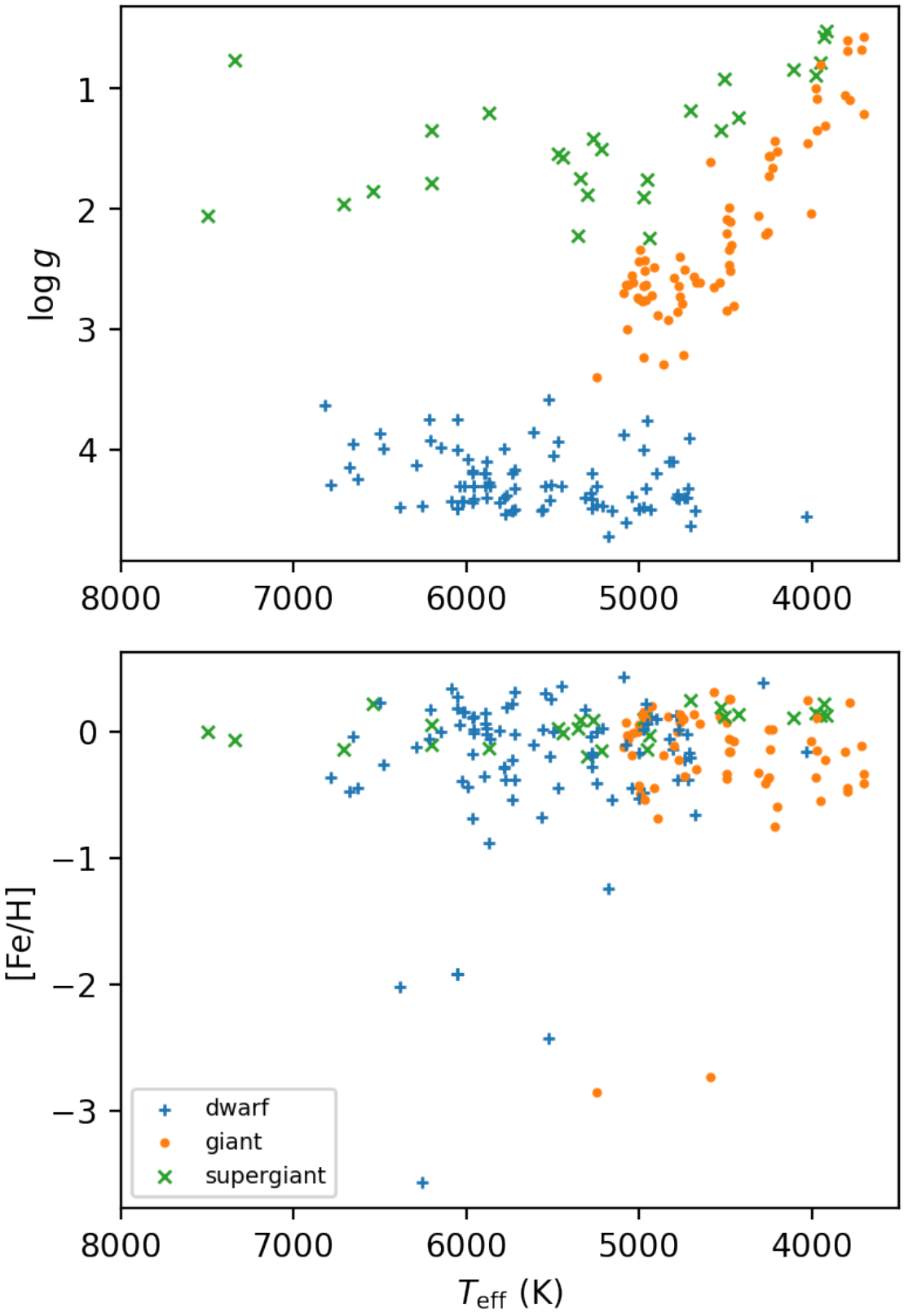


Figure 3.2: The Kiel and [Fe/H]–$T_{\rm eff}$ diagram for the field-WD sample.

3.3 The field-XSL sample

The field-XSL sample is adopted from the X-shooter Spectral Library (XSL). X-SHOOTER (Vernet et al., 2011) is a multi-wavelength, medium resolution spectrograph mounted at one of the Very Large Telescopes, UT3 Melipal. It can acquire the three spectra with wavelength ranges of 300 – 559.5 nm (UVB), 559.5 – 1024 nm (VIS) and 1024 – 2480 nm (NIR) simultaneously, with a resolution of $\sim$ 10000. The X-shooter Spectral Library (Chen et al., 2014) is an observational spectral library to achieve (1) a wide coverage of the stellar parameter and evolutionary phase; (2) simultaneous observations in UVB, VIS and NIR to avoid variations on spectral features, and (3) good calibration of the flux and wavelength. The data release 2 of XSL (Gonneau et al., 2020) provides more than 813 spectra of 666 field stars. They are homogeneously reduced and calibrated, and stellar parameters are available for most of the stars (Arentsen et al., 2019). Similar to GIANO-B, the XSL data is also a dataset with chromospheric lines observed simultaneously. Also, this data set covers wider ranges of stellar parameters than the field-WD sample. The medium resolution of X-SHOOTER can also provide hints on how the He line would behave under this resolution.

We then classify the stars in the field-XSL sample into dwarf, giant and supergiant, similar to that in the field-WD sample. The sample was first cross-matched with the Gaia DR2 catalog (Gaia Collaboration et al., 2018) to get their luminosity. The supergiants are massive stars with solar metallicity. The 63 solar-neighbor supergiants reported by Lyubimkov et al. (2010) have a minimum metallicity of -0.22, and mass between 2.8 $M_\odot$ and 23.9 $M_\odot$. Assuming that the supergiants in the field-XSL sample share a similar range mass and metallicity, we separated the supergiants using the stellar evolutionary track from PARSEC (Bertelli et al., 2008). As shown in the upper panel of Figure 3.3, the HR diagram was separated into 4 areas by the greed dashed lines. The dashed lines in the middle follow the evolutionary track of a star with $Z = 0.001, Y = 0.25, M = 3\,M_\odot$. Then all the stars in area-S are classified as supergiants, those in area-D as dwarfs and those in area-G as giants. Stars in Area-M are a mix of supergiants and giants. Considering the supergiants are with solar metallicity, those in the area-M with [Fe/H] > -0.25 are classified as supergiants, and the others are as giants. For the stars with no Gaia luminosity, we repeated the process in the $\log g$–$T_{\rm eff}$ plane, as in the lower panel of Figure 3.3. We marked the stars classified as horizontal branch (HB) stars and post-AGB stars in SIMBAD. HB stars tend to show stronger absorption strength compared with giants (Dupree et al.,

2009), so it would be useful to check if such behavior also appears in the XSL sample. We note that such separation is only a rough one that could be improved with more information, but this is enough for our purpose.

The stellar parameters of the field-XSL sample after the classification are presented in Figure 3.4. Compared with the field-WD sample, the dwarfs in the field-XSL sample have extended coverage in $T_{\rm eff}$, ranging from 4000 to 10 000 K. Such wide coverage is essential for detecting the variations in low- and high-temperature ends. The metallicity for dwarfs and giants are also covering a wider range, reaching down to [Fe/H] ~ -2.5.

As summarized in Table 3.1, the samples included in this thesis are enough for refining new empirical relations between He 10 830 EW and stellar parameters. Especially, the Stock-2 sample will be used to calibrate the oscillator strength of contaminating lines, and the field samples will be used to present the new relations.

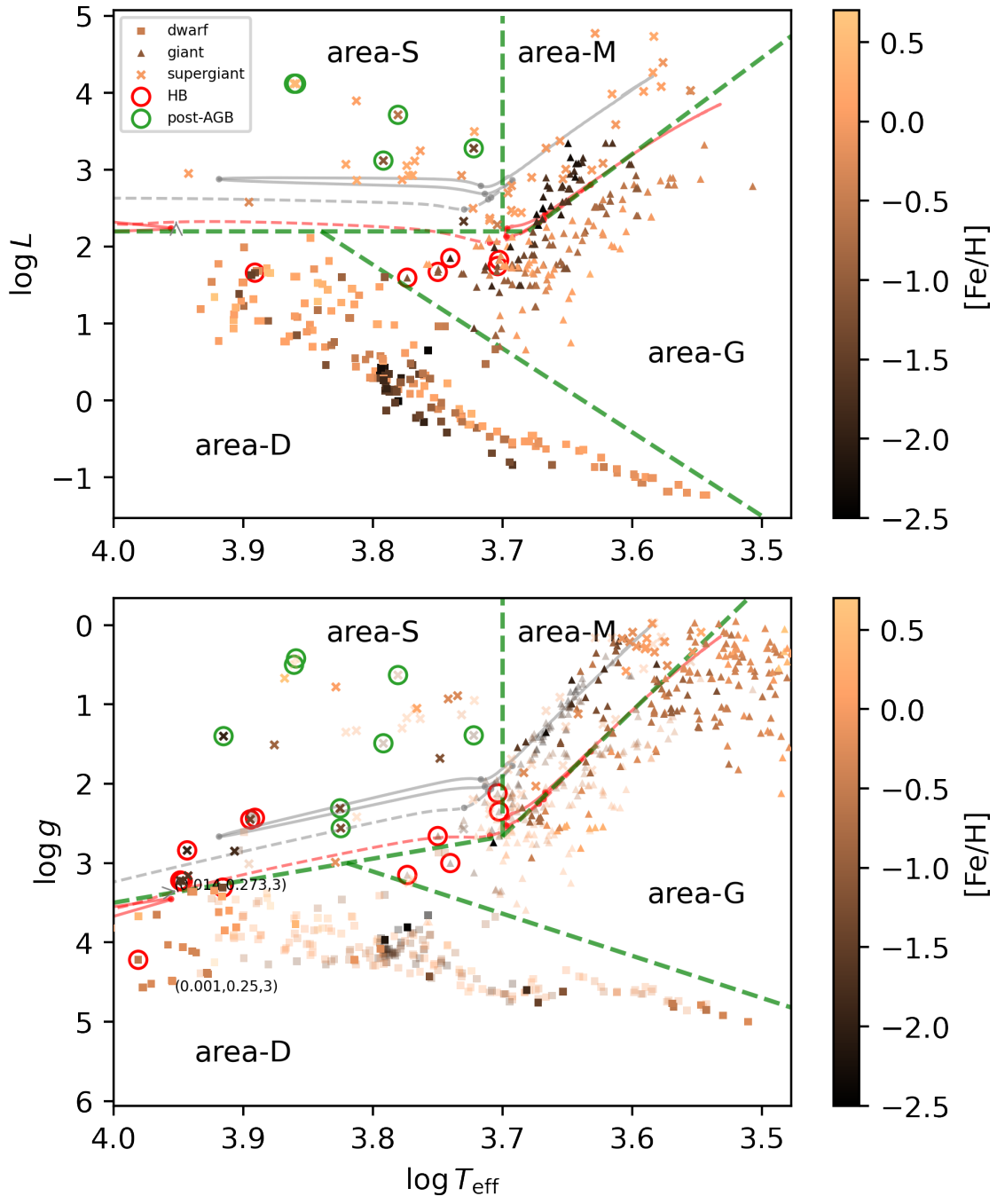


Figure 3.3: The classification for the field-XSL sample, in HR diagram (upper panel) and Kiel diagram (lower panel). The stars in area-D, G and S are classified as dwarf, giant and supergiant respectively, and those in area-M are classified as giant or supergiant if their metallicity is smaller or larger than −0.25.

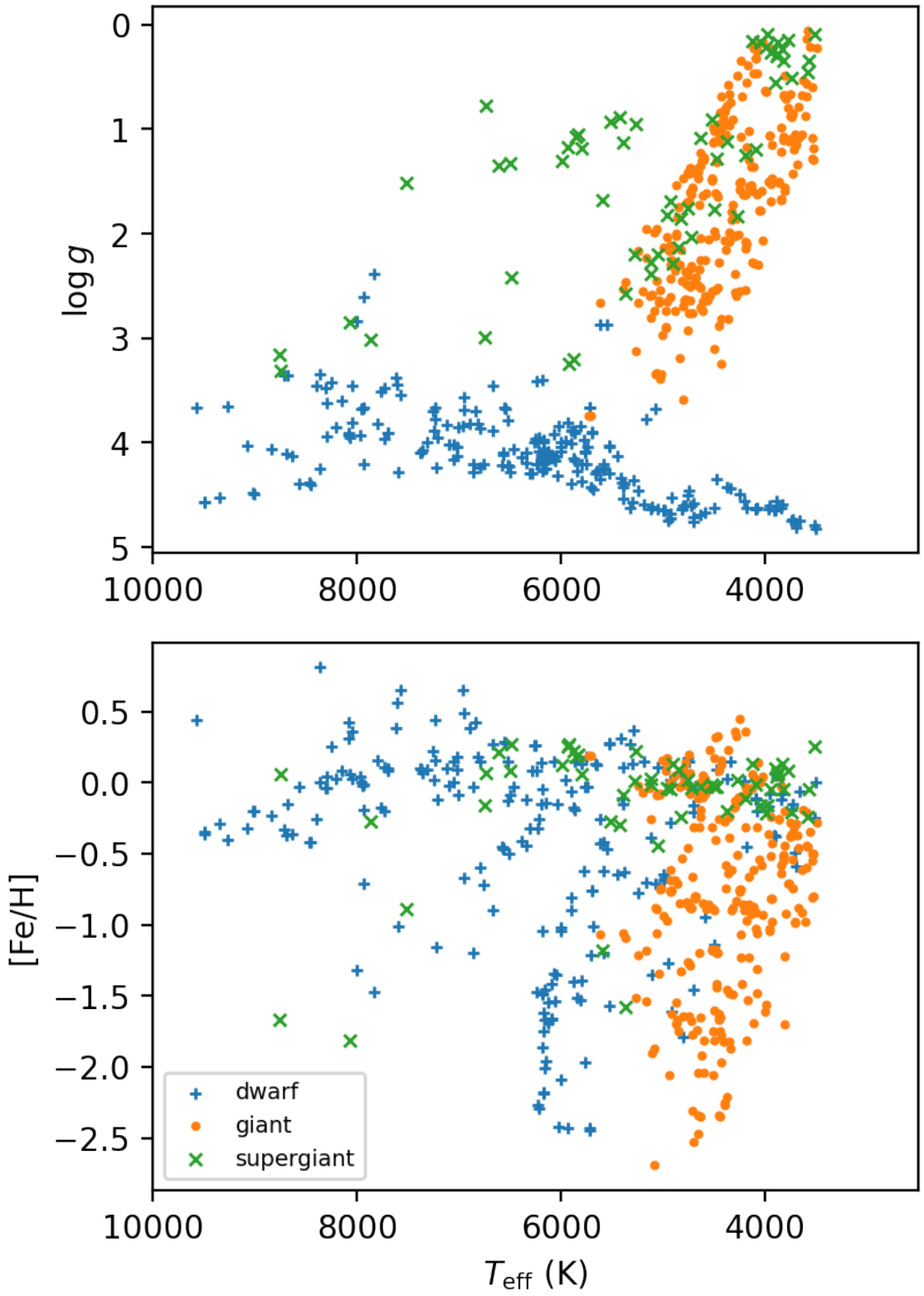


Figure 3.4: The Kiel and [Fe/H]–$T_{\rm eff}$ diagram for field-XS sample.

Chapter 4

Data reduction and calibration of blending line parameters

The main goal of this Chapter is to produce a clean helium feature from the raw data. Two steps are included in this process: data reduction and calibration of the parameters of the blending lines. They will be described in the following sections.

4.1 Data reduction

Reduction of the spectral data refers to the process of transforming the observed image (usually a 2D image, in the case of echelle spectrograph) to a list of values indicating the wavelength and flux in each pixel. Such a process transforms the raw data into the ready-to-analysis spectra in the absolute flux scale or continuum scale. The spectrum in the latter case, or the continuum normalized spectrum, sets the overall shape of the spectrum (continuum) as one, thus a flat spectrum with spectral lines spread in various wavelengths is presented. Most of the high-resolution spectra are continuum normalized, since (1) they usually only cover a small wavelength range (e.g., from a few tens to one hundred Å per order), and/or (2) it is not trivial to eliminate the small variation between pixels (e.g., fringing pattern). Continuum normalized spectra will be used in this study. The process of normalization is done by a sigma clipping process similar to the continuum in the Image Reduction and Analysis Facility (IRAF) package. The sigma clipping process selects the pixels in the continuum region by removing the pixels $n\sigma$ away from the mean value iteratively (with n determined by the user) and fits the continuum pixels using polynomials. The scatter of the continuum pixles, $\sigma_{\rm con}$, are used to estimate the signal-to-noise ratio (S/N) by S/N = $1/\sigma_{\rm con}$.

Some extra spectral features (mostly in the NIR wavelength range) will be added to the spectra when the starlight goes through the atmosphere of the Earth. These features, or the telluric lines, may blend with the lines from the star. The main absorption species in the YJ-band is H_2O, O_2 and CO_2. Figure 4.1–4.4 present the model telluric spectra in the YJ-band, split according to the orders of the WINERED-WIDE mode. The strength of the H_2O telluric features are strong in some of the orders, e.g., 42, 48–50 and 59–61. The position of the helium 10 830 Å line is not affected by the telluric absorption, but when a star has a positive radial velocity (RV), He 10 830 may red-shift to the wavelength of the H_2O telluric line. Further, the other atomic lines will be used to determine some stellar parameters such as microturbulence (see section 4.2.1), thus correcting the telluric features is necessary.

A typical procedure to remove the telluric lines includes using the observed spectra with only a few intrinsic features as the telluric standard (Vacca et al., 2003), or directly using the synthesized telluric spectra to perform the correction (Gullikson et al., 2014). The former method usually uses an A0V star as the telluric standard, since only a few spectral lines appear in their spectra. Such stars close to the target will usually be observed before or after the target's observation, to minimize the difference in air conditions and atmospheric depth between the target and telluric standard. This method does not rely on the atmospheric model and the line list used for generating the synthetic telluric spectra, thus can provide an accurate correction when the telluric model is not precise. On the other hand, observing the telluric standard requires the telescope time that could otherwise be used to observe other scientific targets, and the intrinsic features in the telluric standard have to be removed before the telluric correction. Recently, the number of tools for fitting the synthetic telluric spectra with the observed scientific spectra is increasing (see, e.g., `molecfit`, Kausch et al. 2015 and `telfit`, Gullikson et al. 2014).

The telluric correction procedure is different among the sample spectra, depending on their wavelength ranges, and whether the observed telluric standard is available. They will be described in the following sections.

4.1.1 Reduction of the Stock-2 spectra

The spectra of the Stock-2 sample are reduced by data reduction pipeline software GOFIO (Rainer et al., 2018). The pipeline performs the necessary correction (including bad pixel and cosmic removal, subtraction of sky and dark, and flat-field and blaze correction) to the calibration and scientific frames. The 1D spectra are then extracted by the pipeline, followed by the wavelength calibration and telluric correction using

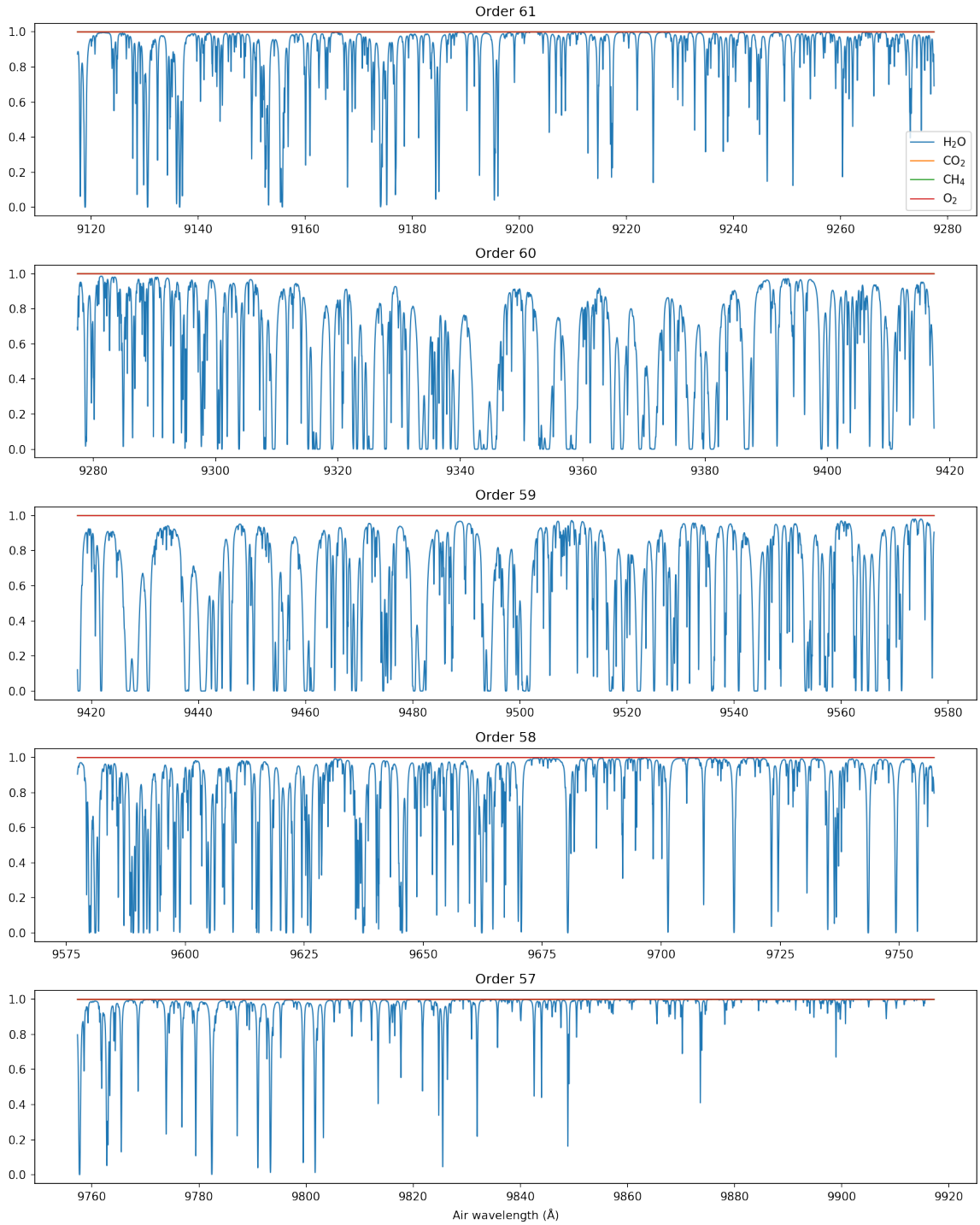


Figure 4.1: The model telluric spectra for orders 57–61 in WINERED-WIDE mode. The spectra, generated by `telfit`, are separated into four main species (H_2O, CO_2, CH_4 and O_2) contributing to the telluric absorption in these wavelengths.

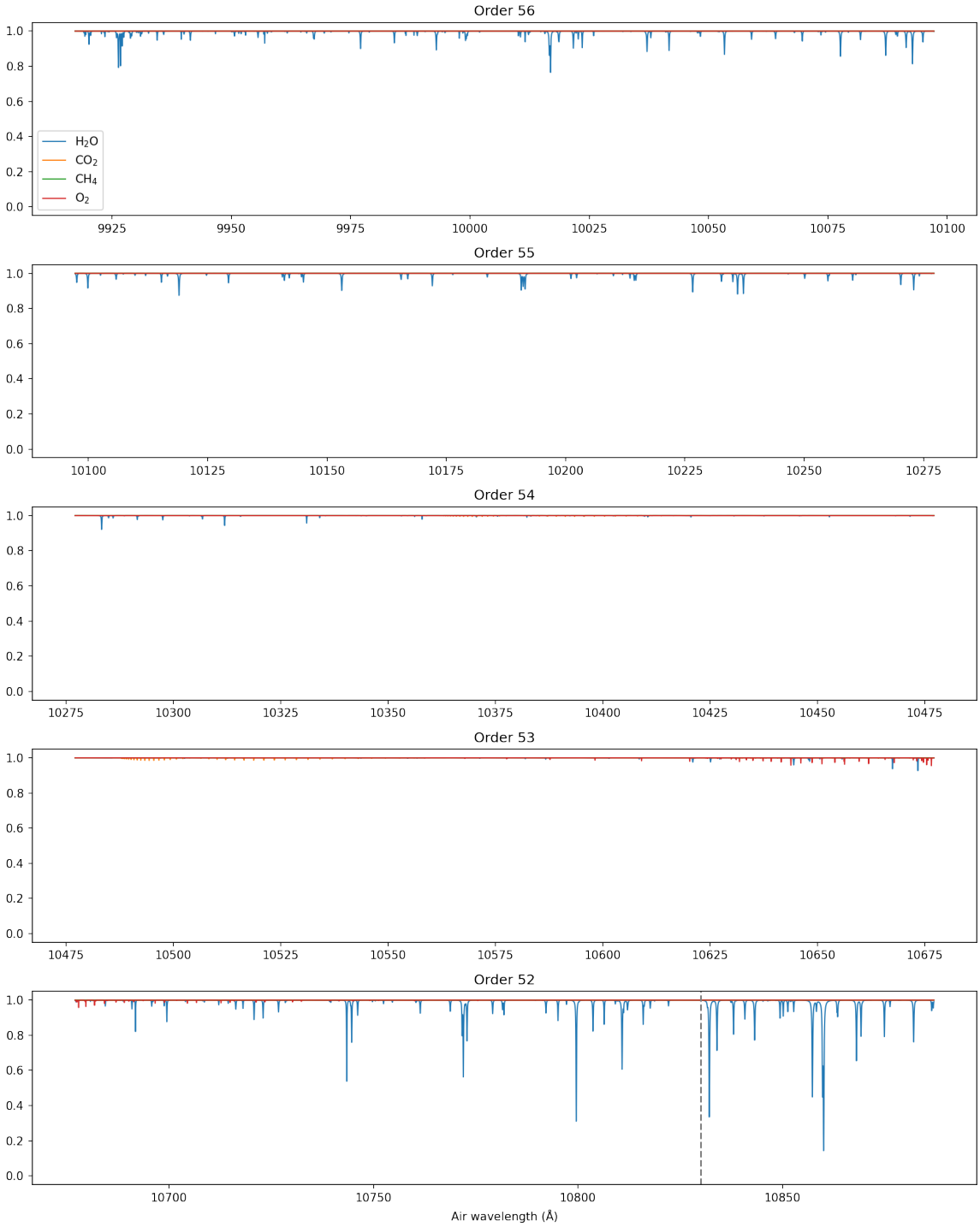


Figure 4.2: Same as Figure 4.1, but for orders 52–56. The position of He 10 830 is indicated by the vertical dashed line in the panel of order 52.

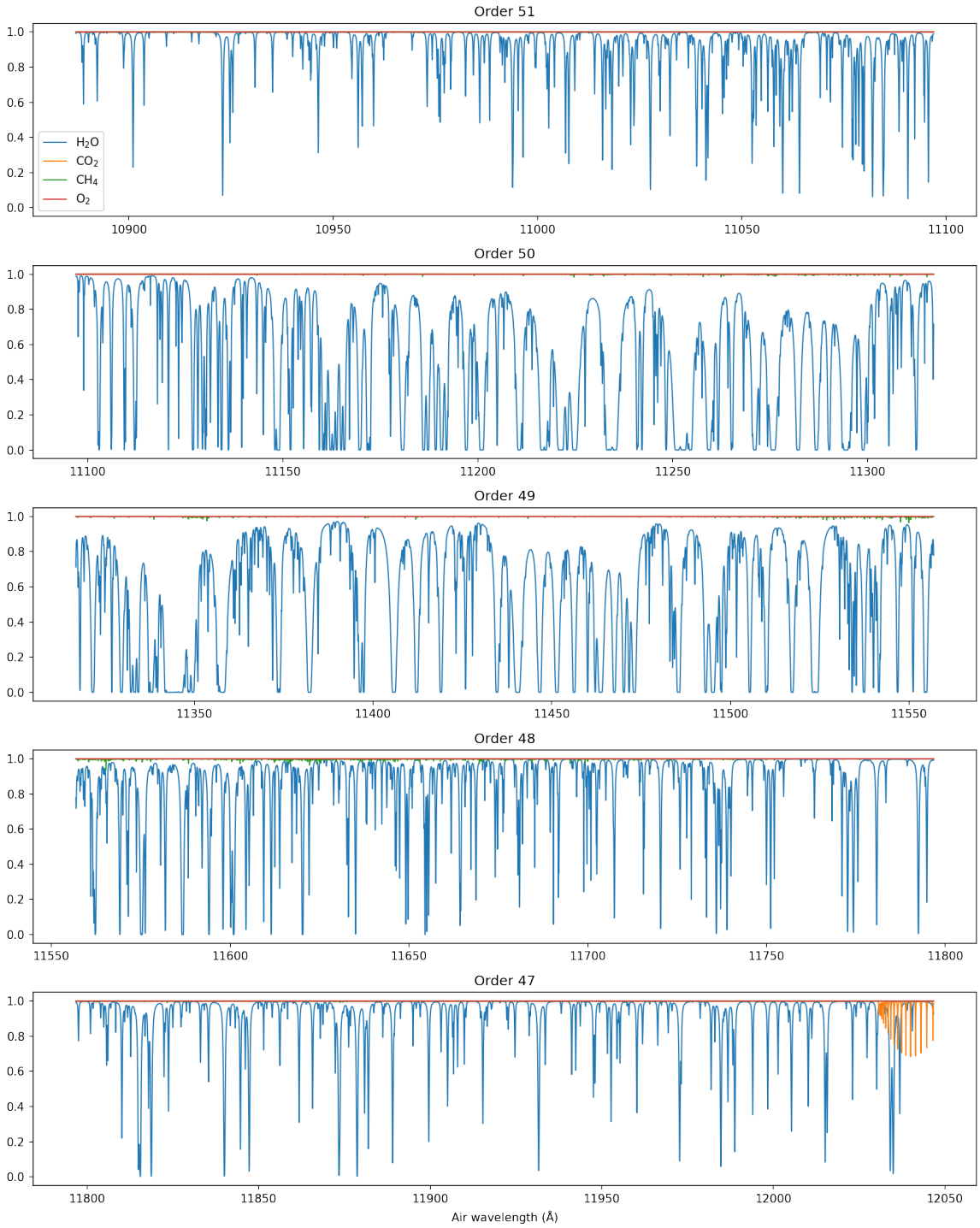


Figure 4.3: Same as Figure 4.1, but for orders 47–51.

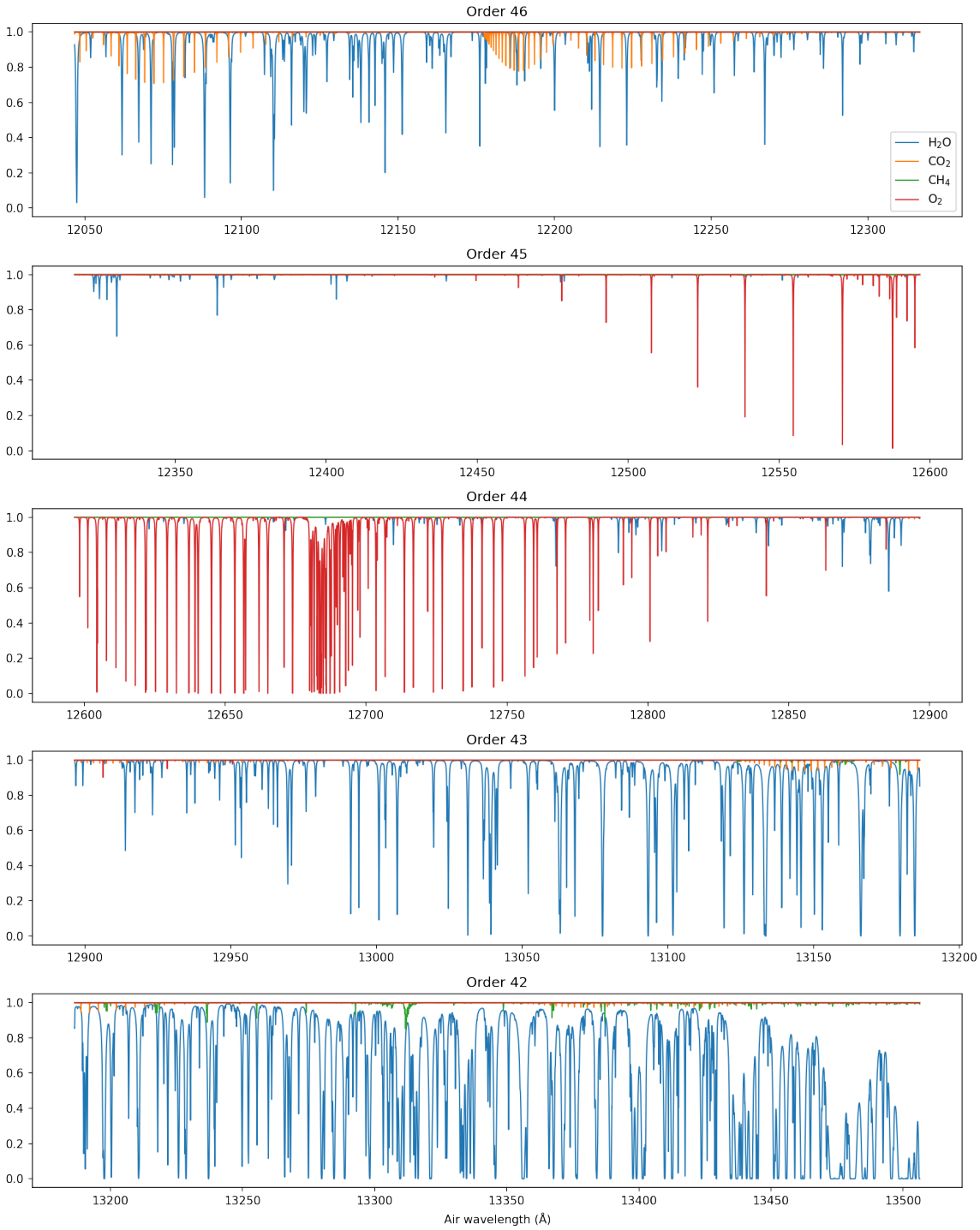


Figure 4.4: Same as Figure 4.1, but for orders 42–46.

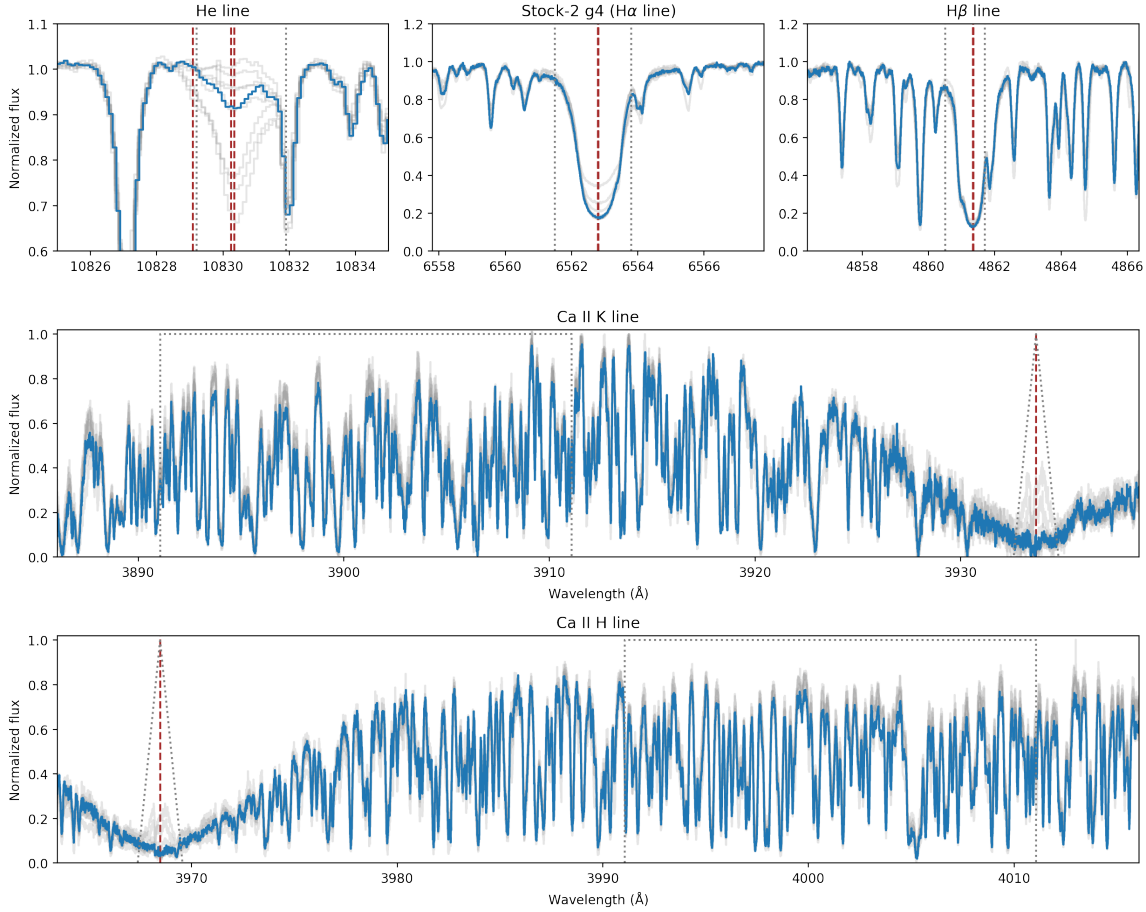


Figure 4.5: The spectra of Stock-2 g4 star in He 10 830, Hα, Hβ and Ca II H&K wavelength range. The dotted squares and triangles are the wavelength bands for measuring the S-index. The spectra of other Stock-2 stars are in gray.

the spectra of an O-type standard star. However, the airmass of the telluric standard might not match the target, and therefore the standards taken at different airmass values has to be combined with different weights to the adopted telluric standard. Thus, the correction may cause some artifacts in the He 10 830 profile, and we didn't use the telluric corrected spectra from GOFIO. Instead, the telluric absorption lines are removed by the python package `telfit`[6]. The parameters of the telluric atmosphere and observation, e.g., humidity, pressure, CO_2 mixing ratio and resolution are varied automatically in Telfit, to provide the best-fitted telluric spectra from the observed ones. Finally, the continuum of the spectra was traced and normalized to the unity again, to remove the possible fluctuation introduced in the telluric correction. Figure 4.5 present an example of the Stock-2 spectra (g4).

[6] https://telfit.readthedocs.io/en/latest/

4.1.2 Reduction of the field-WD spectra

A set of raw data for a WINERED observation consists of 2D scientific, dome/sky-flat and ThAr lamp images. These images are processed by the WINERED Automatic Reduction Pipeline (WARP; Hamano, 2022, private communication) written in Python. WARP corrects the scientific images using the calibration data, extracts the 1D spectra and calibrates them to the wavelength scale. Both the spectra in the air and vacuum wavelength scales are produced, and we will use the air wavelength throughout this study.

Telluric correction is performed using the A0V type telluric standard, and the correction process is proposed and summarized by Sameshima et al. (2018). As described at the beginning of this Chapter, though not many, the A0V stars still hold spectral lines in the YJ-band. These lines need to be removed before the spectra of the telluric standard can be used for telluric correction. The spectra of the telluric standard stars were first fit by Telfit, and the telluric lines are removed from the observed spectra. The intrinsic lines which remain in the spectra were then fit by Gaussian profile(s) through visual examination. Most of the atomic lines can be well removed by a single Gaussian profile, but two or three Gaussians are usually required for some strong lines such as Hydrogen lines. We then got the "clean" telluric standard spectra, i.e., the spectra with telluric features only. Such an approach for telluric correction, though requires longer observation time and is more cumbersome than directly using `telfit`, is considered to have better performance (Sameshima et al., 2018) for the WINERED spectra.

The telluric corrected and continuum normalized spectra were then shifted to the rest wavelength by minimizing the cross-correlation between the target and a template. Visual examination of the corrected spectra then confirmed the wavelength correction, or applied a further adjustment to the radial velocity. Figure 4.6 presents the field-WD spectra in around 10 830 Å.

4.1.3 Reduction of the field-XSL spectra

The field-XSL spectra are adopted from the data release 2 of XSL database[7]. The data reduction was performed by and thoroughly described in Gonneau et al. (2020). These spectra are well-calibrated, with wavelength correction done by using the telluric lines, telluric lines removed, and the absolute flux calibrated. Normalization for the spectra around He 10 830 and Hydrogen line is performed as described above, but the search

[7] http://xsl.u-strasbg.fr/page_dr2.html

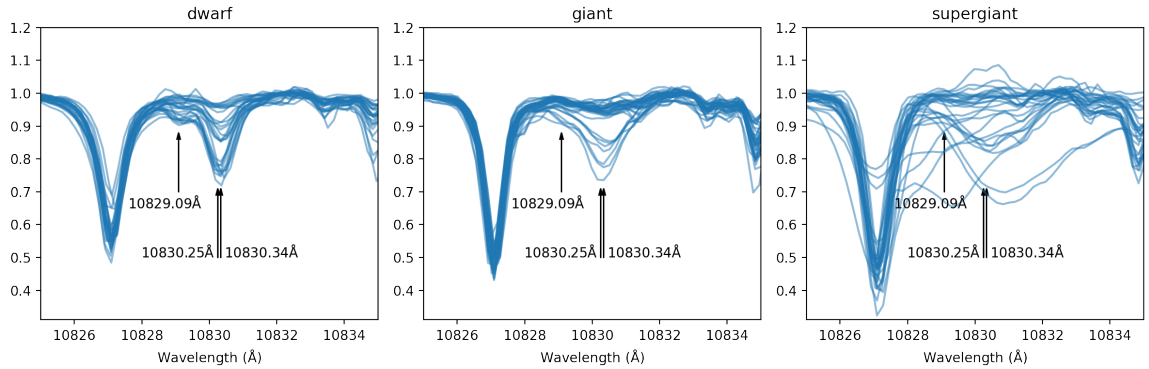


Figure 4.6: The He 10 830 spectra of field-WD sample, divided into dwarfs, giants and supergiants. The He 10 830 appear in most of the late-type stars in this sample. The atlas of all the spectra is presented in Appendix C.

on the continuum part for the Ca II lines is difficult. As shown in Figure 3.4, the wavelength range around the Ca II lines are occupied by a large number of lines. Here we simply set the maximum of the pixel value in $3910 < \lambda < 3990$ Å as 1, and performed no more continuum normalization. The measurement of Ca II index, as described in section 5.2, involves the scaling of the spectra to match the model, thus whether continuum normalization is performed in this stage will not affect the measurement.

4.2 Contamination on He 10 830

The spectra after data reduction, telluric correction and continuum normalization are left with the spectral features from the target star only. As shown in Figure 1.6 and described in the previous studies, the width of the helium 10 830 Å is larger than other atomic lines. Thus this line may be blended with other lines as shown in Figure 4.8, and it is necessary to account for the contribution of the blending lines to the line strength. Since the blending lines are usually weaker than He 10 830, its strength cannot be measured directly in the observed spectra, but have to be calculated from the synthetic spectra. However, the parameters of the lines in the YJ-band used for generating the synthetic spectra, especially the oscillator strengths are not precise.

There are five parameters that determine the appearance, strength and profile of a line in spectral synthesis. They are wavelength, atomic identification, line excitation potential, oscillator strength and the van der Walls damping parameter. The wavelength determines the position of the line in the spectra, and atomic identification

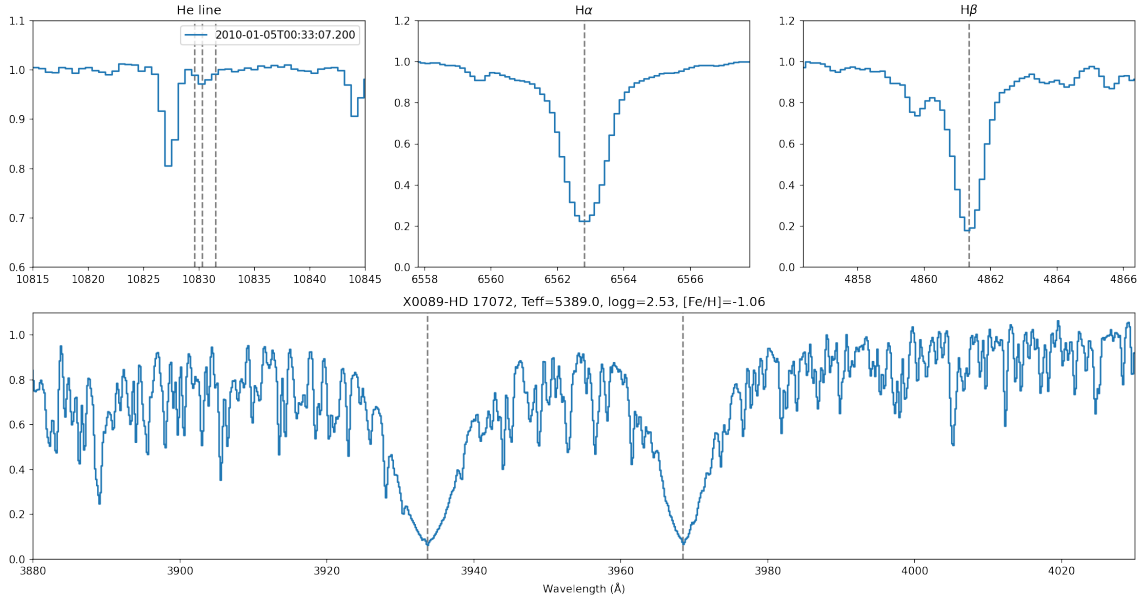


Figure 4.7: The He 10 830, Hα, Hβ and Ca II H&K spectra for HD 17072 in the field-XSL sample. The chromosphere lines are clearly seen under a resolution of 10 000.

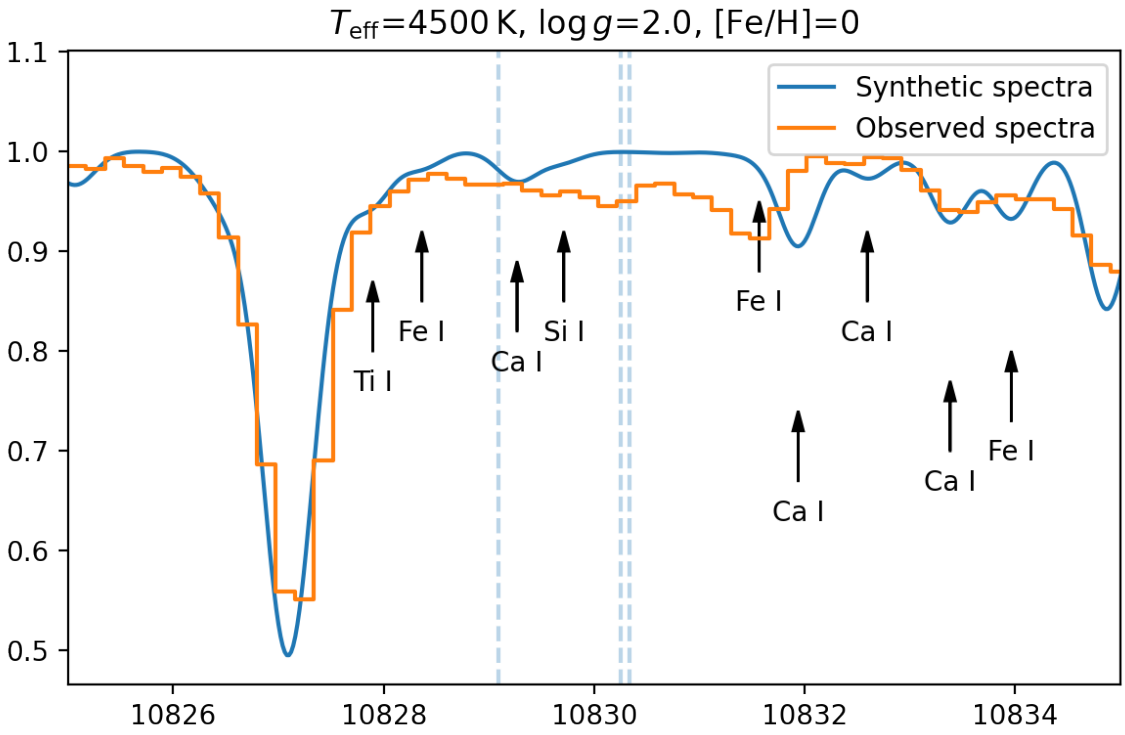


Figure 4.8: The blending lines around He 10 830. The spectra in blue is synthesized using the stellar parameters in the title with a resolution of 28 000, and the orange spectra is a giant star with similar stellar parameters observed by WINERED. Black arrows indicate the location of relatively strong atomic lines other than the He 10 830.

assigns the line to an atom species. The last three parameters determine the strength and profile of the line, when the atmosphere model is given.

Here we discuss how the oscillator strength values are introduced into spectral synthesis. If we treat the absorption of the radiation by an atom as an oscillator that is forced into an oscillation by an imposing electric field, then according to Gray (2005), the absorption coefficient per atom, α, would be:

$$\alpha = \frac{2\pi e^2}{mc} \frac{\gamma/2}{\Delta\omega^2 + (\gamma/2)^2}, \tag{4.1}$$

where m stands for the mass of the electron, γ is the natural damping constant and $\Delta\omega = \omega_0 - \omega$ is the difference between line transition frequency and the one of interest. The total energy taken from a light beam with a specific intensity of I_ν is the integration of α:

$$\int_0^\infty \alpha \mathrm{d}\nu = \frac{\pi e^2}{mc}, \tag{4.2}$$

note that the integral of $\frac{\gamma/2}{\Delta\omega^2+(\gamma/2)^2}$ is unity. The model of the oscillator is purely classical, while the transition is a quantum mechanical process, so a quantum mechanical correction term, f, is added to equation 4.3:

$$\int_0^\infty \alpha \mathrm{d}\nu = \frac{\pi e^2}{mc} f_{lu} \tag{4.3}$$

Relate these equations with the probability of absorption times the energy of the transition:

$$\int_0^\infty \alpha \mathrm{d}\nu = B_{lu} h\nu \tag{4.4}$$

we have:

$$\frac{\pi e^2}{mc} f_{lu} = B_{lu} h\nu \Rightarrow \frac{f_{lu}}{B_{lu}} = \frac{h\nu mc}{\pi e^2} \tag{4.5}$$

The frequency corresponding to the absorption and emission of the transition is the same. Combining equation 4.5 and the relation between Einstein coefficient and statistical weight, $B_{ul} g_u = B_{lu} g_l$ (see also Hubeny & Mihalas 2014, eq. 5.108c):

$$g_l f_{lu} = g_u f_{ul} = gf \tag{4.6}$$

Thus the gf has the same value for upward and downward transitions. This number is frequently used in spectral synthesis, so its accuracy is essential. However, the $\log gf$ values of the lines in the YJ-band may not be precise, as stated in Andreasen

et al. (2016). Thus the $\log gf$ values of the contaminating lines need to be calibrated using the observed spectra.

We use the Stock-2 sample for the calibration. The contaminating lines could be more separate from each other (if they are close) in the higher spectral resolution. The giant stars in the sample have precise stellar parameters from their HARPS spectra, including $T_{\rm eff}$, $\log g$, [Fe/H] and other chemical abundances. These values will be used as the input parameters for generating the synthetic spectra. The sample size of 9 stars ensures that the contaminating lines close to He 10 830 could still be measured in the stars with the weakest helium absorption, thus all the lines would have at least three calibrations.

4.2.1 Microturbulence, metallicity and broadening velocity measurement of the Stock-2 sample

The calibration of the $\log gf$ values is performed by comparing the synthesized and observed spectra and minimizing their difference by varying $\log gf$. Such comparison requires that the parameters which affect the line strength or shape be well determined. For the case of the Stock-2 sample, most of the stellar parameters are derived in Alonso-Santiago et al. (2021). However, the microturbulence velocity of the sample stars is not given in the paper, and concerning that adopting the broadening velocities derived from the optical spectra may produce some discrepancies with the actual line profile in the NIR, the microturbulence, metallicity and broadening velocities are measured using the GIANO spectra in this section.

There are a few mechanisms that affect the spectral line broadening, such as pressure, thermal motion and turbulence. The turbulence refers to the bulk mass motion due to the buoyancy caused by the vertical density gradient. Since the stellar atmosphere model used in this work are in 1D, i.e., the stellar atmosphere model only depends on radial distance, such turbulence cannot be included physically, but is simulated by two free parameters, microturbulence and macroturbulence velocity. Microturbulence and macroturbulence refer to the "simulated" turbulence motion with a scale smaller or larger than the free mean path (the mean length from the photon creation to destruction) of a photon. Such small-scale bulk motion of gas decreases the number of atoms suitable for absorbing the light in the line core, and increases the number in the line wing, thus increasing the line strength. Figure 4.9 present the curve of growth (or CoG, the curve in the diagram of reduced EW, $\log W/\lambda$, versus abundance, $\log A$) of a spectral line in different microturbulence velocity, ξ. The increase of ξ moves the middle part of the curve upward (when

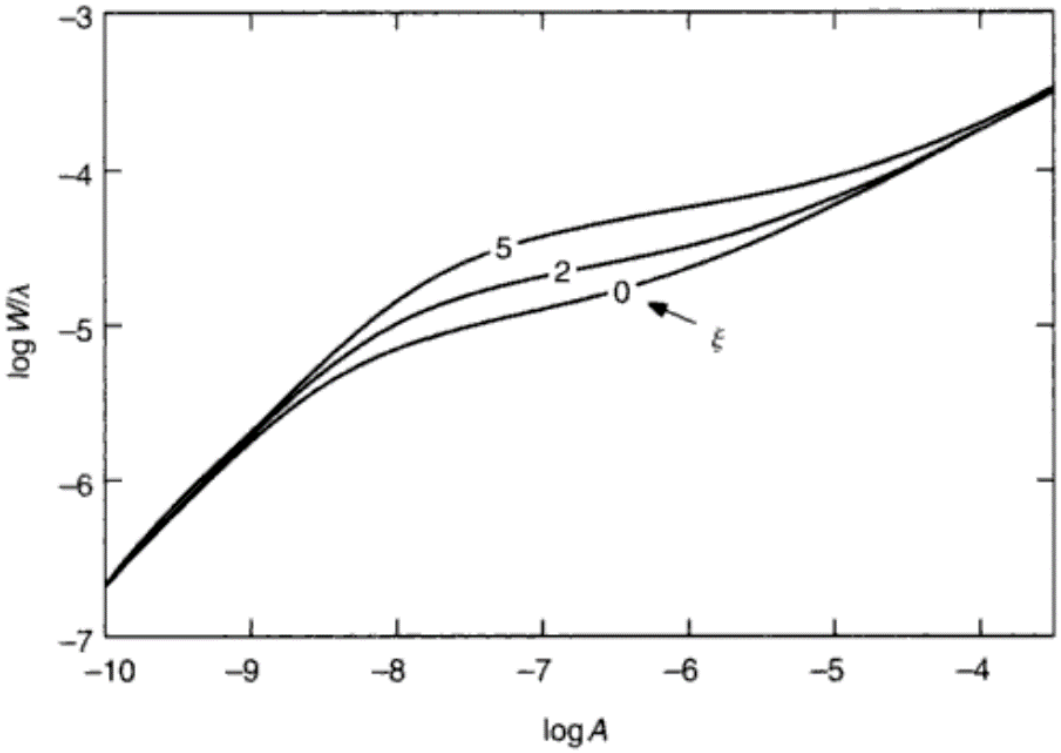


Figure 4.9: Curve of growth for a spectral line with different ξ values. In a fixed line EW, ξ and abundance ($\log A$) degenerate when the line is saturated. The MPFIT algorithm use this feature to determine ξ and metallicity by matching the observed and synthesized spectra of multiple Fe lines. Adopted from Gray (2005)

the line is saturated), and the metallicity and ξ are correlated. On the other hand, macroturbulence does not affect the line strength, but only the line shape. It will be included in the broadening velocity along with other line broadening mechanisms.

The values of ξ and broadening velocity are determined by the MPFIT algorithm described in Takeda (1995). MPFIT is an algorithm for determining various parameters involved with stellar spectra. It starts from an initial guess of the to-be-determined parameters, then uses the Newton-Raphson method to modify the initial parameters until their synthesized spectra are sufficiently close to the observed ones. This algorithm was later implemented in some packages such as SPTOOL and `pymoog`[8]. Kondo et al. (2019) used MPFIT to determine the microturbulence and metallicity for two giants, Arcturus and μ Leo. Here we adopt the same process as in Kondo et al. (2019). We first selected the Fe lines in the wavelength regions covered by the GIANO spectra using the LTE radiative transfer code MOOG (Sneden et al.,

[8]A python wrapper for MOOG developed by the author. The MPFIT algorithm is also integrated into this package. Available in https://github.com/MingjieJian/pymoog.

2012) with the stellar atmosphere model from ATLAS9 (Kurucz, 2005) and the line list from VALD3 database (Ryabchikova et al., 2015). The lines with weak absorption (whose depth $d < 0.05$) and some amount of blending (those with blending line contribution in line depth larger than 20%) are removed from the line list. 179 Fe lines from 9820 to 22 473 Å are selected for the measurement.

Then we matched the observed and synthetic profile of the Fe lines by varying ξ, [Fe/H] and $V_{\rm broad}$. As shown in the upper panel of Figure 4.10, the values of [Fe/H] and $V_{\rm broad}$ are first derived for a 20-point grid of ξ from 0.5 to 2.5 km/s using MPFIT in pymoog. For each ξ, we got a group of [Fe/H] from each of the 179 lines. The metallicity determined from a strong line will be affected by the selection of ξ due to saturation, e.g., the metallicity will be overestimated if ξ is smaller than the actual value, and vice versa. Thus, the middle panels show what will happen when ξ is too small, just right and too large. The relation between [Fe/H] and the X index (defined as $X \equiv \log gf - \mathrm{EP} \times 5040/(0.86T_{\rm eff})$ will have a nonzero slope when the choice of ξ is not appropriate. Then the ξ value which is closest to 0, is set as the final ξ, and the [Fe/H] as well as $V_{\rm broad}$ are calculated. The above process is repeated 1000 times with a random selection of the lines (allowing duplicated selection), derives the final ξ, [Fe/H] and $V_{\rm broad}$ and their errors. The derived parameters are listed in Table 3.2. As shown in Figure 4.11, the derived ξ is roughly consistent with the trend reported in Holtzman et al. (2018) from APOGEE giants, and the metallicities measured using GIANO spectra are also compatible with the values from HARPS spectra.

4.2.2 $\log gf$ calibration of contaminating lines and blending situation

The stellar parameters determined in the last section were then used to calibrate the $\log gf$ values of the blending lines. The blending lines are defined as the strong lines with a wavelength close to that of He 10 830. As present in Table 4.1, eight lines near the helium 10830 Å lines with the largest contribution to the absorption features are selected as calibration targets. The contribution of the rest lines is negligible, i.e., the maximum depth of other lines is smaller than 0.01 in the parameter ranges we are interested in. A strong Si line appears on the left side of He 10 830. Since the calibration of $\log gf$ for such a strong line is difficult, it will not be treated as a blending line and we remove it by profile fitting when measuring the He 10 830 EW (see section 5.1). Then we varied their $\log gf$ values, starting from that of the strongest line, to find the best value that fits the observed spectra. The calibration result was rejected when the line is affected by telluric absorption or by He 10 830.

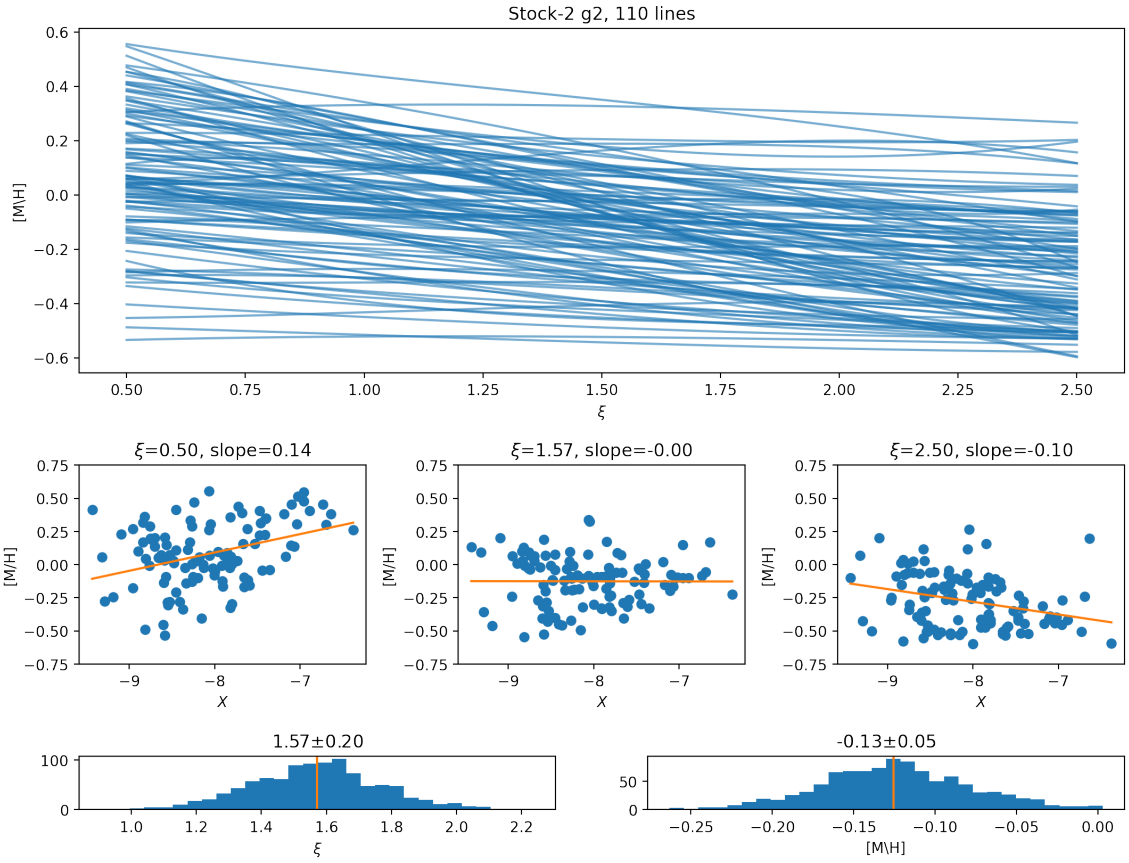


Figure 4.10: The [M/H]–ξ diagram (upper panel), [M/H]–X (middle panels) in three ξ values and the histogram of ξ and [M/H] of the 1000 times repeated MPFIT algorithm. These panels are used to determine ξ and [Fe/H] for Stock-2 g2 star, shown as an example (for the detail of MPFIT algorithm, please refer to the text in section 4.2.1).

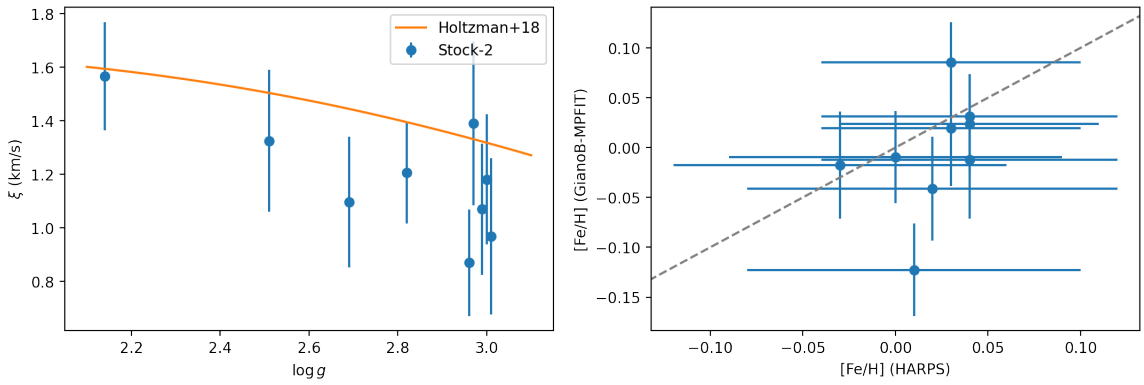


Figure 4.11: Comparison of the MPFIT determined ξ with the trend for giants from Holtzman et al. (2018) (right panel), and [Fe/H] with those from Alonso-Santiago et al. (2021).

An example of calibrating process is shown in Figure 4.12. We have a few stars showing weak helium absorption, so the number of calibrated $\log gf$ values is smaller for the two lines around 10829.6 Å. Fig. 4.13 presents the comparison of the initial and calibrated $\log gf$ values. As shown in Table 4.1, most of the calibrated $\log gf$ values are smaller than those in the VALD line list. However, the synthetic spectra generated from the linelist with the calibrated $\log gf$ values are more consistent with the observed ones, including that for the Arcturus (Figure 4.14).

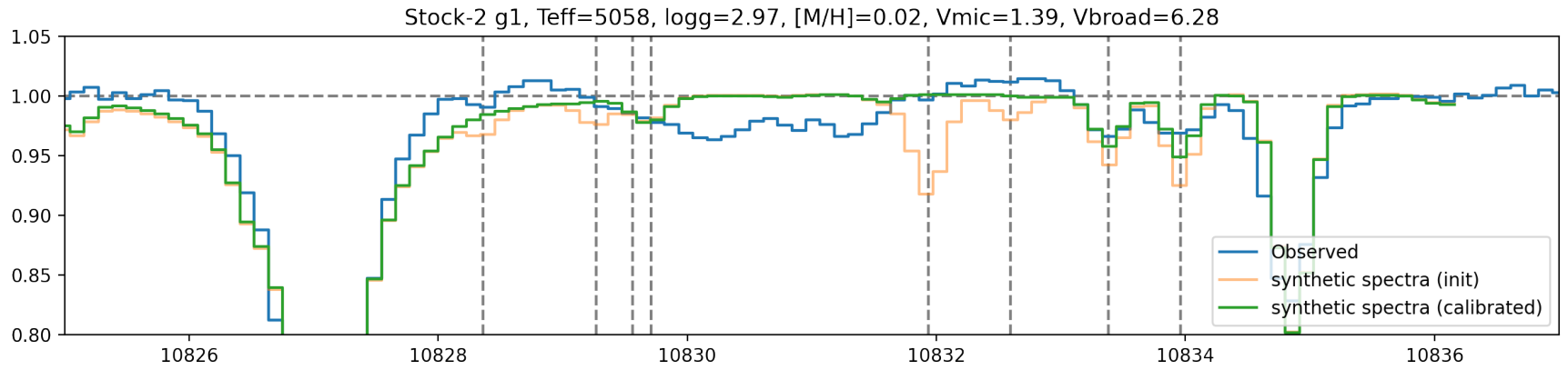


Figure 4.12: Example spectra (the g1 star) for the $\log gf$ calibration. The vertical dashed lines indicate the wavelengths of the lines being calibrated, while the lines with red crosses are excluded from the calibration for this star. The spectra for all stars are presented in Appendix D.

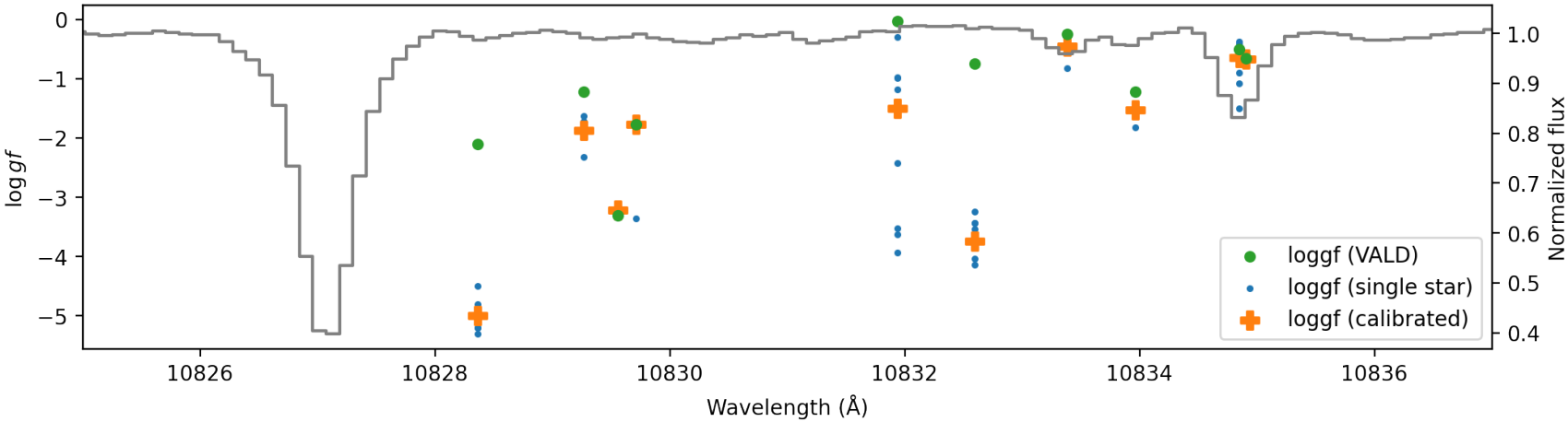


Figure 4.13: The $\log gf$ calibration result is plotted with the spectra of star Stock-g7.

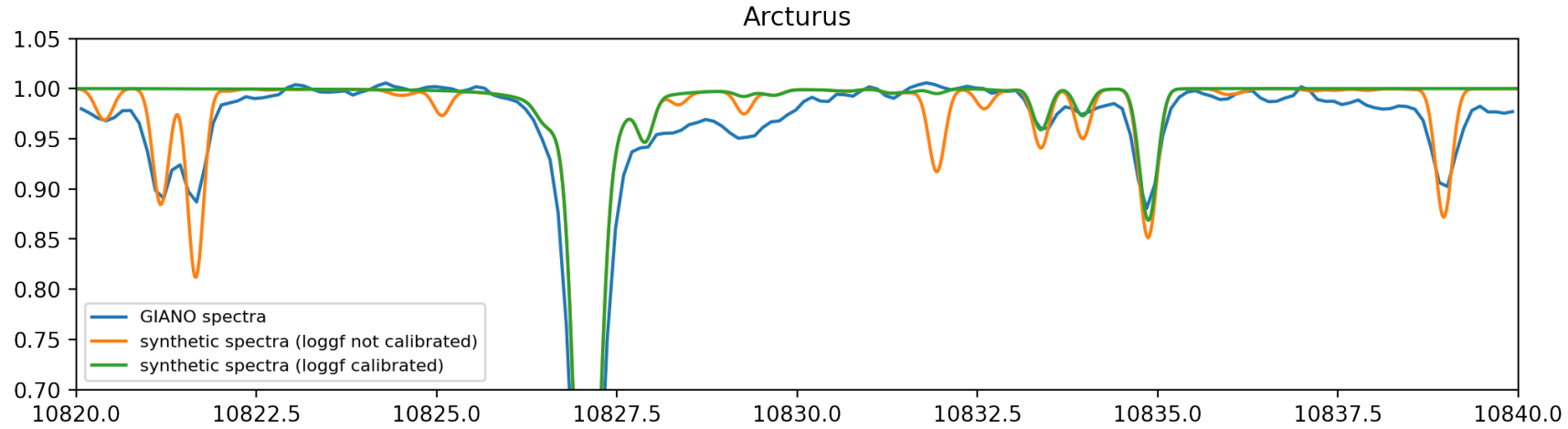


Figure 4.14: Comparison between the observed Arcturus spectra and the synthetic spectra before and after the $\log gf$ calibration. The spectra after $\log gf$ calibration are more consistent with the observed one.

wavelength	id	EP	$\log gf$	C6	$\log gf_{\text{calibrated}}$
10827.088	14.0	4.954	0.302	-7.266	–
10831.938	20.0	4.878	-0.029	-6.940	-1.479
10833.382	20.0	4.877	-0.244	-7.590	-0.43775
10834.846	11.0	3.617	-0.503	0.000	-0.353
10833.963	26.0	5.587	-1.223	-7.540	-1.523
10829.267	20.0	4.441	-1.224	-7.090	-1.874
10834.905	11.0	3.617	-0.658	0.000	-0.65175
10829.711	14.0	6.727	-1.765	-6.860	-1.765
10832.595	20.0	4.878	-0.742	-6.930	-3.742
10829.560	26.1	5.585	-3.312	-7.871	-3.212
10828.363	26.0	5.446	-2.104	-7.520	-5.004

Table 4.1: Parameters and calibrated $\log gf$ values of the blending lines.

4.2.3 Contamination situation around He 10 830

The contamination situation around He 10 830 can now be estimated. The value of contamination, i.e., blending EW, is defined as the EW of all the lines between $10829.6 < \lambda < 10831.51$ Å. The blending EW is calculated from the synthetic spectra using the linelist with calibrated $\log gf$ values and specified spectral resolution. Figure 4.15 present the variation of the blending EW in $\log g$–T_{eff} plane under the resolutions of our sample. The blending EW is similar for those in $R = 28000$ and 50000, but larger when the resolution is smaller. For a dwarf with [Fe/H] = 0.5, the blending EW is between 40 and 50 mÅ for field-XSL sample and between 30 and 40 mÅ for other samples. The blending for giants and supergiants are also around 30 and 40 mÅ. These values decrease to around or less than 10 mÅ with [Fe/H] $= -0.5$. There is no large variation in the blending EW along the main-sequence or red giant branch in a fixed metallicity, thus blending is negligible for the fluctuation in He 10 830 strengths between stars with the same metallicity. On the other hand, the blending would have a contribution of around 30 mÅ for stars with different metallicity.

To account for the contamination, we will first measure the initial EW of He 10 830 in the following analysis, then calculate the blending EW according to the stellar parameters (T_{eff}, $\log g$ and [Fe/H]) of the target star. The final EW of He 10 830 is then derived by subtracting the initial EW(He) by the blending EW.

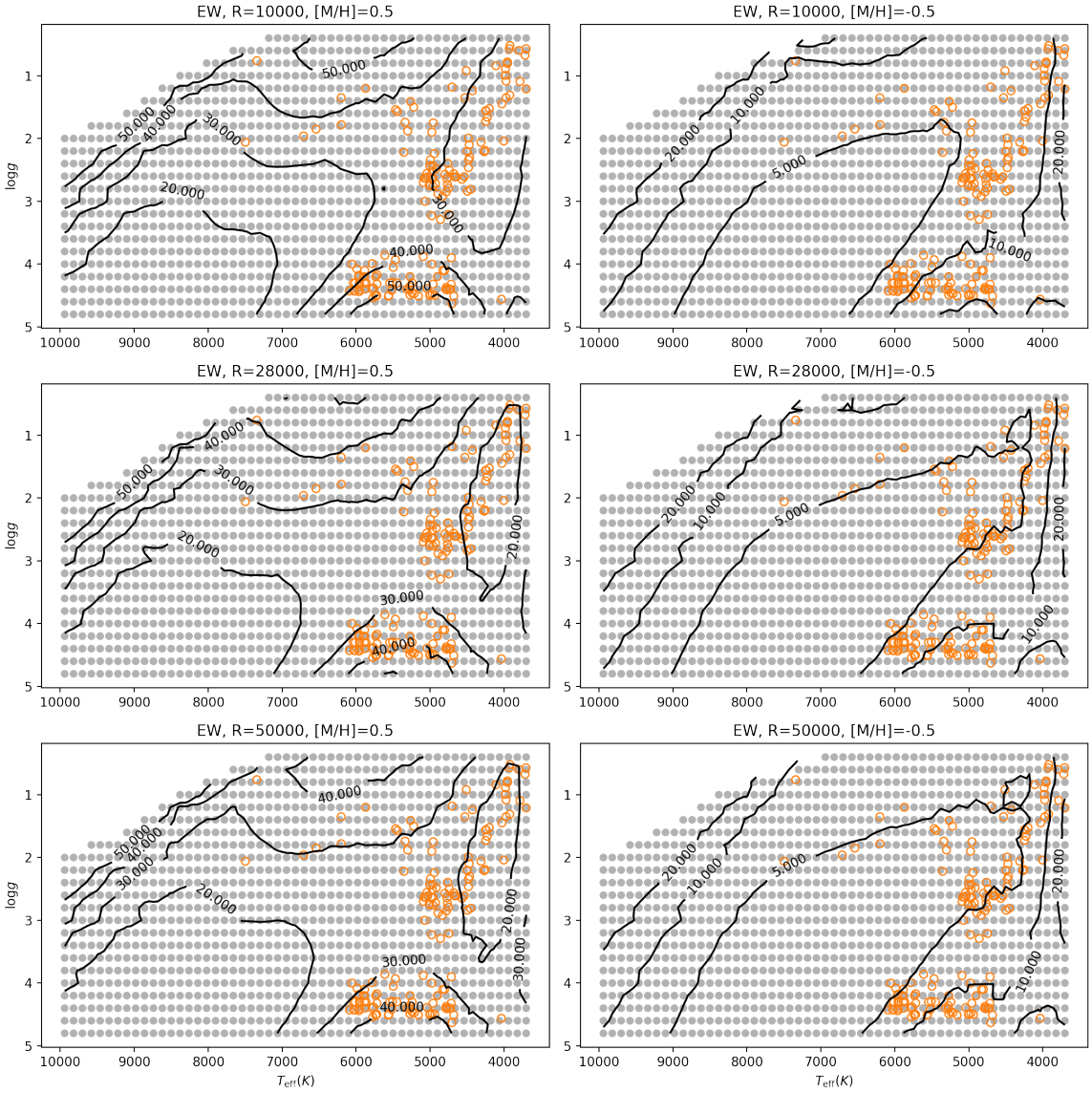


Figure 4.15: The contamination situation of the blending lines in different metallicity and resolutions. The black contours show contamination EW in various stellar parameters, and the gray points are the grid points used to calculate the contours. The field-WD sample stars are labeled by orange circles.

Chapter 5

Measurement of the line strengths and indices

This chapter describes the method for measuring the lines and indices in our spectra. They include the strength of He 10 830, the Ca II H&K indices and fractional X-ray luminosity. The measurement of He 10 830 includes the line strength and line profile, while that of the Ca lines includes the line indices indicating the extent of core emission. The measured values will be compared in the next chapter to derive the empirical trends.

5.1 Measurement of He 10 830

Measurement of He 10 830 refers to measuring its strength and profile. When a line profile is symmetric, the parameters representing its strength and profile are equivalent width (EW), peak position, and full width at half maximum (FWHM). On the other hand, when a line shows some extent of asymmetry, another parameter accounting for the asymmetry is required. Here we define these parameters with the fabricated line shown in Figure 5.1. The blue profile represents the line to be measured, and the red point is the minimum of the whole profile. Assuming the wavelength of the red point is $\lambda_{\rm min}$ and the distance between unity and the point is $d_{\rm min}$, $\lambda_{\rm min}$ is then set as the peak position of this line. The width of this line in the depth of $d_{\rm min}/2$, represented by the horizontal orange line, is the full width at half maximum, or FWHM. The area between the profile and unity on the left and right side of $\lambda_{\rm min}$ represent the blue and red absorption components of the line, and they are named as $S_{\rm B}$ and $S_{\rm R}$. The line asymmetry is then quantified by the B/R ratio defined as $S_{\rm B}/S_{\rm R}$, and the equivalent width (EW) is defined as the total absorption:

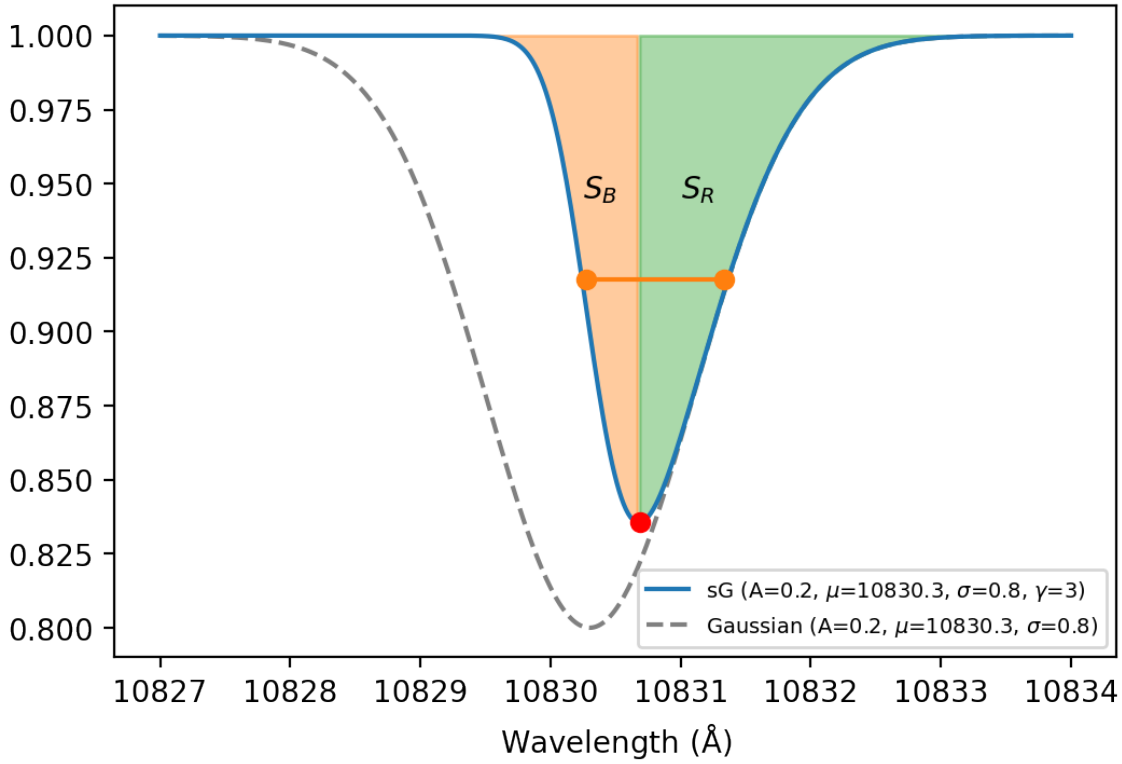


Figure 5.1: Definition of the line parameters to be measured. The blue curve shows a fabricated line with asymmetry, and the gray dashed curve shows a line with a Gaussian profile for comparison. The definition of line parameters are described in section 5.1.

$S_B + S_R$. The unit of λ_{min} and FWHM is Å, but since the strength of He 10 830 is weak, we use mÅ as the unit of EW.

The Gaussian profile is the one widely used for measuring He 10 830 in previous studies, such as in Takeda & Takada-Hidai (2011). To better preserve the consistency, here we use a similar profile to perform the measurement. However, simply applying Gaussian fitting to all the spectra in our sample would not derive a good measurement for some of the stars. The following factors make the Gaussian fitting not appropriate for strength and profile measurement in some cases:

1. The Gaussian fitting for very weak lines may derive unrealistic parameters;
2. The Gaussian profile cannot account for the line asymmetry;
3. The spectral resolution of our samples is different, so Gaussian fitting cannot be applied to the spectra which cover He 10 830 with only 3 pixels (i.e., those in the field-XSL sample).

The following measurement process is then proposed to take the above points into account. For the spectra observed by GIANO-B or WINERED, since their resolution is high, the number of pixels sampling He 10 830 is larger than 8. Skewed Gaussian profile is used to fit the feature. We then examine the quality of the fitting. If the fitting is bad, e.g., the profile is fitting some other features instead of He 10 830, or $\lambda_{\rm min}$ is far from the expected wavelength, the sum of the depths for the pixels in a specified wavelength range will be used as the line EW. In this case, $\lambda_{\rm min}$, FWHM and B/R ratio are not determined for this star. For the stars observed by X-Shooter, the direct summing method is always adopted since we cannot fit a profile with four parameters with only 3 pixels. The skew Gaussian profile is defined as:

$$f(x; A, \mu, \sigma, \gamma) = \frac{A}{\sigma\sqrt{2\pi}} e^{-\frac{(x-\mu)^2}{2\sigma^2}} \left\{1 + \mathrm{erf}\left[\frac{\gamma(x-\mu)}{\sigma\sqrt{2}}\right]\right\}, \tag{5.1}$$

where A, μ and σ are the amplitude, center and width of the distribution, γ representing its skewness, and erf is the error function:

$$\mathrm{erf}(x) = \frac{2}{\sqrt{\pi}} \int_0^x e^{-x^2} \mathrm{d}x \tag{5.2}$$

There are two strong lines located near He 10 830. The one on the left, with a wavelength of 10 827.1 Å is a Si line formed in the stellar atmosphere. The other one on the right, at around 10 832.2 Å is a telluric line, and its appearance depends on whether the telluric correction is performed. These lines may blend with our target feature and affect the fitting result. They are then removed by a fitting with the Voigt profile. The Voigt profile is the convolution of Gaussian and Lorentzian profile. It is considered to be the profile for most of the lines in stellar atmosphere (Gray, 2005). Here we summarize the process of line measurement using the example shown in Figure 5.2:

1. The continuum normalized spectra and their S/N are used as the input of the line measurement. They are shown as the gray step line and in the title of the figure.

2. The 10 827.088 Å Si line is fit by a Voigt profile and removed.

3. (Only for Stock-2 sample) The 10 832.2 Å telluric line is fit and removed. The spectrum with these two lines removed is plotted as blue step lines in the figure.

4. The pixels between 10 829.6 and 10 831.5 Å are used for summing up and calculating the EW (field-XSL sample), or used for fitting He 10 830 (other samples).

Star	EW(He)	R/B	FWHM	$\lambda_{\rm min}$	EW type	S-index	$\log R'_{\rm HK}$
g1	60.1 ± 7.9	2.15	2.09	10830.64	sG	0.0075	-5.52
g2	358.8 ± 6.6	1.09	1.47	10830.45	sG	0.0281	-4.71
g3	54.3 ± 6.8	1.71	1.61	10830.39	sG	0.0065	-5.16
g4	34.2 ± 6.9	1.02	1.70	10830.74	sG	0.0069	-5.24
g5	386.4 ± 6.3	1.01	1.50	10830.56	sG	0.0103	-4.95
g6	109.8 ± 6.3	1.02	1.31	10830.46	sG	0.0079	-5.11
g7	33.7 ± 5.4	1.09	1.04	10830.36	sG	0.0059	-5.46
g9	95.8 ± 5.7	1.32	1.19	10830.50	sG	0.0064	-5.51
g10	440.9 ± 6.1	0.92	1.40	10830.60	sG	0.0161	-4.62

Table 5.1: Measurement result of He 10 830 and Ca II lines for the Stock-2 sample stars.

5. When there are other features that affect the summing or fitting (e.g., in the case shown in Figure 5.2), the wavelength above is manually adjusted to get a better result (in this case the range is 10 829.3–10 830.9 Å)

6. The line parameters are derived from the fitted profile (the orange dashed curve).

The error of the EW is then calculated according to the formula derived by Cayrel (1988):

$$\sigma_{\rm EW} = 1.6 \times ({\rm FWHM} \times \delta x)^{1/2} \times ({\rm S/N})^{-1} \tag{5.3}$$

where δx is the pixel size in the unit of wavelength. The direct summing method does not derive the parameters related to line profile, i.e., peak location, FWHM and B/R ratio. Thus, the error of the EW is derived from 1000 times Monte-Carol simulation of the observed spectra, according to their S/N. Table 5.1 lists the measurement result of He 10 830 and that of the Ca II H&K line (described in next section) for the Stock-2 sample stars. The measurement result for other samples are listed in Appendix C and E.

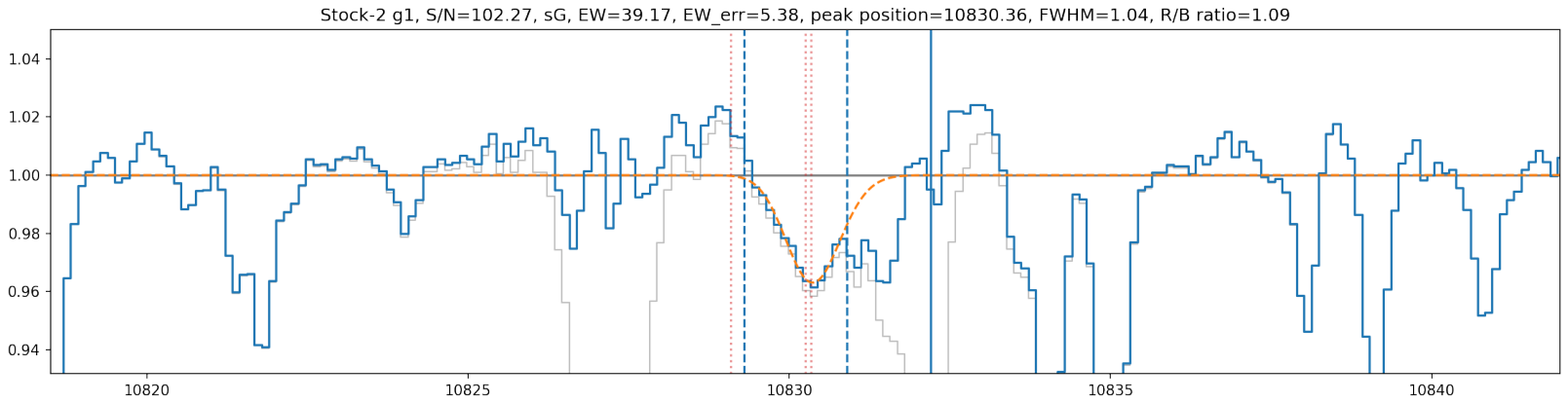


Figure 5.2: The observed spectra (gray) of Stock2-g1, and the spectra after the removal of Si and telluric lines (blue). The measurement of He 10 830 is done by skew-Gaussian fitting shown as the orange dashed curve, and the fitting parameters are listed in the title.

Figure 5.3 presents the histogram of the line parameters, separated into dwarf, giant and supergiant. The FWHM for dwarfs and giants are concentrated at 1.1 Å and 1.7 Å, respectively. This is consistent with the result reported in Zirin (1982), where the line widths for giants are found to be larger than that for dwarfs. For supergiants, their line width is larger than those of dwarfs and giants. The logarithmic R/B ratio is plotted in the middle column of Figure 5.3. The line profile of dwarfs are symmetric, with a peak at $\log(\mathrm{R/B}) = 0$. The giants have a larger scatter in $\log(\mathrm{R/B})$, and their mean value shifted to the longer-wavelength end. The R/B ratio for supergiants is sparse, with a few stars showing a strong asymmetric towards the blue end. No strong λ_{min} bias is found for our sample stars.

Temporal variation of He 10 830 is reported in previous studies. Zirin (1976) stated that over half of the stars in his sample show changes. The ratio of stars showing variability in his later study, Zirin (1982), is 1/4. There are 35 dwarfs, 59 giants and 5 supergiants in the field-XSL sample with more than one observation. We examined the spectra of all these stars, and found no clear evidence of temporal variation. The relatively low resolution and S/N may smear out the possible variation in the strength of ~ 20 mÅ, similar to the measurement error in EW. Two stars, HD188262 and Cl* NGC 5139 SAW V1 show variation in their He 10 830, as presented in Figure 5.4 and 5.5. HD188262 is found to be a spectrum binary by Hartkopf & McAlister (1984), and Cl* NGC 5139 SAW V1 is a type II Cepheid. Thus these stars are expected to show some extent of temporal variation.

5.2 Measurement of stellar Ca II and X-ray indices

Some parameters are considered to be related to the strength of the helium 10 830 Å line. The Ca II H&K lines are formed by collisional excitation of the ionized Calcium atom with the electron (Rutten, 2003). It is tightly related to the density and temperature of the formation region of its line core, the upper chromosphere. Since He 10 830, at least in the solar case, also formed in this region, the measurement of Ca II H&K indices can reveal the relation between helium lien strength and the structure of the chromosphere. The amount of X-ray radiation, quantified by the total flux in a particular X-ray band divided by the luminosity of the star, is a measurement of high-energy photons which contribute to the ionization of the helium atom. The Ca II H&K indices and X-ray flux thus measure the contribution of CE and PR formation mechanism in He 10 830. This chapter describes the method for measuring these parameters. We note that though the strength of the Hα line is also considered as a

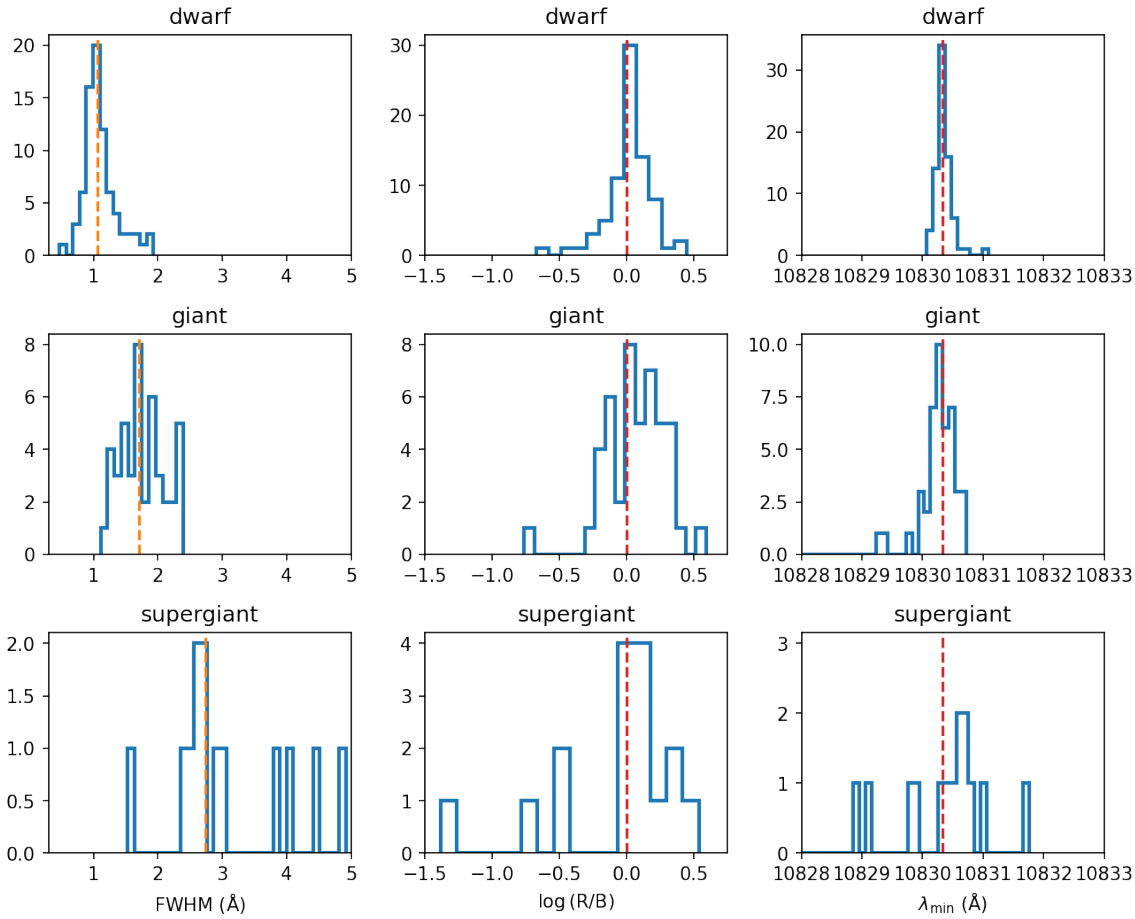


Figure 5.3: The FWHM, $\log \mathrm{R/B}$ and λ_{min} for the field-WD sample stars. The vertical dashed line in the FWHM, $\log \mathrm{R/B}$ and λ_{min} panels indicate the median value of FWHM, $\log \mathrm{R/B} = 0$ and $\lambda = 10\,830.336\,\text{Å}$ (the rest wavelength of the strongest component of He 10 830), respectively .

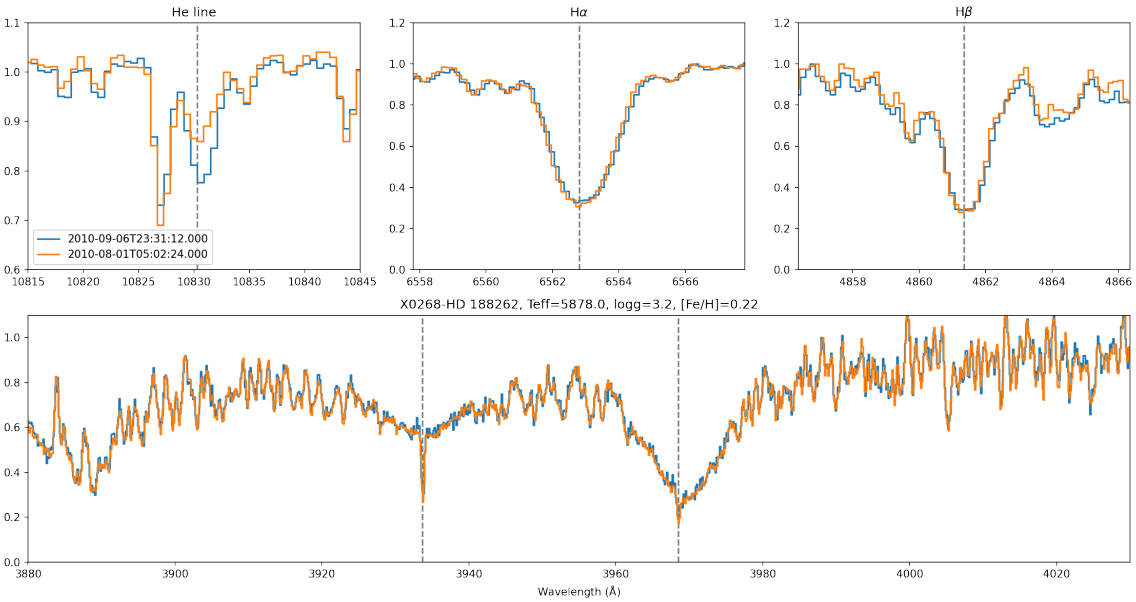


Figure 5.4: The He I 10 830, Hα, Hβ and Ca II H&K spectra of HD188262 from the field-XSL sample.

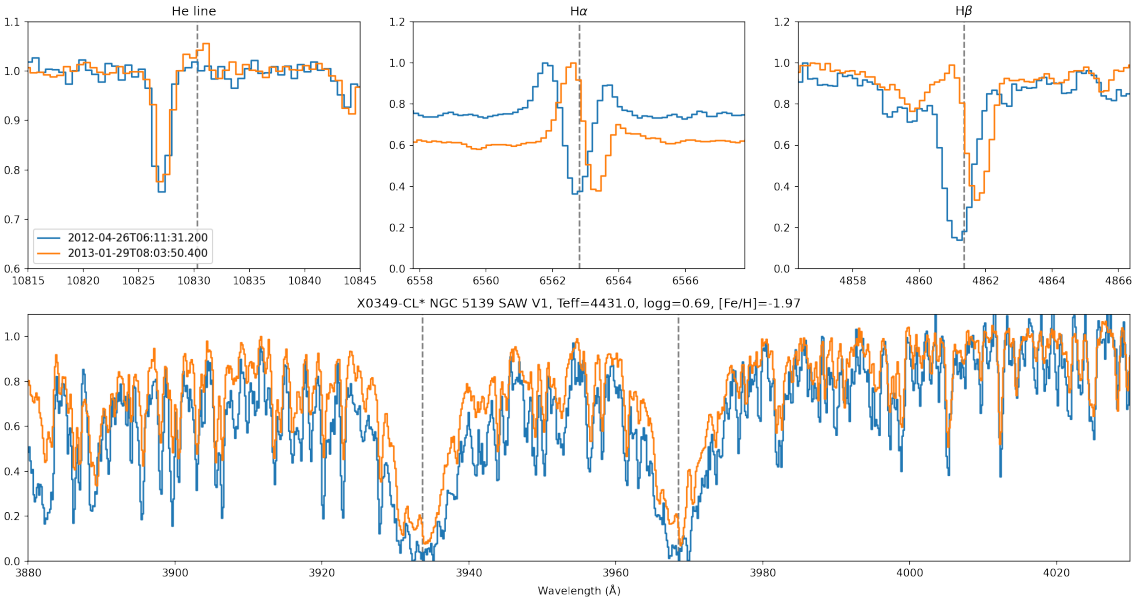


Figure 5.5: Same as Figure 5.4, but for Cl* NGC 5139 SAW V1

chromosphere diagnostic, whether the line is formed by collisional excitation depends on the chromosphere model (Linsky, 2017). Thus the H line indices are not included in our following analysis.

5.2.1 Measurement of the Ca II index

The Ca II H&K lines are ionized calcium lines at 3969 and 3934 Å. They are the resonance lines with the transition between ^2S and ^2P states (Figure 5.6). The Ca atoms are mostly ionized in the FGK-type stars, which explains the broad absorption lines at these wavelengths. The double-peaked emission at the line center can be explained by a temperature rise in the chromosphere. The formation of the Ca II H&K line was discussed thoroughly in Linsky & Avrett (1970). Figure 5.7 presents a spectrum at around Ca II H&K wavelength from the Stock-2 sample. Since only the emission core of the lines is formed in the chromosphere, the measurement of the Ca II indices is also limited in the line core part.

There are three widely used Ca II indices for measuring the Ca line cores, namely S-index, $R_{\rm HK}$ and $R'_{\rm HK}$ index. The S-index is the first index used for quantifying the Ca line core emission. Its first measurement was done using the HK photometer of four wavelength band: two 1 Å windows in the H/K line core, and two 25 Å windows (V and R) on both sides of the lines (Wilson, 1968, also refer to Figure 4.5). The S-index is then defined as:

$$S \equiv \alpha_j \frac{N_{\rm H} + N_{\rm K}}{N_{\rm V} + N_{\rm R}} \tag{5.4}$$

where N is the number or flux of counts in each band, and α_j represents the normalization factor when calibrating the measured S-index with other datasets. For the Stock-2 and field-XSL sample, we measured the fluxes in these four bands and calculated S using equation 5.4. The comparison between the S-indices we measured and those measured from other surveys is beyond the scope of this study, thus the normalization factor, α_j, is set to one.

The measured S-indices of the field-XSL sample are plotted in Figure 5.8 versus $T_{\rm eff}$. The S-index for dwarfs shows a clear lower boundary, with a minimum of 0.05 at $5000 < T_{\rm eff} < 7000$ K, and increase towards lower or higher $T_{\rm eff}$. This trend is similar to those with larger samples, e.g., Figure 2 in Boro Saikia et al. (2018). The decrease in S-index for M-type stars is not obvious in our sample, since there are only a few measurements. The S-index for giants is at a lower level, with most of the giants having $S < 0.02$. The lower boundary is also clear, and it increases as the $T_{\rm eff}$ decreases. No clear trend or boundary is seen in the S-index for supergiants.

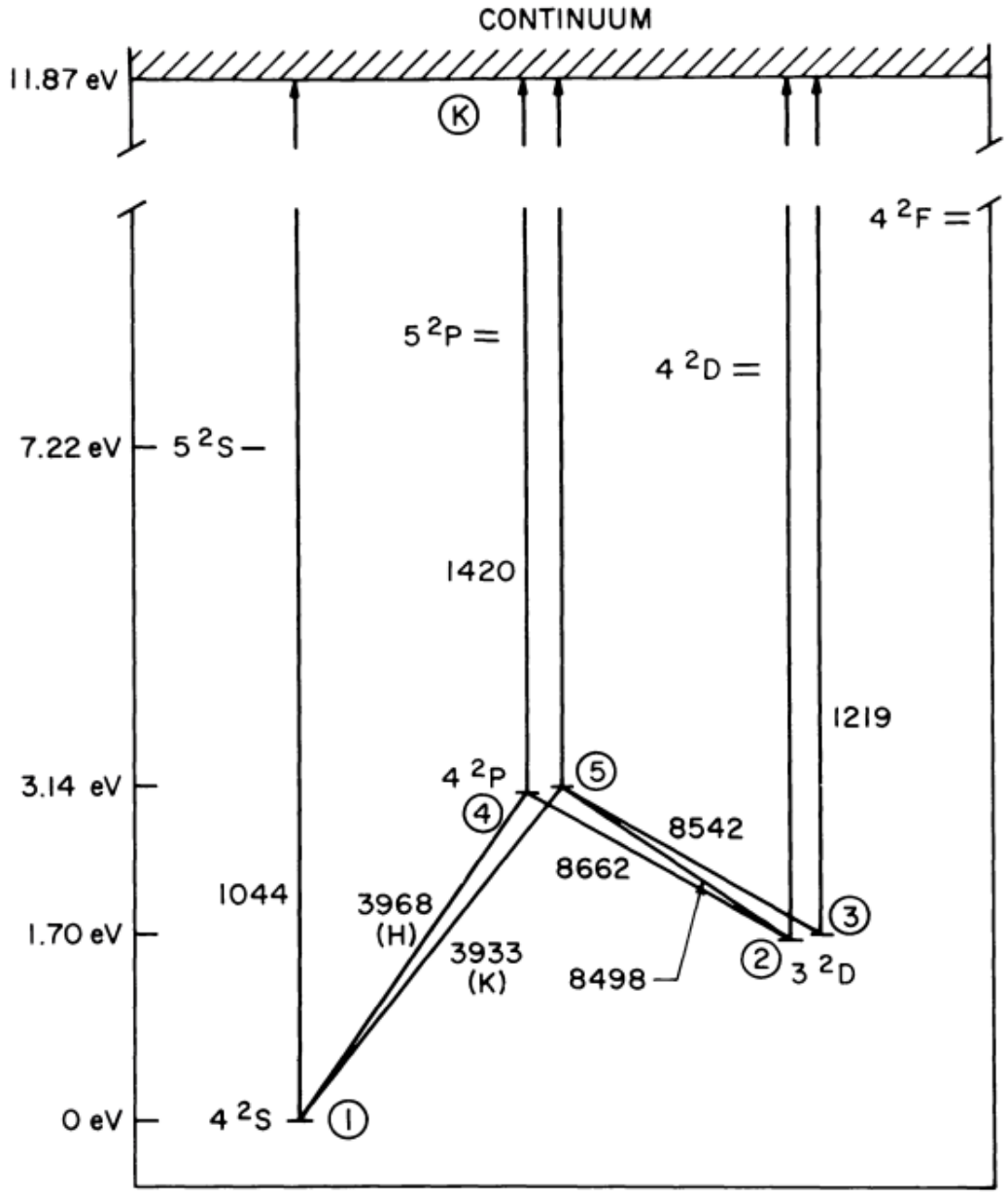


Figure 5.6: The Grotrian diagram of Ca II with the transition of H and K lines labeled. Adopted from Linsky & Avrett (1970).

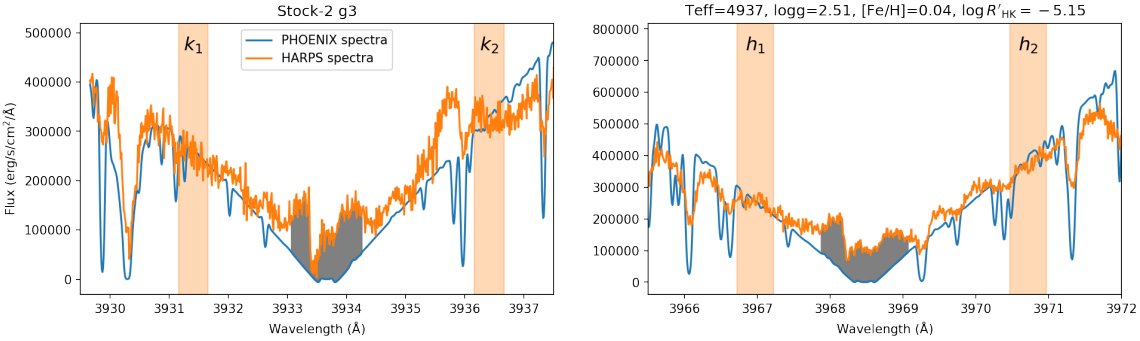


Figure 5.7: The Ca II H&K spectra for Stock-2 g3 star scaled to the PHOENIX scale. The shaded areas are used for measuring the $\log R'_{\rm HK}$ index described in section 5.2.1. The spectra for other stars in the Stock-2 sample are plotted in Appendix D.

Measuring the S-index does not require absolute flux calibration. However, S-index was later found to be sensitive to the color of the star (see, e.g., Figure 1 and 2 in Noyes et al. 1984), and it also includes a photospheric contribution at the line core. Noyes et al. (1984) introduced $R'_{\rm HK}$ index to measure the pure emission contribution from the chromosphere. The $R_{\rm HK}$ and $R'_{\rm HK}$ indices are defined as the ratio of the emission from the chromosphere in the cores of the Ca II H&K lines to the total bolometric emission of the star, with and without the contribution from the photosphere. That says,

$$R_{\rm HK} \equiv \frac{F_{\rm H} + F_{\rm K}}{\sigma {T_{\rm eff}}^4}, \tag{5.5}$$

where the $F_{\rm H}$ and $F_{\rm K}$ is the flux at the stellar surface for the H and K lines, and

$$R'_{\rm HK} \equiv \frac{F'_{\rm H} + F'_{\rm K}}{\sigma {T_{\rm eff}}^4}. \tag{5.6}$$

$F'_{\rm H}$ and $F'_{\rm K}$ follow the same definition but with the photospheric flux excluded. The photospheric flux, similar to the blending line strengths around He 10 830, cannot be measured from the observed spectra, and again we need to use the synthetic spectra. We adopted the method used in Perdelwitz et al. (2021) for measuring the $R'_{\rm HK}$ index. Figure 5.7 shows an example for the measurement, and the process is described as follows:

1. The PHOENIX high-resolution synthetic spectrum with the stellar parameters ($T_{\rm eff}$, $\log g$ and [Fe/H]) from the XSL catalog is extracted using Starfish[9];

[9] https://github.com/Starfish-develop/Starfish

Table 5.2: Wavelength bands used for scaling the observed spectra and measuring the $\log R'_{\rm HK}$ index.

Band	Wavelength range
K	3933.06–3934.26 Å
H	3967.87–3969.07 Å
k_1	3931.16–3931.66 Å
k_2	3936.16–3936.66 Å
h_1	3966.72–3967.22 Å
h_2	3970.47–3970.97 Å

2. The synthetic spectrum is then broadened and resampled according to the spectral resolution;

3. The mean flux from observed and synthetic spectra in the $k_{1/2}$ and $h_{1/2}$ bands, $f_{\rm obs/syn}(\lambda_{h1/k1})$ and $f_{\rm obs/syn}(\lambda_{h2/k2})$, are calculated, and fitted by linear functions:

$$g^{h/k}_{\rm obs/syn} = \frac{f_{\rm obs/syn}(\lambda_{h1/k1}) - f_{\rm obs/syn}(\lambda_{h2/k2})}{\lambda_{h1/k1} - \lambda_{h2/k2}} \cdot \lambda \tag{5.7}$$

$$+ \frac{f_{\rm obs/syn}(\lambda_{h2/k2}) \cdot \lambda_{h1/k1} - f_{\rm obs/syn}(\lambda_{h1/k1}) \cdot \lambda_{h2/k2}}{\lambda_{h1/k1} - \lambda_{h2/k2}}; \tag{5.8}$$

4. The observed spectra are re-scaled using the lienar functions:

$$f^{h'}_{\rm obs}(\lambda) = f^{h}_{\rm obs}(\lambda)\frac{g^{h}_{\rm syn}(\lambda)}{g^{h}_{\rm obs}(\lambda)} \tag{5.9}$$

and

$$f^{k'}_{\rm obs}(\lambda) = f^{k}_{\rm obs}(\lambda)\frac{g^{k}_{\rm syn}(\lambda)}{g^{k}_{\rm obs}(\lambda)}. \tag{5.10}$$

to match the scale of the observed and synthetic spectra.

5. The flux difference in the H and K band between the scaled observe spectra and synthetic spectra are summed as $R'_{\rm HK}$.

Table 5.2 lists the wavelength of each band used in the measurement. The contribution from the photosphere to the H and K bands is accounted for in the PHOENIX model and removed from $R'_{\rm HK}$ indices. Figure 5.9 present the relation between $\log R'_{\rm HK}$ index and $T_{\rm eff}$ for the field-XSL sample. The trend of $\log R'_{\rm HK}$ index for dwarfs are also similar to that of S-index, at around -6 for stars with $5000 < T_{\rm eff} < 7000$ K, and become larger at higher or lower $T_{\rm eff}$. This trend is also consistent with the one in Boro Saikia et al. (2018), except that the lower edge from our sample is not clear since

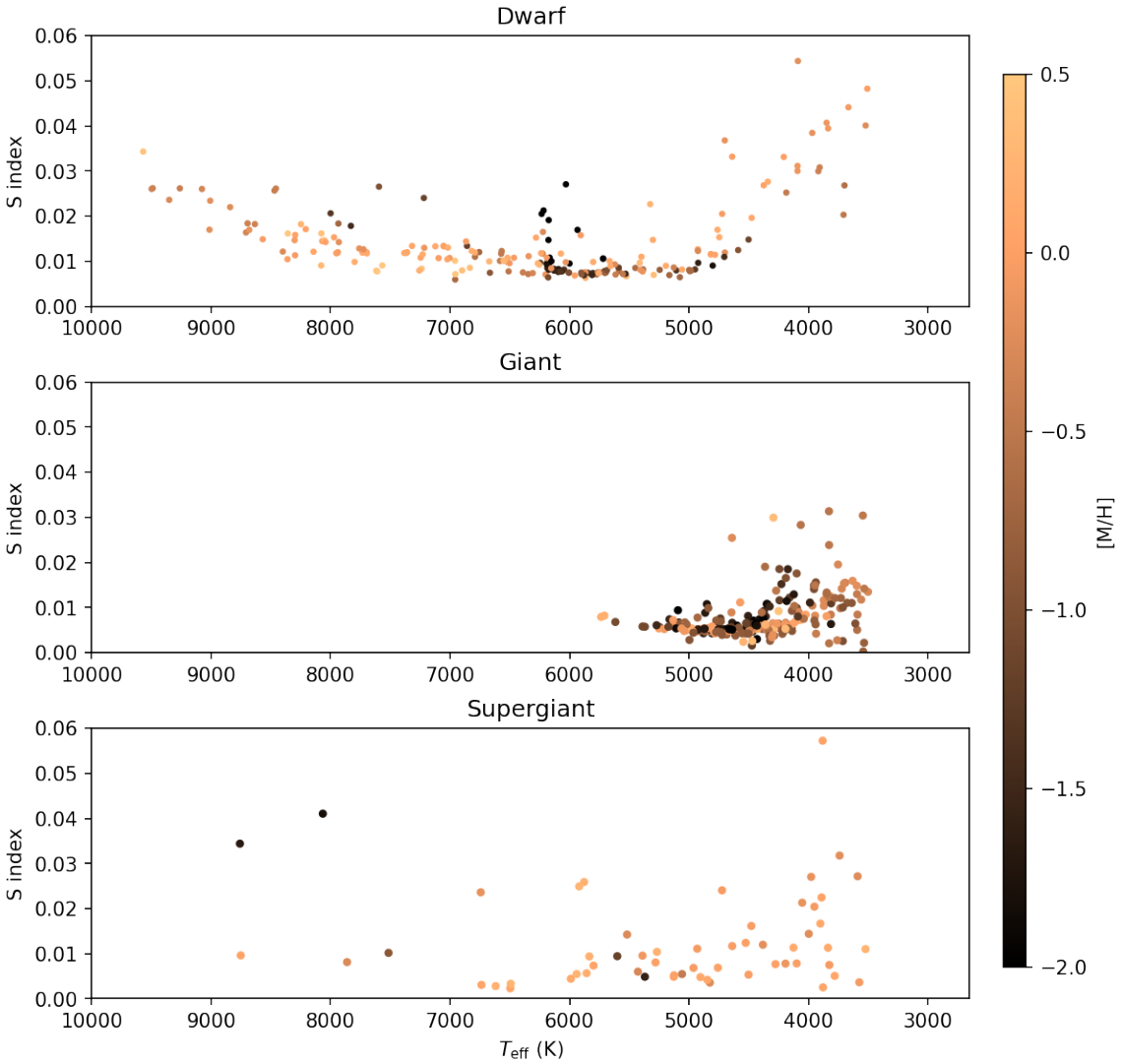


Figure 5.8: S-index versus $T_{\rm eff}$ for field-XSL sample stars, color-coded by their metallicity.

the number of stars with $\log R'_{\rm HK}$ is small. The $\log R'_{\rm HK}$ for giants is weaker than that for dwarfs, and the value decreases as $T_{\rm eff}$ decreases. Those with smaller metallicity tend to have a larger value. The measurement for supergiants also shows a decreasing trend in the figure, though the scatter is larger than that for the giants. Our $\log R'_{\rm HK}$ trends are similar to those reported in Mittag et al. (2013, see their Figure 12-14), with systemic shifts. Thus, we conclude that the $\log R'_{\rm HK}$ measurement can better represent the situation in the stellar chromosphere, compared to S-index, and we will discuss its relation with the He 10 830 EW in the next chapter.

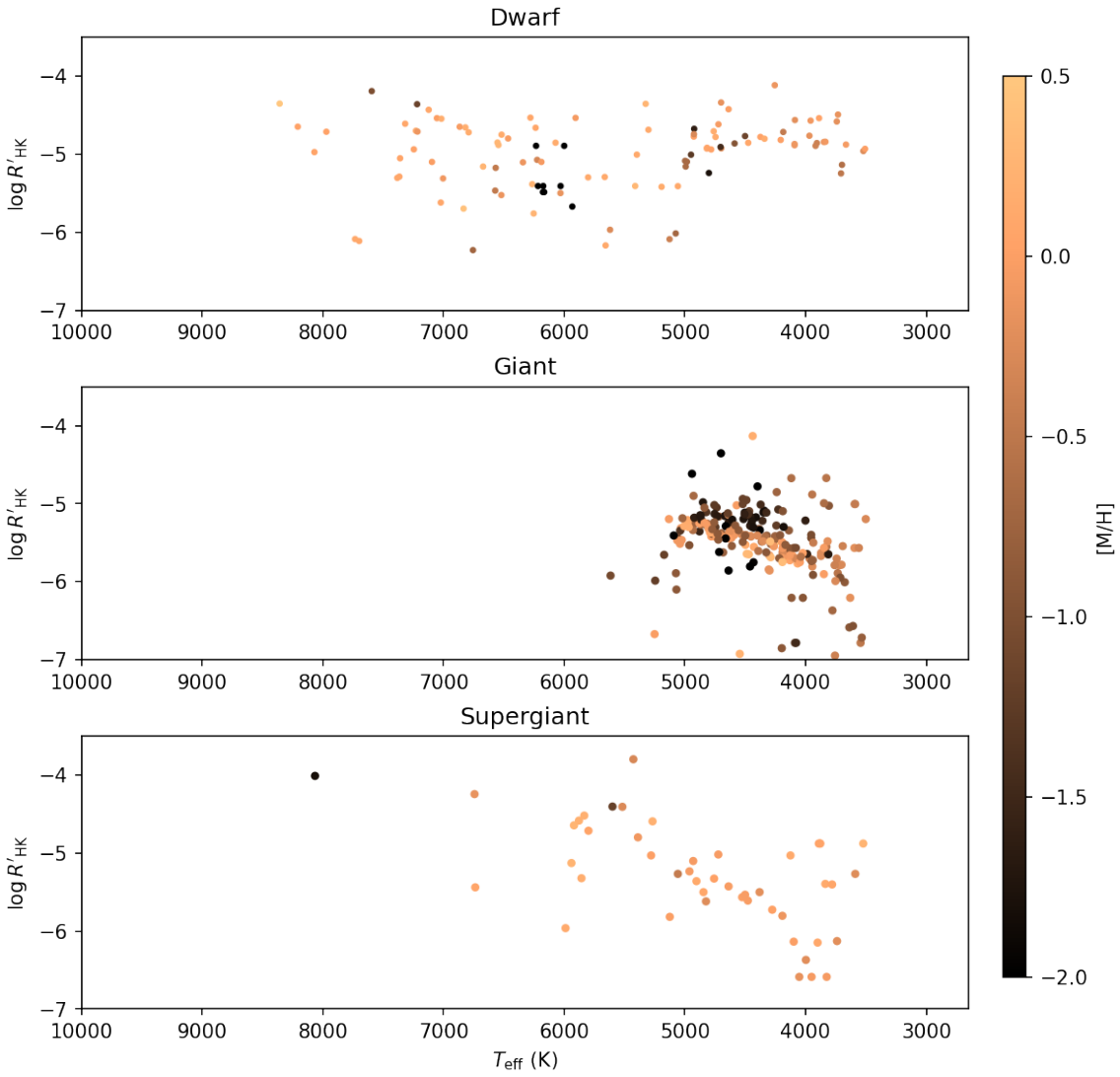


Figure 5.9: $\log R'_{\rm HK}$ index versus $T_{\rm eff}$ for field-XSL sample stars, color-coded by their metallicity.

5.2.2 Measurement of fractional X-ray luminosity

Our main targets, i.e., the FGK stars, only emit a small portion of energy in X-ray, thus stars with X-ray measurement in our sample are limited. We cross-matched our sample with public X-ray photometry surveys, i.e., XMM-Newton (4XMM DR11, Webb et al. 2020), ROSAT (2RXS, Boller et al. 2016), Einstein (Maggio et al., 1990), Chandra (CSC 2.0, Evans et al. 2020a), Swift (2SXPS, Evans et al. 2020b), and Fermi (4FGL-DR2, Ballet et al. 2020). The cross-match with most survey catalogs yielded only a few counterparts, so here we limit ourselves to the XMM-Newton and ROSAT catalogs that give a cross-matched sample larger than 10.

The X-ray Multi-Mirror Newton Mission (XMM-Newton, Jansen et al. 2001) is an X-ray satellite designed and launched by ESO on December 10, 1999. The two main instruments, European Photon Imaging Cameras (EPIC) and Reflection Grating Spectrometers (RGS), performed X-ray photometric and spectroscopic observation in the energy band of 0.15–15 keV and 2.5–0.35 keV. The 4XMM-DR11 catalog contains the detections for point sources with an energy interval of 0.2–12 keV. The catalog provides the photometry from EPIC split into five Bands, 1–5, and the total flux in the whole energy interval as Band 8. The energy of photons in these bands is entirely higher than the ionization energy of a neutral helium atom, thus they are expected to be correlated with the helium 10 830 Å line when the PR formation mechanism kicks in. The separation into multi bands enables us to see whether the correlation with the He 10 830 EW depends on the energy or not.

The second ROSAT all-sky survey (2RXS) is a catalog of the point-like sources detected in the Röntgensatellit (ROSAT, Truemper 1982). The two Position Sensitive Proportional Counters (PSPC) mounted on the satellite provide measurements in a bandpass of 0.1–2.4 keV. The catalog contains about 135 000 X-ray detections in this energy band, and it is the deepest and cleanest X-ray all-sky catalog before eROSITA. The 2RXS band is close to the sum of Bands 1–3 in 4XMM-DR11. Thus the correlation between the ROSAT flux would be similar to those of the XMM-Newton Bands 1–3. Linear correlation between the He 10 830 EW and the ROSAT X-ray flux, $\log f_{\rm X}/f_{\rm bol}$, is found in Takeda & Takada-Hidai (2011) for field dwarf stars.

We used a 15″ radius for the cross-match between the X-ray catalog and our sample. Though this radius is large, the separation in most of the stars is within 5″. The band energy interval or wavelength coverage of these surveys and the cross-matched numbers with our sample are listed in Table 5.3.

Table 5.3: Cross-match count between the XMM-Newton and ROSAT catalogs and our sample.

Instrument	Catalog	Band range	field-WD sample	field-XSL sample
XMM-Newton	4XMM DR11	0.2-12 keV[1]	21	51
ROSAT	2RXS	0.1-2.4 keV	45	31

[1] Band 1: 0.2-0.5 keV; Band 2: 0.5-1.0 keV; Band 3: 1.0-2.0 keV; Band 4: 2.0-4.5 keV; Band 5: 4.5-12 keV; Band 8: 0.2-12 keV

The flux in the X-ray survey is converted to the fractional luminosity, the total energy of the star emitted in a particular band divided by the bolometric luminosity. They will be denoted by L with the name of the band, such as $L_{\rm XMM1}$ or $L_{\rm RXS}$. The unit of the ROSAT catalog values is photon count, thus they are converted to the flux using the conversion factor: $f_{\rm RXS} = 1.8 \times 10^{-11} \times C_{\rm RXS}$. Then the total energy emitted by the star is:

$$L_{\rm band} = f_{\rm band} \times 4\pi d^2 \tag{5.11}$$

where $f_{\rm band}$ is the band flux in erg/cm^2/s, and d is the stellar distance in cm. We adopted the bolometric luminosity, $L_{\rm Gaia}$, and distance measurement from Gaia DR2 (Andrae et al. 2018 and Gaia Collaboration et al. 2018). The fractional luminosity is then:

$$\frac{L_{\rm band}}{L_{\rm Gaia}} = \frac{f_{\rm band} \times 4\pi d^2}{L_{\rm Gaia}} = \frac{1.8 \times 10^{-11} \times C_{\rm RXS} \times 4\pi d^2}{L_{\rm Gaia}}, \tag{5.12}$$

The fractional luminosity measurements for the field-WD and field-XSL samples are listed in Table B.3 and E.3. There are 17 stars in the field-WD sample and 13 stars in the field-XSL sample with the XMM-Newton observation. A larger number of our objects have ROSAT measurements, 37 of the field-WD sample and 25 of the field-XSL sample. The error of $\log L_{\rm band}/L_{\rm Gaia}$ is mostly within 0.1.

Chapter 6

Empirical trends toward stellar parameters

This chapter presents the empirical trend of the He 10 830 EW against stellar parameters and indices measured in Chapter 5. Some of the empirical relations, e.g., between the EW and $T_{\rm eff}$, $\log R'_{\rm HK}$ or X-ray fractional luminosity, are reported in previous studies (Chapter 1). Here we revise these relations, and we aim to discuss the dominant formation mechanism of He 10 830 in our sample.

6.1 Empirical relation with $T_{\rm eff}$ and metallicity

We first revise the most basic relation involving the He 10 830 EW, those between EW(He) and $(T_{\rm eff}, \log g, [{\rm Fe/H}])$. The variation of EW(He) with $T_{\rm eff}$ was reported in Zirin (1982), and their relations are presented in Figure 1.8. The stars in Zirin (1982) are grouped by luminosity types, and they show different trends. The effect of metallicity on the line strength, if any, was not considered, since the sample in Zirin (1982) does not have the homogeneous measurement of the stellar parameters, but only classification in the spectral type and luminosity type. Such measurement is available for the studies after the 1980s, but the limited sample size makes such calibration difficult. Here we adopt a similar approach to revise the relations. EW(He) will be plotted versus $T_{\rm eff}$, with their metallicity labeled by color. $\log g$ are used to classify the stars into the dwarf, giant and supergiant groups (Chapter 3). Such classification preserves the similarity with the relations reported in Zirin (1982), and limits the possible effect of $\log g$ in EW(He): the stars in a group either have similar $\log g$ values (dwarfs and supergiants), or their $\log g$ is correlated with $T_{\rm eff}$ (giants). The result from field-WD, field-XSL and previous studies are plotted in Figure 6.1, and the trend from Zirin (1982) is also included as a reference.

6.1.1 Dwarf

The relation for dwarfs, presented in the upper panel of Figure 6.1, shows a clear trend with $T_{\rm eff}$ and some variation. The measurement from Andretta et al. (2017) includes the weak component of He 10 830. The authors used two Gaussians with a fixed ratio of 5:3 to fit the strong and weak components of He 10 830. Since we only measure the EW of the strong component, the value of their EWs is reduced by 5/8, then plotted in the figure. Perhaps the most obvious feature is the two trends divided by a blue dashed line. The trend on the right side of the dashed line is named the main trend, and the one on the left is named the secondary trend. We will discuss the secondary trend in Chapter 7.

The average line strength for the main trend is close to 0 for stars with $T_{\rm eff} \sim 3100\,{\rm K}$, and increases to around 200 mÅ at $T_{\rm eff} \sim 4250\,{\rm K}$. The EW then decreases with increasing $T_{\rm eff}$ and vanishes again at $T_{\rm eff} \sim 6250\,{\rm K}$. We notice that there is a lower boundary in the main trend. The boundary is slightly lower than the average strength, with a maximum of ~ 150 mÅ at 4000 K. The metal-poor stars are close to the boundary. For the lower temperature side where the peak of the line appears, the boundary is not so clear since the metallicity of the stars from Fuhrmeister et al. (2019) is around solar. Nevertheless, the variation of the lower boundary in He 10 830 is discovered for the first time with the help of our sample. The secondary trend is separated from the main trend in $T_{\rm eff}$ and EW. A group of stars with strong EWs, located above the blue dashed line, appear at $T_{\rm eff} = 6000\,{\rm K}$. The strength of these stars then decreases as $T_{\rm eff}$ become larger, and approach 50 mÅ with $T_{\rm eff} > 7000\,{\rm K}$.

There is a vertical scatter in the line strength for the stars in the main trend. The metallicity effect is most evident at $T_{\rm eff} \sim 4750\,{\rm K}$, with many metal-rich stars having large EW while metal-poor stars are found only around the lower boundary. At the higher $T_{\rm eff}$, the helium absorption becomes weak regardless of the metallicity and the metallicity effect is less obvious. On the other hand, the metallicity effect may also appear at a lower temperature, but the number of metal-poor stars is limited, and the effect cannot be seen clearly. We do not find a significant metallicity effect in the secondary trend.

The 4 gray points in the dwarf panel indicate the measurement of the average EW(He) from Zirin (1982). The points for G and K types are consistent with the average strength in the main trend. The F-type measurement (at around 6500 K) is higher than those for G- and K-type. This point is actually measuring the average strength in the secondary trend. As for the M-type measurement, the value is consistent with the maximum line strength in the M-type stars. The EW measurement

in our sample transforms the 4-points trend in Zirin (1982) to detailed trends varied with $T_{\rm eff}$ and probably [Fe/H]. However, the formation mechanism of He 10 830 indicates that the line strength is related to the structure of the chromosphere or high-energy radiation. Whether the trends shown in the panel are caused by $T_{\rm eff}$ and [Fe/H] directly or the local condition in the chromosphere and transition region requires the measurement of $\log R'_{\rm HK}$ index and fractional X-ray luminosity of these stars. They will be discussed in the following sections.

6.1.2 Giant

The line strength for giants in our sample is weaker than that for the dwarfs, with EW(He) close to 0 at $T_{\rm eff} \sim 3750$ K. The line strength then increases as $T_{\rm eff}$ increases, and reach a level of 50 mÅ in $T_{\rm eff} > 5000$ K. Metallicity effect, though weaker, also presents in the giants, with metal-rich stars having slightly larger line strength. The measurement for luminosity type III stars in Zirin (1982) has a similar trend towards $T_{\rm eff}$, with a smaller EW(He) for cooler stars. His trend, however, is systematically higher than our measurement, which may be due to the bias toward more active stars in their sample. We note that there are a few stars with $T_{\rm eff} > 4750$ K having EW(He) > 200 mÅ. Most of them from the previous studies are field horizontal branch (HB) stars (Dupree et al., 2009) or HB stars (Strader et al., 2015). The He 10 830 EW in HB stars is tightly correlated with $T_{\rm eff}$. Their EWs are around 0 mÅ at 5200 K and they rapidly increases to ~ 300 mÅ at 5500 K. Whether such a difference between red giants and horizontal branch stars comes from a stronger PR or CE formation mechanism is still under debate. Seven stars in the field-WD sample and three stars in the Stock-2 sample also have a strong helium absorption. Comparing these strengths with their chromosphere indices and fractional X-ray luminosity, if any, would help distinguish the reason for the strong absorption.

6.1.3 Supergiant

Though the number of supergiants is limited, stars with $6000 < T_{\rm eff} < 4500$ K show a large scatter in He 10 830 EW, while those outside this range are weak. The distribution of sample stars is consistent with the measurements from Zirin (1982). The large scatter in EW(He) is not related to the metallicity since most of our supergiants are around solar metal.

Our sample provides more than 300 measurements of He 10 830 for dwarfs and giants, and 87 for supergiants. The high resolution and S/N enable us to measure the

equivalent widths with high precision. They can be used to give a rough prediction of the EW(He) depending on $T_{\rm eff}$ and [Fe/H]. We then compare the He 10 830 EW with chromosphere indices and fractional luminosity and discuss how this variation is related to the two formation mechanism of He 10 830.

6.2 Empirical relation with chromosphere indices

The chromosphere indices, measuring the strength of core emission in Ca II H&K lines, are found to be correlated with the He 10 830 EW. The positive correlation with Ca II K line intensity was reported in Vaughan & Zirin (1968); Zirin (1976) and Zirin (1982). Later Smith (2016) reported a tighter relation between $\log R'_{\rm HK}$ and EW(He) for dwarf stars. Their targets are mostly active stars with relatively large $\log R'_{\rm HK}$ or $L_{\rm X}$. Here we present the relation between these parameters from the field-XSL and Stock-2 samples.

Figure 6.2 presents the He 10 830 EW versus the $\log R'_{\rm HK}$ and S-index for dwarf and giant stars. As discussed in Chapter 5, we focus on the comparison with $\log R'_{\rm HK}$. The dwarfs tend to have larger $\log R'_{\rm HK}$ than the giants, with a range from -6 to -4.5. The stars with $\log R'_{\rm HK} > -5$ tend to have a larger strength, with EW(He) larger than 100 mÅ and a positive correlation is found. Most of the giants have a weaker Ca II H&K core emission, with $-6 < \log R'_{\rm HK} < -5$, and weaker EW(He). A few giants with $\log R'_{\rm HK} > -5$ also show stronger He 10 830 absorption, including the three giants in Stock-2 with EW(He) > 300 mÅ. Thus, EW(He) in dwarfs and giants follow a similar trend with $\log R'_{\rm HK}$. This is the evidence that the CE formation mechanism, which depends on the physical condition in the line formation region, appears or even dominates the helium absorption in the stars with $\log R'_{\rm HK} > -5$.

We note that the distribution of stars in the EW(He)–$T_{\rm eff}$ diagram shares some similarity with that in $\log R'_{\rm HK}$–$T_{\rm eff}$ diagram, at least for dwarfs. The distribution for dwarfs in $\log R'_{\rm HK}$ versus $T_{\rm eff}$ diagram has been revealed by previous studies (e.g., Mittag et al. 2013 and Boro Saikia et al. 2018) thanks to the large-scale observation in the Ca II lines from the Mount Wilson Observatory (Wilson, 1978) or HARPS. Figure 6.3 presents the variation of $\log R'_{\rm HK}$ index for dwarfs. A clearer boundary can be seen in this figure. Most of the stars, including the most inactive ones, have non-zero Ca II emissions from the chromosphere (see also, Wilson 1978 and Schrijver 1987). The most obvious feature in Figure 6.3 is the "hole" in $1.1 < B - V < 1.4$, with the stars in this color range concentrated on a higher level of $\log R'_{\rm HK}$ than the basal level of -5. Such feature is also observed in nearly all studies involving $\log R'_{\rm HK}$

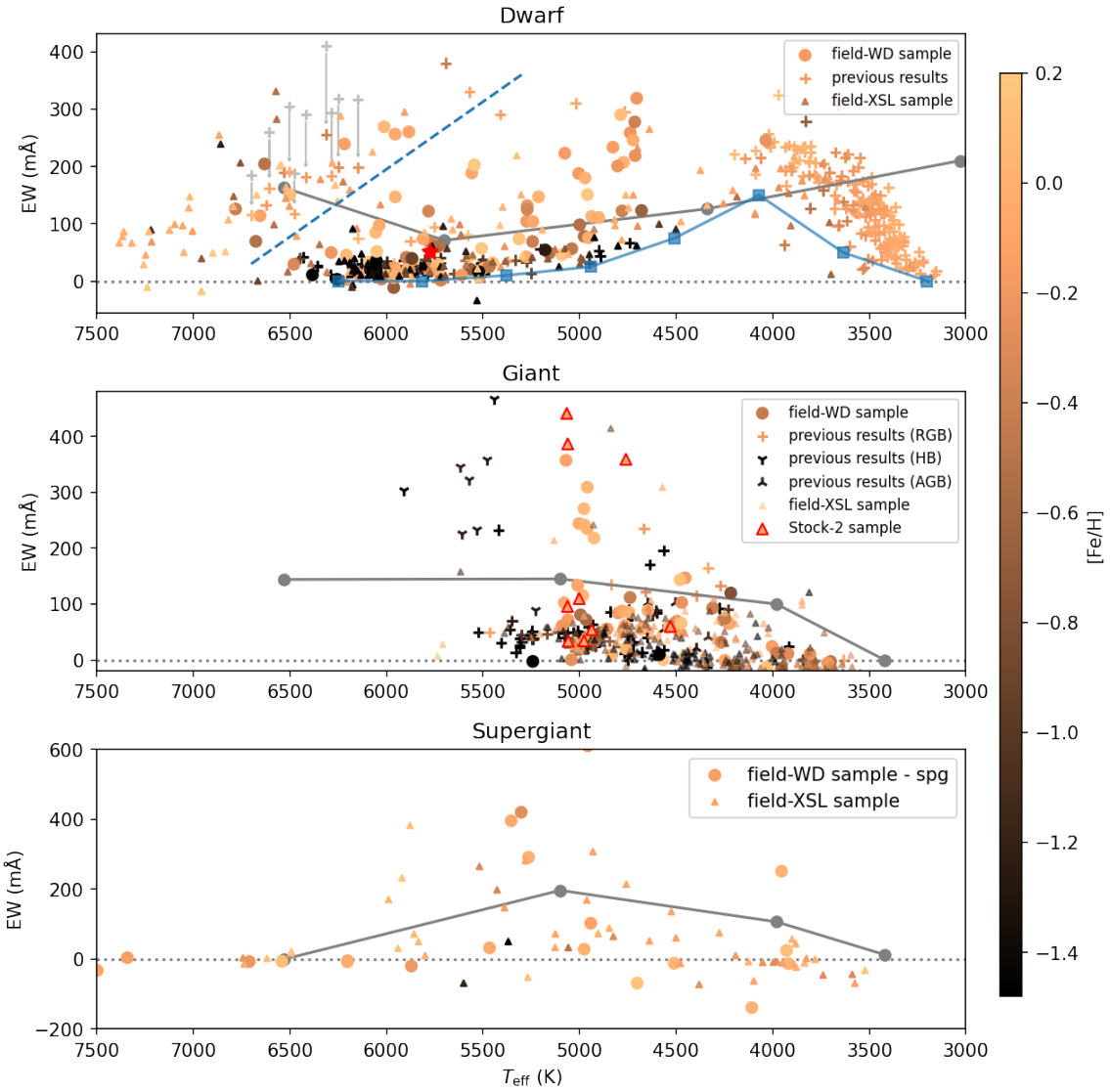


Figure 6.1: The He 10 830 EW versus $T_{\rm eff}$, for dwarf, giant and supergiant and color-coded by their [Fe/H]. The gray plus signs are the stars from Andretta et al. (2017), and they are scaled down by a factor of 5/8 to exclude the absorption from the weak component. The gray dotted lines are those reported in Zirin (1982), with luminosity types V, III and I (also see Figure 1.8).

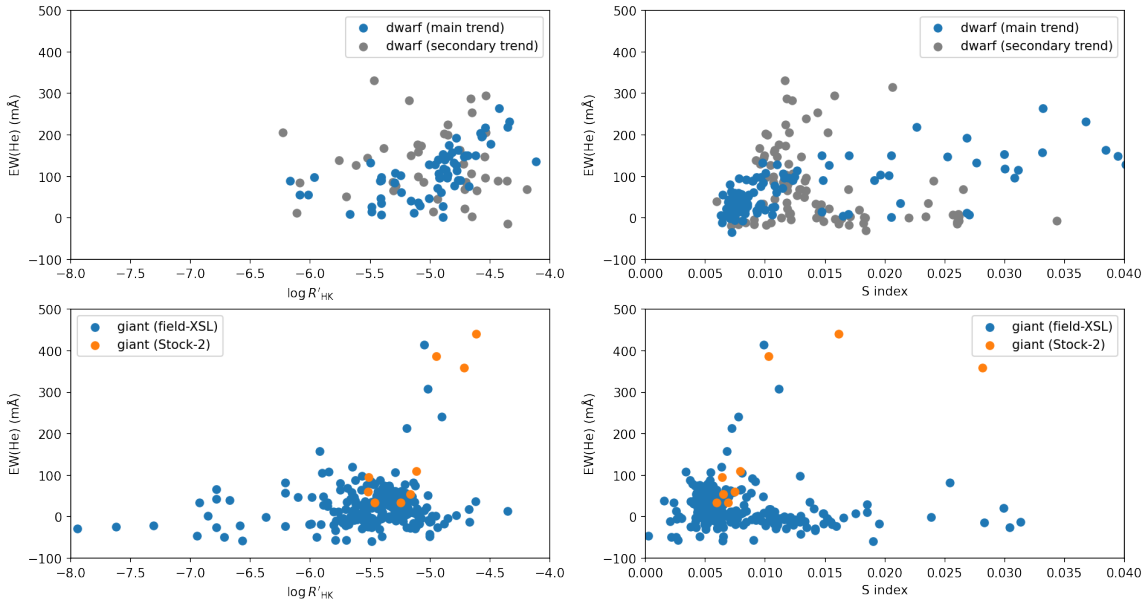


Figure 6.2: EW(He) versus $\log R'_{\rm HK}$ and S-index for stars in field-XSL and Stock-2 sample. The dwarfs are separated by the main and secondary trends.

or S-index, e.g., Isaacson & Fischer (2010, Figure 9), Zhao et al. (2013, Figure 4) and Boro Saikia et al. (2018, Figure 3). However, why such an increase in $\log R'_{\rm HK}$ level exists lacks explanation. The lower boundary of He 10 830 shares a similar shape with the basal level in $\log R'_{\rm HK}$ index. It is the first time that the behavior of basal level in $\log R'_{\rm HK}$ is found in He 10 830, and the stellar atmosphere model should explain the variation in basal level in both $\log R'_{\rm HK}$ and EW(He).

The trends between the He 10 830 EW and $T_{\rm eff}$ are presented in Figure 6.4, color-coded by $\log R'_{\rm HK}$ index. The effect of $\log R'_{\rm HK}$ index on the lower boundary level for the main trend in dwarfs is clear. Smaller $\log R'_{\rm HK}$ seen in 5000 to 6000 K is accompanied by a low boundary level, and both of the values increase as $T_{\rm eff}$ decreases. No strong correlation between $\log R'_{\rm HK}$ and EW(He) in a fixed $T_{\rm eff}$ is found, suggesting the vertical spread is not related to the variation of the CE formation mechanism. On the other hand, the stars with different $\log R'_{\rm HK}$ levels are mixed in the scattered secondary trend, also suggesting that the CE mechanism is not the dominant mechanism for these stars. The variation of $\log R'_{\rm HK}$ in giants is smaller, with cooler giants having smaller $\log R'_{\rm HK}$ values and also a weaker He 10 830 strength. The $\log R'_{\rm HK}$ values for supergiants is large in a narrow $T_{\rm eff}$, from 5250 to 6000 K. Future observation on these lines with a larger sample size would reveal the possible trend for supergiants in more detail.

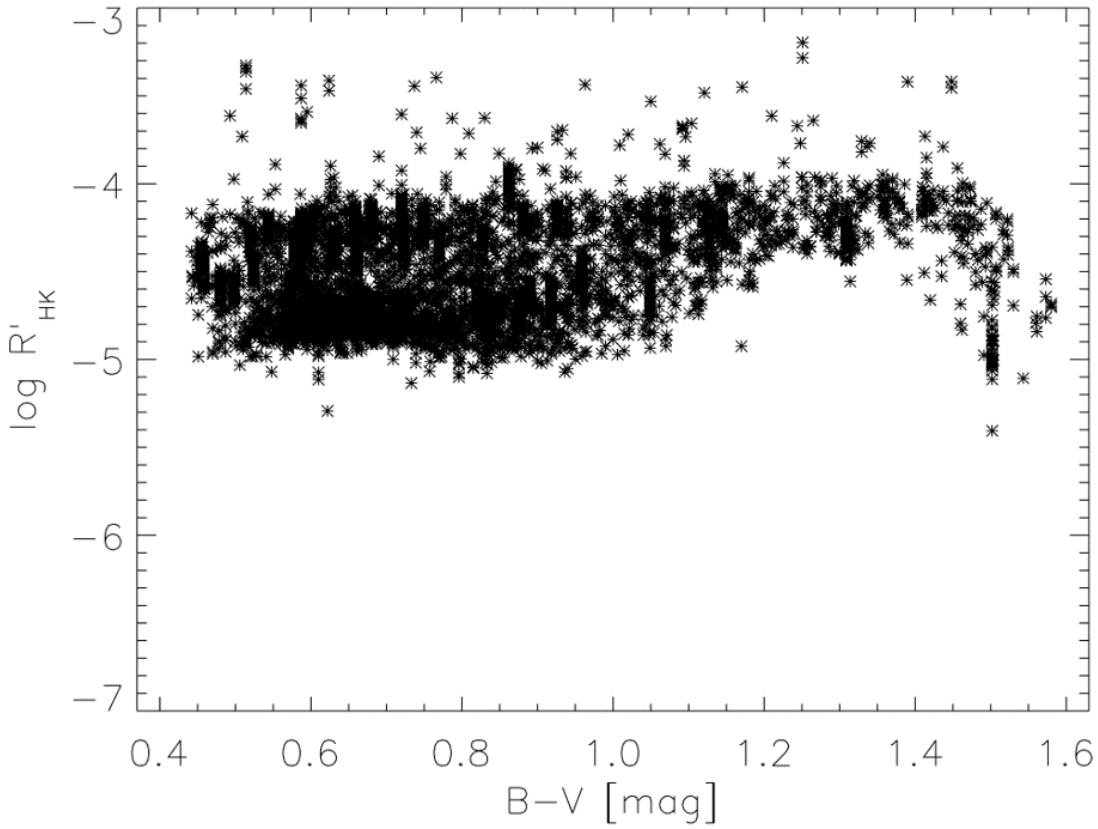


Figure 6.3: $\log R'_{\rm HK}$ versus $(B-V)$ color for dwarf stars. An increase in $\log R'_{\rm HK}$ is seen in $1 < B-V < 1.4$, similar to that in the EW(He)–$T_{\rm eff}$ relation. Adopted from Mittag et al. (2013).

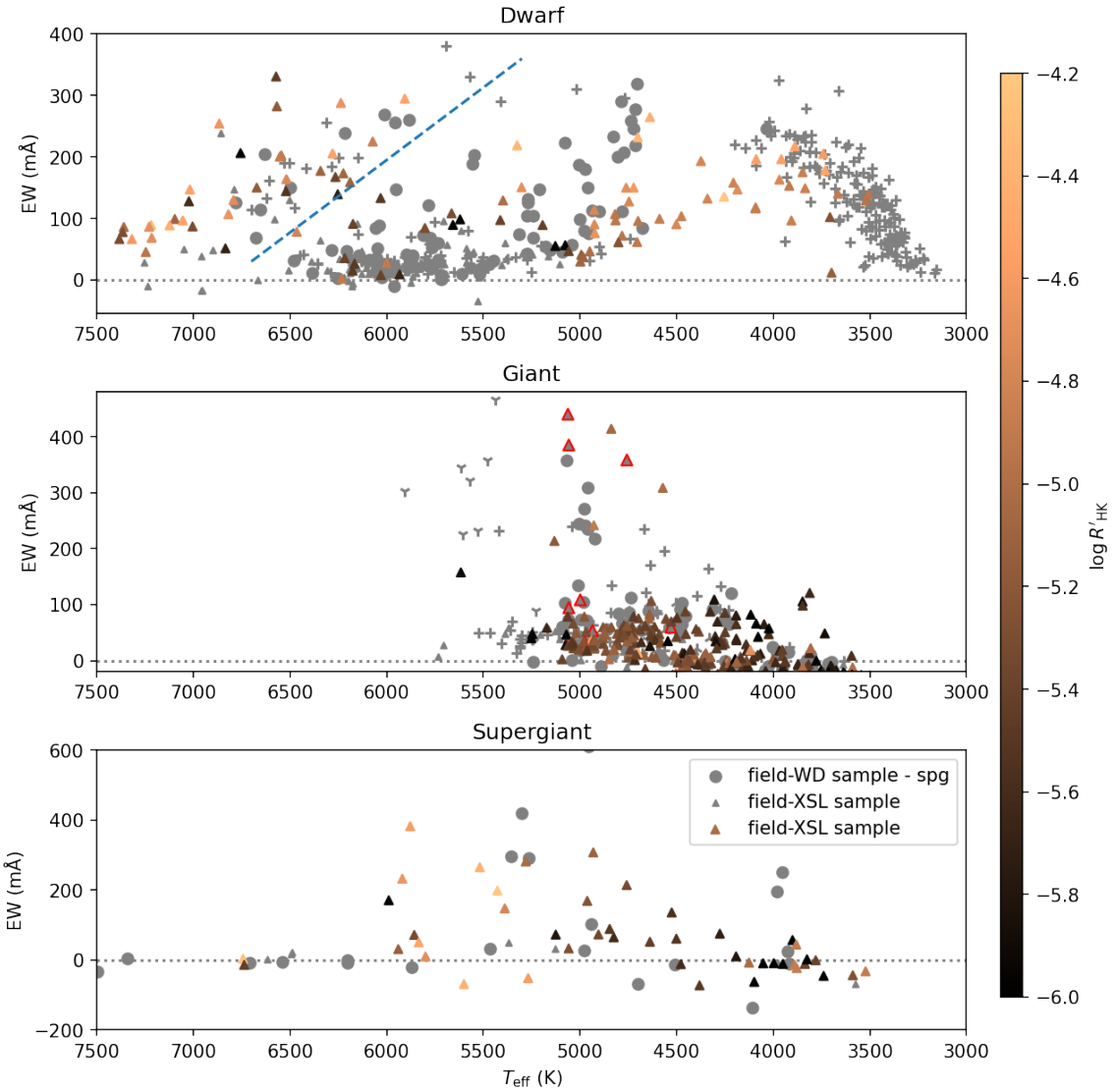


Figure 6.4: Similar to Figure 6.1, but color-coded by $\log R'_{\rm HK}$.

6.3 Empirical relation with X-ray luminosity

The fractional X-ray luminosity is considered a suitable measure of the EUV photon which can ionize the helium atom (Hirayama, 1971), thus the PR formation mechanism would be dominant when EW(He) is related to the fractional X-ray luminosity. Here we compare these values and test whether this is the case for the stars in our sample. The results are presented in Figure 6.5–6.7 with the relation between EW(He) and fractional X-ray luminosity from XMM-Newton and ROSAT.

Tight relations for dwarfs are seen in XMM-Newton observation Bands 1 and 3. The EW increases as the X-ray luminosity becomes larger for the stars with $\log L_{\rm x}/L_{\rm Gaia} > -7$. Such a linear relation is also reported in previous, such as Sanz-Forcada & Dupree (2008) and Takeda & Takada-Hidai (2011). However, their targets are mainly active stars, so the shape at the lower end of the relation is unclear. A plateau of EW(He) appears when the fractional X-ray luminosity is small. The stars with $\log L_{\rm X1}/L_{\rm Gaia} < -7$ have no correlation between their EWs and fractional X-ray luminosity, with a EW(He) around 50 mÅ. Such correlation can also be found for Bands 2 and 3 with a slightly larger scatter, but it vanished in Bands 4 and 5. The photometry in Band 8 represents the sum of all the radiation from Bands 1 to 5. Since the X-ray luminosity in the XMM-Newton wavelength is dominated by those in Band 1–3, the correlation also appears in the Band 8 panel. Only five giants have $L_{\rm X}$ measurement in the XMM-Newton bands. They seem to follow a similar trend shown in dwarfs, but such a small number limits the discussion on the possible trend. Since XMM-Newton Band 1 is closer to the ionization energy of the helium atom, 24.6 eV, it is expected that the He 10 830 strength would have a stronger relation with it than the other bands with higher energy. A similar trend is also seen in the flux derived from ROSAT observation, since the ROSAT band energy interval is similar to that of XMMM-Newton Bands 1–3.

We now discuss how the two formation mechanisms, indicated by the $\log R'_{\rm HK}$ and fractional X-ray luminosity, affect the line strength. EW(He) is plotted versus $T_{\rm eff}$ in Figure 6.7, but colored by the ROSAT fractional X-ray luminosity. The stars with ROSAT observation cover parts of the main and secondary trend with $4750 < T_{\rm eff} < 6750$ K. It is clear that the dwarfs with weaker He 10 830 strength also have a smaller $\log L_{\rm RXS}/L_{\rm Gaia}$ value. Those with $\log L_{\rm RXS}/L_{\rm Gaia} \sim -7$ are located near the lower boundary curve, and the stars with larger luminosity are on top of those stars. Such a tendency also appears in the secondary trend, though the number of points is limited. Considering that there is no strong correlation between the vertical spread

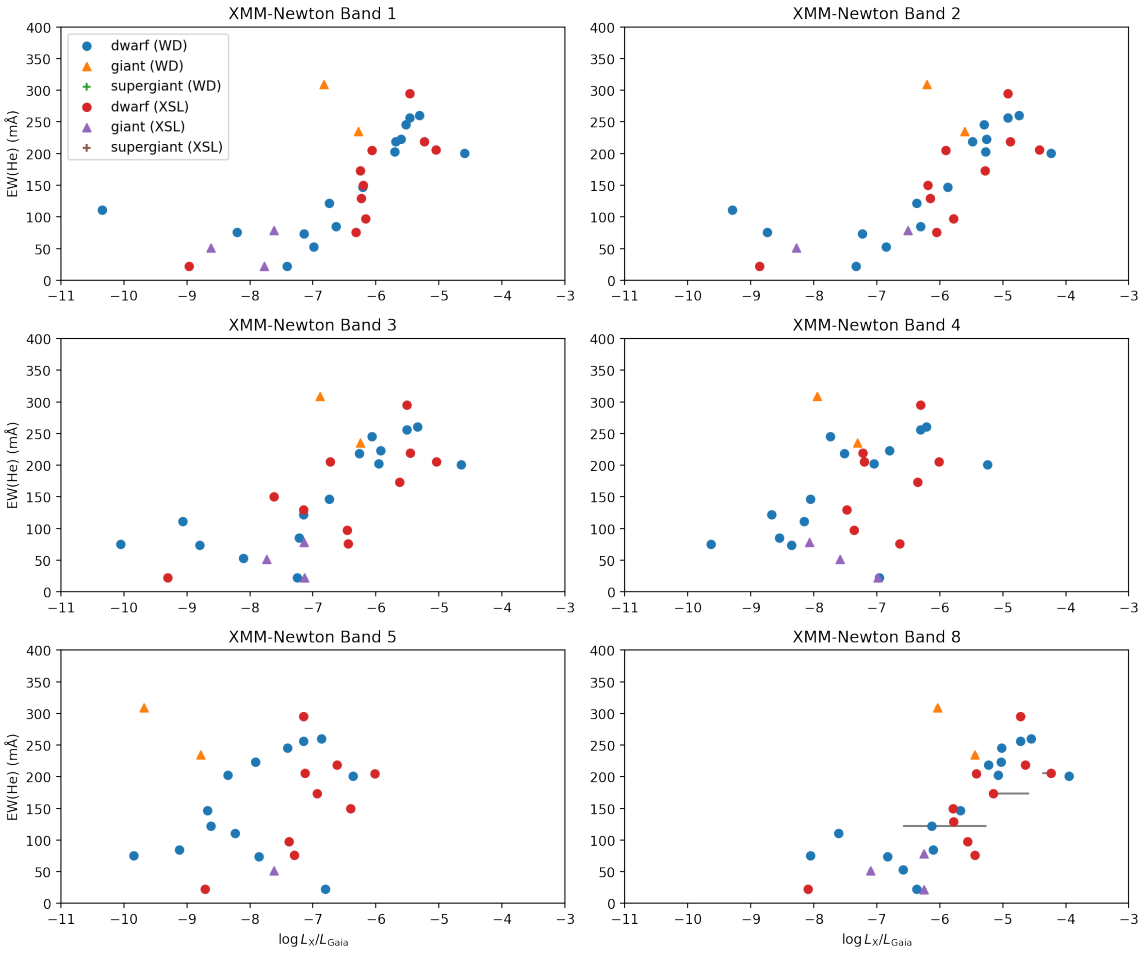


Figure 6.5: The He 10 830 EW versus the fractional X-ray luminosity from XMM-Newton bands.

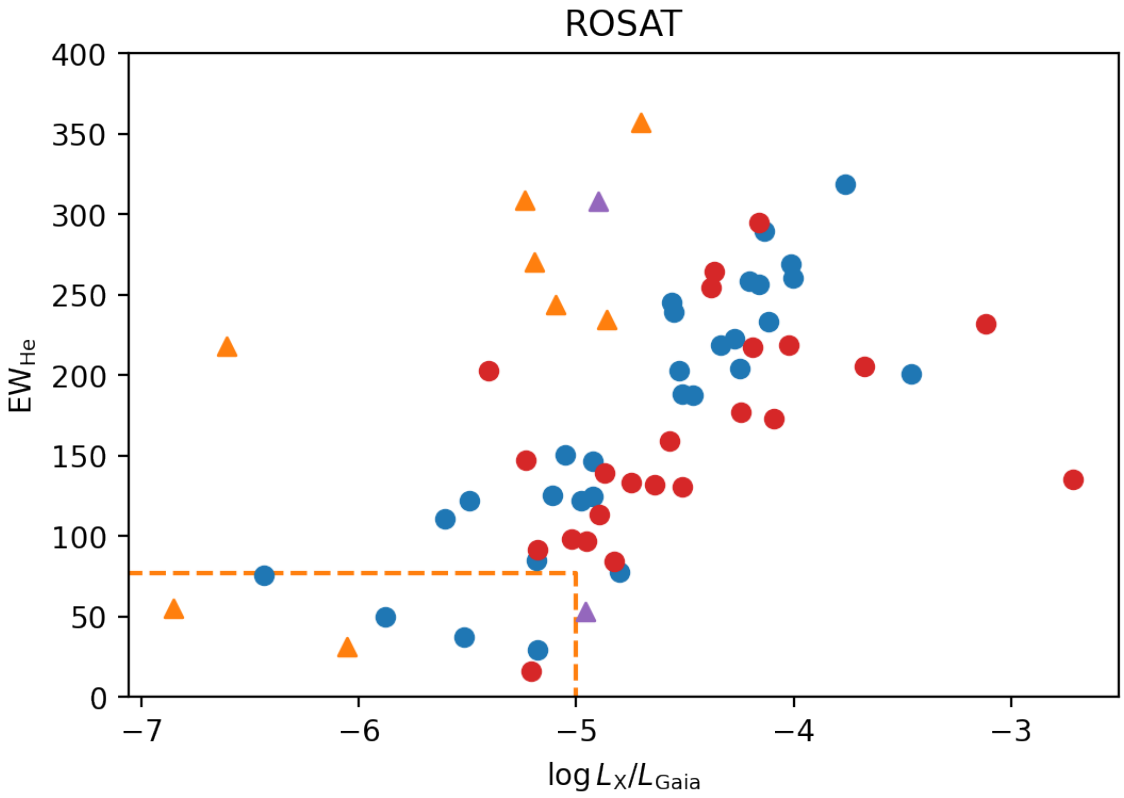


Figure 6.6: The He 10 830 EW versus the fractional X-ray luminosity from ROSAT bands. The labels are the same as those in Figure 6.5

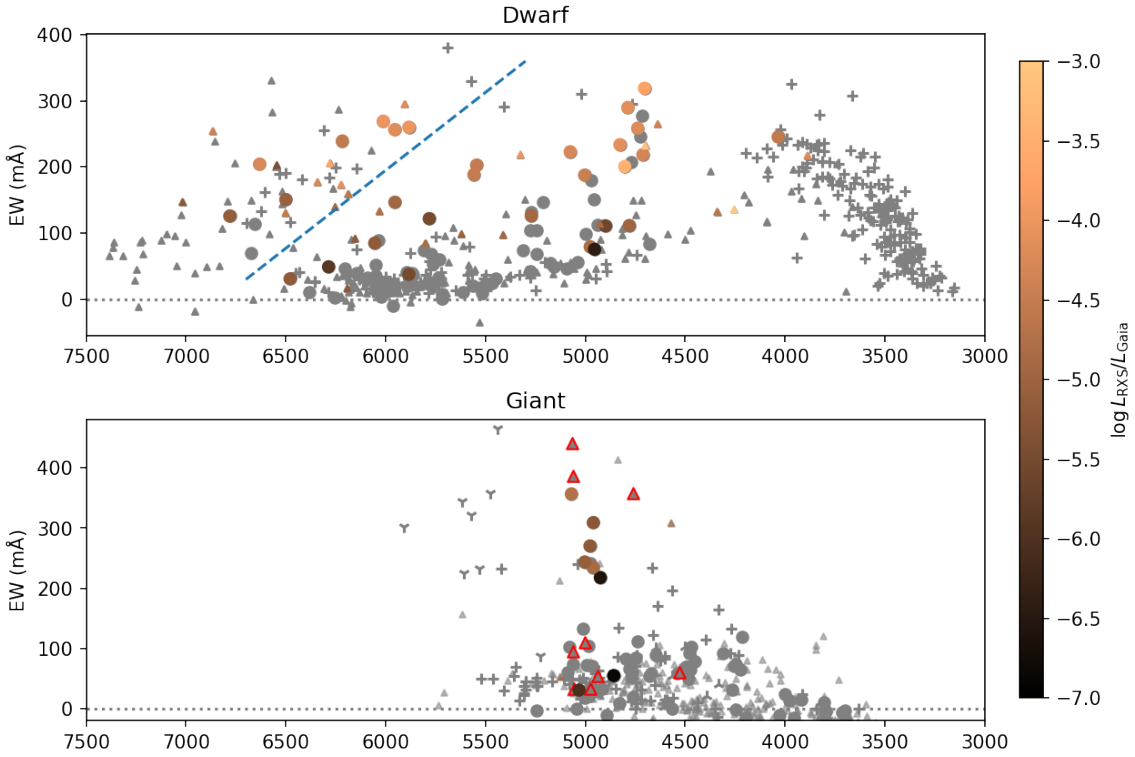


Figure 6.7: Similar to Figure 6.1, but color-coded by ROSAT fractional X-ray luminosity. Note that no X-ray measurement is available for supergiants, thus the panel for supergiant is omitted.

and $\log R'_{HK}$ index, such scatter is likely caused by the variation of the PR mechanism indicated by the fractional luminosity, but not by the variation of metallicity.

Such a scenario may also explain the lower panel of Figure 6.7, for the giants. The field-WD stars with EW(He) ~ 250 mÅ tend to have a larger $\log L_{RXS}/L_{Gaia}$ than their weaker counterparts, but the difference is smaller. We note that the vertical spread for cooler giants gets smaller, with no stars having strong helium absorption and no available X-ray measurement. Such a decrease in the scatter would imply the effect of PR mechanism is smaller.

We now conclude the dominant formation mechanism for the stars in our sample. The variation of the helium lower boundary EW seen in the dwarfs is related to the variation of $\log R'_{HK}$ index. The CE mechanism is considered to be dominant for the stars close to the lower boundary curve. On top of that, the vertical spread of EW(He) for the main trend is tightly correlated with the fractional X-ray luminosity. Thus, He 10 830 for stars above the lower boundary curve is dominated by the PR mechanism. The secondary trend is also dominated by the PR mechanism, with no clear correlation with $\log R'_{HK}$ index found. CE mechanism in those stars may exist

but does not have a large effect on the line strength. For giants, those with $T_{\rm eff} \sim 5000\,{\rm K}$ may be dominated by the PR mechanism. The effect of the PR mechanism is expected to be smaller for cooler giants since the spread in helium strength is smaller and their EW decreases as $\log R'_{\rm HK}$ index decreases.

Chapter 7

Discussion

As shown in the previous chapters, the formation of He 10 830 is complex. The line strength can be sensitive to a few parameters at each $(T_{\rm eff}, \log g)$, including chromosphere structure, external radiation and helium abundance. This chapter discusses the features we found in the empirical trends, the behavior of synthetic CE dominated He 10 830 with a giant model, and the possibility of using the helium 10 830 Å line as the helium abundance tracer.

7.1 The secondary trend in dwarf

Here we discuss the observational behavior of the secondary trend in the dwarf stars. The secondary trend is a new empirical trend found in this study. It is distinguished from the main trend by its larger EW(He) in a $T_{\rm eff}$ range of $\sim$ 6000 to 7500 K (also see Figure 6.1). The stars in the secondary trend are mainly with solar metallicity, as shown in Figure 7.1. Only a few stars in the secondary trend are with [Fe/H] < -1, while tens of stars in the main trend are metal-poor, and usually with smaller EW(He).

The $\log R'_{\rm HK}$ of the stars in the secondary trend also differ from that in the main trend. As shown in the upper-left panel of Figure 6.2, a positive correlation between EW(He) and $\log R'_{\rm HK}$ appears in the main trend stars with $\log R'_{\rm HK} \gtrsim -5$. The distribution of the secondary stars is more dispersed, and the increase of EW(He) on the right-hand side is not obvious. Such difference may indicate that the atmosphere structure in the upper chromosphere and transition part, at least, for the stars in the main and secondary trend are different. The temperature and density in the formation region of the He 10 830 and Ca II H&K lines or the main-trend stars are more coupled, while the change of physical condition in the Ca II H&K lines region has little effect on that in the He 10 830 line region for the secondary-trend stars.

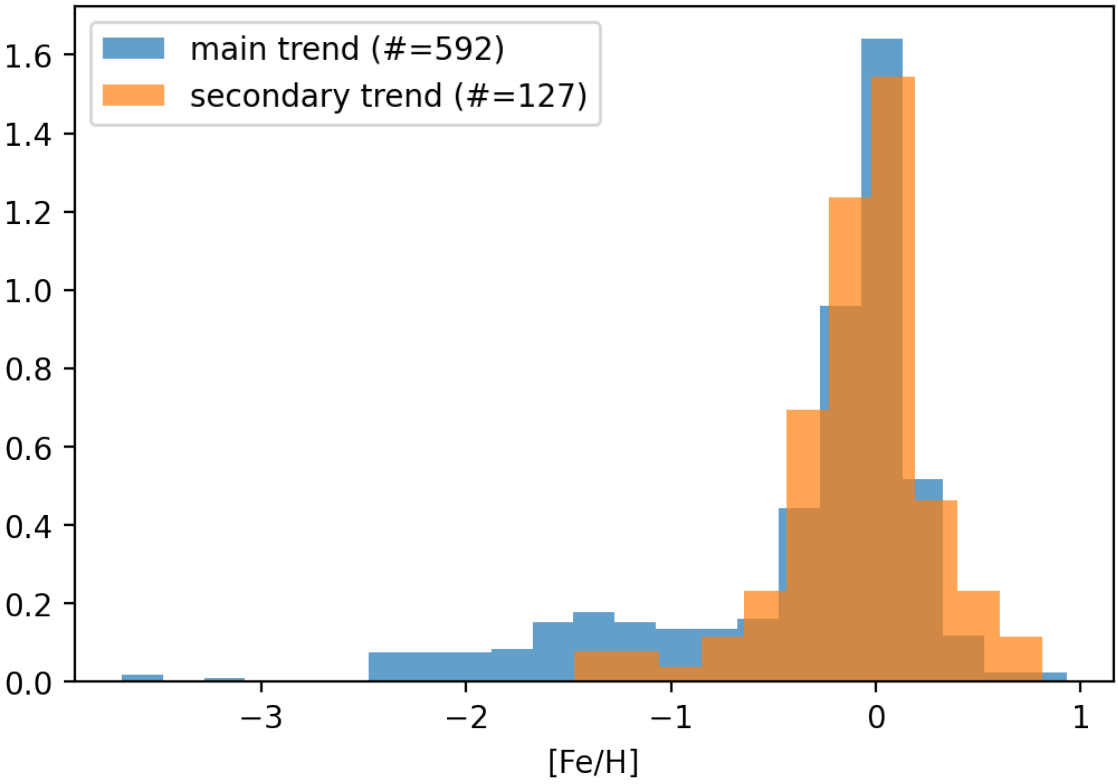


Figure 7.1: The [Fe/H] histogram of dwarfs, divided into the main and secondary trends. Most of the stars in the secondary trend are around solar. The histograms are normalized to better show their distribution in [Fe/H].

The stars in the secondary trend tend to have a relatively large fractional X-ray luminosity, as presented in Figure 7.2. Most of the stars with X-ray measurement in the secondary trend are with $log(L_{\rm X}/L_{\rm Gaia}) > -5.5$, while a few stars in the main trend are with X-ray luminosity of -6.5. Such a larger X-ray luminosity indicates that the formation of He 10 830 is dominated by the PR mechanism. We note that such double trends in the $T_{\rm eff}$ range is also seen in one of the previous X-ray observations. Freund et al. (2018) presented a detailed analysis of the stellar content of XMM-Newton slew survey. They confirmed 6815 among 23 252 sources are stellar sources, and derived their fractional X-ray luminosity. Figure 7.3 presents the distribution of $\log(L_{\rm X}/L_{\rm bol})$ in different $T_{\rm eff}$. Stars with smaller $T_{\rm eff}$ tend to have larger X-ray luminosity, and most of the stars are dwarfs in the low-temperature end. The two vertical dashed lines indicate the $T_{\rm eff}$ range where our secondary trend is located. Two groups of stars, one with lower X-ray luminosity and smaller $T_{\rm eff}$ (labeled as "F dwarfs"), and another one with higher X-ray luminosity and extends to $T_{\rm eff} \sim 10\,000$ K. Since most of the stars in the lower group are with $T_{\rm eff} < 6500$ K, they are consistent with the $T_{\rm eff}$ range of the main trend. Thus, the two groups with smaller and larger X-ray luminosity in this figure may be the main and secondary trends we found in the He 10 830. Further observation of more chromosphere lines of the secondary trend stars is necessary to constrain their atmosphere model and to explain the existence of this trend.

7.2 The EW lower boundary in dwarfs

As stated in section 6.2, the lower boundary of the EW lower boundary in dwarfs reaches the maximum at $T_{\rm eff} \sim 4000$ K. Such variation is accompanied by the increasing of $\log R'_{\rm HK}$ index in this temperature. The appearance of such variation is not well understood yet. Here we quantify the lower boundary and discuss the possible explanation which can explain the variation in $\log R'_{\rm HK}$ index.

We used the approach similar to that in Jian et al. (2017) to determine the quantities of the lower boundary in different $T_{\rm eff}$, where the lower boundary is set as the mean or median value of the 20% smallest EWs in the whole group. The stars in the main trend are first divided by each $T_{\rm eff}$ bins with a width of 200 K. If the number of stars in a bin is larger than 10, then the mean value of the 20% stars with the smallest EW(He) is taken as that for the lower boundary. If the number is smaller, then the minimum EW(He) of the stars is used. These values are plotted in Figure 7.4 as orange points. Since the size of our sample is much smaller than that in

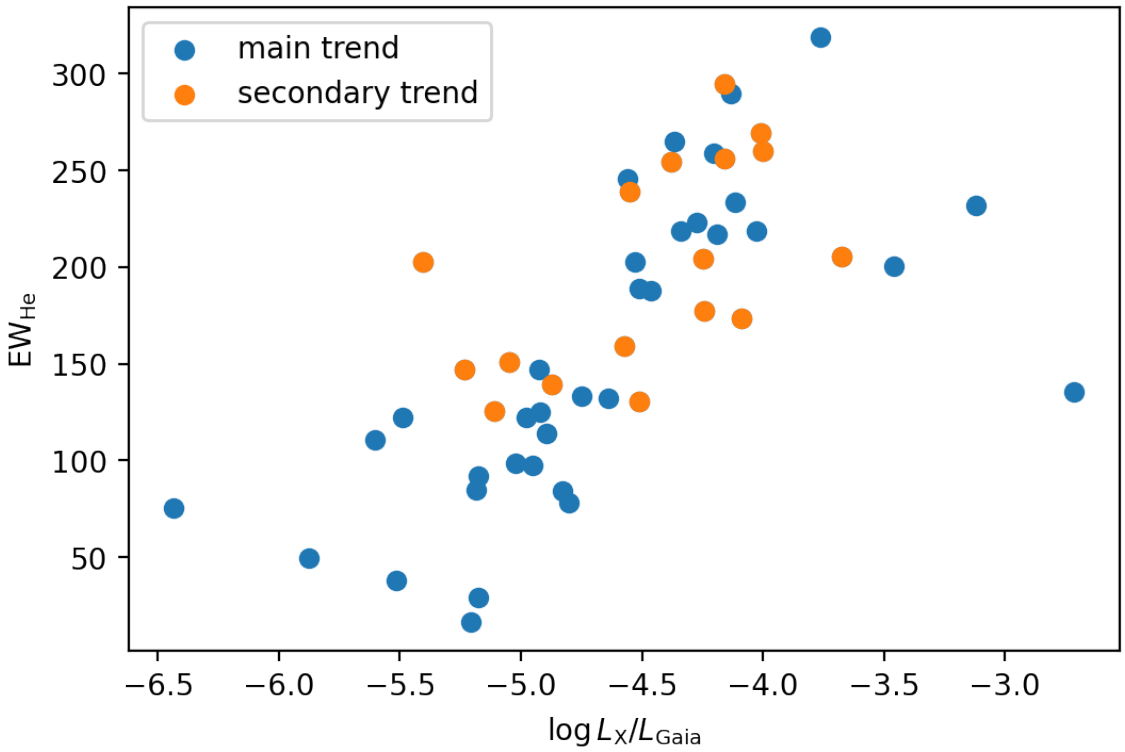


Figure 7.2: EW(He) versus ROSAT X-ray luminosity for the dwarfs in main and secondary trends.

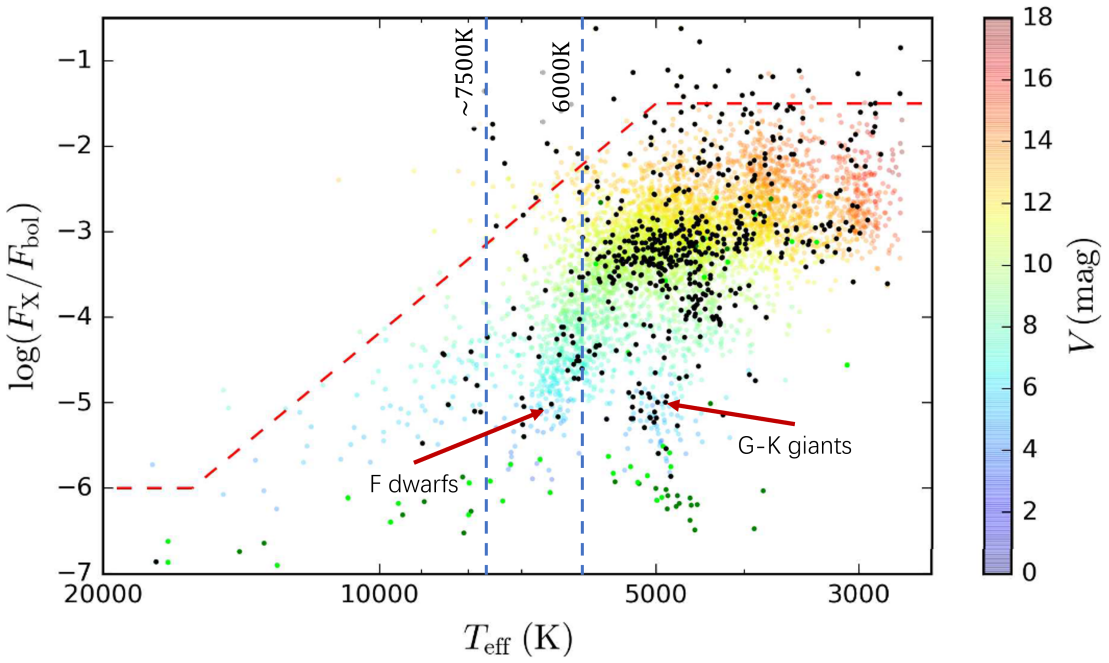


Figure 7.3: Fractional X-ray luminosity from XMM-Newton measurement versus $T_{\rm eff}$ distribution for field stars. The two blue dashed vertical lines indicate the $T_{\rm eff}$ range where the secondary trend appears, and the main component of the stars in the two areas with low $\log(F_{\rm X}/F_{\rm Gaia})$ are labeled. Adopted from Freund et al. (2018).

Jian et al. (2017), we use mean instead of median values here. We then used a 6-order polynomial function to fit the lower boundary points. The resultant function for the lower boundary is:

$$\begin{aligned} EW_{\rm LB} = {} & 1.3085 \times 10^{-17} {T_{\rm eff}}^6 - 3.9549 \times 10^{-13} {T_{\rm eff}}^5 \\ & + 4.9059 \times 10^{-9} {T_{\rm eff}}^4 - 3.1918 \times 10^{-5} {T_{\rm eff}}^3 \\ & + 1.1467 \times 10^{-1} {T_{\rm eff}}^2 - 2.1533 \times 10^{2} T_{\rm eff} + 1.6499 \times 10^{5}, \end{aligned} \tag{7.1}$$

and it is plotted as orange solid curve in Figure 7.4. The fitted lower boundary reaches a maximum of 120 mÅ at $T_{\rm eff} \sim 4000$ K, and decrease in lower or higher $T_{\rm eff}$.

As seen in Figure 6.5 and 6.6, a few stars with lower fractional X-ray luminosity shows no correlation with EW(He). The dwarfs with such X-ray luminosity are close to the lower boundary, and assuming that all the dwarfs in Figure 7.4 also follow this trend, we can define an area where the PR formation mechanism is weak. This area is derived by shifting the lower boundary upward in 27 mÅ (the orange dashed curve), the mean EW(He) of the stars in the lower left box in Figure 6.6. The stars in this area are expected to have weak X-ray luminosity and thus weak PR mechanism, while those in the upper areas would be PR dominated. The sun is located slightly upper

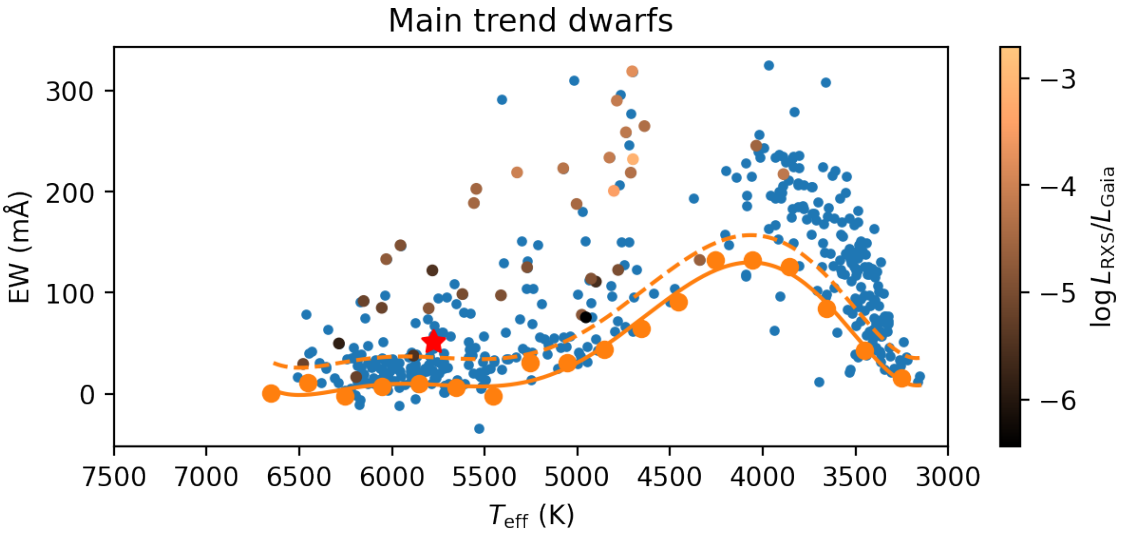


Figure 7.4: The lower boundary for the main trend dwarfs. Blue points are the dwarfs in the main trend, and those with ROSAT X-ray luminosity measurement are color coded. Orange points are the lower boundary EWs in each $T_{\rm eff}$ bin determined in section 7.2, and the orange solid (dashed) curve is the fitted lower boundary (the boundary shiftred by 27 mÅ).

than the dashed curve, which is consistent with the conclusion that its He 10 830 is PR dominated.

Recently, Brown et al. (2022) calculated the $\log R'_{\rm HK}$ index and longitudinal magnetic field (B_l) for more than 900 FGK type dwarfs. They divided their sample into young and mature stars according to their Li line strength in 6707.8 Å: the stars with relatively strong Li lines are considered as young stars, and those with weak Li lines are considered as mature stars. Most of the young stars with $T_{\rm eff} \sim 4000$ K are having a larger $\log R'_{\rm HK}$, with values larger than -4.3 (see their Figure 3). The mature stars, on the other hand, are with $\log R'_{\rm HK} \sim -5$. Further, the young stars with larger $\log R'_{\rm HK}$ are also having larger B_l, with $\log B_l > 1$. Brown et al. (2022) suggested that if such difference in $\log R'_{\rm HK}$ and b_l is a real phenomenon, then it could be explained by the stellar core-envelope recouple when a star reaches its main sequence phase. Such scenario is proposed by Barnes (2003), in which the author measured the rotation period of open clusters in various ages and those from the Mount Wilson stars. He found that two sequences in the period-$(B-V)_0$ diagram appear in the stars with ages smaller than 600 Myr (see their Figure 2). More stars are located in the lower sequence (C sequence, with a smaller rotation period) for those in the young open clusters, while most of the stars are located in the upper sequence (I sequence, with a larger rotation period) for the stars with larger ages. The stars in the C sequences

are those with their surface convective zone and inner radiative zone decoupled, thus their rotation of the surface area is not drained by the inner parts, and their rotation periods are smaller. On the other hand, the convective zone and radiative zone of the stars in the I sequence are coupled, thus their rotation period is larger. If all stars in our sample are young stars with their convective and radiative zome de-coupled, then such a scenario may explain the strengthening of the EW lower boundary in dwarfs. Further observation of the stellar rotation period or age of our sample stars is necessary.

7.3 CE dominated He 10 830 in a simple model for giants

Though the chromosphere and transition region models for the giant are not well constrained, it is instructive to show whether obvious He 10 830 can appear in giants when the CE formation mechanism is dominant using the synthetic spectra.

Previous empirical models for giants usually consist of three parts: a photosphere part from LTE model calculation at the bottom, a chromosphere part in the middle, and a transition region part at the top. Three parameters control the structure of chromosphere in this case: the minimum temperature which marks the border of photosphere and chromosphere, the location (usually column density, $\log \rho x$, or optical depth, $\log \tau$) where the chromosphere ends, and the temperature at this point. The transition region is usually a thin layer with a steep increase of temperature by a factor of 10 or more. The synthetic line profiles are controlled by these values, and compared with observations. For example, Mauas et al. (2006) uses such models to detect the evidence of mass loss from RGBV stars, and similar models are used in Dupree et al. (2011) to derive the stellar helium abundance of Ω cen giants with other chromosphere lines.

A simple model for giant with $T_{\rm eff} = 4000\,{\rm K}, \log g = 0.5$ and [Fe/H] $= 0$ is constructed according to the process of empirical modelling introduced above. As shown in Figure 7.5, the photosphere profile with the specified stellar parameters from the ATLAS9 model grid is first adopted. The model was then extended to the outer layers, starting from $\log \rho x \sim 0$ where the temperature minimum is located. The temperature profile deviates from the ATLAS9 profile from this point, and the chromosphere part in between the vertial dashed lines is fixed by two control points: $T = 8000\,{\rm K}$ at $\log \rho x \sim -4$, and $T = 20\,000\,{\rm K}$ at $\log \rho x \sim -5.5$. A steep temperature rise in the outmost layer resembles the transition region, where the temperature

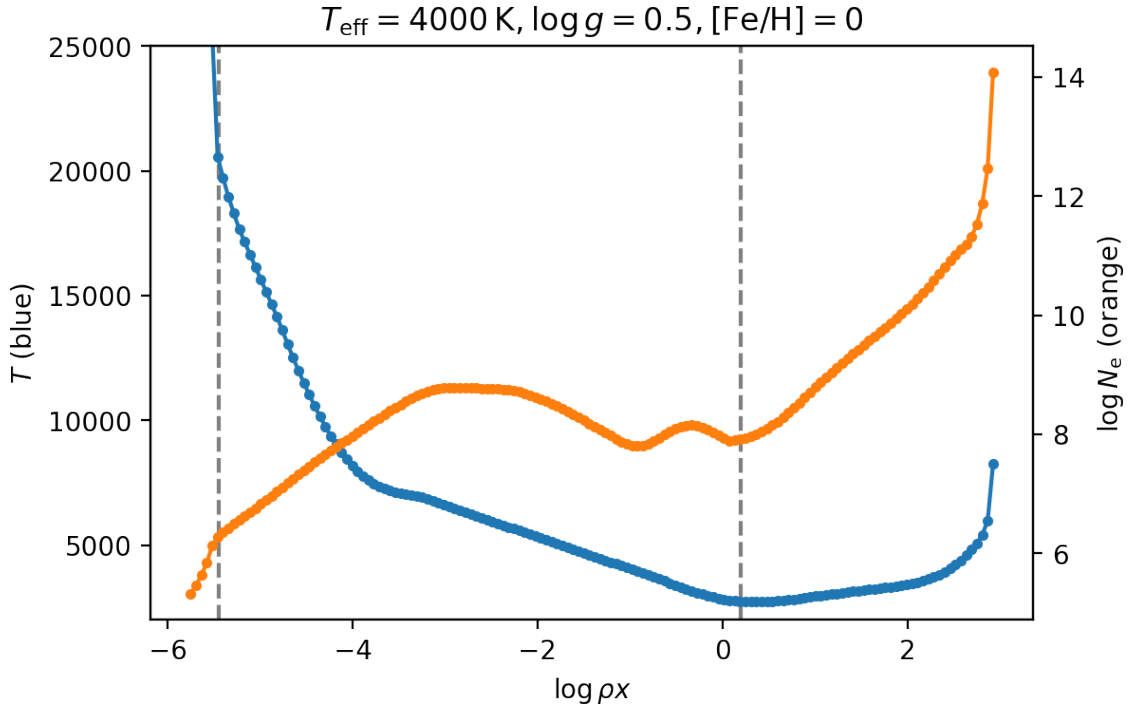


Figure 7.5: The giant model used for generating the synthetic spectra in section 7.3, similar to Figure 2.1. The two vertical dashed lines indicate the separation of the transition region and chromosphere, and that of the chromosphere and photosphere parts, from left to right.

increases from 20 000 K to 100 000 K in a $\log \rho x$ range of 0.1. External radiation is 0 in the calculation. The electron density is then calculated in the MULTI Hydrogen run.

The above temperature profile is chosen to give a relatively strong He 10 830. Figure 7.6 presents the synthetic chromosphere line profiles of the H, Ca and He lines. Since external radiation is 0 for this model, the formation mechanism is purely CE. The depth of the He 10 830 is relatively deep, with a value of 0.3. Thus strong He 10 830, dominated by the CE formation mechanism, can be produced in giants. Increasing the number of control points or moving the control points can alter the profile of these lines and produce better fits with observation (such practice is beyond the scope of this thesis). Finally, the CE dominated He 10 830 in giants have similar sensitivity on the helium abundance to that in dwarfs, as shown in Figure 7.7.

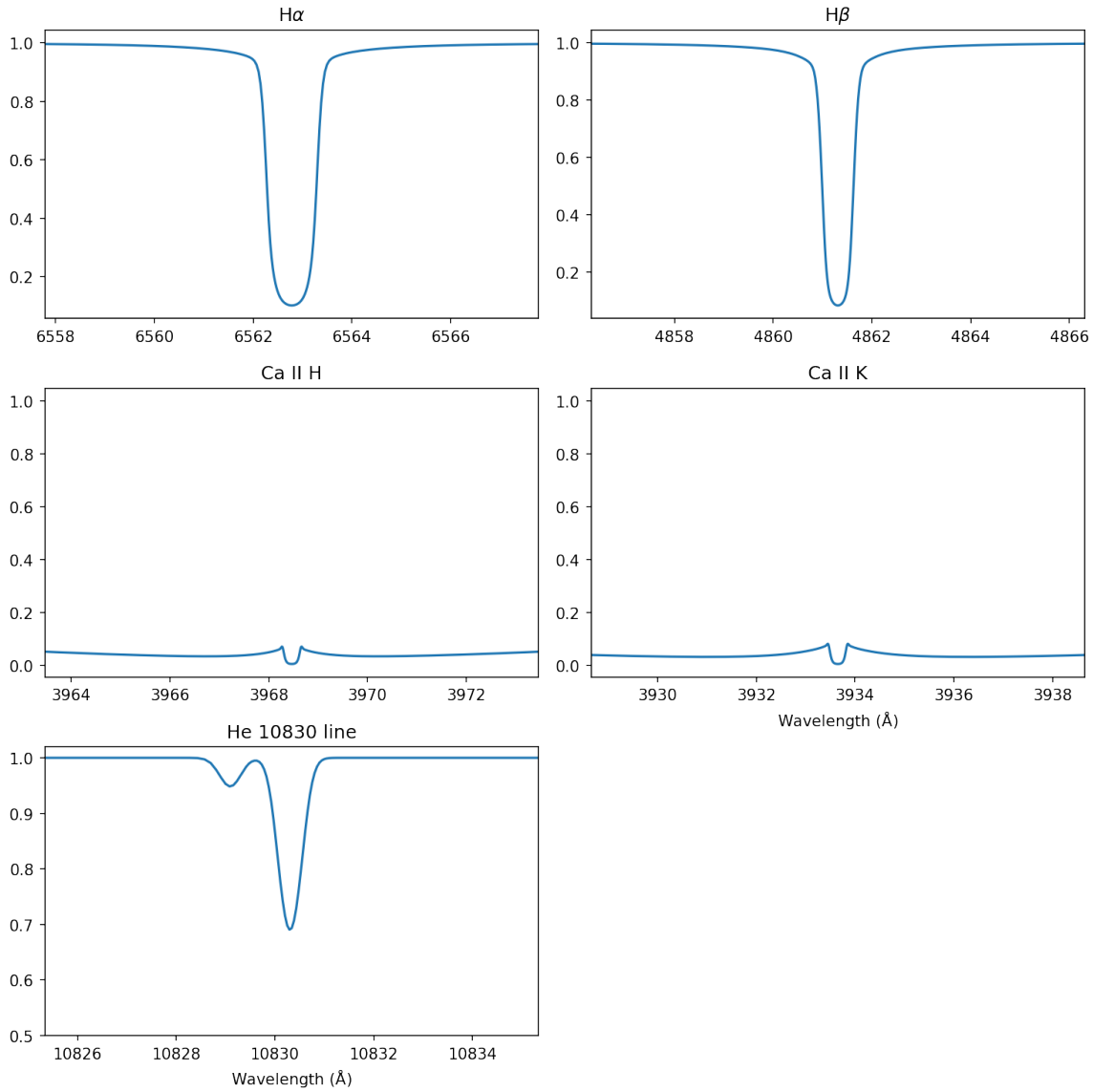


Figure 7.6: Synthetic spectra of chromospheric lines generated using the giant model in Figure 7.5.

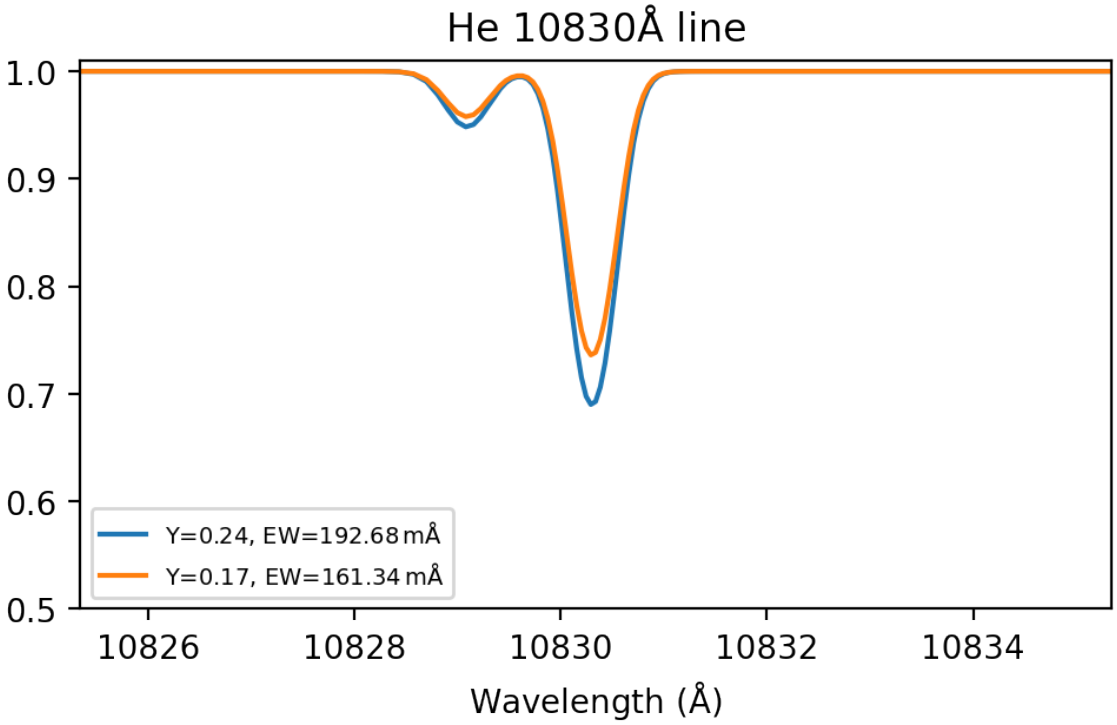


Figure 7.7: The He 10 830 with two helium abundances, generated using the giant model in Figure 7.5.

7.4 The usage of helium 10 830 Å line as a helium abundance tracer

Using He 10 830 as a helium abundance tracer requires that the line strength is sensitive to helium abundance. Since the line strength is not sensitive to the helium abundance when the PR mechanism is dominant, it would be hard to determine helium abundance with the PR dominant line. Our results show that He 10 830 in dwarfs are dominated by the PR mechanism, and the He 10 830 strength of dwarfs would have small sensitivities to the helium abundance, if any.

For giants, we could not determine whether the scatter in the He 10 830 EW is related to their X-ray luminosity since only a few giants have X-ray photometry. Nevertheless, we can make some predictions taking into account the dividing line that separates the giants with and without well-developed corona. He 10 830 in warmer stars are affected significantly by the PR mechanism and it would be difficult to measure helium abundance. In contrast, the giants with $T_{\rm eff} < 4500$ K are considered to have relatively weak corona and coronal radiation, as discussed in Chapter 1. The dominant formation mechanism of He 10 830 in these stars would be CE, and therefore

the strength of He 10 830 line is sensitive to the helium abundance. Besides measuring the line strength precisely, a crucial step is to determine the chromosphere structure of each star. As suggested by Pasquini et al. (2011), changing the chromosphere structure introduces a large variation in the Ca II H&K line, thus the observation of Ca lines can provide a strong constraint to the chromosphere structure. Other lines formed in the layers closer to that of He 10 830, e.g., the Lymanα line, can also be used to fix the chromosphere model. He 10 830 of metal-rich stars with $T_{\rm eff} \sim 4500$ K can be detected in our spectra. The required S/N and resolution will be discussed in the next section.

Constructing the chromosphere model and deriving the helium abundance requires all the chromosphere lines observed. The state-of-the-art modeling would be time-consuming and require some extent of computational resources, too. There is a different approach, with which we can bypass the complex modeling and detect relative variations of the helium abundance. In particular, the stars in GCs would provide a good sample with similar stellar parameters to each other. Here we revisit the studies of GC member stars introduced in Chapter 1, and discuss their possibility of detecting the helium abundance variation. Figure 7.8 summarizes the result of previous GC observation. These samples cover a wide range of $T_{\rm eff}$, from 3800 to 5600 K, and EW(He) ranges from tens to a few hundreds mÅ. Most of them are hotter than 4500 K, thus they are expected to be PR dominated, or at least affected by PR. These stars are thus expected to show little helium abundance sensitivity on the He 10 830 EW, which is consistent with the flat distribution versus [Na/Fe] as shown in the right panel of Figure 7.8. In contrast, the two stars with $T_{\rm eff} \sim 3800$ K observed in Pasquini et al. (2011) are expected to be CE dominated. The spectral synthesis on these stars shows that EW(He) is sensitive to the abundance, and the relative helium abundance difference could be detected with the Ca II lines observed simultaneously.

The observation of He 10 830 in low-temperature stars, especially those in GCs, is still sparse. In fact, after Smith et al. (2004) concluded that the giants with $T_{\rm eff} < 4600$ K show weak He 10 830 absorption, the succeeding studies preferred to observe high $T_{\rm eff}$ giants. Thus, the possibility of using the CE-dominated line as a helium abundance tracer still needs to be validated. The targets most suited for detecting EW(He) variation caused by the helium abundance would be the GC stars with the extended Na-O anticorrelation. Such an anticorrelation is considered to be accompanied by a large helium abundance variation between the populations. Considering the metallicity dependence of He 10 830, relatively metal-rich GCs would

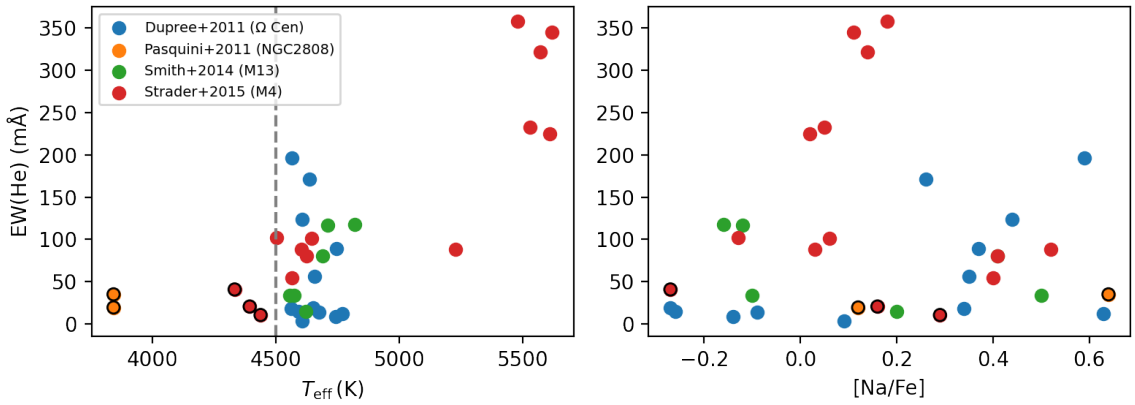


Figure 7.8: The He 10 830 EW from previous GC observations are plotted against $T_{\rm eff}$ (left) and [Na/Fe] (right). Stars rightward of the CDL (with $T_{\rm eff} < 4500$ K) are emphasized with black circle.

be easier in observational perspective. These targets include the giants in NGC104 ([Fe/H] $= -0.72$ from Carretta et al. 2009, $\Delta Y_{\rm max} = 0.049$ from Milone et al. 2018, same below), NGC6388 ([Fe/H] $= -0.54$, $\Delta Y_{\rm max} = 0.067$) and NGC6441 ([Fe/H] $= -0.39$, $\Delta Y_{\rm max} = 0.081$).

7.5 Relations between EW(He) and metallicity for cool giants

We now discuss the behavior of He 10 830 in the cool giants, $T_{\rm eff} < 4500$ K, which are considered to be unaffected by the PR formation mechanism. Figure 7.9 presents the relation between EW(He) and $\log R'_{\rm HK}$ for the field-XSL giants, split into 9 $T_{\rm eff}$ bins. Their $\log R'_{\rm HK}$, as shown in Chapter 6, are mostly around -6 and -5. No clear correlation between EW(He) and $\log R'_{\rm HK}$ is found in each panel since the stars are limited in $T_{\rm eff}$, but the average $\log R'_{\rm HK}$ in different panels becomes smaller as the $T_{\rm eff}$ decreases. The large scatter in EW(He), on the other hand, indicates that it is affected by other factor(s). The distribution of EW(He) against [Fe/H] for the giants are shown in Figure 7.10. The giants in the panels with a number larger than 10 are fitted by the linear relation, and they show some interesting tendencies. The EW in hotter giants are larger, and those in cooler giants ($T_{\rm eff} < 4000$ K) are around 0. No strong correlation is seen for the stars with $4800 < T_{\rm eff} < 5000$ K. The panels with $T_{\rm eff}$ between 4300 and 4700 K show positive correlations. Their correlation coefficients and slopes are larger than those in other panels. The line strengths in metal-poor stars are around 0, while those in metal-rich stars can reach 50 or even 100 mÅ. Such

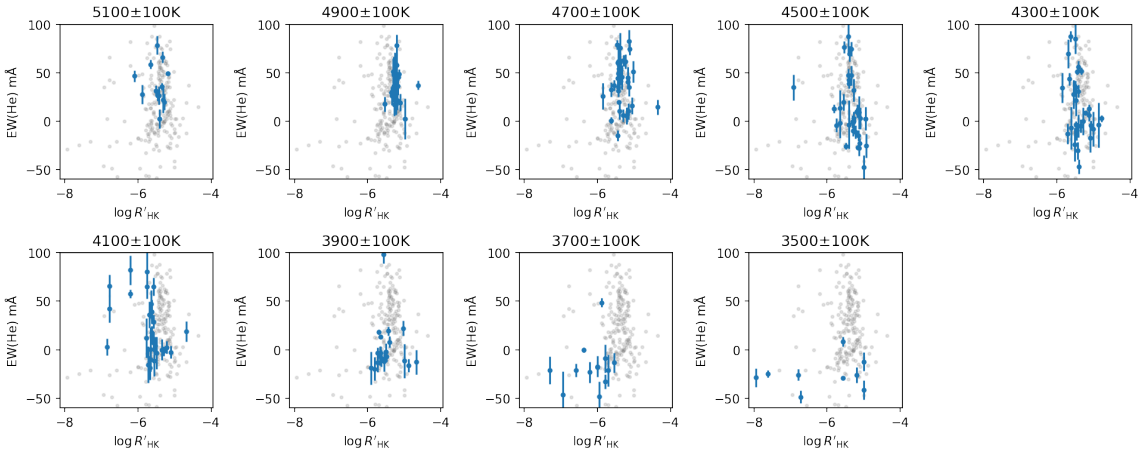


Figure 7.9: EW(He) versus $\log R'_{\rm HK}$ for field-XSL giants separated in $T_{\rm eff}$ bins. The title of each panel indicates the $T_{\rm eff}$ range.

a correlation could not be detected, if any, on the panel with lower $T_{\rm eff}$, because He 10 830 becomes too weak.

Figure 7.11 clearly presents that the correlation between [Fe/H] and EW(He) varies with $T_{\rm eff}$. The correlation coefficient inside the orange span is systematically higher than outside. This range, 4123–4688 K, is roughly consistent with the $T_{\rm eff}$ threshold, 4500 K, corresponding to the CDL for giants. Thus EW(He) of the giants in this $T_{\rm eff}$ range is expected to be sensitive to the helium abundance, and the positive correlations shown in the panels may reflect such sensitivity. Assuming the slope of the helium enrichment law, $\Delta Y/\Delta Z$, is 1.54 among field stars (adopted from The Dartmouth Stellar Evolution Program, Dotter et al. 2008), the helium abundance difference of stars with [Fe/H] $= -1.5$ and 0.5 is 0.06. This value is similar to the helium abundance difference among the stellar populations in NGC104 reported by Milone et al. (2018). Whether the positive correlation seen in the panels is caused by the helium abundance variation can be tested by observing the giants with similar $T_{\rm eff}$ but a large difference in Na and O abundance in NGC104. In order to detect the difference of 50 mÅ in EW(He), the S/N of 50 and 70 is required to detect when using WINERED ($R = 28000$) and X-SHOOTER ($R = 10000$). If the difference is 25 mÅ, then the required S/N are increased to 105 and 150, respectively.

Here we discuss whether other factors, besides the helium abundance, can explain the positive EW(He)–[Fe/H] trend seen in cool giants. The effect of [Fe/H] may change the chromosphere structure, thus affecting EW(He). No correlation between $\log R'_{\rm HK}$ and [Fe/H] is found for the field-XSL giants. Further, Cuntz & Ulmschneider (1994) states that increasing [Fe/H] may slightly decrease the chromospheric

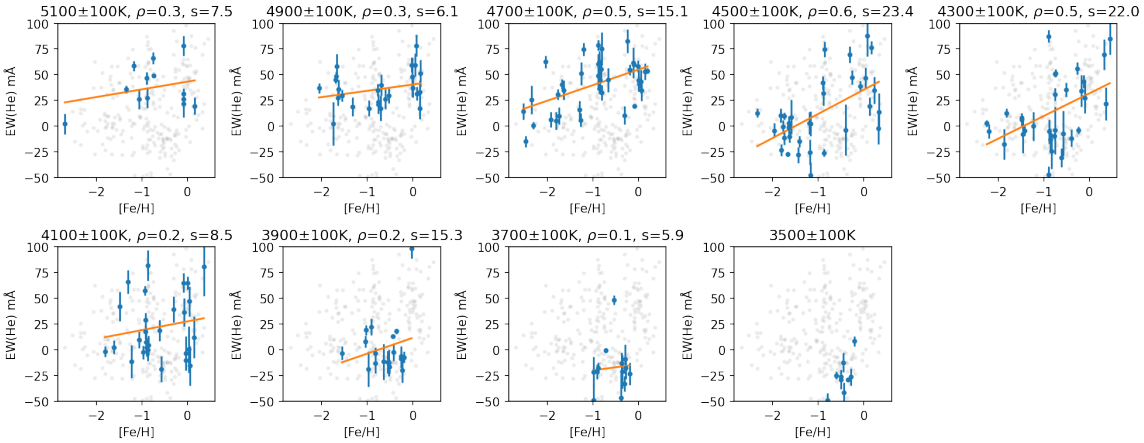


Figure 7.10: EW(He) versus [Fe/H] for field-XSL giants separated in $T_{\rm eff}$ bins. The title of each panel indicates the $T_{\rm eff}$ range, Pearson correlation coefficient ρ and slope s of the linear fitting.

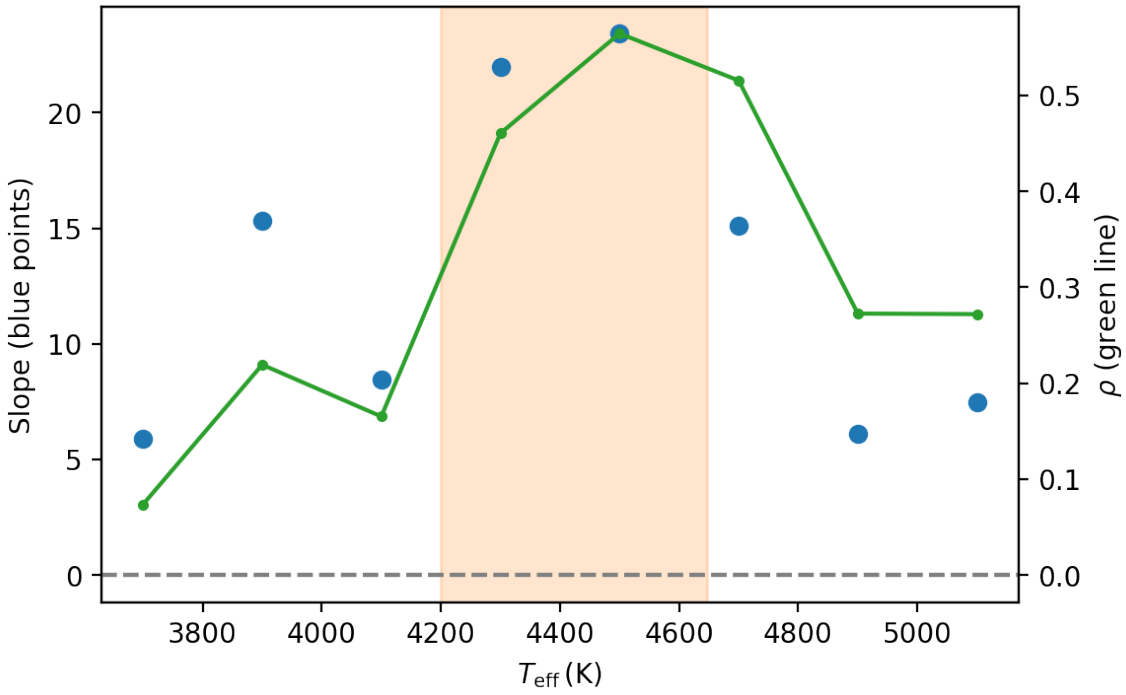


Figure 7.11: The slope and correlation relation of the linear fits in Figure 7.10. The orange shaded area highlights the $T_{\rm eff}$ range with larger slopes and correlation coefficients.

temperature. If this is also the case for our sample, then we should see a negative EW(He)–[Fe/H] relation due to the smaller chromosphere temperature in metal-rich stars. Lambert (1987) reported the temporal variation of the He 10 830 strength in Arcturus is around 100 mÅ, similar to the EW range shown in Figure 7.10. However, temporal variation with such an amplitude, if present in many of our sample stars, should have smeared out the increasing trend in the figure. We also expect that there would be a correlation between $\log R'_{\rm HK}$ and EW(He), since stellar activity usually affects both the chromosphere and upper layers. The local condition where He 10 830 is formed is the most possible factor affecting the EW(He) and creating positive trends. If the temperature or density of He 10 830 formation region varies systematically with [Fe/H], then EW(He) may vary accordingly. Our dataset cannot provide a direct constraint on the condition of He 10 830 formation region, since the Lyman-α line or Mg II h&k lines are not included in the observation, and the formation region the Ca II H&K lines is deeper than that of He 10 830. Further spectroscopic observation of UV spectra is necessary.

In summary, the positive correlations appearing in the EW(He)–[Fe/H] panels in Figure 7.10 with $T_{\rm eff}$ around 4500 K infers that He 10 830 under such stellar parameters may be sensitive to the helium abundance variation, but further observation on stars with clear helium abundance variation and other chromosphere lines, including Ca II H&K and Lyman α lines, is necessary.

Chapter 8

Conclusions

We summarize the work presented in the thesis in this final chapter. This thesis focuses on the behavior of the He 10 830 feature, their connection with the line formation mechanism, and the possible constraints on the stellar chromosphere model. These results form an important step towards measuring the helium abundance using He 10 830.

We first used the NLTE synthesis of chromosphere lines with the commonly adopted solar chromosphere model to study how these lines vary when the PR or CE mechanism is dominant for He 10 830. The strength of He 10 830, when dominated by the PR mechanism, is sensitive to the external radiation, since the radiation ionized the neutral helium atom and populate the number of atoms in 2s state. The strength of other chromosphere lines are not affected by external radiation, since they are either dominated by collisions (Ca II H&K lines) or formed in the lower layers (Hα and Hβ lines). Such a result implies that the PR mechanism appears or dominates when there is a correlation between EW(He) and fractional X-ray luminosity. EW(He) in this case is not sensitive to helium abundance since the amount of external radiation is not necessarily related to helium abundance. On the other hand, EW(He) is sensitive to the chromosphere density when CE meachanism dominates. The amount of core emission in Ca II H&K line is also correlated with EW(He), since the density in Ca II line formation region also increases. We should observe positive relation between $\log R'_{\rm HK}$ index and EW(He) when the CE mechanism appears or dominates, though increasing the chromosphere density may also increase the X-ray radiation. EW(He) is sensitive to helium abundance in the CE dominant case, thus helium abundance could be measured, at least relatively, for stars with CE dominant He 10 830 and those with similar chromosphere model.

The empirical relations between EW(He) and other stellar parameters were then revised with a sample of more than 700 FGK type stars. Besides EW(He), $\log R'_{\rm HK}$

and fractional X-ray luminosity are also measured or calculated from corresponding observations. Two trends were found in the EW(He)–$T_{\rm eff}$ diagram for dwarfs, with the main trend consistent with those reported in Zirin (1982), and a newly found secondary trend. The main trend cover a $T_{\rm eff}$ range of $\sim$ 3000 to 6500 K, with a clear lower boundary increasing from 0 at 3250 K to 120 mÅ at 4000 K, and decrease to 0 again as $T_{\rm eff}$ increases. Such boundary also appear in the empirical relation between $\log R'_{\rm HK}$ and $T_{\rm eff}$, and positive relation between EW(He) and $\log R'_{\rm HK}$ is found in main trend stars, implying that CE mechanism appears, at least, in the main trend stars around the lower boundary. PR mechanism is observed and dominated in the dwarf stars located on top of the lower boundary, since these stars show a correlation between EW(He) and X-ray luminosity. Stars in the secondary trend are medium- to high-temperature stars having larger EW(He) than those in the main trend. Their $\log R'_{\rm HK}$ is not correlated with the EW(He), unlike the stars in the main trend. PR mechanism also dominates these stars. Further observation of other chromosphere lines for the secondary trend stars is necessary to fully explain why they have different behavior than those in the main trend. We also conclude that PR and CE mechanisms both appear in the warm giants (those with $T_{\rm eff} \sim 5000$ K).

We then discussed what kind of stars He 10 830 is expected to be sensitive to helium abundance. Since the PR mechanism appears in both dwarfs and warm giants, their EW(He) is not sensitive to their helium abundance. The cool giants, on the other hand, are expected to be sensitive to helium abundance since they are located on the right side of the coronal dividing line, where very weak or no high-energy radiation is found in their atmosphere. We conclude that, on the contrary to the suggestion from previous studies, giants with $T_{\rm eff} < 4500$ K are adequate targets. NLTE line synthesis with a simple giant atmosphere model shows that obvious absorption of He 10 830 can appear in the CE dominated case. The giants from the field-XSL sample show a positive correlation between EW(He) and [Fe/H] for the stars with $4200 < T_{\rm eff} < 4600$ K. This is consistent with our expectation that the increase in EW(He) is caused by helium abundance, though there are other factors that may affect He 10 830. Further observations on He 10 830 and other chromosphere lines are required to confirm this conclusion.

To conclude, we present detailed empirical trends between EW(He) and other stellar parameters. These trends, accompanied by the NLTE line synthesis from solar and giant atmosphere models, constraints the formation mechanism of He 10 830, and also serve as constraints on future empirical modeling of stellar chromosphere. With modern high-resolution spectrographs covering larger wavelength ranges, several

chromosphere lines can be obtained simultaneously, and these datasets would lead to more precise stellar chromosphere models. The strength of He 10 830 is expected to be sensitive to helium abundances in cool giants. Future observations with the aim of probing helium abundance using this feature should focus on these targets.

Appendix A

Stellar parameters and He 10 830 measurement for previous studies

This appendix lists the stellar parameter and He 10 830 EW compiled from the previous studies. The error of $T_{\rm eff}$, $\log g$ and [Fe/H] for Fuhrmeister et al. (2019) is 51 K, 0.07 and 0.16, respectively.

References: 1 – Zirin (1982); 2 – Zarro & Zirin (1986); 3 – Obrien & Lambert (1986); 4 – Lambert (1987); 5 – Sanz-Forcada & Dupree (2008); 6 – Dupree et al. (2009); 7 – Pasquini et al. (2011); 8 – Dupree et al. (2011); 9 – Takeda & Takada-Hidai (2011); 10 – Smith et al. (2012); 11 – Dupree & Avrett (2013); 12 – Strader et al. (2015); 13 – Strader et al. (2015); 14 – Andretta et al. (2017); 15 – Dupree et al. (2018); 16 – Fuhrmeister et al. (2019).

Table A.1: Stellar parameters and the He 10 830 EW for the stars in the previous studies discussed in Chapter 1. The name of each star is HD number, if not specified.

Target (HD)	$T_{\rm eff}$ (K)	$\log g$	[Fe/H]	EW(He) (mÅ)	Ref	Target (HD)	$T_{\rm eff}$ (K)	$\log g$	[Fe/H]	EW(He) (mÅ)	Ref
282624				3160	1	125451	6700	4.12	0.01	0	2
58061				0	1	114378	6365	4.19	-0.23	200	2
234677	4622	4.65	0.2	150	1	61421	6623	3.94	-0.1	0	2
60179C	3885	4.5	0.03	0	1	88215	6776	3.96		0	2
BD +09 5427				4100	1	43318	6253	3.94	-0.19	0	2
244138				2530	1	27483				0	2
BD +47 781				400	1	33564	6554	4.49	0.211	0	2
284419				2650	1	113337	6796	4.61	0.17	0	2
10216				500	1	38393	6306	4.21	-0.12	100	2
10420				150	1	11443	6273	3.91		320	2
28	4736	2.6	-0.12	60	1	173667	6436	3.95	-0.11	50	2
166	5363	4.5	0.16	240	1	126660	6377	4.11	-0.03	133	2
358	12938	4.19	0.42	0	1	85217	6473			230	2
432	6792	3.59	-0.15	200	1	170153	5861	4.05	-0.62	0	2
886	22000	3.95	0.01	150	1	8774	6537			200	2
1522	4446	2.1	-0.09	18	1	90839	6156	4.39	-0.11	0	2
1967				120	1	35296	6171	4.31	0.01	257	2
3196	6107	4.56	0.03	350	1	114284				100	2
3421	5225	2.15	-0.35	550	1	102870	6162	4.11	0.15	0	2
3546	5109	2.83	-0.5	0	1	13974	5640	4.32	-0.46	200	2
3627	4315	2.4	0.04	50	1	39587	5935	4.52	0.0	275	2
3712	4666	1.96	-0.1	25	1	113583				130	2
4128	4848	2.25	0.05	510	1	141004	5877	4.11	-0.01	100	2
4502	5064	2.88	-0.05	750	1	19373	5901	4.06	0.04	0	2
4656	3956	1.85	-0.09	0	1	114710	5976	4.35	0.02	50	2
5234	4448	2.1	-0.21	65	1	157214	5718	4.15	-0.43	50	2
5395	4885	2.64	-0.46	70	1	121370	6121	3.88	0.31	0	2
5516	4999	3.07	0.07	475	1	64096				0	2
6186	4829	2.3	-0.31	0	1	65626	5792			230	2

Continued on next page

(Continued)

Target (HD)	$T_{\rm eff}$ (K)	$\log g$	[Fe/H]	EW(He) (mÅ)	Ref	Target (HD)	$T_{\rm eff}$ (K)	$\log g$	[Fe/H]	EW(He) (mÅ)	Ref
6582	5331	4.54	-0.81	0	1	98230	5692	4.46	-0.35	295	2
6805	4770	2.96	0.24	0	1	9562	5831	4.03	0.19	0	2
6860	3762	1.07	-0.49	0	1	81809	5782	4.0	-0.28	0	2
7087	4908	2.39	-0.04	0	1	143761	5745	3.99	-0.3	50	2
7106	4701	2.58	0.01	0	1	sun	5780	4.44	0.0	50	2
8207	4842	2.65	0.31	80	1	72905	5814	4.55	-0.06	175	2
8512	4820	2.7	-0.13	0	1	217014	5748	4.31	0.2	0	2
8723	6690	4.12		200	1	76151	5761	4.43	0.09	100	2
8774	6537			200	1	82210	5299	3.49	-0.21	200	2
9270	4937	2.8	-0.14	100	1	78418	5625	3.98	-0.26	0	2
9826	6180	4.14	0.03	0	1	161797	5580	3.99	0.29	25	2
9927	4356	2.04	-0.04	150	1	20630	5605	4.4	0.04	210	2
10072	5109	2.83	-0.13	325	1	75732	5211	4.28	0.35	50	2
10307	5783	4.17	-0.05	0	1	10700	5590	4.75	-0.47	50	2
10476	5190	4.51	-0.03	0	1	131156	5410	4.48	-0.05	200	2
10697	5600	3.96	0.13	0	1	101501	5335	4.34	-0.07	100	2
10700	5590	4.75	-0.47	0	1	3651	5222	4.49	0.16	0	2
11502				0	1	165341A				200	2
11443	6273	3.91		350	1	26965	5568	4.75	-0.54	0	2
12533	4248	1.03	0.0	20	1	17925	5069	4.41	0.12	200	2
12929	4643	2.78	-0.26	0	1	22049	5020	4.62	0.02	150	2
13480	5070			725	1	32147	4687	4.25	0.25	50	2
13611	5129	2.47	-0.05	90	1	165341B				200	2
13974	5640	4.32	-0.46	200	1	88230	4043	4.02	-0.29	200	2
13994	4974	2.44	-0.11	430	1	201091	4310	4.14	-0.36	150	2
14214	5984	4.06	0.05	0	1	16160	4831	4.24		125	2
14386				0	1	178248				700	2
16160	4831	4.24		83	1	109379	5145	2.56	-0.01	0	2
16901	5624	1.42	0.0	150	1	13480	5070			800	2
17361	4768	2.54	0.19	0	1	36079	5209	2.45	-0.25	0	2
17506	4308	1.0	-0.15	21	1	13994	4974	2.44	-0.11	430	2
17878	5059	2.97	-0.19	0	1	148856	5080	2.71	-0.13	0	2

Continued on next page

(Continued)

Target (HD)	$T_{\rm eff}$ (K)	$\log g$	[Fe/H]	EW(He) (mÅ)	Ref	Target (HD)	$T_{\rm eff}$ (K)	$\log g$	[Fe/H]	EW(He) (mÅ)	Ref
17925	5069	4.41	0.12	200	1	203387	5157	3.17	-0.09	650	2
18449	4500	2.65	-0.07	0	1	3546	5109	2.83	-0.5	0	2
18884	3867	1.15	-0.22	0	1	148387	5055	2.82	-0.04	0	2
18925	5170	2.83	-0.19	30	1	180711	4870	2.76	-0.23	0	2
19356	12800			724	1	28307	5080	3.21	0.14	300	2
19373	5901	4.06	0.04	0	1	3712	4666	1.96	-0.1	25	2
19476	4941	3.08	0.1	63	1	95689	4660	2.46	-0.2	0	2
19656	4717	2.35	0.05	0	1	197989	4775	2.65	-0.26	0	2
19787	4940	3.05	0.16	0	1	27696	6668			220	2
20468	4359	1.4	-0.04	200	1	4128	4848	2.25	0.05	455	2
20630	5605	4.4	0.04	223	1	62509	4835	2.93	0.04	0	2
20797				0	1	27371	5038	3.016	0.16	0	2
20902	6582	1.85	0.22	0	1	25604	4818	2.73	0.07	150	2
21120	5094	2.43	-0.13	15	1	129989	4800	2.2	0.36	0	2
21242	5041	3.0		336	1	124897	4251	1.72	-0.6	0	2
22049	5020	4.62	0.02	187	1	12929	4643	2.78	-0.26	0	2
22468	4232	1.47	-0.97	166	1	168723	4904	3.06	-0.33	0	2
23249	4949	3.62	0.09	150	1	140573	4540	2.61	0.16	0	2
23302	8000	4.0		0	1	81797	4395	2.09	-0.11	25	2
23630	13490	4.0		0	1	31398	4207	1.33	0.1	90	2
24398	22040			0	1	131873	3992	1.32	-0.23	0	2
24760	27160			0	1	50778	4081	1.7	-0.22	50	2
25025	3811	1.0		0	1	29139	3885	1.3	-0.28	0	2
25604	4818	2.73	0.07	150	1	164058	3965	1.41	-0.15	0	2
25998	6147	4.35	-0.11	250	1	187929	5508	1.8	0.08	68	2
26574	6963	3.39		300	1	54605	6476	0.89	0.28	0	2
26630	5351	1.23	-0.04	17	1	31910	5502	1.57	-0.01	1400	2
26690	6820	3.92		275	1	204867	5465	1.08	-0.02	0	2
26722	5186	2.79	-0.04	0	1	209750	5232	1.1	0.03	75	2
26965	5568	4.75	-0.54	38	1	159181	5234	1.48	-0.04	800	2
27022	5314	2.92	-0.01	240	1	204075	5428	2.37	0.18	280	2
27371	5038	3.016	0.16	0	1	206859	4921	1.42	-0.01	75	2

Continued on next page

(Continued)

Target (HD)	$T_{\rm eff}$ (K)	$\log g$	[Fe/H]	EW(He) (mÅ)	Ref	Target (HD)	$T_{\rm eff}$ (K)	$\log g$	[Fe/H]	EW(He) (mÅ)	Ref
27697	4871	2.71	0.1	220	1	218356	4539	1.76	-0.05	1115	2
28100	5060	2.89	-0.01	350	1	48329	4525	0.75	0.16	100	2
28305	5016	2.97	0.1	200	1	206778	4276	1.17	0.21	225	2
28307	5080	3.21	0.14	300	1	200905	4005	1.25	0.12	150	2
28319	7950	3.7	0.01	200	1	3712	4666	1.96	-0.1	235	4
29094	4260	2.21	-0.29	137	1	62509	4835	2.93	0.04	135	4
29139	3885	1.3	-0.28	0	1	81797	4395	2.09	-0.11	115	4
29317	4640	2.49	-0.21	400	1	95689	4660	2.46	-0.2	122	4
30504	4102	1.12	-0.3	0	1	156283	4334	1.74	0.06	165	4
30652	6420	4.24	-0.02	150	1	HR7417	4270	1.79	-0.17	133	4
31398	4207	1.33	0.1	65	1	BD+41 395				198	4
31767	4367	1.41	0.08	50	1	206778	4276	1.17	0.21	163	4
31910	5502	1.57	-0.01	1435	1	210475				515	4
31964	7175	0.5	-0.05	0	1	39801	3633	0.4	0.01	0	4
32008	5235	3.21	-0.25	280	1	89758	3700	1.35	0.0	nan	4
32068	3920	1.33	-0.26	15	1	HR6134				0	4
32147	4687	4.25	0.25	0	1	156014J				16	4
32357				455	1	20902	6582	1.85	0.22	91	4
32887	4243	1.88	-0.24	60	1	61421	6623	3.94	-0.1	133	4
33856	4599	2.34	0.22	150	1	159181	5234	1.48	-0.04	1255	4
33904	12600	3.5	-0.39	0	1	204867	5465	1.08	-0.02	50	4
34029	5272	3.15	0.18	700	1	4128	4848	2.25	0.05	890	5
34085	12100	1.75		990	1	7672	5044	3.05	-0.38	880	5
34334	4308	1.87	-0.4	100	1	17433				400	5
35296	6171	4.31	0.01	250	1	21242	5041	3.0		240	5
35411	18197	4.0		0	1	22049	5020	4.62	0.02	310	5
35468	21700	4.0		140	1	22468	4232	1.47	-0.97	90	5
36079	5209	2.45	-0.25	0	1	34029	5272	3.15	0.18	630	5
36389	3706	0.7	0.11	0	1	62044	4500	2.4	-0.02	1110	5
36486				0	1	98230	5692	4.46	-0.35	380	5
36861	34000	3.82		150	1	118216	6531	3.69	-0.27	190	5
37043	32200			50	1	146361	5904			320	5

Continued on next page

(Continued)

Target (HD)	$T_{\rm eff}$ (K)	$\log g$	[Fe/H]	EW(He) (mÅ)	Ref	Target (HD)	$T_{\rm eff}$ (K)	$\log g$	[Fe/H]	EW(He) (mÅ)	Ref
37128	27000	2.85		0	1	210334	5386			760	5
37160	4734	2.64	-0.58	0	1	222107	4510	2.66	-0.63	1010	5
38393	6306	4.21	-0.12	100	1	224085				300	5
39003	4642	2.45	-0.1	50	1	BD +01 3070	5130	3.1	-1.85	146	6
39400	4356	1.37	-0.18	150	1	BD +05 3098	4930	1.3	-2.74	52	6
39587	5935	4.52	0.0	275	1	BD +09 2574	4860			56	6
39801	3633	0.4	0.01	15	1	BD +09 2860	5240	2.98	-1.99	38	6
40035	4786	2.7	-0.15	0	1	BD +09 2870	4600	1.4	-2.37	16	6
40239	3736			50	1	BD +09 3223	5310	2.0	-2.26	26	6
41116	5220	3.03	0.04	0	1	BD +10 2495	4920	1.85	-2.16	25	6
41597	4542	1.92	-0.65	75	1	BD +11 2998	5360	2.0	-1.38	54	6
43232	4270	2.22	-0.18	80	1	BD +12 2547	4610	1.5	-2.07	9	6
44478	3926	1.0	0.0	0	1	BD +17 3248	5250	2.3	-2.02	45	6
44537	3055		0.08	0	1	BD +18 2757	4840	1.5	-2.19	86	6
47731	4900	1.7	0.12	100	1	BD +18 2976	4550			17	6
48329	4525	0.75	0.16	106	1	BD +30 2611	4275	0.8	-1.49	93	6
48432	4891	2.83	-0.11	60	1	233891	4750	1.6	-1.58	0	6
48433	4493	2.06	-0.28	0	1	233666	5300	2.5	-1.65	45	6
48737	6478			280	1	237846	4950	2.2	-2.45	37	6
48915	9880	4.4	0.5	0	1	BD -03 5215	5420	2.3	-1.57	232	6
50877	3900	0.65	-0.32	0	1	CD -30 8626	5000	1.21	-1.91	26	6
52497	5090			250	1	83212	4543	1.17	-1.504	-44	6
53791				0	1	93529	4650	1.7	-1.67	40	6
54131	4737	2.37	-0.18	50	1	101063	5070	3.21	-1.09	68	6
54605	6476	0.89	0.28	0	1	104207	3916	0.6	-1.93	24	6
54716	4020	1.88	-0.26	0	1	105546	5300	2.5	-1.27	32	6
58207	4831	2.7	-0.18	0	1	107752	4750	0.8	-2.6	72	6
59294	4400	1.8	0.12	70	1	108317	5310	2.77	-2.35	23	6
59686	4740	2.54	0.28	0	1	108577	4975	1.7	-2.28	21	6
59693	5719	1.55	-0.39	12	1	110184	4250	0.3	-2.56	0	6
60178	8842	4.25	0.45	0	1	110885	5330	2.54	-1.44	14	6
60414				0	1	111721	5080	2.56	-1.3	48	6

Continued on next page

(Continued)

Target (HD)	$T_{\rm eff}$ (K)	$\log g$	[Fe/H]	EW(He) (mÅ)	Ref	Target (HD)	$T_{\rm eff}$ (K)	$\log g$	[Fe/H]	EW(He) (mÅ)	Ref
61241				0	1	113002	5007	2.53	-1.08	30	6
62044	4500	2.4	-0.02	1256	1	115444	4721	1.74	-2.71	33	6
62509	4835	2.93	0.04	0	1	119516	5440	1.73	-2.16	466	6
63700	4925	1.19	0.13	0	1	121135	4934	1.91	-1.37	63	6
65626	5792			230	1	122956	4600	1.5	-1.78	84	6
65695	4568	2.4	-0.25	0	1	126587	4960	1.9	-3.01	21	6
67594	5290	1.78	0.13	100	1	126778	4847	2.34	-0.61	34	6
69267	4087	1.45	-0.07	0	1	135148	4275	0.8	-1.9	2390	6
72905	5814	4.55	-0.06	175	1	141531	4340	1.11	-1.62	-13	6
73108	4430	2.08	-0.38	50	1	161770	5406	2.68	-1.84	30	6
73593	4755	2.62	-0.23	30	1	195636	5370	3.4	-2.86	314	6
74395	5257	1.68	-0.07	0	1	103036	4350	0.6	-1.9	0	6
74442	4722	2.57	0.0	0	1	LEID 31095	4658	1.55	-1.76	57	8
74485	5016	2.8	-0.08	690	1	LEID 31152	4637	1.55	-1.74	171	8
74739	5028	2.4	0.25	0	1	LEID 35228	4563	1.4	-1.87	18	8
75732	5211	4.28	0.35	50	1	LEID 38269	4607		-1.16	4	8
77137	6881	4.63		240	1	LEID 41236	4607		-1.5	124	8
78418	5625	3.98	-0.26	0	1	LEID 43010	4592	1.4	-1.85	15	8
79028	5973	4.13	0.05	0	1	LEID 54018	4565	1.6	-1.5	196	8
80493	3882	1.5	-0.26	0	1	LEID 54064	4741	1.6	-1.86	9	8
81797	4395	2.09	-0.11	25	1	LEID 54084	4745	1.6	-1.79	90	8
81799	4490	2.43	-0.01	400	1	LEID 55056	4769	1.7	-1.76	12	8
82210	5299	3.49	-0.21	200	1	LEID 58030	4650		-1.87	20	8
82635	5023	2.8	-0.15	300	1	LEID 63027	4675	1.5	-1.79	14	8
82885	5438	4.34	0.33	116	1	P48889	3843	0.52	-1.22	1	7
83618	4275	1.96	-0.07	0	1	P46422	3843	0.42	-1.08	0	7
84441	5385	2.18	-0.09	256	1	BD +44 493	5510	3.7	-3.68	31	9
85127				233	1	G 64-37	6432	4.24	-3.08	42	9
86146	6391	3.98	-0.32	0	1	BD -18 5550	4750	1.4	-3.06	44	9
87901	11962	3.56		0	1	115444	4721	1.74	-2.71	16	9
88084	5694	4.232	-0.13	200	1	122563	4572	1.36	-2.61	nan	9
88230	4043	4.02	-0.29	200	1	BD +23 3130	5000	2.2	-2.6	44	9

Continued on next page

(Continued)

Target (HD)	$T_{\rm eff}$ (K)	$\log g$	[Fe/H]	EW(He) (mÅ)	Ref	Target (HD)	$T_{\rm eff}$ (K)	$\log g$	[Fe/H]	EW(He) (mÅ)	Ref
89484	4428	1.97	-0.41	36	1	140283	5788	3.56	-2.393	32	9
89485	4454	1.91	-0.42	0	1	108317	5310	2.77	-2.35	38	9
90250	4808	2.55	0.17	100	1	BD +26 2606	5875	4.1	-2.3	26	9
90537	4926	2.85	0.09	50	1	19445	6130	4.39	-2.05	30	9
92125	5468	2.22	0.03	360	1	204543	4672	1.49	-1.72	nan	9
94264	4733	2.73	-0.11	35	1	G 29-23	6194	4.04	-1.69	39	9
95272	4621	2.44	-0.11	0	1	G 18-39	6093	4.19	-1.46	28	9
95418	9620	3.89	0.249	0	1	219617(NE)	5825	4.3	-1.4	25	9
95689	4660	2.46	-0.2	0	1	219617(SW)	5825	4.3	-1.4	23	9
95735	3574	4.73	-0.93	0	1	121135	4934	1.91	-1.37	nan	9
98230	5692	4.46	-0.35	200	1	166161	5350	2.56	-1.22	70	9
98262	4133	1.65	-0.17	233	1	194598	5998	4.33	-1.148	30	9
98430	4603	2.4	-0.48	0	1	193901	5721	4.42	-1.109	40	9
99167	4010	1.3	-0.29	0	1	201891	5900	4.19	-1.1	26	9
101501	5335	4.34	-0.07	100	1	148816	5876	4.16	-0.79	30	9
102509	5102	2.89	-0.64	300	1	224930	5275	4.1	-0.9	33	9
103095	5203	4.72	-1.27	100	1	6582	5331	4.54	-0.81	37	9
103578	8509	3.8	-0.19	0	1	Arcturus	4281	1.72	-0.55	nan	9
105707	4475	2.3	-0.18	0	1	142373	5776	3.83	-0.51	45	9
106365			-0.16	40	1	165908	6183	4.35	-0.46	36	9
106677				300	1	10700	5590	4.75	-0.47	36	9
107325	4742	3.1	0.16	0	1	15096	5375	4.3	-0.2	35	9
107383	4670	2.38	-0.51	0	1	131156	5410	4.48	-0.05	291	9
108123	4635	2.14	0.16	0	1	141004	5877	4.11	-0.01	70	9
108225	4969	2.71	0.04	75	1	196755	5750	3.83	0.09	95	9
108381	4979	2.71	0.08	0	1	161797	5580	3.99	0.29	80	9
109370				0	1	182572	5566	4.11	0.33	38	9
109551	4210	2.2	-0.21	25	1	Sun	5780	4.44	0.0	58	9
109822				0	1	3179	5300	2.6	-1.0	45	10
110379	6857	4.14	-0.19	90	1	3567	6035	4.08	-1.3	15	10
110646	5029	2.9	-0.45	0	1	7424	5727	4.5	-0.5	60	10
111028	4834	3.1	-0.04	0	1	16031	6100	4.2	-1.7	16	10

Continued on next page

(Continued)

Target (HD)	$T_{\rm eff}$ (K)	$\log g$	[Fe/H]	EW(He) (mÅ)	Ref	Target (HD)	$T_{\rm eff}$ (K)	$\log g$	[Fe/H]	EW(He) (mÅ)	Ref
112185	10080	3.5	0.0	0	1	23439B	4950	4.71	-1.1	31	10
112300	3650	0.8	0.18	0	1	25329	4741	4.68	-1.7	67	10
112413	11658	3.78	0.68	0	1	31128	5909	4.9	-1.6	37	10
113226	5043	2.82	0.13	0	1	59374	5800	4.4	-0.9	38	10
114378	6365	4.19	-0.23	200	1	59984	5900	4.18	-0.7	22	10
114519				200	1	64090	5530	4.7	-1.5	19	10
114710	5976	4.35	0.02	50	1	64606	5250	4.4	-0.9	14	10
115043	5860		-0.03	0	1	74000	6025	4.1	-2.1	14	10
115383	6087	4.42	0.13	130	1	76932	5840	4.0	-0.9	21	10
115404	4901	4.43	-0.17	150	1	84937	6357	4.14	-2.1	27	10
115659	5136	2.79	0.18	0	1	94028	6049	4.31	-1.3	35	10
117287				0	1	97916	6450	4.2	-0.9	40	10
118216	6531	3.69	-0.27	0	1	103095	5203	4.72	-1.27	56	10
119228	3684	1.02	0.0	0	1	188510	5495	4.1	-1.7	13	10
120164	4900	2.77	-0.08	0	1	194598	5998	4.33	-1.148	27	10
120709	18000	3.7	0.53	150	1	201889	5500	3.9	-1.0	37	10
121370	6121	3.88	0.31	0	1	201891-1			-1.0	17	10
123139	5040	2.93	0.04	0	1	201891-2				27	10
124294	4235	1.83	-0.43	0	1	221337			-0.8	39	10
124897	4251	1.72	-0.6	0	1	I-12				15	11
125161	7691			0	1	I-18				81	11
125351	4688	2.4	-0.03	0	1	II-41				118	11
126868	5651	3.63	-0.06	200	1	IV-19				117	11
127665	4258	1.85	-0.13	0	1	A1				34	11
129312	4993	2.53	0.01	290	1	J3				34	11
129336	4973	2.81	-0.19	0	1	X24				nan	11
129972	4976	2.69	-0.01	0	1	CD-30 1121	4955	2.07	-1.919	59	12
129989	4800	2.2	0.36	0	1	CD-62 1346	5524	2.16	-1.399	50	12
131156	5410	4.48	-0.05	175	1	110621	6212	4.04	-1.522	nan	12
131873	3992	1.32	-0.23	0	1	111721	5080	2.56	-1.3	41	12
131977	4772	4.38	-0.12	0	1	13979	5023	1.47	-2.441	nan	12
133208	5071	2.59	-0.08	0	1	181007	4979	2.23	-1.721	43	12

Continued on next page

(Continued)

Target (HD)	$T_{\rm eff}$ (K)	$\log g$	[Fe/H]	EW(He) (mÅ)	Ref	Target (HD)	$T_{\rm eff}$ (K)	$\log g$	[Fe/H]	EW(He) (mÅ)	Ref
133640	5800	4.15	-0.25	0	1	181743	5998	4.26	-1.795	nan	12
135722	4861	2.63	-0.37	0	1	186478	4568	0.88	-2.5	nan	12
137107	6026	4.38	-0.08	0	1	188031	6288	4.24	-1.649	11	12
137759	4527	2.58	-0.05	45	1	193242	5031	2.35	-1.778	49	12
137909	8620	3.96	1.0	0	1	208069	5065	2.47	-1.741	50	12
138905	4762	2.59	-0.37	20	1	21022	4524	0.89	-2.204	nan	12
139087				190	1	215601	4972	1.67	-1.46	nan	12
140573	4540	2.61	0.16	0	1	215801	6065	3.69	-2.183	11	12
141004	5877	4.11	-0.01	50	1	BD+02 3375	6009	4.01	-2.19	23	12
141527	7048	1.38	0.77	0	1	CD-61 0282	5815	4.3	-1.234	22	12
141714	5362	3.29	-0.12	680	1	113083	5800	4.35	-0.93	nan	12
142373	5776	3.83	-0.51	0	1	121004	5651	4.31	-0.784	13	12
142574				0	1	140283	5788	3.56	-2.393	10	12
142908	7038	3.98	-0.02	0	1	148816	5876	4.16	-0.79	23	12
142980	4523	2.69	-0.01	200	1	193901	5721	4.42	-1.109	32	12
143107	4436	1.94	-0.22	460	1	194598	5998	4.33	-1.148	34	12
143333	6373	4.44	-0.01	440	1	3567	6035	4.08	-1.3	31	12
143761	5745	3.99	-0.3	50	1	84937	6357	4.14	-2.1	25	12
144284	6309	4.13	0.2	100	1	102200	6113	4.15	-1.222	26	12
145328	4843	3.03	0.01	0	1	116064	6010	4.16	-1.848	nan	12
146051	3783	1.45	-0.03	0	1	128279	5245	2.79	-2.123	52	12
146361	5904			300	1	134439	4956	4.6	-1.44	nan	12
146364				300	1	134440	4795	4.6	-1.426	nan	12
146791	4940	2.64	-0.04	0	1	142948	5024	2.52	-0.72	17	12
148349				0	1	145417	4900	4.6	-1.349	54	12
148387	5055	2.82	-0.04	0	1	151559	5167	2.54	-0.769	46	12
148478				0	1	17072	5398	2.37	-1.128	nan	12
148786	5110	2.69	0.17	0	1	184266	5908	2.2	-1.463	302	12
148856	5080	2.71	-0.13	0	1	190287	5108	2.78	-1.429	50	12
148897	4285	0.6	-1.02	0	1	199289	5842	4.27	-1.09	14	12
149661	5156	4.47	0.05	100	1	211998	5233	3.25	-1.519	nan	12
149757	32000	3.85		0	1	219617	5981	4.4	-1.427	nan	12

Continued on next page

(Continued)

Target (HD)	$T_{\rm eff}$ (K)	$\log g$	[Fe/H]	EW(He) (mÅ)	Ref	Target (HD)	$T_{\rm eff}$ (K)	$\log g$	[Fe/H]	EW(He) (mÅ)	Ref
150680	5792	3.79	0.03	0	1	221580	5245	2.3	-1.215	38	12
150997	5075	3.01	-0.23	0	1	222434	4517	1.21	-1.77	nan	12
153210	4529	2.5	-0.03	50	1	222925	5710	2.32	-1.371	215	12
156014	3271			0	1	23798	4396	0.64	-2.22	nan	12
156283	4334	1.74	0.06	0	1	26169	5010	2.06	-2.396	52	12
156681	4170	2.1	-0.21	0	1	83212	4543	1.17	-1.504	nan	12
157214	5718	4.15	-0.43	0	1	9051	4884	2.08	-1.652	46	12
157999	4080	1.52	-0.07	150	1	L1404	5570	2.68	-1.21	322	13
158512				50	1	L1407	5226	2.45	-1.25	88	13
159181	5234	1.48	-0.04	763	1	L1408	4394	1.4	-1.23	21	13
159532				0	1	L1617	4564	1.63	-1.28	54	13
160269	5902	4.42	-0.18	100	1	L1701	4503	1.6	-1.2	102	13
160346	4824	4.32	-0.04	100	1	L2413	5530	2.62	-1.27	232	13
160922	6595	4.19	-0.03	0	1	L2519	4333	1.41	-1.04	41	13
161096	4588	2.59	0.1	13	1	L3207	4646	1.73	-1.35	102	13
161797	5580	3.99	0.29	40	1	L3215	4699	1.88	-1.14	-54	13
162076	5106	3.32	0.0	630	1	L3310	5616	2.68	-1.16	345	13
163506	6675	1.01	-0.25	0	1	L3503	5252	2.52	-1.16	-69	13
163700				270	1	L4206	4623	2.17	-1.11	80	13
163770	4255	1.25	-0.11	-250	1	L4406	5477	2.62	-1.24	357	13
163930				200	1	L4412	5607	2.67	-1.2	225	13
163993	5082	3.18	0.02	430	1	L4413	4603	2.0	-1.22	88	13
164058	3965	1.41	-0.15	0	1	L4415	4438	1.8	-1.1	11	13
164259	6897	4.1	-0.1	200	1	49933	6631	4.25	-0.45	nan	14
164349	4623	1.76	-0.01	0	1	29992	6666	3.63		364	14
164764				300	1	219693	6606	4.06	0.0	260	14
165341	5215	4.5	0.04	240	1	32743	6698	4.25	0.15	184	14
165760	5080	3.0	0.1	0	1	104731	6618	4.1	-0.11	nan	14
166207				0	1	3302	6503	4.03	0.04	305	14
166208	5095	3.0	0.05	350	1	77370	6699	4.18	0.93	nan	14
168723	4904	3.06	-0.33	0	1	68456	6523	4.14	-0.23	nan	14
169305				0	1	30652	6477	4.29	0.0	188	14

Continued on next page

(Continued)

Target (HD)	$T_{\rm eff}$ (K)	$\log g$	[Fe/H]	EW(He) (mÅ)	Ref	Target (HD)	$T_{\rm eff}$ (K)	$\log g$	[Fe/H]	EW(He) (mÅ)	Ref
170153	5861	4.05	-0.62	0	1	88697	6666			nan	14
170829	5425	4.0	0.15	50	1	76653	6422	4.32	0.12	nan	14
171443	4263	2.21	0.01	150	1	201647	6538	4.21		175	14
171779	4726	2.31	-0.12	160	1	79940	6367	3.42	-0.14	nan	14
172167	9550	4.05	-0.7	0	1	37495	6417	3.79	-0.09	290	14
172764				465	1	219482	6249	4.36	-0.21	318	14
173399				750	1	33262	6147	4.44	-0.17	317	14
173667	6436	3.95	-0.11	50	1	189245	6312	4.35	-0.32	410	14
173819	4456	1.14	-0.24	66	1	199260	6284	4.34	-0.06	294	14
174974	4702	0.92	0.09	-800	1	25329	4893	4.8	-1.6	43	15
175190	4516	1.03	-0.13	-100	1	79210	3829	4.04	-0.65	279	15
175225	5279	3.78	0.14	100	1	84737	5960	4.24	0.17	31	15
175306	4355	1.84	-0.64	580	1	88230	3970	4.51	0.28	325	15
175775	4595	2.4	-0.01	0	1	GJ 412A	3636	4.91	-0.29	139	15
176411	4688	2.7	0.0	275	1	102870	6146	4.06	0.15	75	15
176670	4220	2.21	-0.03	50	1	131156A	5570	4.65	-0.04	330	15
176678	4690	2.95	0.02	25	1	131156B	4767	5.0	-0.02	296	15
178428	5656	4.2	0.15	700	1	GJ 1101	3400	5.5		93	15
178596	7149	4.11	-0.04	0	1	GJ 1154	3277		0.34	66	15
179094				900	1	NLTT 35712	3500	5.5		67	15
180711	4870	2.76	-0.23	0	1	Gl 2	3675	4.84	-0.16	225	16
180809	4500	1.6	0.28	125	1	Gl 15A	3615	4.91	-0.25	105	16
181391	4932	3.2	-0.21	200	1	Gl 15B	3291	5.11	-0.19	25	16
183439	3847	1.4	-0.38	0	1	GJ 1012	3398	4.98	0.07	75	16
183912	4270	1.79	-0.17	40	1	Gl 26	3537	4.89	-0.05	139	16
185758	5503	2.99	-0.1	75	1	G 172-030	3426	4.99	-0.06	118	16
186408	5731	4.18	0.09	0	1	Gl 47	3529	4.94	-0.16	133	16
186427	5678	4.24	0.01	70	1	Gl 48	3488	4.91	0.02	181	16
186791	4197	1.26	0.01	-180	1	Gl 49	3805	4.69	0.13	236	16
187013	6262	4.06	0.03	0	1	GJ 1028	3154	5.14	-0.02	17	16
187691	6108	4.17	0.06	50	1	Gl 70	3532	4.91	-0.09	139	16
187796				0	1	GJ 3117A	3555	4.9	-0.08	199	16

Continued on next page

(Continued)

Target (HD)	$T_{\rm eff}$ (K)	$\log g$	[Fe/H]	EW(He) (mÅ)	Ref	Target (HD)	$T_{\rm eff}$ (K)	$\log g$	[Fe/H]	EW(He) (mÅ)	Ref
187929	5508	1.8	0.08	0	1	GJ 3126	3489	4.93	-0.05	134	16
188119	4995	2.64	-0.48	0	1	Gl 87	3663	4.81	-0.05	96	16
190007	4554	4.26	0.12	200	1	Gl 96	3935	4.67	0.07	234	16
191026	5116	3.73	0.0	215	1	Gl 104	3585	4.89	-0.13	193	16
192713	5088	1.71	0.31	0	1	Gl 105B	3327	5.03	0.05	62	16
192876	5251	1.89	0.22	0	1	Gl 109	3472	4.95	-0.06	106	16
194093	5939	0.63	0.04	0	1	Gl 119A	3896	4.66	0.18	199	16
195564	5631	3.99	0.05	0	1	Gl 134	3861	4.66	0.2	211	16
197345	8700	1.2	0.23	0	1	Gl 133	3549	4.93	-0.18	138	16
197912	4677	2.5	-0.24	220	1	Gl 154	3993	4.65	0.12	243	16
197963	4757	2.98	0.14	90	1	K2-155	3940	4.76	-0.33	63	16
197989	4775	2.65	-0.26	0	1	Gl 169	4199	4.59	0.23	221	16
198149	4943	3.27	-0.27	0	1	Gl 173	3621	4.85	-0.07	127	16
200905	4005	1.25	0.12	150	1	2MASS J04425586+2128230	3437	4.97	-0.03	118	16
201091	4310	4.14	-0.36	211	1	Gl 179	3393	5.0	0.01	115	16
201092	3942	4.04	-0.65	153	1	Gl 180	3572	4.9	-0.12	119	16
201745				50	1	Gl 181	4022	4.65	0.09	257	16
202109	5027	2.66	-0.08	66	1	GJ 3325	3409	5.02	-0.11	50	16
203387	5157	3.17	-0.09	650	1	Gl 192	3582	4.9	-0.13	123	16
203504	4612	2.56	-0.04	0	1	Gl 203	3362	5.03	-0.05	32	16
204075	5428	2.37	0.18	280	1	Gl 205	3891	4.64	0.23	235	16
204867	5465	1.08	-0.02	0	1	GJ 3357	3380	4.99	0.08	69	16
205512	4700	2.55	-0.11	150	1	Gl 212	3875	4.69	0.08	229	16
206088	7095	3.45	0.29	0	1	Gl 213	3311	5.05	0.01	37	16
206301	5682	3.98	-0.04	100	1	Gl 226	3521	4.92	-0.11	135	16
206778	4276	1.17	0.21	56	1	Gl 229A	3837	4.7	0.07	225	16
206859	4921	1.42	-0.01	75	1	Gl 232	3237	5.11	-0.07	13	16
206901	6579	3.99	-0.37	120	1	Gl 239	3737	4.89	-0.42	158	16
206936				200	1	GJ 3404A	3454	4.95	0.0	97	16
207089	4482	1.24	0.14	-820	1	Gl 258	3461	4.95	-0.04	141	16
207130	4789	2.8	0.04	60	1	Gl 273	3365	5.01	0.02	73	16
207757				-500	1	GJ 3452	3520	4.94	-0.16	80	16

Continued on next page

(Continued)

Target (HD)	$T_{\rm eff}$ (K)	$\log g$	[Fe/H]	EW(He) (mÅ)	Ref	Target (HD)	$T_{\rm eff}$ (K)	$\log g$	[Fe/H]	EW(He) (mÅ)	Ref
207760	6884			200	1	GJ 3459	3426	5.0	-0.1	62	16
208606	4731	1.18	0.25	25	1	Gl 281	4014	4.66	0.07	234	16
208816	3480	0.0	0.16	50	1	GJ 1105	3367	5.02	-0.01	57	16
209750	5232	1.1	0.03	100	1	Gl 300	3342	5.01	0.11	24	16
210027	6504	3.96	-0.22	110	1	GJ 2066	3568	4.89	-0.1	156	16
210334	5386			650	1	LSPM J0840+3127	3393	5.01	-0.01	93	16
210434	4949	3.0	0.09	270	1	Gl 317	3432	4.95	0.08	126	16
210460	5478	3.53	-0.38	370	1	Gl 338A	4024	4.68	-0.05	240	16
210745	4337	1.12	0.17	0	1	Gl 357	3505	4.94	-0.12	39	16
212943	4603	2.56	-0.45	50	1	Gl 361	3613	4.87	-0.11	174	16
213310				0	1	GJ 1129	3362	5.02	0.03	39	16
213389				400	1	Gl 366	3680	4.78	-0.01	126	16
214680	33690	4.27		0	1	Gl 369	3777	4.76	-0.07	183	16
215665	4866	2.24	-0.11	0	1	Gl 378	3785	4.72	0.05	186	16
216131	5068	3.04	-0.1	50	1	Gl 382	3610	4.87	-0.13	221	16
216228	4794	2.76	-0.09	0	1	LP 092-048	3406	5.0	-0.05	64	16
216286				0	1	Gl 386	3532	4.88	0.01	144	16
216380				430	1	Gl 390	3780	4.72	0.06	207	16
216385	6241	3.85	-0.29	100	1	Gl 393	3579	4.88	-0.09	158	16
216489	4796	2.87	-0.11	1012	1	Gl 399	3554	4.88	-0.02	139	16
216946	4021	0.15	-0.03	-50	1	Gl 402	3345	5.03	0.01	77	16
217476	5137	1.52	-1.5	-650	1	Gl 408	3499	4.94	-0.11	122	16
217906	3864	1.0	-0.11	0	1	Gl 411	3601	4.87	-0.09	61	16
218356	4539	1.76	-0.05	1100	1	LP 672-042	3422	4.98	-0.01	87	16
218594	4435	2.15	-0.2	50	1	GJ 1148	3375	4.99	0.09	87	16
218658	5226	3.05	0.29	450	1	Gl 436	3505	4.91	-0.04	95	16
218935	4927	3.07	-0.09	75	1	Gl 445	3369	5.02	0.0	42	16
219113	4829			600	1	Gl 447	3264	5.09	-0.04	33	16
219134	4735	4.36	0.09	70	1	Gl 450	3645	4.87	-0.17	184	16
219615	4920	2.73	-0.63	0	1	GJ 3704	3338	5.02	0.1	77	16
220321	4655	2.65	-0.26	0	1	GJ 3707	3375	4.98	0.17	101	16
220954	4767	2.73	-0.01	0	1	GJ 3708A	3471	4.95	-0.06	94	16

Continued on next page

(Continued)

Target (HD)	$T_{\rm eff}$ (K)	$\log g$	[Fe/H]	EW(He) (mÅ)	Ref	Target (HD)	$T_{\rm eff}$ (K)	$\log g$	[Fe/H]	EW(He) (mÅ)	Ref
221345	4620	2.33	-0.49	0	1	Gl 458A	3933	4.7	-0.03	193	16
221650				-2350	1	Gl 465	3485	4.98	-0.17	36	16
222107	4510	2.66	-0.63	780	1	Gl 471	3914	4.71	-0.07	200	16
222404	4758	3.14	0.0	10	1	Gl 476	3572	4.85	0.02	170	16
222800				-820	1	Gl 486	3389	5.0	0.03	46	16
223047	4834	1.35	-0.02	120	1	Gl 507.1	3812	4.67	0.18	207	16
223075	3036		-0.4	0	1	Gl 508.2	3763	4.73	0.03	173	16
223719	4082	1.31	-0.17	0	1	GJ 3779	3324	5.05	0.0	72	16
224014	6000	0.25	0.05	-150	1	Gl 512A	3482	4.92	0.01	147	16
224930	5275	4.1	-0.9	0	1	Gl 513	3449	4.93	0.09	138	16
20902	6582	1.85	0.22	45	3	Gl 514	3714	4.81	-0.15	172	16
34029	5272	3.15	0.18	500	3	Gl 525	3806	4.85	-0.43	127	16
48329	4525	0.75	0.16	239	3	Gl 526	3678	4.79	-0.04	149	16
61421	6623	3.94	-0.1	121	3	GJ 3804	3402	4.99	0.01	56	16
63700	4925	1.19	0.13	87	3	Gl 536	3724	4.77	-0.04	178	16
84441	5385	2.18	-0.09	360	3	Gl 549B	3521	4.91	-0.07	112	16
113226	5043	2.82	0.13	230	3	Gl 552	3671	4.76	0.06	168	16
121370	6121	3.88	0.31	135	3	Gl 553	4089	4.63	0.14	186	16
159181	5234	1.48	-0.04	1105	3	Gl 555	3337	5.01	0.12	70	16
194093	5939	0.63	0.04	50	3	GJ 3873	3379	5.0	0.06	107	16
204867	5465	1.08	-0.02	430	3	GJ 3885	3425	4.99	-0.06	124	16
3712	4666	1.96	-0.1	150	3	GJ 3892	3492	4.92	-0.01	121	16
4128	4848	2.25	0.05	429	3	Gl 581	3441	4.98	-0.08	58	16
12533	4248	1.03	0.0	200	3	Gl 592	3370	5.0	0.07	62	16
12929	4643	2.78	-0.26	148	3	Gl 606	3625	4.89	-0.19	216	16
17506	4308	1.0	-0.15	240	3	G 137-084	3450	4.98	-0.1	126	16
22049	5020	4.62	0.02	490	3	Gl 617B	3488	4.93	-0.03	170	16
31398	4207	1.33	0.1	-18	3	Gl 617A	4090	4.62	0.15	228	16
32068	3920	1.33	-0.26	220	3	Gl 628	3389	5.0	0.0	69	16
32887	4243	1.88	-0.24	64	3	GJ 1203	3487	4.91	0.01	86	16
62509	4835	2.93	0.04	128	3	GJ 3972	3506	4.92	-0.06	126	16
81797	4395	2.09	-0.11	145	3	Gl 649	3734	4.78	-0.08	205	16

Continued on next page

(Continued)

Target (HD)	$T_{\rm eff}$ (K)	$\log g$	[Fe/H]	EW(He) (mÅ)	Ref	Target (HD)	$T_{\rm eff}$ (K)	$\log g$	[Fe/H]	EW(He) (mÅ)	Ref
89484	4428	1.97	-0.41	106	3	GJ 3988	3243	5.08	0.05	51	16
95689	4660	2.46	-0.2	128	3	Gl 655	3486	4.94	-0.07	123	16
105707	4475	2.3	-0.18	185	3	GJ 3992	3426	4.97	0.01	97	16
105841	6609			-42	3	GJ 2128	3543	4.91	-0.1	83	16
123139	5040	2.93	0.04	160	3	Gl 678.1 A	3812	4.77	-0.15	185	16
127665	4258	1.85	-0.13	155	3	Gl 685	3893	4.69	0.06	206	16
129989	4800	2.2	0.36	180	3	Gl 686	3656	4.87	-0.23	98	16
131873	3992	1.32	-0.23	-35	3	GJ 1222	3322	5.02	0.12	77	16
137759	4527	2.58	-0.05	69	3	Gl 699	3273	5.11	-0.15	25	16
140573	4540	2.61	0.16	115	3	GJ 4040	3441	4.97	-0.04	149	16
151680	4560	2.49	-0.17	138	3	GJ 1223	3163	5.12	0.03	12	16
153210	4529	2.5	-0.03	123	3	Gl 701	3663	4.86	-0.2	308	16
156283	4334	1.74	0.06	140	3	G 140-051	3226	5.09	0.04	36	16
161096	4588	2.59	0.1	145	3	GJ 4048A	3440	4.98	-0.08	38	16
163770	4255	1.25	-0.11	300	3	Gl 710	4143	4.66	-0.11	214	16
164058	3965	1.41	-0.15	nan	3	Gl 712	3405	4.99	0.0	43	16
169916	4778	2.59	-0.11	100	3	GJ 1227	3219	5.11	-0.04	33	16
HR7417	4270	1.79	-0.17	135	3	GJ 4062	3413	5.01	-0.07	124	16
186791	4197	1.26	1.63	nan	3	GJ 4063	3400	4.97	0.11	163	16
197989	4775	2.65	-0.26	130	3	Gl 720A	3932	4.68	0.06	167	16
200905	4005	1.25	0.12	408	3	Gl 724	3812	4.7	0.08	209	16
206778	4276	1.17	0.21	147	3	GJ 4070	3471	4.96	-0.1	72	16
210745	4337	1.12	0.17	-121	3	GJ 4077	3496	4.94	-0.11	117	16
6860	3762	1.07	-0.49	70	3	Gl 745A	3536	4.94	-0.2	21	16
14386				200	3	Gl 745B	3526	4.96	-0.23	24	16
18884	3867	1.15	-0.22	30	3	GJ 4098	3454	4.96	-0.03	82	16
19058	3500	0.8	-0.15	0	3	GJ 1232	3259	5.08	0.02	28	16
39801	3633	0.4	0.01	20	3	Gl 752A	3534	4.9	-0.04	174	16
40239	3736			0	3	Gl 763	4062	4.69	-0.17	215	16
42995	3600	1.5	0.04	-30	3	Gl 793	3471	4.96	-0.1	151	16
89758	3700	1.35	0.0	nan	3	Gl 806	3586	4.89	-0.15	132	16
97778	3734			-55	3	LP 816-060	3321	5.05	-0.02	69	16

Continued on next page

(Continued)

Target (HD)	$T_{\rm eff}$ (K)	$\log g$	[Fe/H]	EW(He) (mÅ)	Ref	Target (HD)	$T_{\rm eff}$ (K)	$\log g$	[Fe/H]	EW(He) (mÅ)	Ref
112300	3650	0.8	0.18	0	3	Gl 809A	3843	4.71	0.04	183	16
133216				0	3	Gl 816	3507	4.92	-0.08	167	16
146051	3783	1.45	-0.03	0	3	LSPM J2116+0234	3485	4.94	-0.08	137	16
HR6134				0	3	TYC 2187-512-1	3705	4.83	-0.2	190	16
148783	3250	0.2	-0.01	0	3	GJ 4205	3497	4.91	0.0	140	16
156014	3271			-25	3	LSPM J2146+3813	3307	5.06	-0.03	21	16
217906	3864	1.0	-0.11	0	3	GJ 1263A	3352	5.03	0.02	61	16
137909	8620	3.96	1.0	0	2	G 264-012	3360	5.01	0.07	57	16
28052	7379			100	2	Gl 843	3422	4.99	-0.04	60	16
208294	5226	3.83		130	2	Gl 846	3915	4.69	0.03	237	16
112412	6462	4.3	-0.3	0	2	GJ 4258	3653	4.86	-0.17	176	16
110379	6857	4.14	-0.19	90	2	Gl 851	3550	4.93	-0.13	215	16
40136	6989	4.17	-0.1	100	2	GJ 9773	3501	4.92	-0.04	87	16
26690	6820	3.92		275	2	GJ 4276	3387	4.97	0.12	121	16
8723	6690	4.12		200	2	GJ 1270	3317	5.03	0.1	46	16
128167	6787	4.3	-0.4	50	2	Gl 875	3904	4.72	-0.1	193	16
105452	7049	4.11	-0.21	0	2	GJ 4306	3834	4.7	0.06	235	16
432	6792	3.59	-0.15	200	2	Gl 880	3805	4.69	0.12	224	16
129502	6763	4.36	-0.01	0	2	GJ 4333	3364	5.0	0.1	130	16
116568	6627	4.16	-0.23	0	2	Gl 895	3842	4.68	0.14	233	16
210027	6504	3.96	-0.22	11	2	Gl 899	3559	4.86	0.0	118	16
160922	6595	4.19	-0.03	0	2	GJ 4367	3347	5.02	0.05	99	16

Appendix B

List of parameters and measurements on the field-WD sample

This appendix lists the stellar parameters and measurement of 10 830 Å line strength, Ca II indices and fractional X-ray luminosity for the field-WD sample.

Table B.1: Target list of the field-WD sample with their stellar parameters. References: 1: Zhang & Zhao (2005), 2: Yong et al. (2013), 3: Cottaar et al. (2014), 4: Luck (2017), 5: Aguilera-Gómez et al. (2018), 6: Luck (2018), 7:Ahumada et al. (2020), 8: Adibekyan et al. (2012), 9: Heiter et al. (2015) and Jofré et al. (2014), 10: Kovtyukh et al. (2003), 11: Kovtyukh et al. (2004), 12: Kovtyukh et al. (2006), 13: Kovtyukh (2007)

Target	Obs. Date	Type	$T_{\rm eff}$ (K)	$\log g$	[Fe/H]	Ref
HD49933	2013.12.08	dwarf	6631	4.25	−0.45	6
PROCYON	2013.12.08	dwarf	6654	3.95	−0.04	4
δ Eri	2013.12.11	dwarf	4954	3.76	0.06	9
ϵ Eri	2013.12.23	dwarf	5076	4.61	−0.10	9
HD281159	2014.09.11	dwarf	6815	3.63		3
18Sco	2015.07.20	dwarf	5810	4.44	0.01	9
HD140283	2015.07.26	dwarf	5522	3.58	−2.43	9
HD219134	2015.10.25	dwarf	4900 ± 8	4.20	0.10	11
HD28343	2015.10.25	dwarf	4284 ± 20		0.39 ± 0.08	10
HD10476	2015.10.31	dwarf	5242 ± 3	4.30	0.00	11
HD101501	2016.01.26	dwarf	5558 ± 6	4.50	0.02	11
HD114710	2016.01.26	dwarf	5954 ± 7	4.30	0.12	11
HD143761	2016.01.26	dwarf	5865 ± 11	4.30	−0.06	11
HD117176	2016.01.26	dwarf	5611 ± 5	3.86 ± 0.10	-0.10 ± 0.05	10
HD115383	2016.01.26	dwarf	6012 ± 9	4.30	0.16	11
HD137107	2016.01.26	dwarf	6037 ± 7	4.30	0.05	11
HD102870	2016.01.27	dwarf	6055 ± 7	4.00	0.18	11
HD72905	2016.01.27	dwarf	5884 ± 7	4.40	−0.02	11
HD81809	2016.01.27	dwarf	5782 ± 7	3.99 ± 0.01	-0.28 ± 0.03	10

Continued on next page

(Continued)

Target	Obs. Date	Type	$T_{\rm eff}$ (K)	$\log g$	[Fe/H]	Ref
HD95128	2016.02.03	dwarf	5887 ± 4	4.30	0.06	11
HD122064	2016.02.03	dwarf	4937 ± 8	4.50	0.12	11
HD109358	2016.02.03	dwarf	5897 ± 6	4.20	−0.35	11
HD50281	2016.02.11	dwarf	4712 ± 8	3.90	−0.17	11
HD22879	2016.02.15	dwarf	5868	4.27	−0.88	9
HD19445	2016.02.17	dwarf	6052	4.49	−1.92	4
HD141004	2016.02.27	dwarf	5884 ± 4	4.10	0.03	11
HD84937	2016.02.27	dwarf	6383	4.48	−2.02	4
HD34411	2016.02.28	dwarf	5890 ± 4	4.20	0.15	11
HD19445	2016.02.28	dwarf	6052	4.49	−1.92	4
HD19445	2016.03.07	dwarf	6052	4.49	−1.92	4
HD19373	2016.03.11	dwarf	5963 ± 5	4.20	0.11	11
HD157214	2016.03.11	dwarf	5784 ± 10	4.40	−0.29	11
HD82106	2016.03.12	dwarf	4827 ± 6	4.10	−0.06	11
HD19445	2016.03.15	dwarf	6052	4.49	−1.92	4
HD39587	2016.03.17	dwarf	5955 ± 6	4.30	0.02	11
HD116443	2016.03.17	dwarf	4976 ± 10	4.00	−0.48	11
HD86728	2016.03.17	dwarf	5735 ± 6	4.20	0.22	11
etaBoo	2016.03.17	dwarf	6050	3.75	0.28	4
HD82885	2016.03.21	dwarf	5545 ± 8	4.30	0.30	11
HD89744	2016.04.20	dwarf	6207	3.92	0.17	4
HD157881	2016.04.24	dwarf	4035 ± 4	4.56 ± 0.10	-0.16 ± 0.08	10
HD136064	2016.04.26	dwarf	6144	3.98	0.00	4
σ Boo	2016.04.29	dwarf	6781	4.29	−0.36	4
HD79555	2016.05.01	dwarf	4803 ± 11	4.10	−0.14	11
γ Ser	2016.05.01	dwarf	6286	4.13	−0.12	4
HR3954	2016.05.01	dwarf	6500	3.87	0.23	5
HD99747	2016.05.02	dwarf	6676	4.15	−0.47	4
HD185144	2016.05.04	dwarf	5271 ± 6	4.20	−0.28	11
35LMi	2016.05.04	dwarf	6479	3.99	−0.26	5
ι Vir	2016.05.07	dwarf	6217	3.75	−0.06	4
HD103095	2016.05.13	dwarf	5178	4.72	−1.24	4
HE1346-0427	2017.02.13	dwarf	6255	4.47	−3.57	2
HD63685	2017.12.01	dwarf	5497 ± 62	4.05 ± 0.10	0.00 ± 0.05	8
HD76188	2017.12.01	dwarf	5989 ± 75	4.08 ± 0.11	-0.44 ± 0.06	8
HD42505	2017.12.02	dwarf	4738 ± 115	4.40 ± 0.25	-0.22 ± 0.07	8
HD16714	2017.12.02	dwarf	5518 ± 18	4.42 ± 0.03	-0.20 ± 0.01	8
HD222237	2017.12.02	dwarf	4780 ± 64	4.37 ± 0.14	-0.38 ± 0.04	8
HD17970	2017.12.02	dwarf	5040 ± 48	4.39 ± 0.08	-0.45 ± 0.04	8
HD1388	2017.12.02	dwarf	5954 ± 10	4.41 ± 0.02	-0.01 ± 0.01	8
HD23356	2017.12.02	dwarf	5004 ± 60	4.50 ± 0.11	-0.17 ± 0.03	8
HD219495	2017.12.02	dwarf	4787 ± 118	4.40 ± 0.25	0.13 ± 0.09	8
HD1461	2017.12.02	dwarf	5765 ± 18	4.38 ± 0.03	0.19 ± 0.01	8
HD21749	2017.12.02	dwarf	4723 ± 143	4.40 ± 0.33	-0.02 ± 0.08	8
HD224393	2017.12.02	dwarf	5774 ± 17	4.54 ± 0.04	-0.38 ± 0.01	8
HD21019	2017.12.02	dwarf	5468 ± 13	3.93 ± 0.02	-0.45 ± 0.01	8
HD55	2017.12.02	dwarf	4679 ± 76	4.51 ± 0.16	-0.66 ± 0.02	8
HD24633	2017.12.02	dwarf	5276 ± 73	4.36 ± 0.12	-0.04 ± 0.06	8
HD45289	2017.12.02	dwarf	5717 ± 18	4.32 ± 0.01	-0.02 ± 0.01	8
HD967	2017.12.02	dwarf	5564 ± 16	4.51 ± 0.03	-0.68 ± 0.01	8

Continued on next page

(Continued)

Target	Obs. Date	Type	$T_{\rm eff}$ (K)	$\log g$	[Fe/H]	Ref
HD59984	2017.12.02	dwarf	5962 ± 27	4.18 ± 0.02	-0.69 ± 0.02	8
HD69655	2017.12.03	dwarf	5961 ± 12	4.44 ± 0.03	-0.18 ± 0.01	8
HD25565	2017.12.03	dwarf	5212 ± 52	4.47 ± 0.09	0.03 ± 0.03	8
HD43197	2017.12.03	dwarf	5449 ± 73	4.30 ± 0.13	0.36 ± 0.06	8
HD26729	2017.12.03	dwarf	5718 ± 69	4.17 ± 0.11	0.31 ± 0.06	8
HD5349	2017.12.03	dwarf	5092 ± 94	3.88 ± 0.16	0.43 ± 0.08	8
HD11608	2017.12.03	dwarf	4959 ± 185	4.32 ± 0.37	0.22 ± 0.15	8
HD222335	2017.12.03	dwarf	5271 ± 34	4.49 ± 0.05	-0.20 ± 0.02	8
BD-140184	2017.12.03	dwarf	4714 ± 155	4.32 ± 0.29	-0.38 ± 0.12	8
HD4838	2017.12.03	dwarf	4704 ± 72	4.63 ± 0.17	-0.21 ± 0.06	8
HD10002	2017.12.03	dwarf	5313 ± 44	4.40 ± 0.07	0.17 ± 0.03	8
BD-130321	2017.12.03	dwarf	4772 ± 132	4.41 ± 0.28	0.02 ± 0.10	8
HD40865	2017.12.03	dwarf	5719 ± 16	4.50 ± 0.03	-0.38 ± 0.01	8
HD4597	2017.12.03	dwarf	6025 ± 67	4.43 ± 0.10	-0.39 ± 0.05	8
HD37986	2017.12.03	dwarf	5507 ± 38	4.29 ± 0.06	0.26 ± 0.03	8
HD38858	2017.12.03	dwarf	5733 ± 12	4.51 ± 0.01	-0.22 ± 0.01	8
HD33725	2017.12.03	dwarf	5274 ± 30	4.41 ± 0.05	-0.17 ± 0.02	8
HD56274	2017.12.03	dwarf	5734 ± 22	4.51 ± 0.03	-0.54 ± 0.02	8
HD72673	2017.12.03	dwarf	5243 ± 22	4.46 ± 0.04	-0.41 ± 0.01	8
HD73524	2017.12.03	dwarf	6017 ± 13	4.43 ± 0.03	0.16 ± 0.01	8
HD9246	2017.12.04	dwarf	4999 ± 40	4.49 ± 0.08	-0.53 ± 0.02	8
HD457	2017.12.04	dwarf	6089 ± 64	4.43 ± 0.10	0.34 ± 0.05	8
HD283	2017.12.04	dwarf	5157 ± 28	4.51 ± 0.05	-0.54 ± 0.02	8
HD8326	2017.12.04	dwarf	4971 ± 79	4.48 ± 0.15	0.02 ± 0.04	8
muLeo	2013.02.23	giant	4474	2.51	0.26	9
α Cet	2013.11.30	giant	3796	0.68	-0.45	9
ϵ Vir	2014.01.23	giant	4983	2.77	0.13	9
HD122563	2014.01.23	giant	4587	1.61	-2.74	9
HD107328	2014.01.23	giant	4496	2.09	-0.34	9
γ Sge	2015.07.19	giant	3807	1.05	-0.16	9
HD220009	2015.07.20	giant	4217	1.43	-0.75	9
HD11559	2015.10.23	giant	4977 ± 7	3.23 ± 0.24	0.16 ± 0.08	12
HD28292	2015.10.25	giant	4453 ± 9	2.81 ± 0.28	-0.08 ± 0.11	12
HD28305	2015.10.25	giant	4925 ± 9	2.72 ± 0.15	0.20 ± 0.06	12
HD27348	2015.10.25	giant	5003 ± 6	2.75	0.05	12
HD27697	2015.10.25	giant	4975 ± 8	2.64	0.12	12
HD198149	2015.10.26	giant	4858 ± 8	3.29 ± 0.11	-0.19 ± 0.05	12
HD85503	2015.10.28	giant	4567 ± 13	2.65 ± 0.15	0.31 ± 0.06	12
HD76813	2015.10.28	giant	5060 ± 6	2.63 ± 0.09	-0.06 ± 0.04	12
HD78235	2015.10.28	giant	5070 ± 6	3.00	-0.03	12
HD27371	2015.10.28	giant	4960 ± 8	2.76 ± 0.11	0.15 ± 0.05	12
HD48433	2015.10.28	giant	4471 ± 8	2.10 ± 0.17	-0.16 ± 0.07	12
HD25604	2015.10.28	giant	4764 ± 7	2.73 ± 0.31	0.07 ± 0.11	12
HD8207	2015.10.31	giant	4750 ± 8	2.79 ± 0.26	0.11 ± 0.09	12
HD195636	2015.10.31	giant	5242	3.40	-2.86	1
HD17361	2016.01.19	giant	4646 ± 6	2.61 ± 0.13	0.06 ± 0.05	12
HD37984	2016.01.19	giant	4267 ± 16	2.21 ± 0.16	-0.41 ± 0.07	12
HD34559	2016.01.19	giant	5010 ± 5	2.74	0.00	12
HD104979	2016.01.26	giant	4915 ± 10	2.48	-0.45	12
HD102224	2016.01.26	giant	4311 ± 13	2.06 ± 0.22	-0.33 ± 0.10	12

Continued on next page

(Continued)

Target	Obs. Date	Type	$T_{\rm eff}$ (K)	$\log g$	[Fe/H]	Ref
HD137759	2016.01.26	giant	4537 ± 7	2.61 ± 0.15	0.12 ± 0.06	12
HD28307	2016.01.26	giant	4961 ± 9	2.63	0.10	12
HD58207	2016.01.26	giant	4799 ± 5	2.57 ± 0.12	-0.11 ± 0.05	12
HD113226	2016.01.26	giant	5079 ± 8	2.63	0.07	12
HD108381	2016.01.26	giant	4680 ± 10	2.56	0.14	12
HD142091	2016.01.26	giant	4746 ± 7	3.21	0.10	12
HD72722	2016.01.27	giant	3700 ± 16	1.21	-0.41	12
HD61935	2016.01.27	giant	4780 ± 6	2.85 ± 0.27	0.00 ± 0.09	12
HD54810	2016.01.27	giant	4669 ± 10	2.61 ± 0.11	-0.30 ± 0.05	12
HD62345	2016.01.27	giant	5032 ± 6	2.61 ± 0.12	-0.01 ± 0.05	12
HD76291	2016.02.08	giant	4495 ± 10	2.84 ± 0.27	0.07 ± 0.10	12
HD19787	2016.03.11	giant	4832 ± 7	2.92 ± 0.26	0.12 ± 0.08	12
HD161074	2016.03.11	giant	4003 ± 11	2.04 ± 0.17	-0.08 ± 0.06	12
HD68312	2016.03.15	giant	5090 ± 5	2.70	-0.12	12
HD71377	2016.03.17	giant	4465 ± 10	2.30		12
HD188119	2016.04.19	giant	4995 ± 12	2.34 ± 0.19	-0.49 ± 0.09	12
HD170693	2016.05.14	giant	4256 ± 12	2.19 ± 0.15	-0.37 ± 0.06	12
HD195617	2016.05.14	giant	3921 ± 9	1.31	-0.22	12
2M06160059+1034002	2017.12.01	giant	4761 ± 73	2.40 ± 0.04	0.14 ± 0.03	7
2M05471870+1227165	2017.12.01	giant	3702 ± 39	0.57 ± 0.05	-0.34 ± 0.02	7
2M05481928+1200588	2017.12.01	giant	3954 ± 46	0.80 ± 0.06	-0.55 ± 0.03	7
2M06275444+0425299	2017.12.01	giant	4969 ± 83	2.51 ± 0.04	0.11 ± 0.03	7
2M06451160-0026434	2017.12.01	giant	4248 ± 54	1.73 ± 0.05	0.01 ± 0.02	7
2M08150238-1326501	2017.12.02	giant	4480 ± 61	2.46 ± 0.05	0.26 ± 0.02	7
2M03193518+0130538	2017.12.02	giant	4478 ± 62	2.34 ± 0.06	-0.16 ± 0.03	7
2M06311754-3214330	2017.12.02	giant	3973 ± 46	1.08 ± 0.05	-0.15 ± 0.02	7
2M07352612-1942301	2017.12.02	giant	4028 ± 47	1.45 ± 0.05	0.25 ± 0.02	7
2M06513741-2405397	2017.12.02	giant	3972 ± 45	1.35 ± 0.05	0.11 ± 0.02	7
2M07583829-1733426	2017.12.02	giant	3797 ± 41	0.60 ± 0.06	-0.48 ± 0.02	7
2M05533070-0400268	2017.12.02	giant	4738 ± 73	2.50 ± 0.06	-0.36 ± 0.04	7
2M05550498-0441304	2017.12.02	giant	4226 ± 53	1.66 ± 0.05	0.02 ± 0.02	7
2M06203639-0111357	2017.12.02	giant	4966 ± 84	2.43 ± 0.05	-0.54 ± 0.05	7
2M07230997-0412142	2017.12.02	giant	3784 ± 40	1.09 ± 0.04	0.23 ± 0.02	7
2M07201361-0510250	2017.12.02	giant	4240 ± 54	1.56 ± 0.05	-0.14 ± 0.02	7
2M06490616+0146200	2017.12.02	giant	3980 ± 46	0.99 ± 0.06	-0.36 ± 0.02	7
2M08490669+1048574	2017.12.03	giant	4198 ± 53	1.52 ± 0.06	-0.59 ± 0.03	7
2M05434312+1205173	2017.12.03	giant	4247 ± 54	1.56 ± 0.06	-0.36 ± 0.03	7
2M06185998-0028595	2017.12.03	giant	5003 ± 86	2.44 ± 0.05	-0.43 ± 0.04	7
2M06521217-1014388	2017.12.03	giant	3715 ± 39	0.67 ± 0.05	-0.11 ± 0.02	7
2M06543924-1316290	2017.12.03	giant	4482 ± 62	1.99 ± 0.05	-0.06 ± 0.03	7
2M08521671-1320444	2017.12.03	giant	5042 ± 87	2.56 ± 0.05	-0.19 ± 0.04	7
2M23163043+1103592	2017.12.04	giant	4495 ± 63	2.20 ± 0.06	-0.37 ± 0.03	7
2M01555653-0317115	2017.12.04	giant	4772 ± 74	2.64 ± 0.06	-0.22 ± 0.03	7
2M03164288+0055085	2017.12.04	giant	4893 ± 81	2.88 ± 0.07	-0.68 ± 0.05	7
HD20902	2015.10.26	supergiant	6541 ± 11	1.85	0.22	13
HD204867	2015.10.26	supergiant	5466 ± 7	1.54	0.03	13
HD194093	2015.10.26	supergiant	6202 ± 12	1.35	0.05	13
HD37536	2015.10.28	supergiant	3918 ± 76	0.52 ± 0.19	0.13 ± 0.09	13
HD52497	2015.10.28	supergiant	5090 ± 12			13
HD26630	2015.10.28	supergiant	5337 ± 7	1.74	0.09	13

Continued on next page

(Continued)

Target	Obs. Date	Type	$T_{\rm eff}$ (K)	$\log g$	[Fe/H]	Ref
HD48329	2015.10.28	supergiant	4510 ± 11	0.92 ± 0.09	0.12 ± 0.07	13
HD25291	2015.10.28	supergiant	7497 ± 8	2.06	0.00	13
HD52005	2015.10.28	supergiant	3954 ± 38	0.78 ± 0.14	0.13 ± 0.06	13
HD7927	2015.10.31	supergiant	7341 ± 42	0.76	-0.07	13
HD31910	2015.10.31	supergiant	5441 ± 10	1.57	-0.01	13
HD206778	2015.10.31	supergiant	4108 ± 30	0.84 ± 0.13	0.11 ± 0.07	13
HD219978	2015.10.31	supergiant	3928 ± 47	0.57 ± 0.18	0.22 ± 0.08	13
HD3421	2015.10.31	supergiant	5302 ± 10	1.88	-0.20	13
HD208606	2015.10.31	supergiant	4702 ± 8	1.18	0.25	13
HD9900	2015.10.31	supergiant	4529 ± 16	1.35	0.19	13
HD207089	2015.11.15	supergiant	4428 ± 36	1.24	0.14	13
HD74395	2016.01.27	supergiant	5264 ± 6	1.41 ± 0.08	0.09 ± 0.04	13
HD159181	2016.02.03	supergiant	5220 ± 6	1.50	-0.15	13
HD18391	2016.02.18	supergiant	5871 ± 16	1.20	-0.13	13
HD17958	2016.03.11	supergiant	3974 ± 24			13
HD171635	2016.03.11	supergiant	6201 ± 8	1.78	-0.10	13
HD99648	2016.03.12	supergiant	4942 ± 14	2.24 ± 0.12	-0.03 ± 0.06	13
HD92125	2016.03.21	supergiant	5354 ± 10	2.22	0.03	13
HD77912	2016.03.21	supergiant	4957 ± 10	1.75	-0.14	13
HD202109	2016.03.21	supergiant	4976 ± 13	1.90	0.10	13
HD207119	2016.03.26	supergiant	3946 ± 22			13
HD178524	2016.04.24	supergiant	6710 ± 22	1.96	-0.14	13
HD200905	2016.05.14	supergiant	3980 ± 33	0.89 ± 0.18	0.15 ± 0.07	13

Table B.2: Signal-to-noise ratio (S/N) and He 10 830 line parameters of the field-WD sample. The parameters are defined in Chapter 5

Target	S/N	EW(He) (mÅ)	R/B	FWHM (Å)	peak position (Å)	EW type
HD49933	465	204.24 ± 1.73	1.17244	1.4	10830.38	sG
PROCYON	406	113.90 ± 2.15	1.301174	1.65	10830.31	sG
δ Eri	330	75.49 ± 2.45	1.804668	1.42	10830.27	sG
ϵ Eri	161	223.06 ± 3.89	1.106458	0.85	10830.37	sG
HD281159	408					
18Sco	200	73.56 ± 3.42	1.291185	1.02	10830.29	sG
HD140283	344	16.29 ± 1.60				sum
HD219134	137	110.88 ± 4.72	0.919399	0.9	10830.46	sG
HD28343	112					
HD10476	234	104.09 ± 2.64	1.123928	0.83	10830.31	sG
HD101501	251	188.65 ± 2.69	1.21094	0.99	10830.29	sG
HD114710	206	146.79 ± 3.48	1.240853	1.11	10830.31	sG
HD143761	156	37.11 ± 5.29	0.658534	1.48	10831.09	sG
HD117176	125	10.35 ± 4.58				sum
HD115383	234	269.19 ± 3.07	1.206186	1.12	10830.32	sG
HD137107	224	97.25 ± 3.42	1.160464	1.27	10830.37	sG
HD102870	231	84.91 ± 3.13	1.198742	1.13	10830.2	sG
HD72905	280	260.23 ± 2.53	1.122146	1.09	10830.28	sG
HD81809	265	121.96 ± 2.86	1.023401	1.25	10830.34	sG
HD95128	304	22.44 ± 2.24	1.778632	1.0	10830.32	sG

Continued on next page

(Continued)

Target	S/N	EW(He) (mÅ)	R/B	FWHM (Å)	peak position (Å)	EW type
HD122064	440	112.84 ± 1.44	0.932321	0.87	10830.34	sG
HD109358	313	41.36 ± 2.25	1.719873	1.07	10830.38	sG
HD50281	237	218.73 ± 2.80	1.226807	0.95	10830.25	sG
HD22879	297	39.53 ± 2.67	1.503185	1.36	10830.39	sG
HD19445	218	15.85 ± 2.64	1.091196	0.72	10830.3	sG
HD141004	331	37.65 ± 1.87	0.881258	0.83	10830.31	sG
HD84937	324	10.86 ± 1.78				sum
HD34411	504	20.27 ± 1.30	0.612748	0.93	10830.23	sG
HD19445	227	35.66 ± 3.48	1.356287	1.35	10830.31	sG
HD19445	256	12.86 ± 2.34				sum
HD19373	199	5.96 ± 2.95				sum
HD157214	195	22.77 ± 3.40	0.940052	0.95	10830.21	sG
HD82106	238	233.64 ± 2.86	1.285195	1.0	10830.3	sG
HD19445	200	24.50 ± 3.58	2.547786	1.11	10830.21	sG
HD39587	214	256.31 ± 3.38	0.872677	1.13	10830.41	sG
HD116443	244	78.02 ± 2.57	1.048889	0.85	10830.37	sG
HD86728	392	29.57 ± 1.71	1.969299	0.97	10830.3	sG
etaBoo	353	51.78 ± 2.68	0.815061	1.93	10830.16	sG
HD82885	241	202.70 ± 2.79	1.478389	0.98	10830.23	sG
HD89744	182	45.25 ± 4.65	0.554868	1.56	10830.17	sG
HD157881	125	245.42 ± 5.24	1.172929	0.93	10830.3	sG
HD136064	252	11.72 ± 2.32				sum
σ Boo	247	125.74 ± 3.04	0.632384	1.22	10830.37	sG
HD79555	245	200.71 ± 2.73	0.911325	0.97	10830.26	sG
γ Ser	559	49.64 ± 1.55	1.704266	1.62	10830.24	sG
HR3954	355	150.64 ± 2.63	1.185834	1.89	10830.38	sG
HD99747	363	69.30 ± 2.16	0.479733	1.33	10830.54	sG
HD185144	355	125.10 ± 1.87	0.955053	0.96	10830.43	sG
35LMi	213	29.35 ± 3.41	0.21306	1.14	10830.31	sG
ι Vir	318	239.26 ± 2.69	0.900256	1.58	10830.41	sG
HD103095	457	54.32 ± 1.58	1.241926	1.13	10830.26	sG
HE1346-0427	106	3.05 ± 5.37				sum
HD63685	154	22.69 ± 3.84				sum
HD76188	139	12.83 ± 4.12	0.721415	0.71	10830.36	sG
HD42505	143	258.67 ± 4.88	1.179948	1.06	10830.43	sG
HD16714	114	6.93 ± 4.09	2.788335	0.47	10830.3	sG
HD222237	219	122.42 ± 3.24	1.127486	1.09	10830.35	sG
HD17970	103	56.52 ± 6.66	0.706458	1.02	10830.51	sG
HD1388	162	17.79 ± 3.46				sum
HD23356	299	187.71 ± 2.46	1.129526	1.17	10830.5	sG
HD219495	156	290.01 ± 4.58	1.168682	1.1	10830.36	sG
HD1461	459	53.02 ± 1.53	1.463646	1.07	10830.19	sG
HD21749	180	246.06 ± 3.90	1.013344	1.07	10830.39	sG
HD224393	129	67.68 ± 4.96	1.009723	0.89	10830.35	sG
HD21019	185	25.20 ± 3.23				sum
HD55	115	123.17 ± 5.95	0.955076	1.01	10830.42	sG
HD24633	118	42.34 ± 5.93	0.939155	1.07	10830.57	sG
HD45289	187	1.81 ± 3.20				sum
HD967	139	20.50 ± 4.25	1.019949	0.76	10830.23	sG
HD59984	307	-11.38 ± 1.82				sum

Continued on next page

(Continued)

Target	S/N	EW(He) (mÅ)	R/B	FWHM (Å)	peak position (Å)	EW type
HD69655	293	22.68 ± 2.34	0.631263	1.02	10830.33	sG
HD25565	148	147.08 ± 4.43	1.07929	0.93	10830.36	sG
HD43197	66	31.97 ± 10.05	0.978926	0.94	10830.17	sG
HD26729	94	8.44 ± 5.87				sum
HD5349	104	46.03 ± 7.32	1.509155	1.26	10830.24	sG
HD11608	136	150.86 ± 4.91	0.975414	0.97	10830.35	sG
HD222335	293	131.55 ± 2.39	1.175829	1.06	10830.36	sG
BD-140184	264	277.61 ± 2.74	1.234023	1.13	10830.31	sG
HD4838	181	319.03 ± 4.10	1.161673	1.19	10830.41	sG
HD10002	176	73.60 ± 4.26	0.935939	1.22	10830.71	sG
BD-130321	114	207.10 ± 6.49	1.211003	1.19	10830.51	sG
HD40865	128	1.66 ± 4.46				sum
HD4597	109	3.55 ± 5.13				sum
HD37986	119	56.96 ± 5.79	1.758954	1.03	10830.07	sG
HD38858	451	59.63 ± 2.00	0.546071	1.77	10830.65	sG
HD33725	208	104.18 ± 3.36	1.115791	1.06	10830.35	sG
HD56274	261	60.91 ± 2.86	1.065341	1.21	10830.45	sG
HD72673	394	69.01 ± 1.73	1.10809	1.01	10830.26	sG
HD73524	297	20.50 ± 2.32	1.147534	1.03	10830.41	sG
HD9246	356	98.16 ± 1.93	0.850099	1.02	10830.5	sG
HD457	382	33.54 ± 1.76	0.397885	0.98	10830.4	sG
HD283	278	48.76 ± 2.21	1.020842	0.82	10830.29	sG
HD8326	193	179.92 ± 3.57	1.135641	1.03	10830.32	sG
muLeo	315	65.56 ± 2.78	1.552471	1.67	10829.96	sG
α Cet	229	-11.12 ± 2.44				sum
ϵ Vir	432	115.21 ± 2.19	1.793966	1.94	10830.24	sG
HD122563	609	9.68 ± 0.93				sum
HD107328	440	-36.47 ± 1.37				sum
γ Sge	142	10.62 ± 4.10				sum
HD220009	272	119.82 ± 3.83	1.015262	2.35	10829.32	sG
HD11559	205	270.46 ± 3.93	1.328573	1.4	10830.27	sG
HD28292	305	146.89 ± 4.20	0.588373	2.37	10830.62	sG
HD28305	120	218.07 ± 7.27	0.704127	1.66	10830.49	sG
HD27348	205	243.95 ± 4.29	1.461906	1.67	10830.37	sG
HD27697	232	241.54 ± 3.78	0.782228	1.66	10830.46	sG
HD198149	179	55.31 ± 4.35	0.811155	1.31	10830.5	sG
HD85503	63	0.49 ± 9.11				sum
HD76813	221	72.04 ± 4.72	2.304031	2.37	10830.02	sG
HD78235	222	356.93 ± 3.62	1.326806	1.4	10830.26	sG
HD27371	236	309.13 ± 3.51	1.103719	1.49	10830.34	sG
HD48433	518	102.75 ± 1.85	1.52973	1.98	10830.25	sG
HD25604	204	61.86 ± 4.74	2.70414	2.02	10830.11	sG
HD8207	198					
HD195636	236	-2.46 ± 2.58				sum
HD17361	382	88.68 ± 2.57	1.18923	2.08	10830.16	sG
HD37984	104	31.59 ± 7.18	0.837656	1.22	10830.18	sG
HD34559	296	133.80 ± 3.17	1.398386	1.9	10830.14	sG
HD104979	195	33.93 ± 4.43	0.7805	1.62	10830.48	sG
HD102224	205	92.81 ± 4.96	1.724992	2.23	10830.17	sG
HD137759	114	58.50 ± 9.85	1.977781	1.93	10830.29	sG

Continued on next page

(Continued)

Target	S/N	EW(He) (mÅ)	R/B	FWHM (Å)	peak position (Å)	EW type
HD28307	108	235.05 ± 8.13	1.201672	1.68	10830.3	sG
HD58207	145	84.06 ± 6.16	0.751941	1.72	10830.64	sG
HD113226	305	102.30 ± 3.44	2.085204	2.39	10830.31	sG
HD108381	156	54.97 ± 5.62	1.240722	1.66	10830.23	sG
HD142091	298	85.48 ± 3.06	1.596109	1.8	10830.43	sG
HD72722	221	-2.60 ± 2.61				sum
HD61935	356	87.59 ± 3.43	1.438668	1.94	10830.4	sG
HD54810	189	59.33 ± 3.97	1.016668	1.22	10830.34	sG
HD62345	225	31.14 ± 3.70	2.003899	1.5	10830.14	sG
HD76291	204	69.59 ± 4.50	1.002055	1.83	10830.64	sG
HD19787	97	9.64 ± 5.61				sum
HD161074	133	24.20 ± 4.36				sum
HD68312	250	61.08 ± 4.20	1.132227	2.39	10830.42	sG
HD71377	346					
HD188119	239	80.74 ± 4.05	1.456678	2.04	10830.31	sG
HD170693	338	71.73 ± 2.75	1.010006	1.88	10830.44	sG
HD195617	165	11.46 ± 3.63				sum
2M06160059+1034002	151	20.43 ± 3.59				sum
2M05471870+1227165	171	-19.72 ± 3.32				sum
2M05481928+1200588	109	-14.41 ± 5.30				sum
2M06275444+0425299	215	35.43 ± 3.53	0.61511	1.25	10829.97	sG
2M06451160-0026434	167	-0.64 ± 3.49				sum
2M08150238-1326501	57	143.44 ± 17.74	3.88403	2.25	10830.13	sG
2M03193518+0130538	159	66.13 ± 5.62	0.895702	1.73	10830.73	sG
2M06311754-3214330	99					
2M07352612-1942301	167	-12.22 ± 3.53				sum
2M06513741-2405397	131					
2M07583829-1733426	85	-5.00 ± 6.68				sum
2M05533070-0400268	223	111.85 ± 3.81	0.71601	1.57	10830.39	sG
2M05550498-0441304	232	64.84 ± 3.51	1.150287	1.44	10829.79	sG
2M06203639-0111357	209	71.88 ± 4.00	2.179133	1.52	10830.03	sG
2M07230997-0412142	105	-21.34 ± 5.59				sum
2M07201361-0510250	108	-90.52 ± 5.29				sum
2M06490616+0146200	75	12.36 ± 7.84				sum
2M08490669+1048574	166	-14.33 ± 3.37				sum
2M05434312+1205173	97	74.43 ± 8.88	1.648652	1.6	10829.34	sG
2M06185998-0028595	109	18.81 ± 5.46				sum
2M06521217-1014388	133	-5.16 ± 4.31				sum
2M06543924-1316290	127	50.13 ± 6.63	0.491499	1.53	10830.14	sG
2M08521671-1320444	80	0.41 ± 6.84				sum
2M23163043+1103592	400	68.28 ± 2.35	1.876033	1.91	10830.27	sG
2M01555653-0317115	208	53.70 ± 3.82	0.676447	1.37	10830.56	sG
2M03164288+0055085	240	48.77 ± 2.98	1.657647	1.11	10830.52	sG
HD20902	192	-6.27 ± 2.93				sum
HD204867	345	32.41 ± 1.66				sum
HD194093	151	-7.28 ± 3.84				sum
HD37536	138	-12.66 ± 4.16				sum
HD52497	300					
HD26630	268					
HD48329	153	-11.56 ± 3.61				sum

Continued on next page

(Continued)

Target	S/N	EW(He) (mÅ)	R/B	FWHM (Å)	peak position (Å)	EW type
HD25291	155	-31.86 ± 3.93				sum
HD52005	216	251.72 ± 6.66	0.197582	4.47	10831.03	sG
HD7927	366	4.43 ± 1.56				sum
HD31910	326	1248.46 ± 4.09	2.0042	3.85	10830.8	sG
HD206778	232					
HD219978	178	25.11 ± 3.34				sum
HD3421	123	420.56 ± 8.97	1.414061	2.64	10830.56	sG
HD208606	149					
HD9900	202					
HD207089	nan					
HD74395	129	291.74 ± 8.13	1.18318	2.38	10830.47	sG
HD159181	120	1138.96 ± 11.35	2.228094	4.04	10830.74	sG
HD18391	145	-19.45 ± 4.07				sum
HD17958	101					
HD171635	156	-4.44 ± 3.76				sum
HD99648	328	103.06 ± 4.25	1.008103	2.73	10830.34	sG
HD92125	238	396.00 ± 4.59	1.427409	2.59	10830.37	sG
HD77912	269	610.61 ± 5.60	0.322047	4.92	10830.67	sG
HD202109	275	28.80 ± 3.05	0.992371	1.53	10829.95	sG
HD207119	123					
HD178524	225	-6.54 ± 2.70				sum
HD200905	156					

Table B.3: Fractional X-ray luminosity of the field-WD sample.

Target	$\log L_{\rm X1}/L_{\rm Gaia}$	$\log L_{\rm X2}/L_{\rm Gaia}$	$\log L_{\rm X3}/L_{\rm Gaia}$	$\log L_{\rm X4}/L_{\rm Gaia}$	$\log L_{\rm X5}/L_{\rm Gaia}$	$\log L_{\rm X8}/L_{\rm Gaia}$	$\log L_{\rm RXS}/L_{\rm Gaia}$
HD42505							-4.20 ± 0.07
HD222237							-4.98 ± 0.14
HD23356							-4.46 ± 0.08
HD4838							-3.76 ± 0.13
HD219495							-4.13 ± 0.13
HD1461	-6.991 ± 0.037	-6.853 ± 0.027	-8.104 ± 0.186			-6.583 ± 0.027	
HD102870	-6.631 ± 0.007	-6.310 ± 0.006	-7.222 ± 0.011	-8.544 ± 0.091	-9.120 ± 0.632	-6.104 ± 0.006	-5.18 ± 0.04
HD28305							-6.61 ± 0.17
HD157881	-5.525 ± 0.019	-5.302 ± 0.015	-6.066 ± 0.038	-7.738 ± 0.629	-7.402 ± 2.411	-5.022 ± 0.017	-4.56 ± 0.08
HD31910							-5.84 ± 0.11
HD101501							-4.51 ± 0.04
HD78235							-4.70 ± 0.05
HD114710	-6.213 ± 0.005	-5.878 ± 0.004	-6.745 ± 0.008	-8.053 ± 0.070	-8.676 ± 0.646	-5.673 ± 0.004	-4.93 ± 0.03
HD72905	-5.309 ± 0.006	-4.745 ± 0.003	-5.340 ± 0.004	-6.213 ± 0.020	-6.867 ± 0.127	-4.549 ± 0.002	-4.00 ± 0.02
HD39587	-5.464 ± 0.007	-4.919 ± 0.004	-5.512 ± 0.005	-6.309 ± 0.020	-7.146 ± 0.189	-4.719 ± 0.003	-4.16 ± 0.02
HD219134	-10.345 ± 3.116	-9.294 ± 0.584	-9.064 ± 0.362	-8.154 ± 0.187	-8.234 ± 0.806	-7.605 ± 0.204	-5.60 ± 0.13
HD27371	-6.828 ± 0.019	-6.207 ± 0.018	-6.887 ± 0.019	-7.944 ± 0.038	-9.680 ± 1.289	-6.041 ± 0.018	-5.23 ± 0.04
HD50281	-5.684 ± 0.008	-5.486 ± 0.006	-6.263 ± 0.016	-7.514 ± 0.154		-5.228 ± 0.005	-4.34 ± 0.06
HD28307	-6.276 ± 0.015	-5.604 ± 0.014	-6.251 ± 0.014	-7.311 ± 0.024	-8.785 ± 0.413	-5.440 ± 0.014	-4.86 ± 0.02
HD141004							-5.51 ± 0.08
HD82885	-5.705 ± 0.004	-5.276 ± 0.003	-5.956 ± 0.005	-7.045 ± 0.029	-8.351 ± 0.640	-5.073 ± 0.003	-4.53 ± 0.04
HD79555	-4.591 ± 0.007	-4.235 ± 0.005	-4.650 ± 0.008	-5.247 ± 0.028	-6.368 ± 0.352	-3.949 ± 0.004	-3.46 ± 0.03
HD11559							-5.19 ± 0.06
HD28343							-4.03 ± 0.06
HD115383							-4.01 ± 0.02
HD95128	-7.415 ± 0.056	-7.330 ± 0.049	-7.248 ± 0.048	-6.963 ± 0.058	-6.803 ± 0.112	-6.371 ± 0.045	
HD198149							-6.85 ± 0.16
HD27348							-5.09 ± 0.06
HD81809	-6.740 ± 0.020	-6.365 ± 0.020	-7.153 ± 0.021	-8.668 ± 0.089	-8.621 ± 0.249	-6.128 ± 0.020	-5.49 ± 0.13
HD185144							-4.92 ± 0.02
HD116443							-4.80 ± 0.18
HD62345							-6.05 ± 0.09

Continued on next page

(Continued)

Target	$\log L_{\rm X1}/L_{\rm Gaia}$	$\log L_{\rm X2}/L_{\rm Gaia}$	$\log L_{\rm X3}/L_{\rm Gaia}$	$\log L_{\rm X4}/L_{\rm Gaia}$	$\log L_{\rm X5}/L_{\rm Gaia}$	$\log L_{\rm X8}/L_{\rm Gaia}$	$\log L_{\rm RXS}/L_{\rm Gaia}$
HD82106							-4.12 ± 0.05
HD49933							-4.25 ± 0.05
γ Ser							-5.88 ± 0.10
σ Boo							-5.11 ± 0.05
ϵ Eri	-5.599 ± 0.003	-5.262 ± 0.002	-5.924 ± 0.004	-6.800 ± 0.018	-7.910 ± 0.162	-5.029 ± 0.002	-4.27 ± 0.01
δ Eri	-8.206 ± 0.026	-8.739 ± 0.048	-10.050 ± 0.384	-9.629 ± 0.413	-9.842 ± 1.691	-8.052 ± 0.039	-6.44 ± 0.14
18Sco	-7.142 ± 0.039	-7.233 ± 0.043	-8.793 ± 0.481	-8.352 ± 0.470	-7.858 ± 0.680	-6.826 ± 0.070	
ι Vir							-4.55 ± 0.03
HR3954							-5.05 ± 0.09
35LMi							-5.18 ± 0.16

Appendix C

Spectral atlas of the helium line in field-WD stars

This appendix presents the plot of field-WD stars for helium 10 830 Å line.

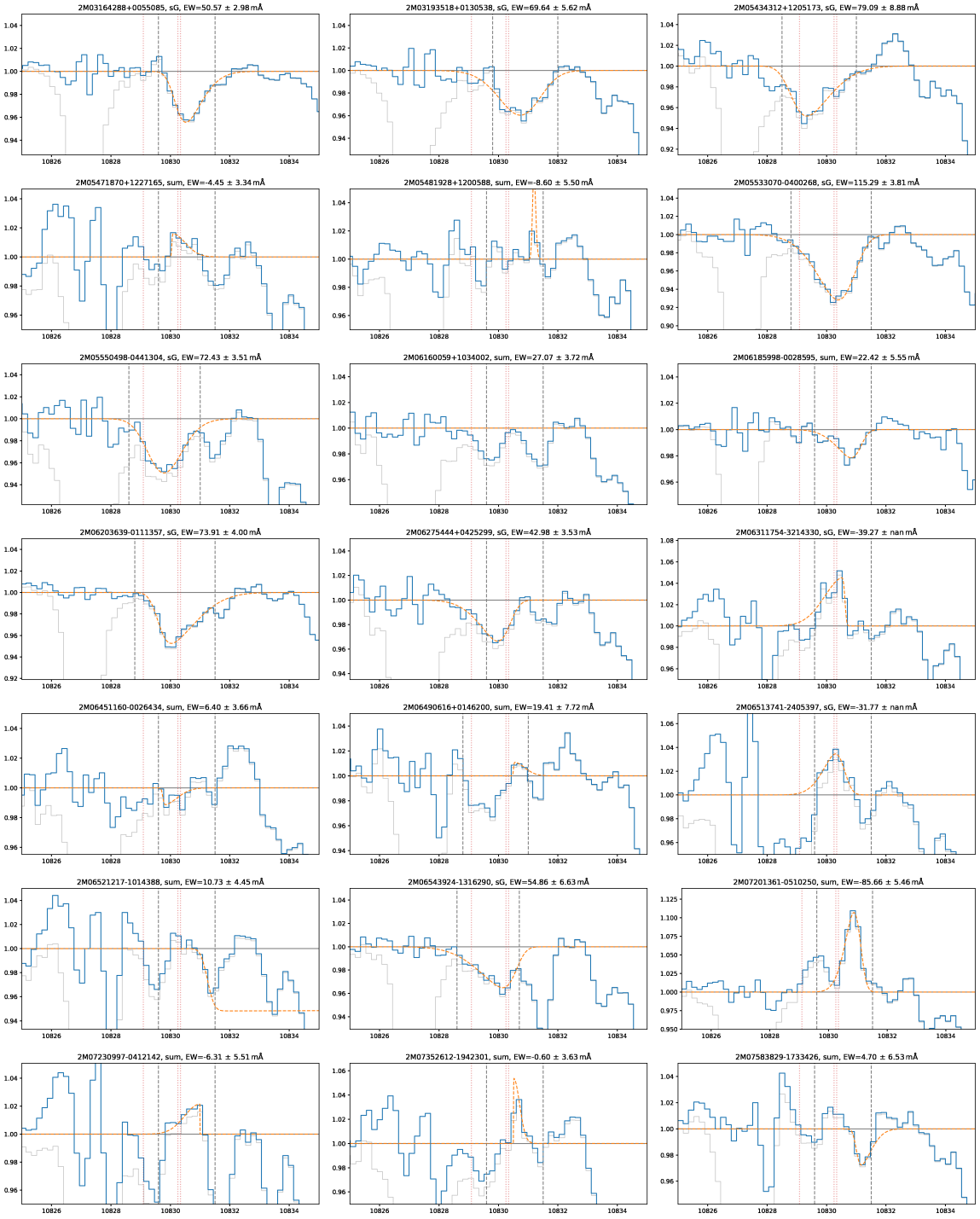


Figure C.1: The atlas of He 10 830 line of field-WD sample, with the measurement result in the title.

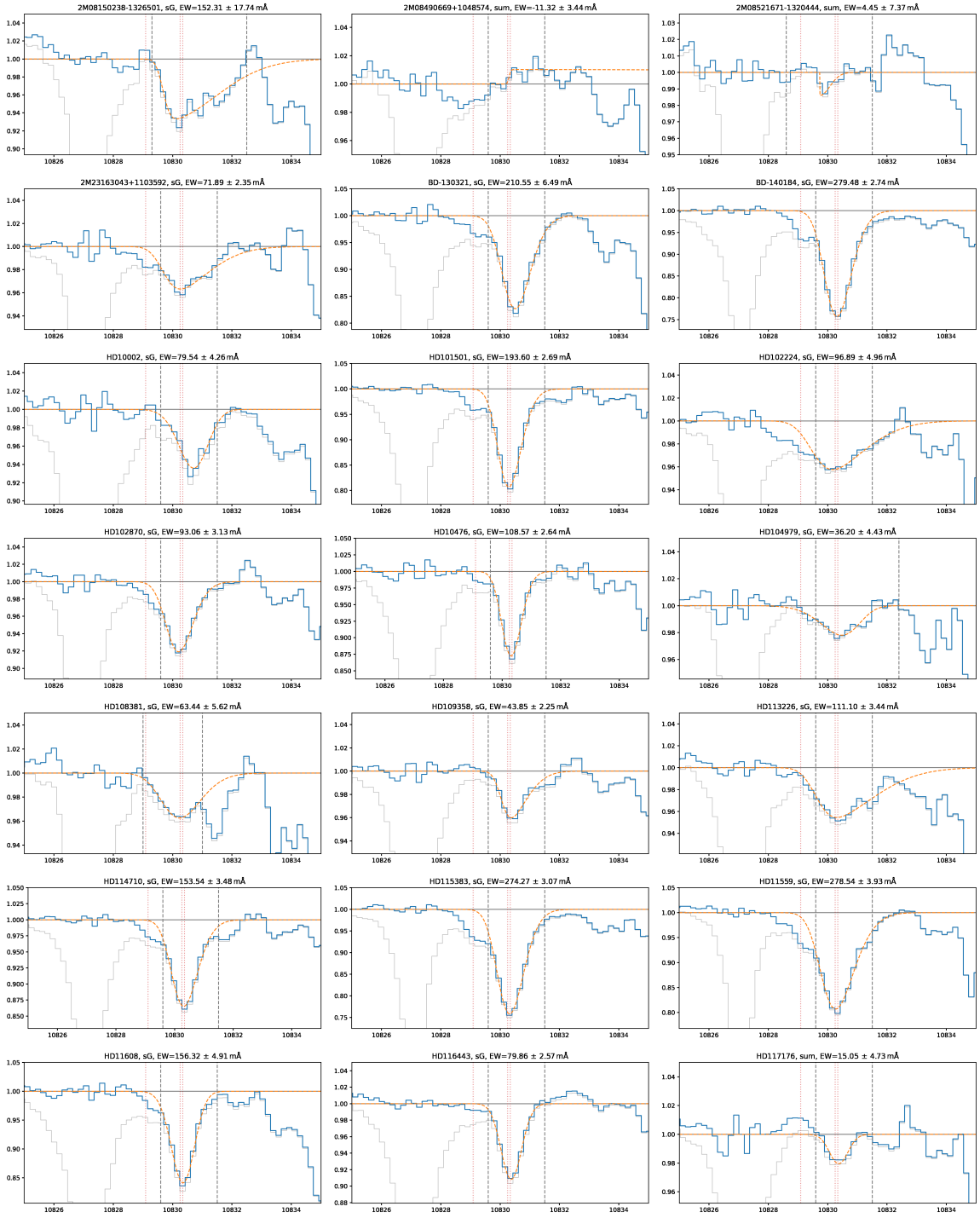


Figure C.2: The atlas of He 10 830 line of field-WD sample, with the measurement result in the title.

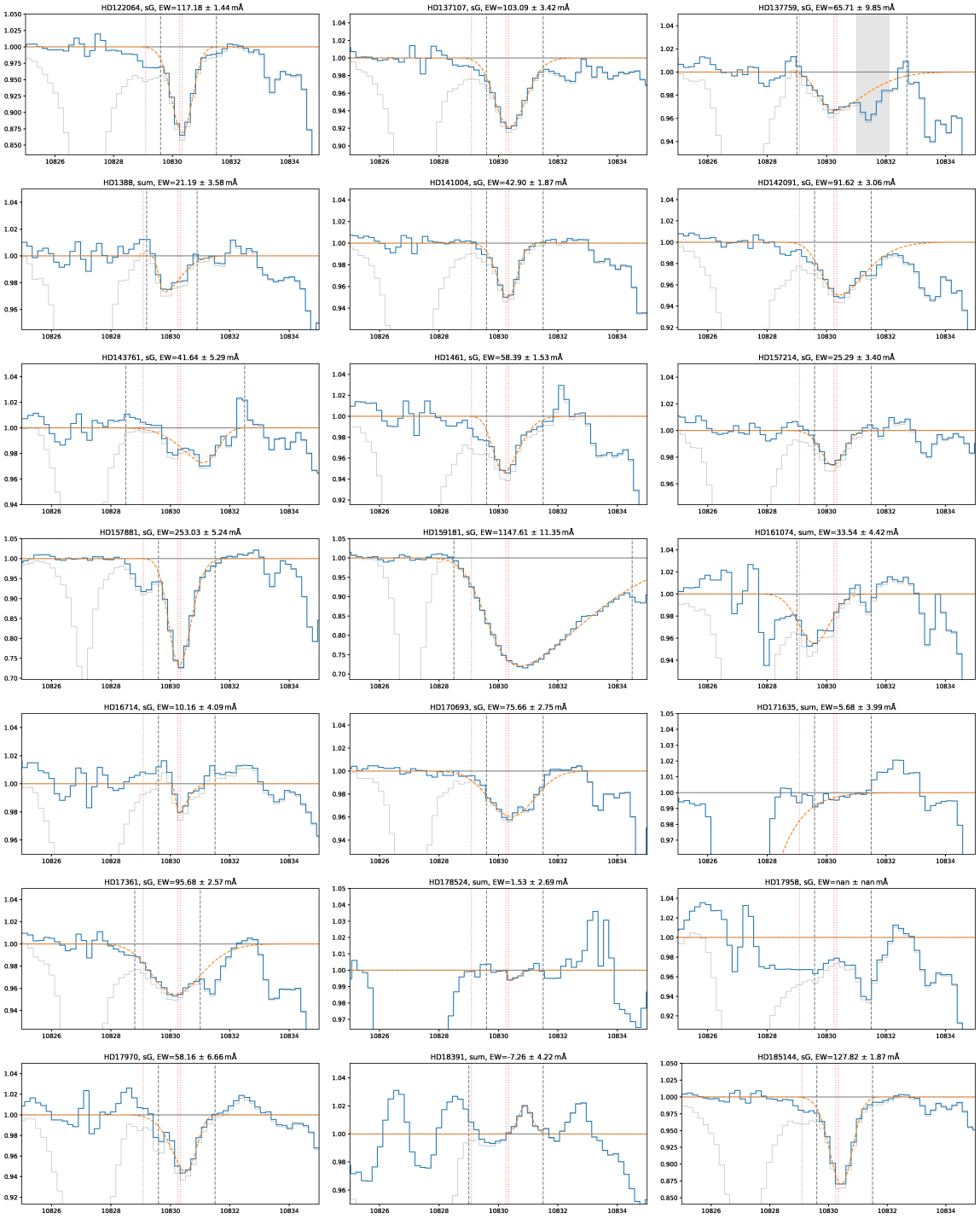


Figure C.3: The atlas of He 10 830 line of field-WD sample, with the measurement result in the title.

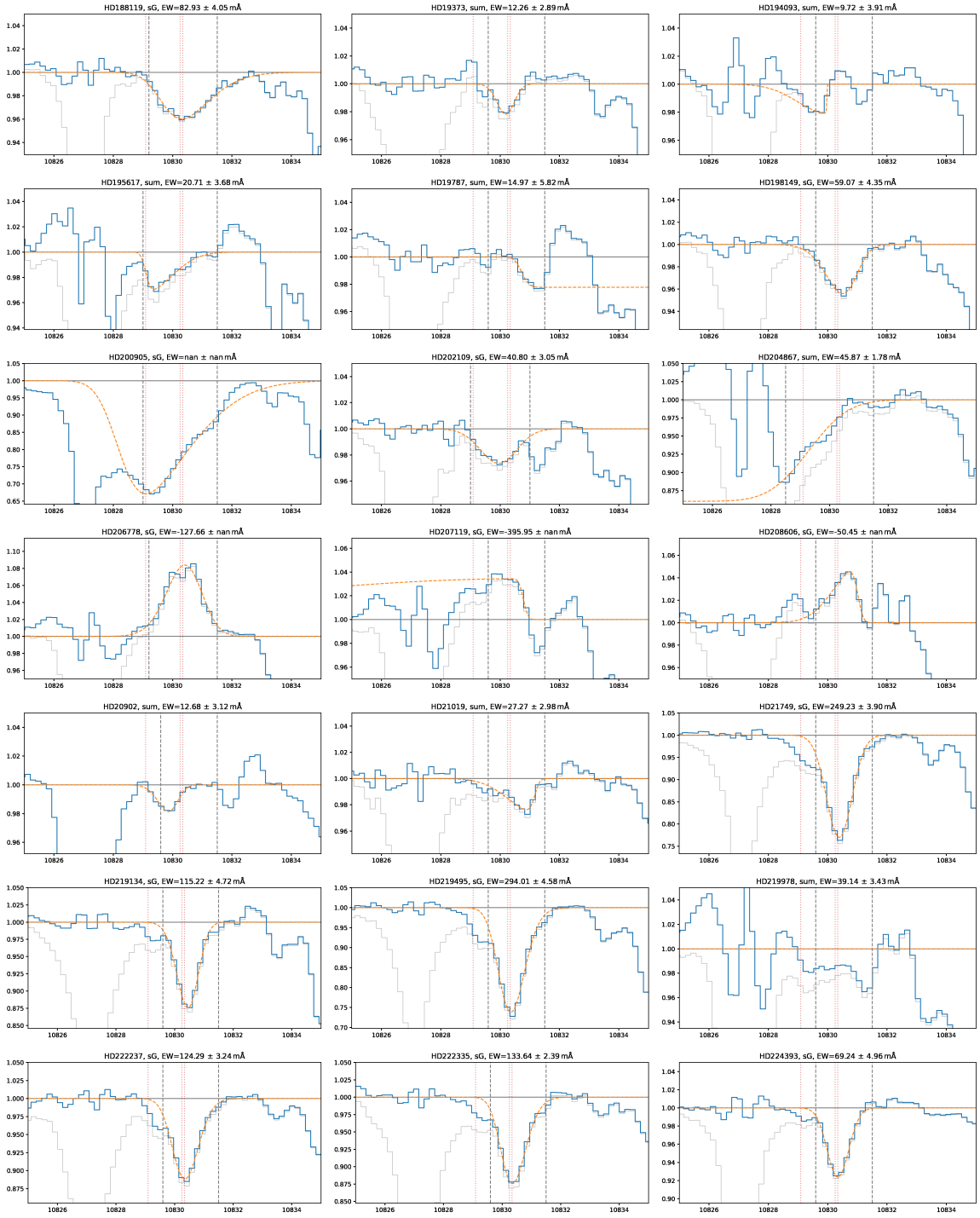


Figure C.4: The atlas of He 10 830 line of field-WD sample, with the measurement result in the title.

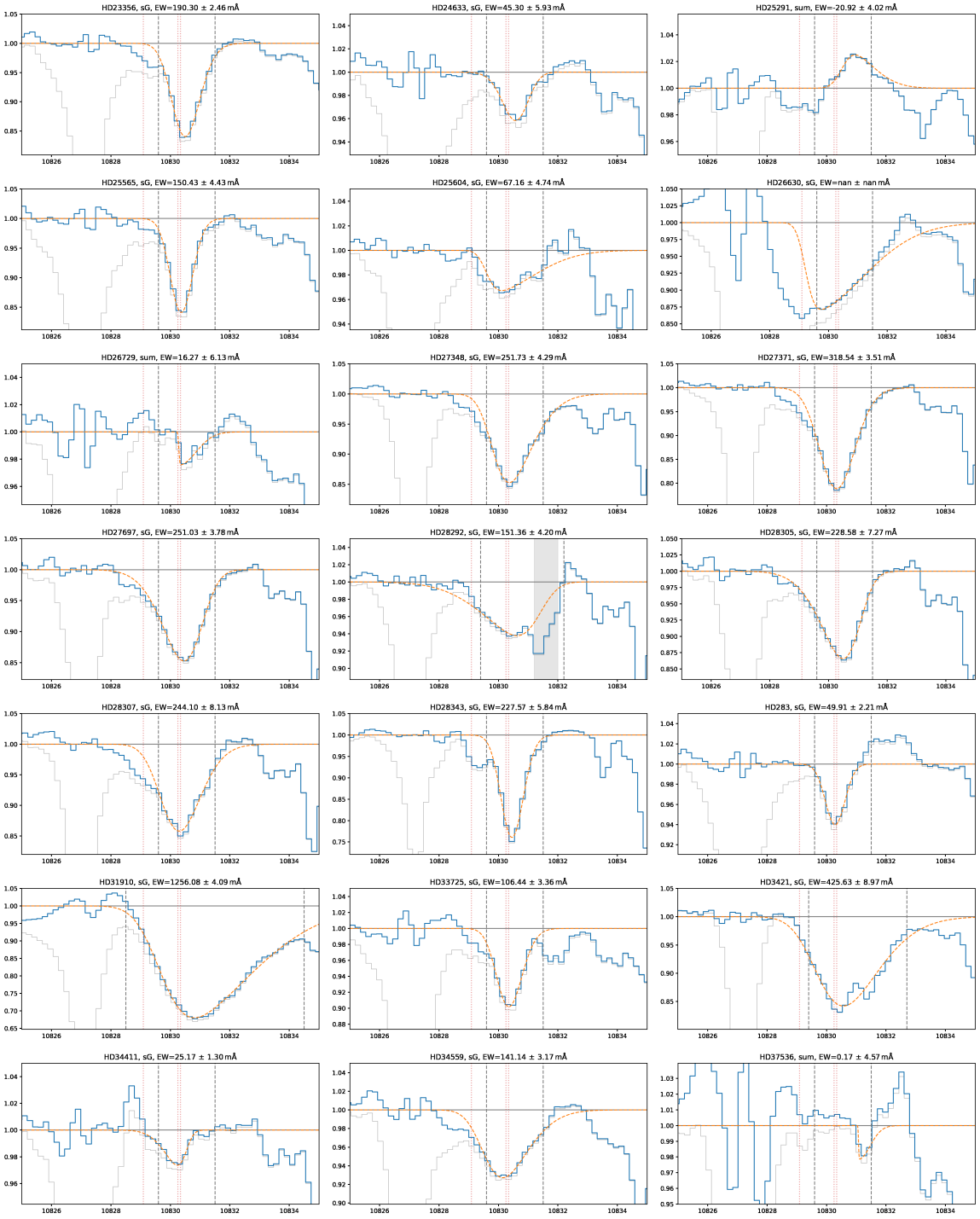


Figure C.5: The atlas of He 10 830 line of field-WD sample, with the measurement result in the title.

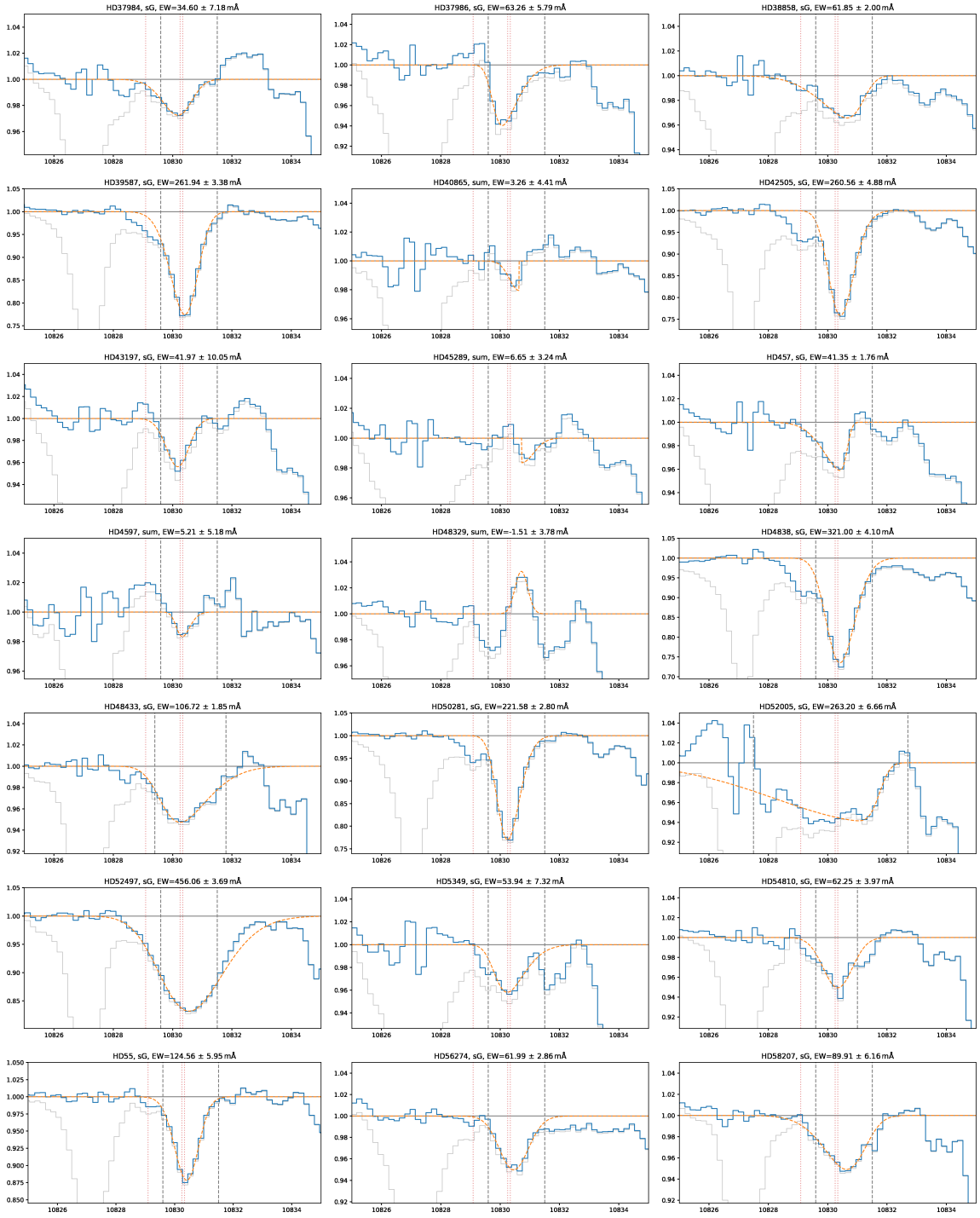


Figure C.6: The atlas of He 10 830 line of field-WD sample, with the measurement result in the title.

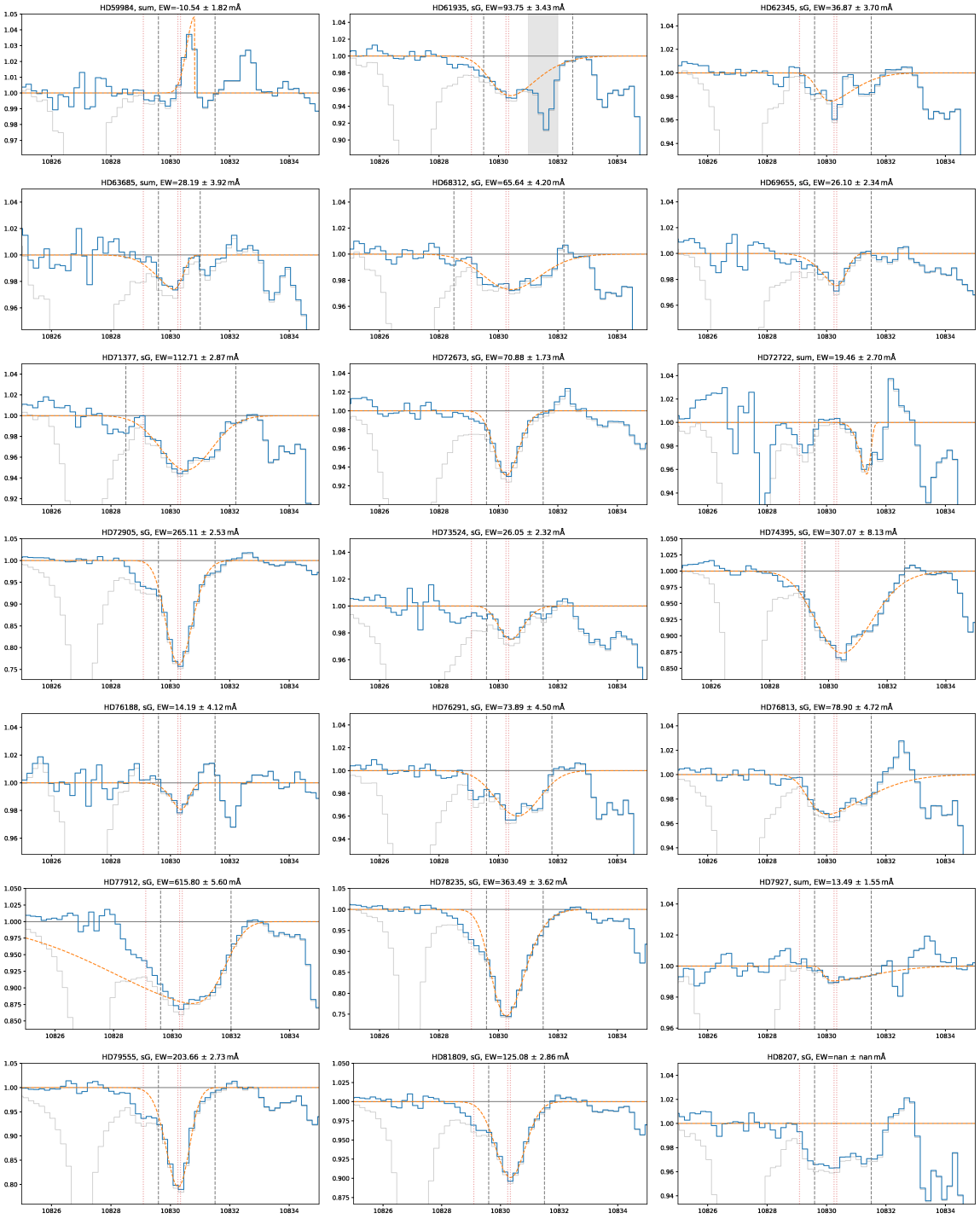


Figure C.7: The atlas of He 10 830 line of field-WD sample, with the measurement result in the title.

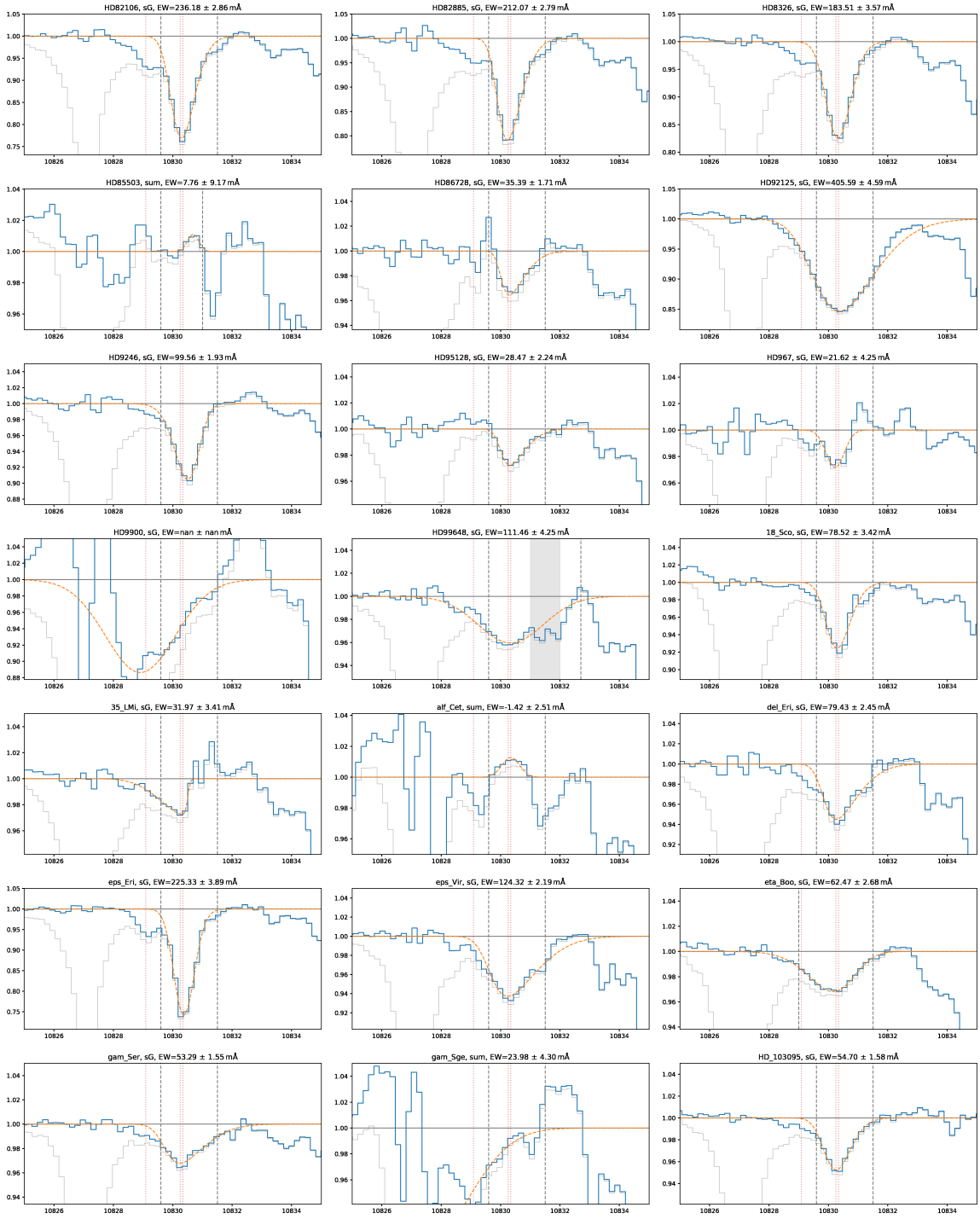


Figure C.8: The atlas of He 10 830 line of field-WD sample, with the measurement result in the title.

Appendix D

The He 10 830 and Ca II line atlas of Stock-2 sample

This appendix contains the figures of Stock-2 sample stars. They are used in $\log gf$ calibration of blending lines, measurement of He 10 830 line strength and the Ca $\log R'_{\rm HK}$ index.

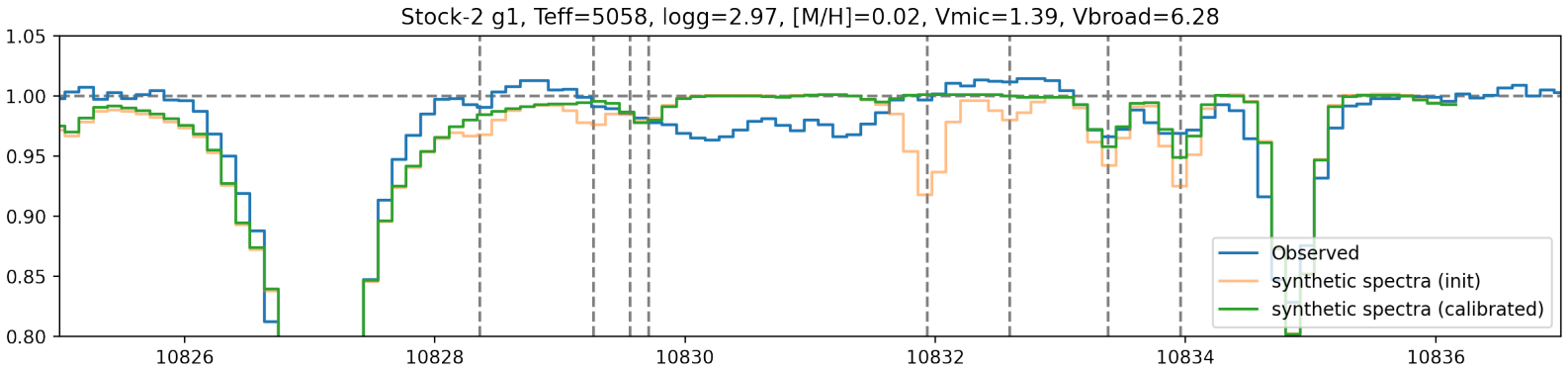


Figure D.1: The spectra around He 10 830 of Stock-2 g1 star, with the synthetic spectra for $\log gf$ calibration.

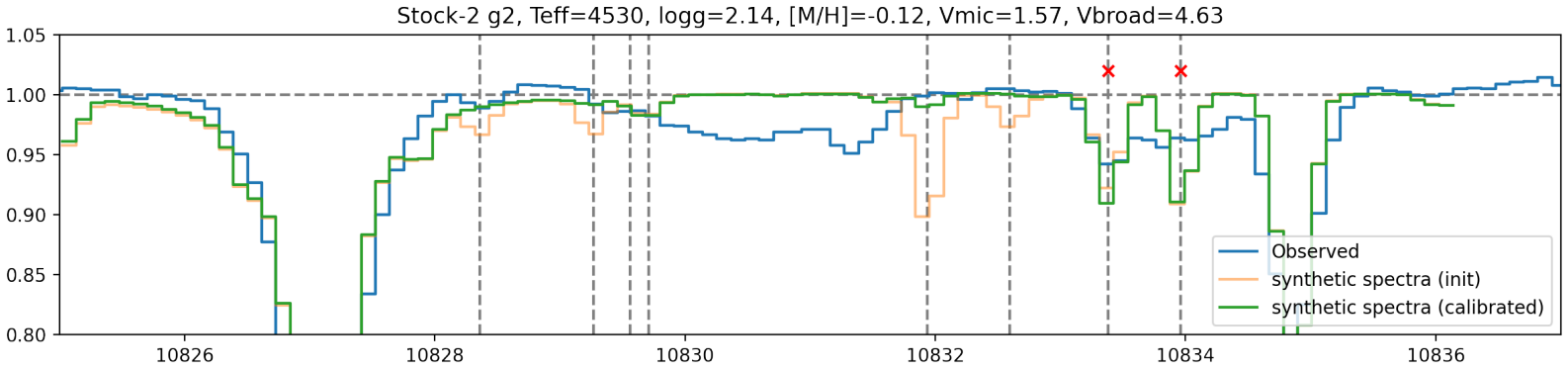


Figure D.2: The spectra around He 10 830 of Stock-2 g2 star, with the synthetic spectra for $\log gf$ calibration.

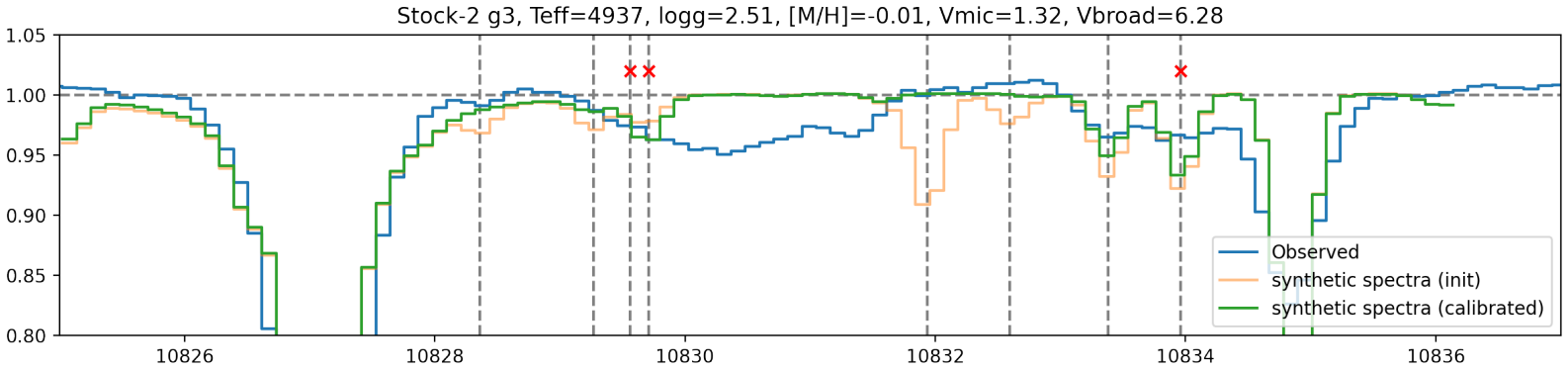


Figure D.3: The spectra around He 10 830 of Stock-2 g3 star, with the synthetic spectra for $\log gf$ calibration.

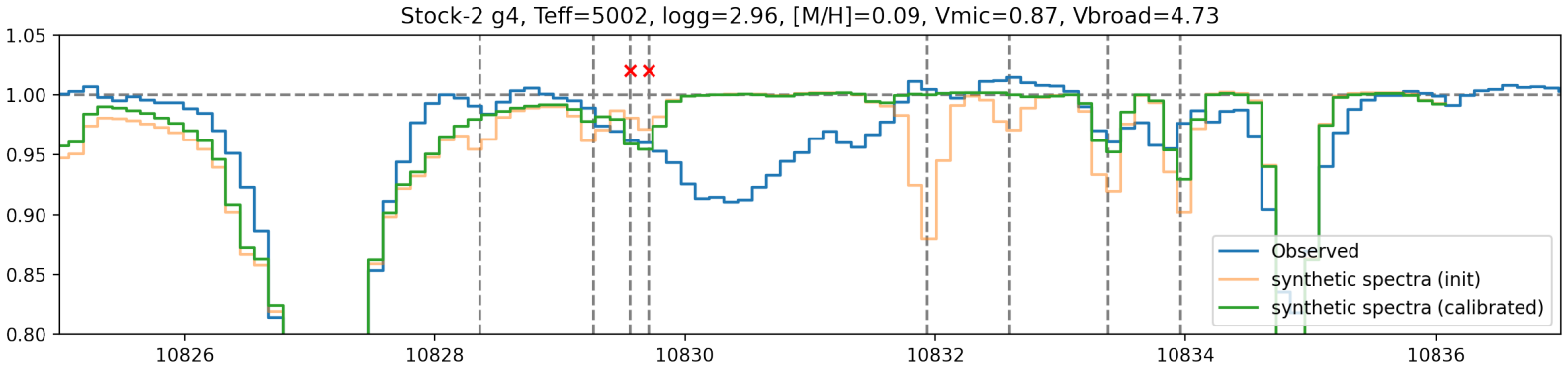


Figure D.4: The spectra around He 10 830 of Stock-2 g4 star, with the synthetic spectra for $\log gf$ calibration.

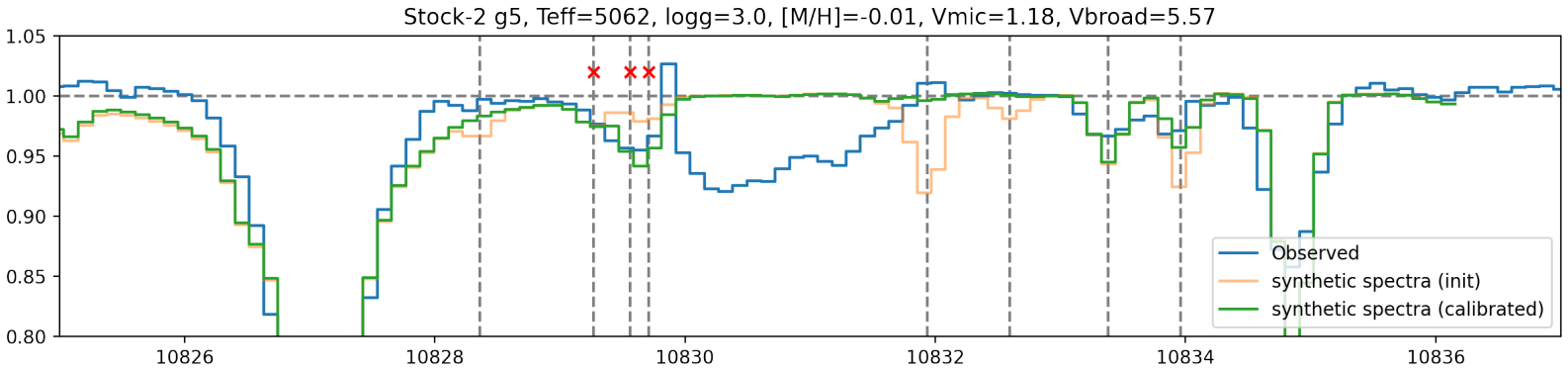


Figure D.5: The spectra around He 10 830 of Stock-2 g5 star, with the synthetic spectra for $\log gf$ calibration.

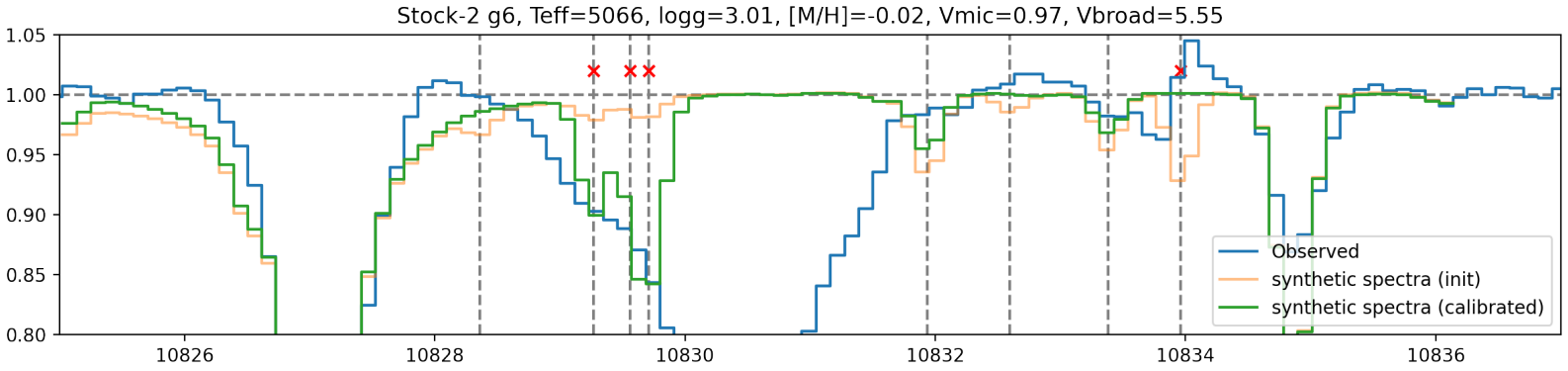


Figure D.6: The spectra around He 10 830 of Stock-2 g6 star, with the synthetic spectra for $\log gf$ calibration.

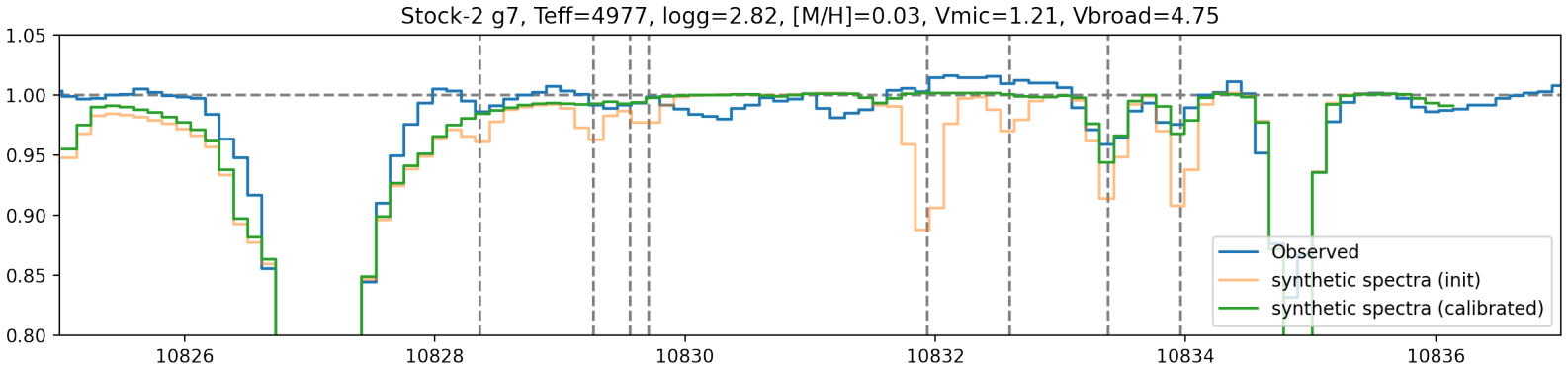


Figure D.7: The spectra around He 10 830 of Stock-2 g7 star, with the synthetic spectra for $\log gf$ calibration.

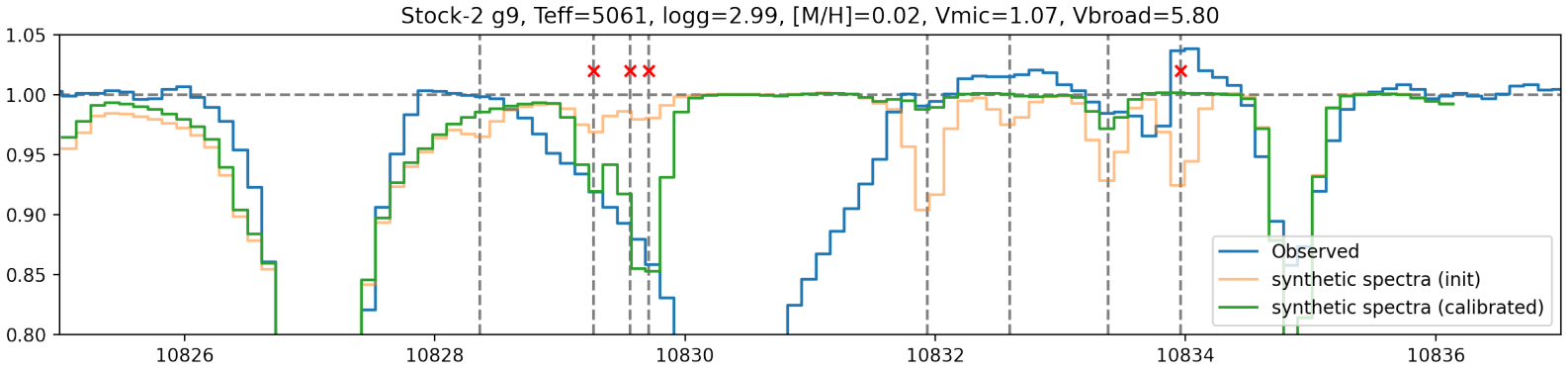


Figure D.8: The spectra around He 10 830 of Stock-2 g9 star, with the synthetic spectra for $\log gf$ calibration.

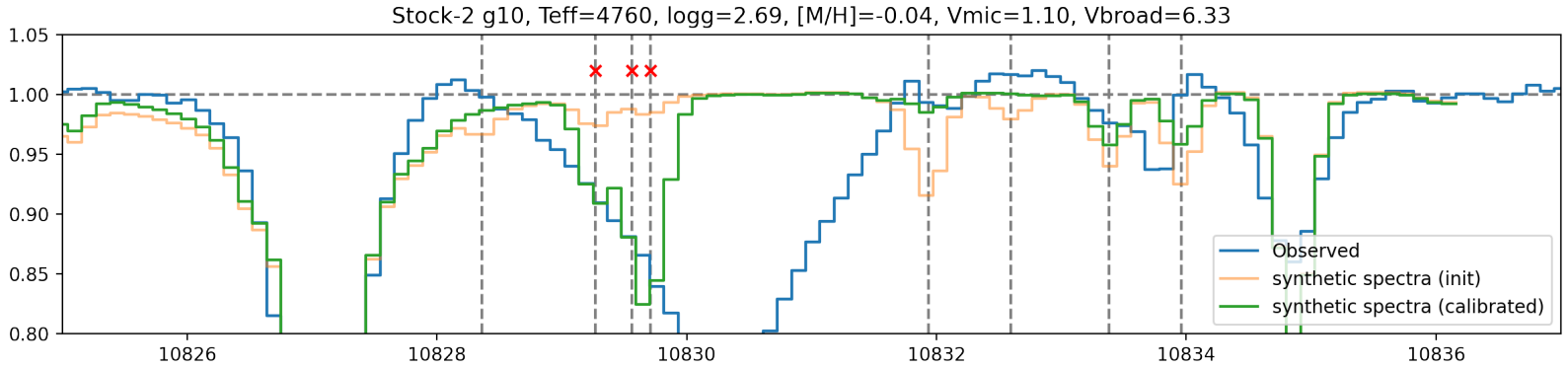


Figure D.9: The spectra around He 10 830 of Stock-2 g10 star, with the synthetic spectra for $\log gf$ calibration.

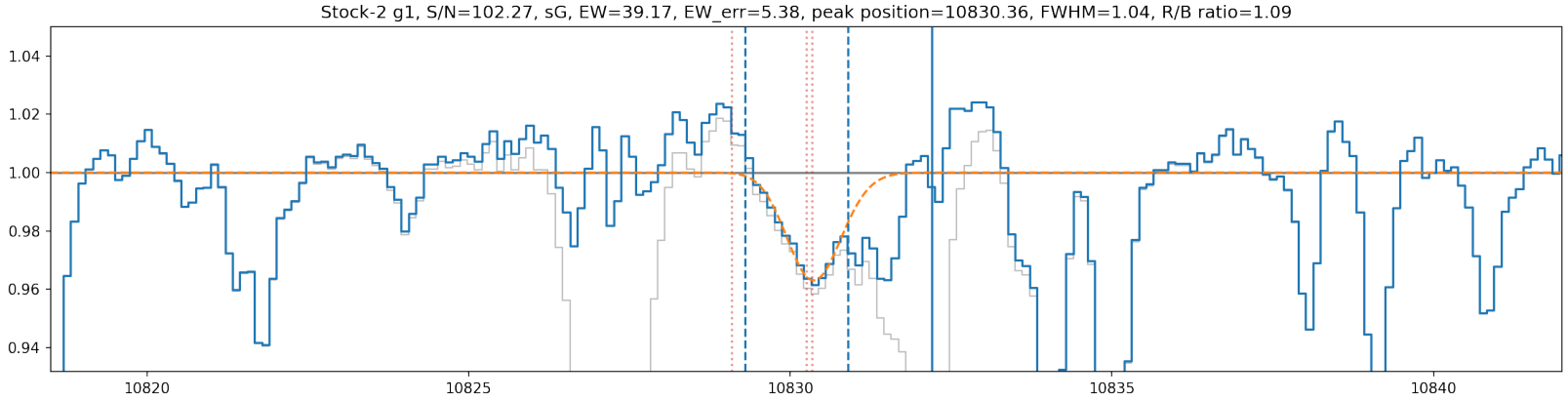


Figure D.10: The He 10 830 line spectra of Stock-2 g1 star, with the measurement result in the title.

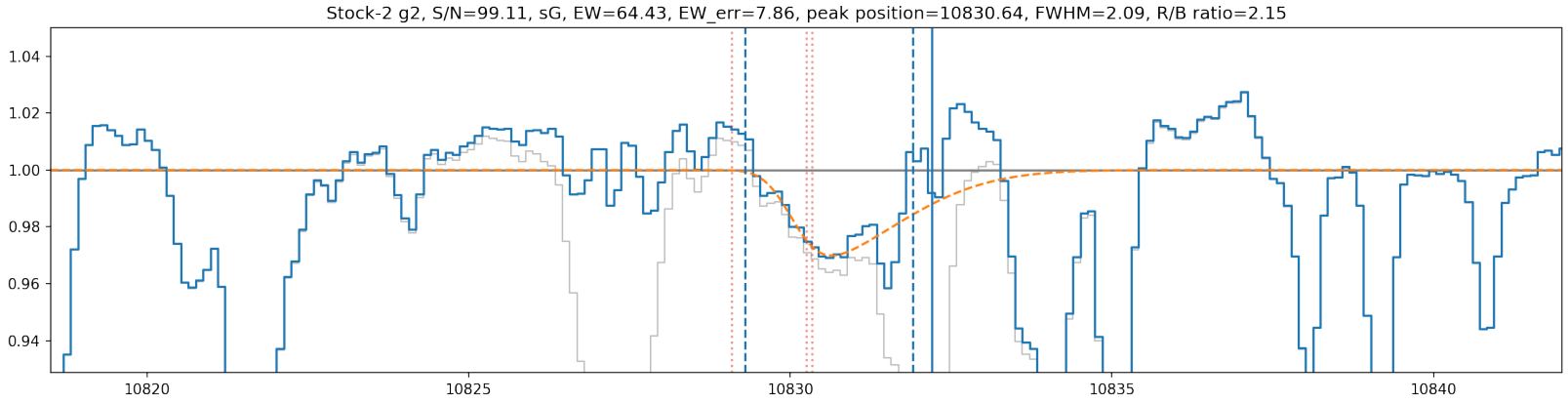


Figure D.11: The He 10 830 line spectra of Stock-2 g2 star, with the measurement result in the title.

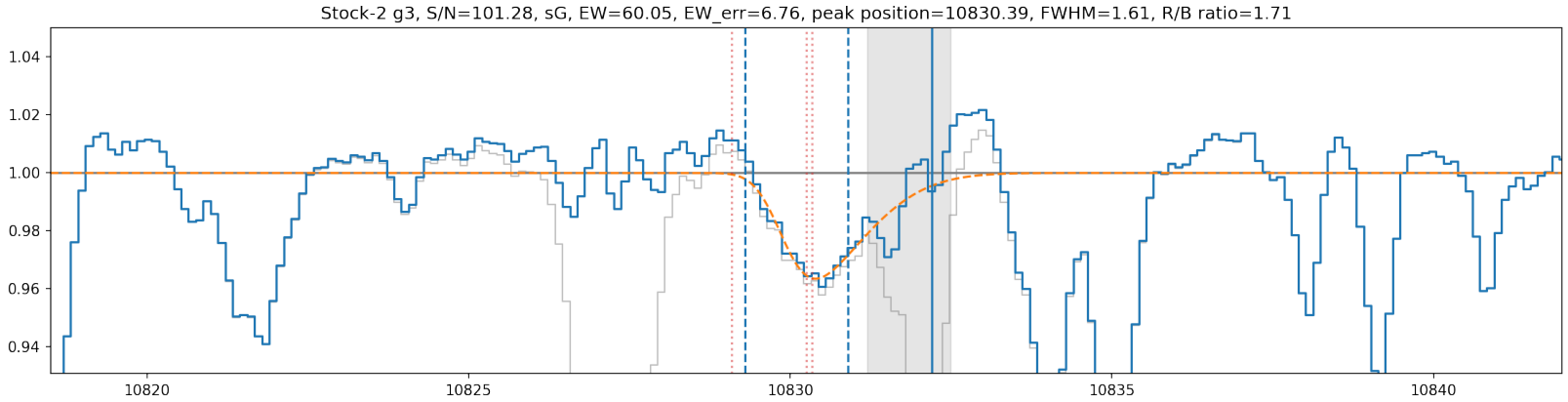


Figure D.12: The He 10 830 line spectra of Stock-2 g3 star, with the measurement result in the title.

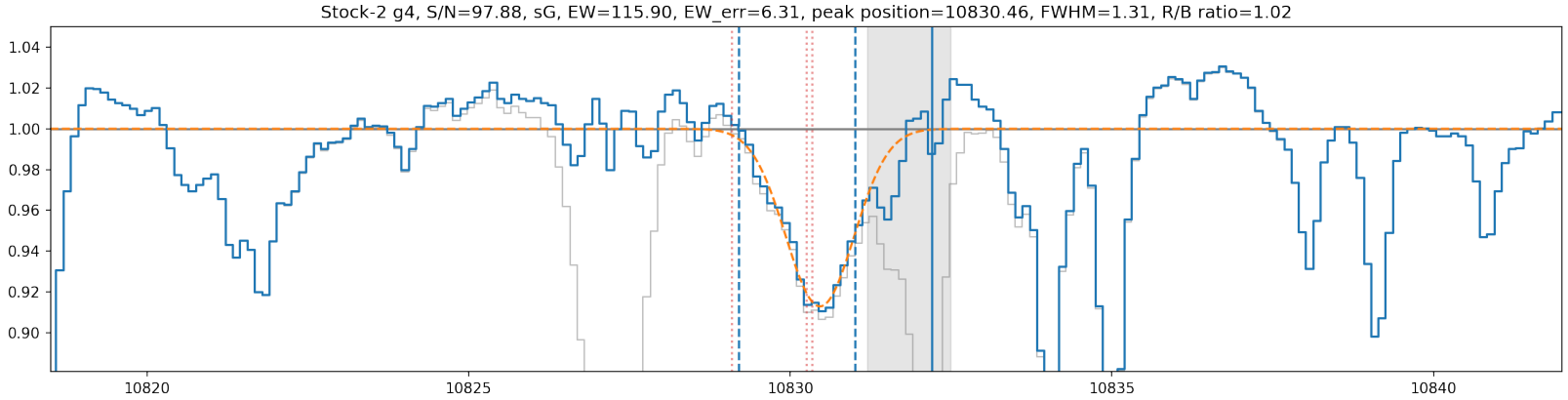


Figure D.13: The He 10 830 line spectra of Stock-2 g4 star, with the measurement result in the title.

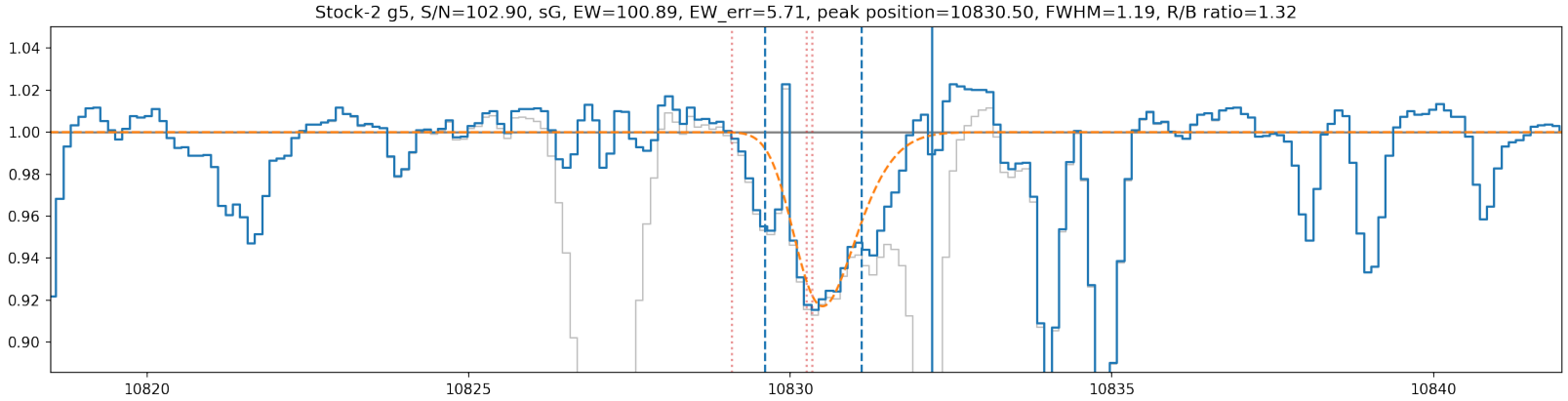


Figure D.14: The He 10 830 line spectra of Stock-2 g5 star, with the measurement result in the title.

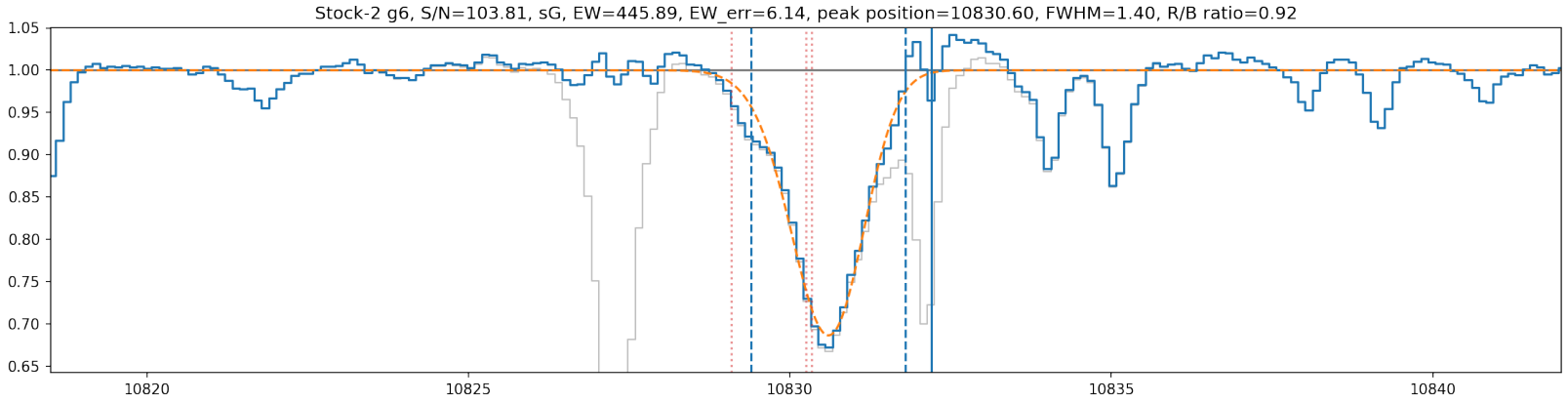


Figure D.15: The He 10 830 line spectra of Stock-2 g6 star, with the measurement result in the title.

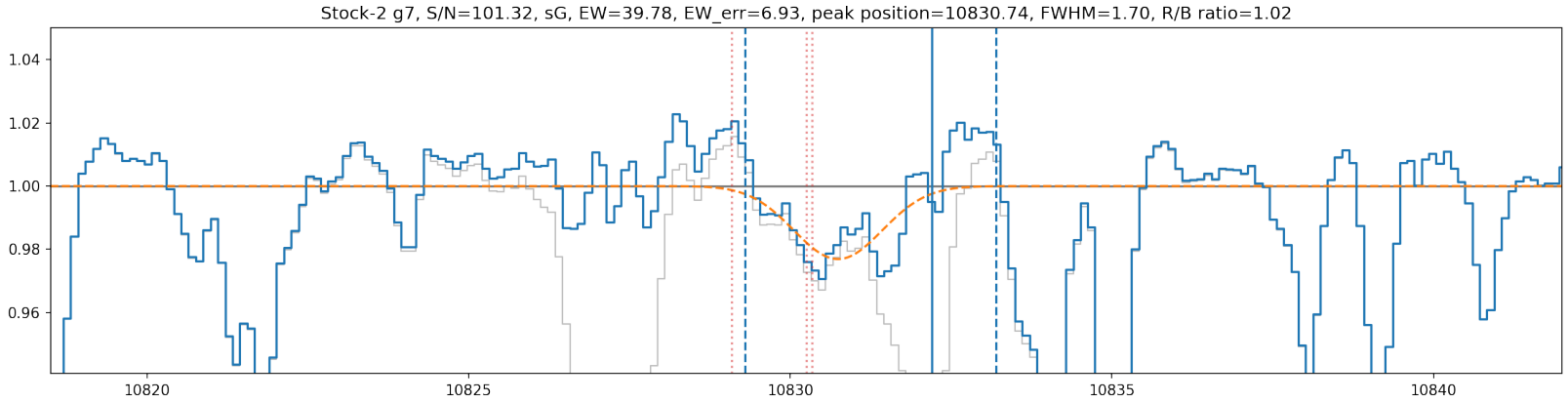


Figure D.16: The He 10 830 line spectra of Stock-2 g7 star, with the measurement result in the title.

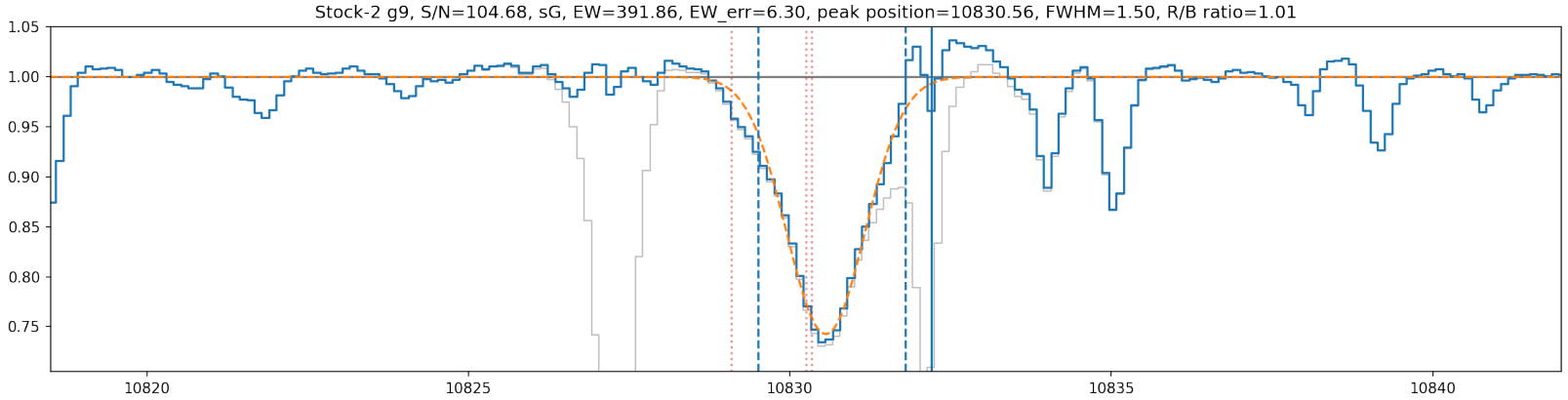


Figure D.17: The He 10 830 line spectra of Stock-2 g9 star, with the measurement result in the title.

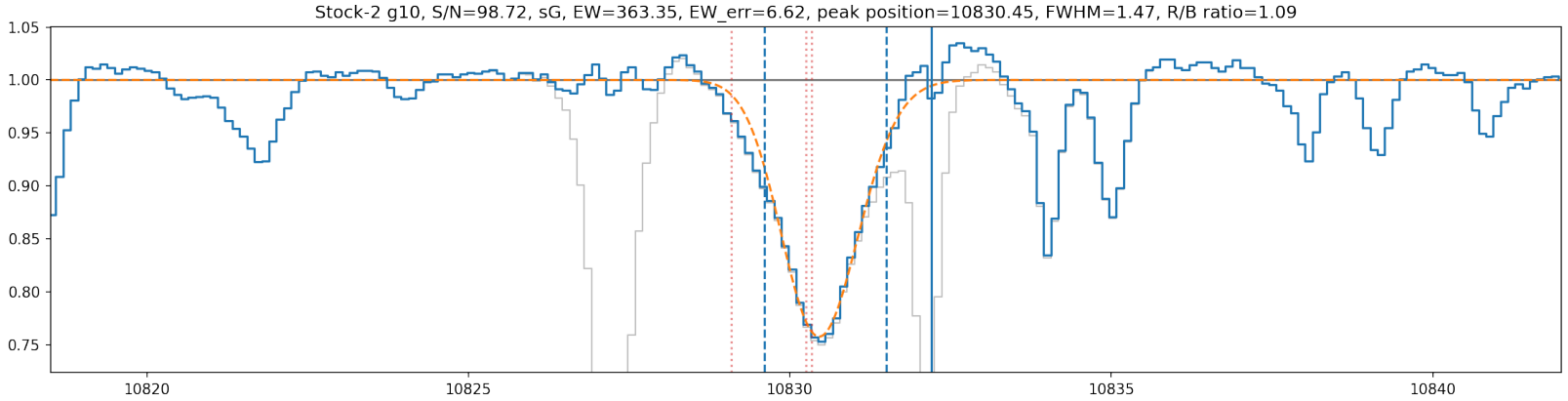


Figure D.18: The He 10 830 line spectra of Stock-2 g10 star, with the measurement result in the title.

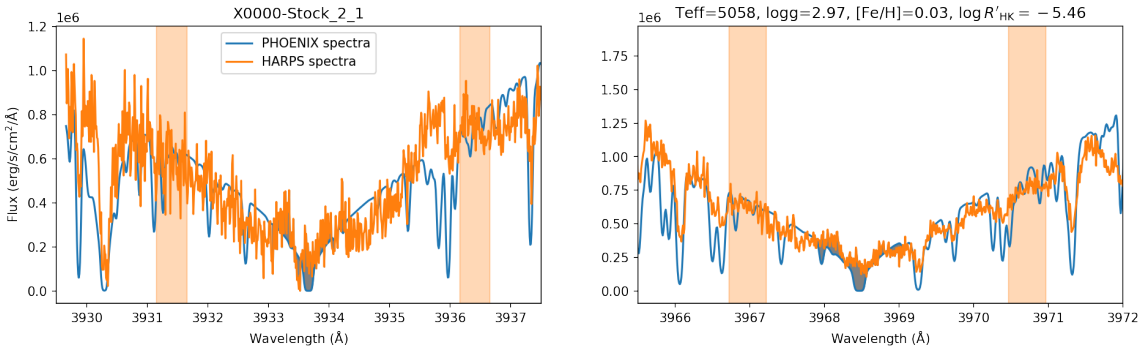


Figure D.19: The Ca II H&K line spectra of Stock-2 g1 star, with the measurement result of $\log R'_{\mathrm{HK}}$ in the title.

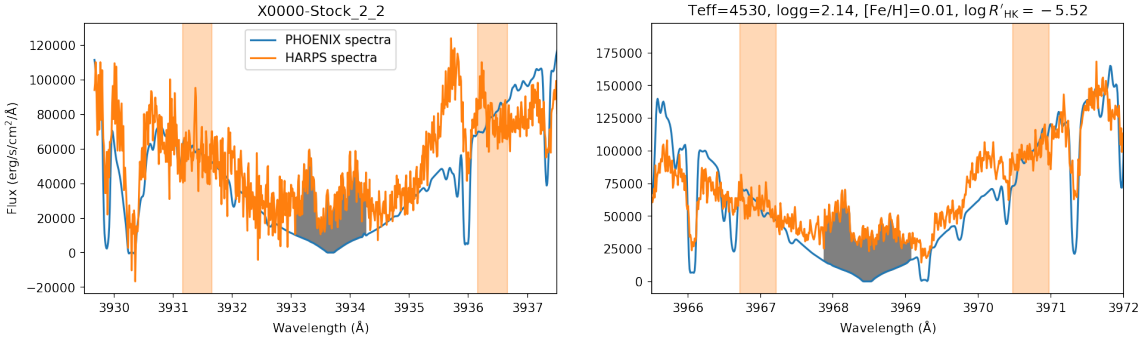


Figure D.20: The Ca II H&K line spectra of Stock-2 g2 star, with the measurement result of $\log R'_{\mathrm{HK}}$ in the title.

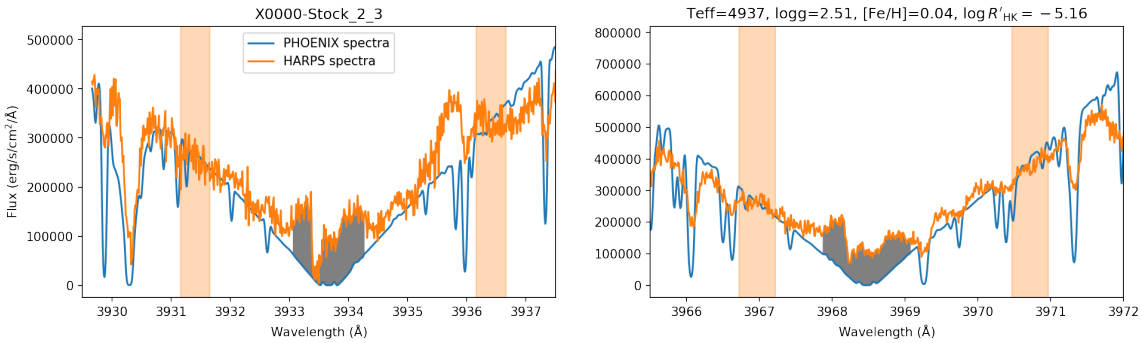


Figure D.21: The Ca II H&K line spectra of Stock-2 g3 star, with the measurement result of $\log R'_{\mathrm{HK}}$ in the title.

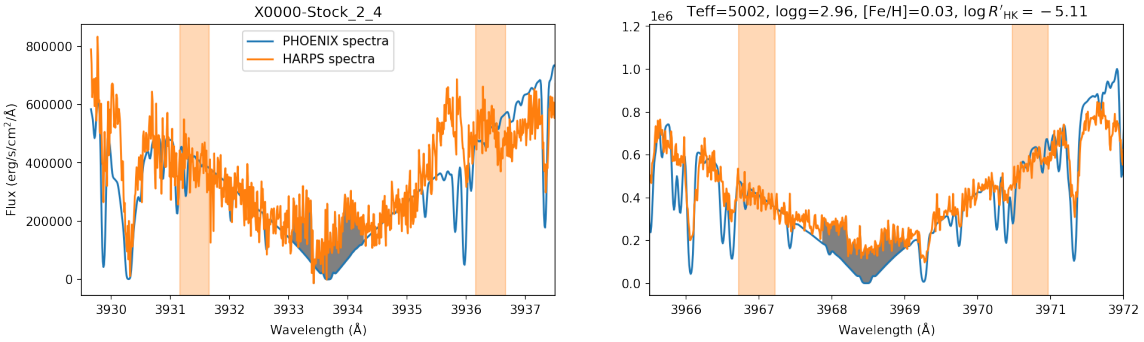


Figure D.22: The Ca II H&K line spectra of Stock-2 g4 star, with the measurement result of $\log R'_{\rm HK}$ in the title.

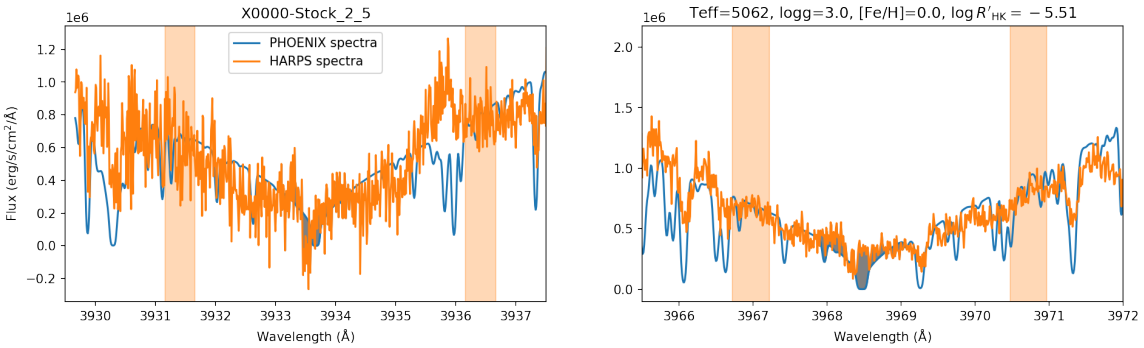


Figure D.23: The Ca II H&K line spectra of Stock-2 g5 star, with the measurement result of $\log R'_{\rm HK}$ in the title.

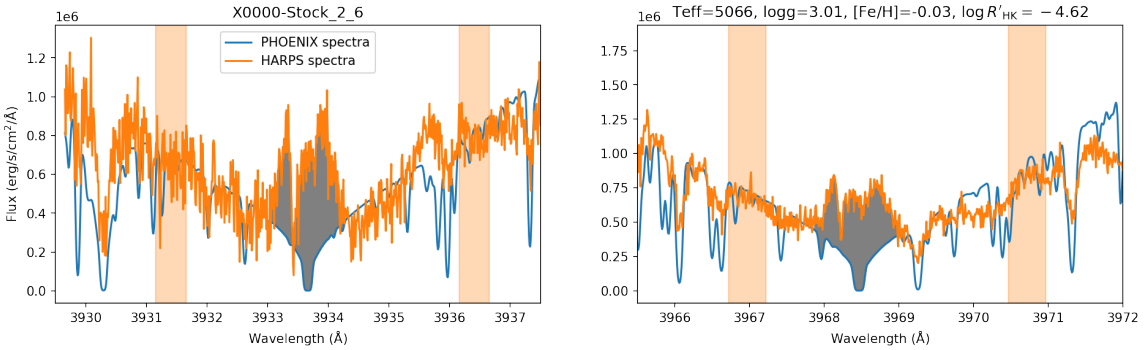


Figure D.24: The Ca II H&K line spectra of Stock-2 g6 star, with the measurement result of $\log R'_{\rm HK}$ in the title.

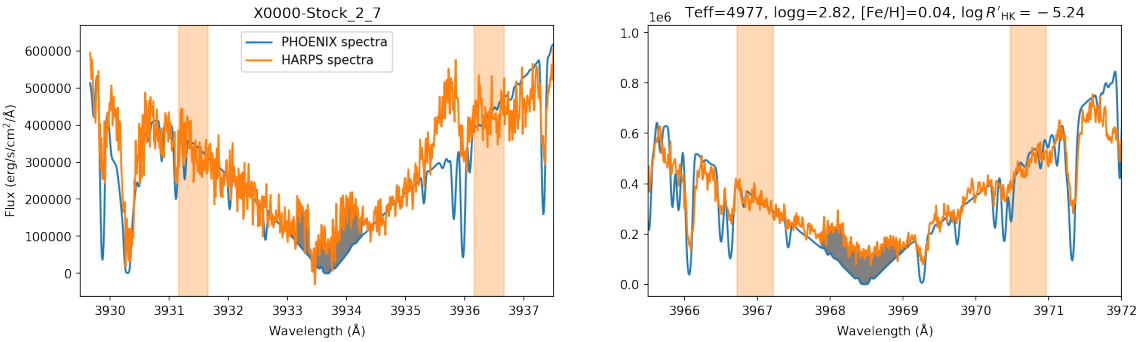


Figure D.25: The Ca II H&K line spectra of Stock-2 g7 star, with the measurement result of $\log R'_{\mathrm{HK}}$ in the title.

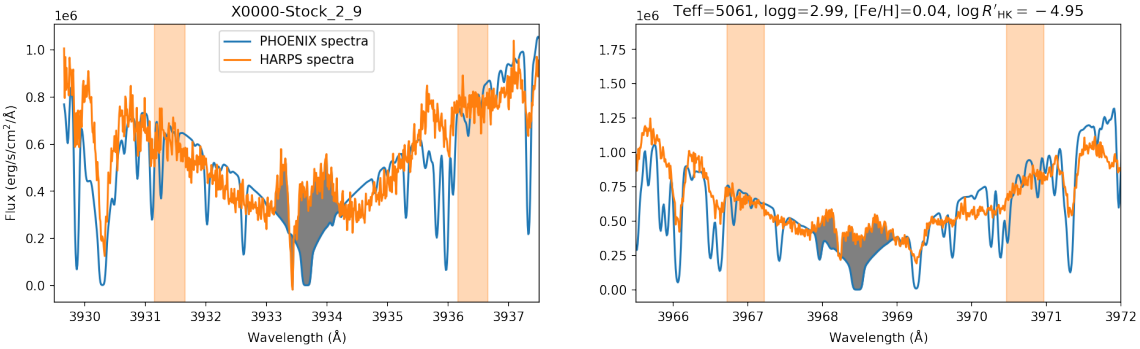


Figure D.26: The Ca II H&K line spectra of Stock-2 g9 star, with the measurement result of $\log R'_{\mathrm{HK}}$ in the title.

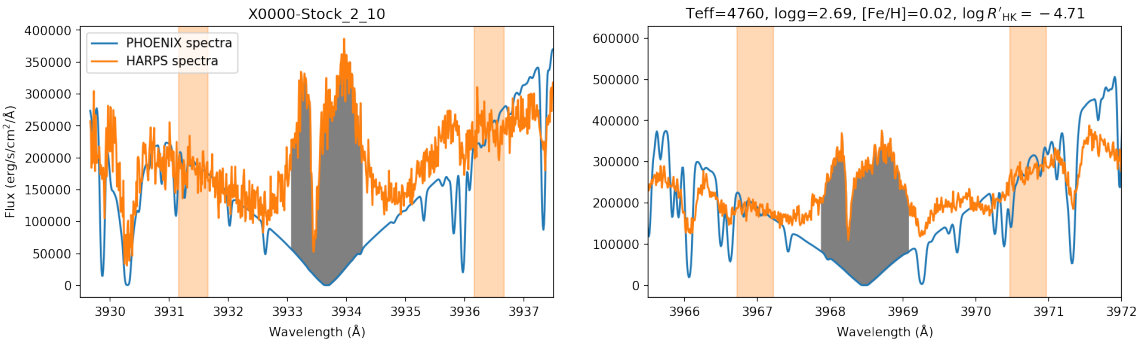


Figure D.27: The Ca II H&K line spectra of Stock-2 g10 star, with the measurement result of $\log R'_{\mathrm{HK}}$ in the title.

Appendix E

List of parameters and measurements on the field-XSL sample

This appendix lists the target list and measurement of 10 830 Å line strength, Ca II indices and fractional X-ray luminosity for the field-XSL sample.

Table E.1: Stellar paraemters and He 10 830 EW of the field-XSL stars

ID	Star	$T_{\rm eff}$ (K)	$\log g$	[Fe/H]	EW(He) (mÅ)
1	2MASS J17535707-2931427	4723 ± 37	2.03 ± 0.15	-0.04 ± 0.05	-2734 ± 36
2	2MASS J18033716-2954227	4250 ± 30	2.55 ± 0.15	0.45 ± 0.05	85 ± 15
3	2MASS J18351799-3428093	4528 ± 31	2.55 ± 0.14	-0.31 ± 0.06	70 ± 8
4	2MASS J18352206-3429112	4631 ± 32	2.52 ± 0.14	-0.09 ± 0.05	107 ± 9
5	2MASS J18352834-3444085	4808 ± 50	1.47 ± 0.15	-1.64 ± 0.07	27 ± 8
6	2MASS J18352834-3444085	4879 ± 52	1.54 ± 0.15	-1.55 ± 0.07	30 ± 6
7	2MASS J18355679-3434481	4287 ± 32	1.86 ± 0.15	-0.83 ± 0.06	-24 ± 17
8	BBB SMC 104	4363 ± 47	0.58 ± 0.19	-0.64 ± 0.11	-59 ± 9
9	BBB SMC 148	4270 ± 47	0.49 ± 0.19	-0.51 ± 0.11	35 ± 7
10	BD+01 2916	4343 ± 68	0.74 ± 0.19	-1.87 ± 0.14	-17 ± 15
11	BD+03 2688	4747 ± 46	1.43 ± 0.14	-1.27 ± 0.07	6 ± 6
12	BD+04 2466	5084 ± 63	1.99 ± 0.15	-1.87 ± 0.08	52 ± 3
13	BD+06 0648	4628 ± 50	1.31 ± 0.15	-1.92 ± 0.07	6 ± 7
14	BD+06 2986	3906 ± 51	4.65 ± 0.14	-0.38 ± 0.09	97 ± 6
15	BD+06 2986	3917 ± 51	4.65 ± 0.14	-0.37 ± 0.09	153 ± 10
16	BD+09 0352	6000 ± 135	4.00 ± 0.14	-2.09 ± 0.09	28 ± 7
17	BD+09 2190	6233 ± 141	4.00 ± 0.14	-2.27 ± 0.09	2 ± 8
18	BD+09 2860	5369 ± 67	2.57 ± 0.15	-1.58 ± 0.09	51 ± 8
19	BD+09 2870	4664 ± 51	1.47 ± 0.15	-2.34 ± 0.07	-18 ± 11
20	BD+09 3223	5498 ± 67	3.00 ± 0.14	-1.90 ± 0.08	38 ± 7
21	BD+17 4708	6245 ± 141	4.20 ± 0.14	-1.47 ± 0.09	34 ± 8
22	BD+17 4708	6189 ± 139	4.13 ± 0.14	-1.49 ± 0.09	32 ± 5
23	BD+17 4708	6186 ± 139	4.15 ± 0.14	-1.48 ± 0.09	28 ± 7
24	BD+18 2890	5042 ± 62	2.35 ± 0.15	-1.56 ± 0.08	42 ± 3
25	BD+20 3603	6166 ± 139	4.09 ± 0.14	-2.01 ± 0.09	26 ± 22

Continued on next page

(Continued)

ID	Star	$T_{\rm eff}$ (K)	$\log g$	[Fe/H]	EW(He) (mÅ)
26	BD+24 1676	6176 ± 139	3.99 ± 0.14	-2.19 ± 0.09	15 ± 6
27	BD+25 1981	6858 ± 196	4.28 ± 0.21	-1.20 ± 0.10	239 ± 7
28	BD+29 2091	5763 ± 130	4.09 ± 0.14	-1.97 ± 0.09	61 ± 1
29	BD+30 2034	4638 ± 46	1.23 ± 0.14	-1.65 ± 0.07	-471 ± 11
30	BD+30 2611	4372 ± 76	0.95 ± 0.21	-1.46 ± 0.14	-8 ± 18
31	BD+30 2611	4357 ± 68	0.96 ± 0.19	-1.48 ± 0.13	8 ± 2
32	BD-01 1792	5074 ± 66	3.34 ± 0.14	-0.88 ± 0.07	28 ± 10
33	BD-01 1792	5070 ± 66	3.33 ± 0.14	-0.89 ± 0.07	47 ± 6
34	BD-09 5831	4716 ± 49	1.56 ± 0.15	-1.77 ± 0.07	31 ± 5
35	BD-11 4126	4722 ± 49	4.60 ± 0.14	-0.04 ± 0.05	150 ± 9
36	BD-14 5890	4941 ± 50	2.17 ± 0.15	-2.06 ± 0.07	37 ± 5
37	BD-16 1934	3871 ± 33	1.51 ± 0.14	-0.26 ± 0.09	-9 ± 9
38	BD-16 1934	3872 ± 33	1.50 ± 0.14	-0.26 ± 0.09	-6 ± 10
39	BPS CS 30336-049	5933 ± 138	3.81 ± 0.15	-2.43 ± 0.09	9 ± 5
40	BS 4432	3967 ± 34	1.50 ± 0.14	-0.36 ± 0.09	18 ± 2
41	BS 4517	3733 ± 39	1.43 ± 0.15	-0.54 ± 0.09	49 ± 5
42	CD-24 15398	8000 ± 148	2.84 ± 0.21	-1.32 ± 0.10	315 ± 4
43	CD-26 10417	4700 ± 49	4.71 ± 0.14	-0.16 ± 0.05	232 ± 7
44	CD-28 9374	5034 ± 66	3.36 ± 0.14	-0.75 ± 0.07	66 ± 6
45	CD-30 18140	6189 ± 139	4.09 ± 0.14	-1.86 ± 0.09	11 ± 3
46	CD-49 11404	4589 ± 33	2.59 ± 0.15	0.03 ± 0.05	47 ± 10
47	CD-49 11404	4619 ± 33	2.65 ± 0.14	0.05 ± 0.05	43 ± 11
48	CD-60 3621	3836 ± 52	0.24 ± 0.19	0.13 ± 0.14	-11 ± 10
49	CD-60 3636	3900 ± 52	0.55 ± 0.19	0.10 ± 0.14	57 ± 9
50	CD-62 1346	5163 ± 63	1.96 ± 0.14	-1.54 ± 0.08	58 ± 9
51	CI Vel	4097 ± 64	0.32 ± 0.19	-1.03 ± 0.14	9 ± 5
52	CL* NGC 121 T V1	3728 ± 61	0.85 ± 0.19	-0.74 ± 0.17	-15 ± 11
53	CL* NGC 121 T V8	4243 ± 68	0.35 ± 0.20	-1.07 ± 0.14	30 ± 10
54	CL* NGC 1978 LE 09	3828 ± 33	1.11 ± 0.16	-0.53 ± 0.10	-13 ± 13
55	CL* NGC 1978 LE 09	3827 ± 33	1.09 ± 0.16	-0.51 ± 0.09	-1 ± 14
56	CL* NGC 1978 LE 09	3827 ± 33	1.07 ± 0.15	-0.55 ± 0.09	-12 ± 11
57	CL* NGC 2324 BSV 10828	4825 ± 33	1.86 ± 0.14	-0.24 ± 0.06	65 ± 2
58	CL* NGC 288 OCH 531	3810 ± 74	0.68 ± 0.19	-1.22 ± 0.20	-28 ± 14
59	CL* NGC 288 OCH 531	3675 ± 38	1.08 ± 0.14	-0.88 ± 0.09	-18 ± 6
60	CL* NGC 330 ROB A3	5518 ± 90	0.93 ± 0.19	-0.27 ± 0.14	265 ± 2
61	CL* NGC 330 ROB A3	5427 ± 74	0.89 ± 0.19	-0.30 ± 0.14	199 ± 8
62	CL* NGC 330 ROB B38	7515 ± 96	1.51 ± 0.21	-0.89 ± 0.09	3 ± 7
63	CL* NGC 371 FTW R20	3977 ± 53	0.09 ± 0.19	-0.16 ± 0.14	-7 ± 4
64	CL* NGC 419 LE 35	6222 ± 186	4.08 ± 0.38	-0.26 ± 0.18	5 ± 68
65	CL* NGC 5139 SAW V1	4431 ± 70	0.69 ± 0.19	-1.97 ± 0.14	-4 ± 7
66	CL* NGC 5139 SAW V1	5600 ± 82	1.68 ± 0.14	-1.18 ± 0.08	-69 ± 7
67	CL* NGC 5904 Arp III-03	4158 ± 42	1.02 ± 0.15	-1.23 ± 0.07	-11 ± 16
68	CL* NGC 5904 Arp IV-19	4242 ± 43	1.07 ± 0.15	-1.23 ± 0.07	-0 ± 14
69	CL* NGC 6121 LEE 2303	6957 ± 138	3.57 ± 0.22	-0.67 ± 0.09	39 ± 6
70	CL* NGC 6121 LEE 2626	4467 ± 54	1.65 ± 0.17	-1.20 ± 0.08	3 ± 11
71	CL* NGC 6121 LEE 2626	4490 ± 52	1.61 ± 0.16	-1.17 ± 0.08	3 ± 12
72	CL* NGC 6121 LEE 2626	4473 ± 62	1.62 ± 0.19	-1.20 ± 0.10	39 ± 10
73	CL* NGC 6121 LEE 4302	4737 ± 55	1.37 ± 0.16	-1.29 ± 0.08	16 ± 9
74	CL* NGC 6121 LEE 4302	4756 ± 58	1.41 ± 0.16	-1.26 ± 0.08	51 ± 11
75	CL* NGC 6121 LEE 4611	3938 ± 35	1.15 ± 0.16	-0.98 ± 0.10	-19 ± 17

Continued on next page

(Continued)

ID	Star	$T_{\rm eff}$ (K)	$\log g$	[Fe/H]	EW(He) (mÅ)
76	CL* NGC 6121 LEE 4611	3953 ± 48	1.06 ± 0.14	-1.04 ± 0.10	8 ± 6
77	CL* NGC 6121 LEE 4613	3953 ± 48	1.06 ± 0.14	-1.03 ± 0.10	19 ± 5
78	CL* NGC 6522 ARP 1021	4470 ± 33	2.52 ± 0.15	0.33 ± 0.05	14 ± 18
79	CL* NGC 6522 ARP 1021	4487 ± 31	2.54 ± 0.14	0.32 ± 0.05	-2 ± 15
80	CL* NGC 6522 ARP 1073	3817 ± 32	1.56 ± 0.14	-0.20 ± 0.09	-7 ± 5
81	CL* NGC 6522 ARP 3190	3813 ± 32	1.59 ± 0.14	-0.44 ± 0.09	13 ± 0
82	CL* NGC 6522 ARP 3213	3811 ± 74	0.49 ± 0.19	-1.70 ± 0.20	121 ± 9
83	CL* NGC 6522 ARP 4126	4300 ± 30	2.38 ± 0.14	-0.13 ± 0.05	43 ± 6
84	CL* NGC 6522 Arp 4329	4321 ± 40	1.72 ± 0.17	-0.88 ± 0.07	-5 ± 12
85	CL* NGC 6838 AH A2	4690 ± 34	2.47 ± 0.15	-0.82 ± 0.06	55 ± 8
86	CL* NGC 6838 AH A2	4683 ± 36	2.42 ± 0.15	-0.80 ± 0.06	33 ± 7
87	CL* NGC 6838 AH A2	4697 ± 40	2.43 ± 0.15	-0.80 ± 0.06	75 ± 16
88	CL* NGC 6838 AH A9	4140 ± 28	1.55 ± 0.14	-0.92 ± 0.06	29 ± 7
89	CL* NGC 6838 AH A9	4137 ± 28	1.54 ± 0.14	-0.92 ± 0.06	18 ± 7
90	G012-021	6045 ± 136	4.13 ± 0.14	-1.35 ± 0.09	20 ± 2
91	G013-035	6091 ± 137	4.12 ± 0.14	-1.67 ± 0.09	29 ± 2
92	G013-035	6095 ± 137	4.13 ± 0.14	-1.66 ± 0.09	10 ± 4
93	G018-039	6095 ± 137	4.15 ± 0.14	-1.42 ± 0.09	31 ± 9
94	G019-013	4185 ± 44	4.62 ± 0.14	-0.45 ± 0.06	147 ± 9
95	G021-024	4088 ± 43	4.62 ± 0.14	-0.20 ± 0.05	197 ± 15
96	G024-003	6062 ± 137	4.17 ± 0.14	-1.54 ± 0.09	25 ± 8
97	G029-023	6132 ± 138	4.08 ± 0.14	-1.69 ± 0.09	10 ± 8
98	G063-026	6129 ± 138	4.16 ± 0.14	-1.55 ± 0.09	48 ± 7
99	G169-28	5805 ± 131	4.20 ± 0.14	-1.39 ± 0.09	29 ± 11
100	G187-40	5846 ± 132	4.27 ± 0.14	-1.51 ± 0.09	12 ± 6
101	G188-22	6074 ± 137	4.14 ± 0.14	-1.34 ± 0.09	14 ± 6
102	G20-15	6161 ± 139	4.25 ± 0.14	-1.46 ± 0.09	18 ± 12
103	HD 100906	5058 ± 43	2.20 ± 0.14	-0.44 ± 0.07	33 ± 5
104	HD 101712	3588 ± 59	0.46 ± 0.19	-0.24 ± 0.17	-43 ± 12
105	HD 102634	6193 ± 97	4.12 ± 0.14	0.14 ± 0.06	16 ± 6
106	HD 103877	6958 ± 138	3.84 ± 0.21	0.65 ± 0.07	-18 ± 7
107	HD 103932	4374 ± 46	4.43 ± 0.14	0.03 ± 0.05	193 ± 8
108	HD 104893	4398 ± 69	0.81 ± 0.19	-2.25 ± 0.14	3 ± 3
109	HD 105740	4718 ± 33	2.76 ± 0.14	-0.66 ± 0.06	45 ± 11
110	HD 106304	8759 ± 250	3.16 ± 0.21	-1.67 ± 0.10	7 ± 5
111	HD 108564	4588 ± 48	4.67 ± 0.14	-0.95 ± 0.06	99 ± 4
112	HD 108915	5033 ± 66	3.39 ± 0.14	-0.08 ± 0.06	22 ± 13
113	HD 109307	8361 ± 166	3.35 ± 0.21	0.00 ± 0.07	-11 ± 6
114	HD 109443	6791 ± 134	4.24 ± 0.21	-0.60 ± 0.09	148 ± 3
115	HD 109871	3944 ± 33	1.69 ± 0.14	-0.24 ± 0.09	-20 ± 12
116	HD 110184	4460 ± 70	0.95 ± 0.19	-2.34 ± 0.14	13 ± 4
117	HD 110885	5616 ± 82	2.66 ± 0.14	-1.07 ± 0.08	158 ± 3
118	HD 111515	5384 ± 70	4.39 ± 0.14	-0.63 ± 0.07	35 ± 5
119	HD 111631	3888 ± 51	4.56 ± 0.14	0.05 ± 0.07	217 ± 10
120	HD 111721	5039 ± 61	2.66 ± 0.14	-1.34 ± 0.08	36 ± 4
121	HD 111786	7595 ± 216	4.28 ± 0.21	-1.01 ± 0.10	69 ± 2
122	HD 112374	6033 ± 97	0.63 ± 0.19	-0.65 ± 0.14	-12 ± 6
123	HD 113002	5062 ± 62	1.95 ± 0.14	-1.06 ± 0.08	26 ± 9
124	HD 11397	5449 ± 71	4.13 ± 0.14	-0.65 ± 0.07	33 ± 4
125	HD 114606	5585 ± 88	4.21 ± 0.14	-0.62 ± 0.07	44 ± 7

Continued on next page

(Continued)

ID	Star	$T_{\rm eff}$ (K)	$\log g$	[Fe/H]	EW(He) (mÅ)
126	HD 114960	4066 ± 28	2.30 ± 0.14	0.14 ± 0.05	12 ± 20
127	HD 116114	8358 ± 166	4.25 ± 0.21	0.81 ± 0.07	-14 ± 12
128	HD 116544	4438 ± 47	3.25 ± 0.14	0.16 ± 0.05	515 ± 5
129	HD 116745	6687 ± 123	2.31 ± 0.22	-1.33 ± 0.10	-24 ± 12
130	HD 116745	6679 ± 123	2.56 ± 0.21	-1.27 ± 0.10	16 ± 9
131	HD 117880	8843 ± 252	3.23 ± 0.21	-1.65 ± 0.10	14 ± 2
132	HD 118055	4411 ± 69	0.90 ± 0.19	-1.82 ± 0.14	11 ± 7
133	HD 118100	4255 ± 44	4.49 ± 0.14	-0.12 ± 0.05	135 ± 10
134	HD 119802	4638 ± 49	4.69 ± 0.14	-0.01 ± 0.05	265 ± 10
135	HD 119850	3521 ± 56	4.79 ± 0.14	-0.25 ± 0.09	129 ± 3
136	HD 122956	4669 ± 48	1.44 ± 0.15	-1.74 ± 0.07	10 ± 8
137	HD 124292	5408 ± 71	4.38 ± 0.14	-0.11 ± 0.06	24 ± 9
138	HD 126053	5588 ± 88	4.24 ± 0.14	-0.42 ± 0.07	28 ± 5
139	HD 126661	7617 ± 151	3.38 ± 0.21	0.38 ± 0.07	-9 ± 7
140	HD 126681	5588 ± 126	4.26 ± 0.14	-1.20 ± 0.09	52 ± 5
141	HD 126778	4814 ± 33	2.45 ± 0.14	-0.53 ± 0.06	30 ± 7
142	HD 128429	6342 ± 99	4.19 ± 0.14	-0.12 ± 0.06	177 ± 6
143	HD 128801	8774 ± 161	2.84 ± 0.21	-1.92 ± 0.10	13 ± 6
144	HD 130095	8882 ± 254	3.22 ± 0.21	-1.68 ± 0.10	7 ± 8
145	HD 130322	5398 ± 70	4.54 ± 0.14	0.11 ± 0.06	129 ± 9
146	HD 13043	5764 ± 90	4.08 ± 0.14	-0.03 ± 0.06	16 ± 7
147	HD 13043	5746 ± 90	4.04 ± 0.14	-0.03 ± 0.06	20 ± 15
148	HD 134063	4866 ± 36	2.30 ± 0.15	-0.71 ± 0.06	17 ± 12
149	HD 134063	4882 ± 35	2.35 ± 0.14	-0.69 ± 0.06	40 ± 10
150	HD 134439	5106 ± 96	4.61 ± 0.14	-1.35 ± 0.09	25 ± 3
151	HD 134440	4949 ± 75	4.75 ± 0.14	-1.27 ± 0.07	46 ± 2
152	HD 138290	6866 ± 136	4.21 ± 0.21	-0.03 ± 0.07	254 ± 2
153	HD 138776	5528 ± 86	4.04 ± 0.14	0.28 ± 0.06	22 ± 11
154	HD 138776	5523 ± 86	4.03 ± 0.14	0.27 ± 0.06	5 ± 10
155	HD 139717	6618 ± 85	1.35 ± 0.21	0.21 ± 0.07	2 ± 4
156	HD 140232	8077 ± 160	3.93 ± 0.21	0.42 ± 0.07	-8 ± 4
157	HD 140283	5719 ± 129	3.66 ± 0.14	-2.45 ± 0.09	25 ± 7
158	HD 140283	5718 ± 129	3.66 ± 0.14	-2.43 ± 0.09	8 ± 5
159	HD 141531	4445 ± 44	1.00 ± 0.14	-1.65 ± 0.07	-1 ± 5
160	HD 141531	4448 ± 43	1.02 ± 0.14	-1.65 ± 0.07	3 ± 7
161	HD 141531	4459 ± 44	1.03 ± 0.14	-1.63 ± 0.07	-10 ± 6
162	HD 141531	4451 ± 44	1.04 ± 0.14	-1.65 ± 0.07	-0 ± 8
163	HD 142575	6756 ± 134	4.21 ± 0.21	-0.72 ± 0.09	206 ± 4
164	HD 142703	7219 ± 206	4.24 ± 0.21	-1.16 ± 0.10	89 ± 2
165	HD 144172	6346 ± 99	4.10 ± 0.14	-0.44 ± 0.07	64 ± 8
166	HD 144921	4122 ± 64	0.47 ± 0.19	-1.69 ± 0.14	-12 ± 8
167	HD 144921	4172 ± 65	0.39 ± 0.19	-1.53 ± 0.13	11 ± 2
168	HD 14625	4753 ± 33	2.76 ± 0.14	0.20 ± 0.05	54 ± 3
169	HD 14938	6224 ± 97	4.20 ± 0.14	-0.32 ± 0.07	173 ± 1
170	HD 150281	5193 ± 68	4.59 ± 0.14	0.15 ± 0.06	89 ± 9
171	HD 157089	5774 ± 90	3.97 ± 0.14	-0.62 ± 0.07	16 ± 5
172	HD 16031	6165 ± 139	4.15 ± 0.14	-1.67 ± 0.09	39 ± 5
173	HD 160346	4926 ± 51	4.68 ± 0.14	0.02 ± 0.05	114 ± 4
174	HD 160365	6237 ± 97	3.41 ± 0.14	0.08 ± 0.06	288 ± 4
175	HD 161149	6899 ± 137	3.82 ± 0.21	0.38 ± 0.07	49 ± 6

Continued on next page

(Continued)

ID	Star	$T_{\rm eff}$ (K)	$\log g$	[Fe/H]	EW(He) (mÅ)
176	HD 161227	7238 ± 143	3.77 ± 0.21	0.44 ± 0.07	-11 ± 1
177	HD 161370	8568 ± 170	4.39 ± 0.21	-0.03 ± 0.07	-9 ± 13
178	HD 16160	4699 ± 49	4.58 ± 0.14	-0.21 ± 0.06	96 ± 8
179	HD 161770	5811 ± 131	3.84 ± 0.14	-1.53 ± 0.09	25 ± 7
180	HD 161817	7779 ± 143	2.43 ± 0.21	-1.31 ± 0.10	2 ± 4
181	HD 16232	6280 ± 98	4.29 ± 0.14	0.08 ± 0.06	206 ± 4
182	HD 162652	4928 ± 33	2.61 ± 0.14	0.00 ± 0.05	37 ± 9
183	HD 163346	7049 ± 140	4.16 ± 0.21	0.15 ± 0.07	50 ± 7
184	HD 1638	4239 ± 31	1.50 ± 0.15	-0.75 ± 0.06	-4 ± 23
185	HD 1638	4255 ± 30	1.58 ± 0.14	-0.77 ± 0.06	-9 ± 3
186	HD 1638	4252 ± 29	1.51 ± 0.14	-0.76 ± 0.06	31 ± 6
187	HD 1638	4249 ± 29	1.51 ± 0.14	-0.75 ± 0.06	51 ± 3
188	HD 163810	5706 ± 129	4.43 ± 0.14	-1.21 ± 0.09	96 ± 9
189	HD 164115	6792 ± 134	3.86 ± 0.21	0.15 ± 0.07	130 ± 6
190	HD 16456	7830 ± 144	2.38 ± 0.21	-1.47 ± 0.10	20 ± 4
191	HD 164967	9351 ± 187	4.52 ± 0.21	-0.29 ± 0.09	36 ± 12
192	HD 165195	4404 ± 69	0.83 ± 0.19	-2.27 ± 0.14	16 ± 2
193	HD 165887	8297 ± 165	3.62 ± 0.21	-0.04 ± 0.07	1 ± 8
194	HD 166161	5246 ± 65	2.17 ± 0.15	-1.21 ± 0.08	48 ± 4
195	HD 166283	8296 ± 165	3.94 ± 0.21	0.04 ± 0.07	-2 ± 11
196	HD 16673	6189 ± 97	4.27 ± 0.14	-0.05 ± 0.06	159 ± 6
197	HD 166991	9008 ± 179	4.49 ± 0.21	-0.20 ± 0.09	4 ± 2
198	HD 167278	6521 ± 130	4.22 ± 0.21	-0.13 ± 0.07	144 ± 8
199	HD 169032	8301 ± 166	3.48 ± 0.22	-0.04 ± 0.07	33 ± 22
200	HD 170413	4740 ± 33	2.51 ± 0.14	-0.08 ± 0.05	20 ± 2
201	HD 17072	5389 ± 65	2.53 ± 0.14	-1.06 ± 0.08	48 ± 5
202	HD 17072	5369 ± 65	2.46 ± 0.14	-1.09 ± 0.08	59 ± 4
203	HD 170756	5274 ± 66	1.39 ± 0.15	-1.36 ± 0.09	59 ± 10
204	HD 170820	4478 ± 31	1.28 ± 0.14	-0.03 ± 0.05	-12 ± 20
205	HD 170899	4640 ± 32	2.04 ± 0.14	-0.24 ± 0.06	83 ± 11
206	HD 171234	8070 ± 160	3.95 ± 0.21	0.06 ± 0.07	14 ± 4
207	HD 171367	4385 ± 30	2.15 ± 0.14	-0.74 ± 0.06	52 ± 4
208	HD 171496	4925 ± 35	2.11 ± 0.14	-0.77 ± 0.06	35 ± 6
209	HD 171496	4924 ± 35	2.15 ± 0.14	-0.76 ± 0.06	23 ± 3
210	HD 171496	4926 ± 35	2.12 ± 0.14	-0.76 ± 0.06	21 ± 9
211	HD 172230	7610 ± 151	3.44 ± 0.21	0.56 ± 0.07	-16 ± 11
212	HD 172365	5989 ± 60	1.30 ± 0.14	0.12 ± 0.06	171 ± 3
213	HD 172472	4931 ± 35	1.69 ± 0.14	-0.05 ± 0.05	308 ± 8
214	HD 172506	7096 ± 140	4.02 ± 0.21	-0.02 ± 0.07	99 ± 3
215	HD 172522	8752 ± 175	3.31 ± 0.21	0.06 ± 0.07	-4 ± 3
216	HD 173073	8400 ± 167	3.45 ± 0.21	-0.26 ± 0.09	-4 ± 7
217	HD 173158	5268 ± 73	0.95 ± 0.19	0.22 ± 0.11	-52 ± 13
218	HD 173369	8052 ± 160	3.46 ± 0.21	0.36 ± 0.07	9 ± 7
219	HD 173669	8841 ± 176	4.06 ± 0.21	-0.23 ± 0.09	-0 ± 4
220	HD 174240	9262 ± 189	3.65 ± 0.21	-0.40 ± 0.09	-6 ± 13
221	HD 174350	4781 ± 33	2.36 ± 0.14	-0.01 ± 0.05	58 ± 6
222	HD 174512	6743 ± 86	2.99 ± 0.21	-0.16 ± 0.07	4 ± 5
223	HD 174866	7971 ± 158	3.93 ± 0.21	0.04 ± 0.07	22 ± 6
224	HD 174966	7697 ± 153	3.91 ± 0.21	0.08 ± 0.07	104 ± 6
225	HD 174966	7699 ± 153	3.91 ± 0.21	0.10 ± 0.07	12 ± 14

Continued on next page

(Continued)

ID	Star	$T_{\rm eff}$ (K)	$\log g$	[Fe/H]	EW(He) (mÅ)
226	HD 174966	7733 ± 154	3.96 ± 0.21	0.11 ± 0.07	85 ± 20
227	HD 175058	7862 ± 156	3.01 ± 0.21	-0.27 ± 0.09	2 ± 6
228	HD 175181	5026 ± 43	2.54 ± 0.14	-0.08 ± 0.06	26 ± 5
229	HD 175376	4289 ± 29	2.59 ± 0.14	0.33 ± 0.05	70 ± 15
230	HD 175545	4454 ± 31	2.88 ± 0.14	0.08 ± 0.05	88 ± 20
231	HD 175805	6265 ± 98	3.99 ± 0.14	0.26 ± 0.06	167 ± 4
232	HD 175805	6253 ± 98	3.96 ± 0.14	0.26 ± 0.06	139 ± 10
233	HD 175892	9014 ± 180	4.48 ± 0.21	-0.20 ± 0.09	-18 ± 7
234	HD 176698	4977 ± 35	2.74 ± 0.14	0.08 ± 0.05	78 ± 11
235	HD 176851	6834 ± 135	3.70 ± 0.21	0.42 ± 0.07	51 ± 6
236	HD 178287	5857 ± 60	1.07 ± 0.14	0.18 ± 0.06	72 ± 5
237	HD 179315	5940 ± 60	1.17 ± 0.14	0.25 ± 0.06	31 ± 3
238	HD 179870	4846 ± 34	2.13 ± 0.14	0.09 ± 0.05	89 ± 5
239	HD 179870	4904 ± 35	2.29 ± 0.14	0.13 ± 0.05	73 ± 3
240	HD 180086	7123 ± 141	3.83 ± 0.21	0.10 ± 0.07	89 ± 10
241	HD 183085	7004 ± 139	3.85 ± 0.21	-0.09 ± 0.07	87 ± 4
242	HD 184266	5935 ± 134	3.15 ± 0.14	-1.13 ± 0.09	165 ± 2
243	HD 184571	6465 ± 101	4.06 ± 0.14	-0.03 ± 0.06	78 ± 5
244	HD 185094	7023 ± 139	4.13 ± 0.21	0.09 ± 0.07	128 ± 4
245	HD 186478	4716 ± 48	1.57 ± 0.15	-2.31 ± 0.07	1 ± 4
246	HD 187111	4458 ± 44	1.12 ± 0.14	-1.67 ± 0.07	-27 ± 2
247	HD 18769	8248 ± 163	3.42 ± 0.21	0.25 ± 0.07	-13 ± 5
248	HD 188262	5878 ± 92	3.20 ± 0.14	0.22 ± 0.06	383 ± 4
249	HD 188262	5919 ± 93	3.25 ± 0.15	0.27 ± 0.06	233 ± 12
250	HD 188510	5531 ± 124	4.29 ± 0.14	-1.57 ± 0.09	-34 ± 4
251	HD 18907	5076 ± 66	3.68 ± 0.14	-0.71 ± 0.07	56 ± 5
252	HD 189511	4962 ± 34	1.82 ± 0.14	-0.04 ± 0.05	169 ± 4
253	HD 190073	8065 ± 151	2.85 ± 0.22	-1.81 ± 0.11	-421 ± 28
254	HD 19019	6031 ± 94	4.32 ± 0.14	-0.15 ± 0.06	133 ± 7
255	HD 190390	6192 ± 90	1.49 ± 0.14	-1.12 ± 0.08	14 ± 5
256	HD 190404	4998 ± 53	4.65 ± 0.14	-0.69 ± 0.06	30 ± 11
257	HD 190404	4993 ± 52	4.65 ± 0.14	-0.65 ± 0.06	41 ± 10
258	HD 190404	4983 ± 52	4.65 ± 0.14	-0.67 ± 0.06	37 ± 8
259	HD 191709	6672 ± 132	3.89 ± 0.21	0.27 ± 0.07	150 ± 3
260	HD 19304	6582 ± 130	4.22 ± 0.21	-0.45 ± 0.09	98 ± 9
261	HD 193225	7318 ± 145	4.00 ± 0.21	0.09 ± 0.07	66 ± 4
262	HD 193281	8634 ± 172	4.13 ± 0.21	-0.36 ± 0.09	2 ± 8
263	HD 193281	8695 ± 175	4.11 ± 0.21	-0.37 ± 0.09	-31 ± 19
264	HD 193326	5127 ± 44	2.80 ± 0.14	-0.26 ± 0.07	53 ± 6
265	HD 193896	5206 ± 44	2.55 ± 0.14	-0.07 ± 0.06	46 ± 6
266	HD 193896	5251 ± 45	2.66 ± 0.14	-0.02 ± 0.06	40 ± 8
267	HD 195729	8143 ± 161	3.60 ± 0.21	0.08 ± 0.07	11 ± 7
268	HD 196125	7246 ± 143	3.89 ± 0.21	0.02 ± 0.07	45 ± 3
269	HD 196218	6200 ± 97	4.15 ± 0.14	-0.15 ± 0.06	-1 ± 10
270	HD 196892	6004 ± 135	4.04 ± 0.14	-1.04 ± 0.09	13 ± 9
271	HD 196892	6007 ± 135	4.08 ± 0.14	-1.02 ± 0.09	29 ± 9
272	HD 19787	4805 ± 32	2.69 ± 0.14	0.09 ± 0.05	32 ± 7
273	HD 200081	5708 ± 90	3.74 ± 0.14	0.19 ± 0.06	28 ± 10
274	HD 200081	5735 ± 90	3.74 ± 0.14	0.19 ± 0.06	7 ± 12
275	HD 200494	4428 ± 30	2.81 ± 0.14	0.12 ± 0.05	20 ± 9

Continued on next page

(Continued)

ID	Star	$T_{\rm eff}$ (K)	$\log g$	[Fe/H]	EW(He) (mÅ)
276	HD 200779	4206 ± 44	4.56 ± 0.14	0.01 ± 0.05	158 ± 12
277	HD 201053	4880 ± 34	2.74 ± 0.14	0.05 ± 0.05	60 ± 11
278	HD 201237	4816 ± 50	4.63 ± 0.14	0.06 ± 0.05	97 ± 15
279	HD 201237	4818 ± 50	4.63 ± 0.14	0.07 ± 0.05	107 ± 17
280	HD 201237	4782 ± 50	4.60 ± 0.14	0.04 ± 0.05	72 ± 11
281	HD 201377	8208 ± 163	3.85 ± 0.21	0.03 ± 0.07	4 ± 7
282	HD 201626	4850 ± 63	1.75 ± 0.18	-1.75 ± 0.09	2 ± 21
283	HD 201626	4864 ± 52	1.85 ± 0.15	-1.67 ± 0.07	58 ± 12
284	HD 202851	4733 ± 33	1.60 ± 0.14	-0.88 ± 0.06	49 ± 12
285	HD 202851	4772 ± 32	1.70 ± 0.14	-0.85 ± 0.06	63 ± 10
286	HD 204041	8458 ± 168	4.40 ± 0.21	-0.42 ± 0.09	9 ± 5
287	HD 204041	8470 ± 168	4.38 ± 0.21	-0.42 ± 0.09	7 ± 14
288	HD 204155	5703 ± 90	3.91 ± 0.14	-0.76 ± 0.07	26 ± 6
289	HD 204155	5695 ± 89	3.90 ± 0.14	-0.76 ± 0.07	9 ± 9
290	HD 204543	4516 ± 71	0.99 ± 0.19	-2.06 ± 0.14	-1 ± 5
291	HD 204587	4091 ± 43	4.63 ± 0.14	-0.12 ± 0.05	118 ± 6
292	HD 204587	4091 ± 43	4.63 ± 0.14	-0.11 ± 0.05	116 ± 9
293	HD 205202	6572 ± 132	4.12 ± 0.22	-0.47 ± 0.09	331 ± 13
294	HD 205202	6568 ± 130	4.09 ± 0.21	-0.46 ± 0.09	282 ± 8
295	HD 205555	7257 ± 144	3.70 ± 0.21	0.22 ± 0.07	29 ± 4
296	HD 205734	7952 ± 158	3.68 ± 0.21	0.00 ± 0.07	36 ± 6
297	HD 205734	7939 ± 158	3.66 ± 0.21	-0.01 ± 0.07	9 ± 6
298	HD 205734	7947 ± 158	3.68 ± 0.21	-0.02 ± 0.07	23 ± 7
299	HD 20619	5620 ± 88	4.35 ± 0.14	-0.26 ± 0.07	98 ± 4
300	HD 207222	9498 ± 191	4.57 ± 0.21	-0.35 ± 0.09	-14 ± 8
301	HD 207222	9077 ± 185	4.03 ± 0.21	-0.32 ± 0.09	-10 ± 4
302	HD 207222	9489 ± 191	4.57 ± 0.21	-0.36 ± 0.09	3 ± 7
303	HD 207795	5302 ± 69	4.57 ± 0.14	0.13 ± 0.06	151 ± 8
304	HD 209290	3741 ± 59	4.75 ± 0.14	-0.19 ± 0.07	205 ± 10
305	HD 209290	3731 ± 59	4.73 ± 0.14	-0.15 ± 0.07	178 ± 16
306	HD 210295	4823 ± 49	2.15 ± 0.15	-1.33 ± 0.07	19 ± 9
307	HD 211075	4349 ± 30	1.99 ± 0.14	-0.39 ± 0.06	-12 ± 8
308	HD 21197	4340 ± 45	4.44 ± 0.14	0.15 ± 0.05	132 ± 14
309	HD 212516	3692 ± 38	1.34 ± 0.14	-0.37 ± 0.09	-13 ± 10
310	HD 213042	4475 ± 47	4.35 ± 0.14	0.09 ± 0.05	104 ± 14
311	HD 215578	4978 ± 34	2.89 ± 0.14	0.15 ± 0.05	33 ± 12
312	HD 215578	4979 ± 34	2.90 ± 0.14	0.15 ± 0.05	17 ± 10
313	HD 215578	5006 ± 43	2.97 ± 0.14	0.16 ± 0.06	20 ± 8
314	HD 216143	4661 ± 48	1.40 ± 0.15	-2.04 ± 0.07	63 ± 6
315	HD 216219	5553 ± 57	2.87 ± 0.15	-0.47 ± 0.07	45 ± 7
316	HD 216219	5614 ± 58	2.87 ± 0.14	-0.43 ± 0.07	81 ± 3
317	HD 217357	3958 ± 52	4.60 ± 0.14	-0.08 ± 0.07	196 ± 2
318	HD 217877	5877 ± 92	4.15 ± 0.14	-0.18 ± 0.06	-5 ± 8
319	HD 217877	5866 ± 92	4.17 ± 0.14	-0.19 ± 0.06	21 ± 5
320	HD 218502	6174 ± 139	4.08 ± 0.14	-1.75 ± 0.09	18 ± 5
321	HD 218566	4761 ± 50	4.50 ± 0.14	0.17 ± 0.05	150 ± 9
322	HD 218566	4746 ± 49	4.46 ± 0.14	0.15 ± 0.05	128 ± 11
323	HD 218857	5107 ± 63	2.58 ± 0.14	-1.90 ± 0.08	38 ± 7
324	HD 220662	4607 ± 46	1.29 ± 0.14	-1.81 ± 0.07	5 ± 9
325	HD 220838	4445 ± 44	1.03 ± 0.14	-1.75 ± 0.07	-11 ± 7

Continued on next page

(Continued)

ID	Star	$T_{\rm eff}$ (K)	$\log g$	[Fe/H]	EW(He) (mÅ)
326	HD 221149	5867 ± 92	3.91 ± 0.14	0.15 ± 0.06	6 ± 12
327	HD 221170	4597 ± 49	1.27 ± 0.15	-2.04 ± 0.07	-27 ± 11
328	HD 222434	4504 ± 44	1.12 ± 0.14	-1.81 ± 0.07	-23 ± 6
329	HD 232078	4001 ± 63	0.63 ± 0.19	-1.61 ± 0.14	3 ± 7
330	HD 232078	3987 ± 77	0.64 ± 0.19	-1.56 ± 0.20	-3 ± 7
331	HD 23924	8079 ± 160	3.91 ± 0.21	0.31 ± 0.07	-4 ± 6
332	HD 24616	5020 ± 66	3.35 ± 0.14	-0.74 ± 0.07	49 ± 2
333	HD 250792	5686 ± 128	4.45 ± 0.14	-1.01 ± 0.09	57 ± 2
334	HD 25329	4923 ± 75	4.52 ± 0.14	-1.61 ± 0.07	76 ± 20
335	HD 25532	5622 ± 82	2.66 ± 0.14	-1.05 ± 0.08	159 ± 5
336	HD 25673	5127 ± 67	4.63 ± 0.14	-0.39 ± 0.07	55 ± 7
337	HD 26297	4514 ± 44	1.13 ± 0.14	-1.75 ± 0.07	10 ± 3
338	HD 270110	4614 ± 31	2.74 ± 0.14	-0.10 ± 0.05	60 ± 2
339	HD 271018	6737 ± 138	0.78 ± 0.29	0.07 ± 0.14	-14 ± 4
340	HD 27771	5325 ± 69	4.62 ± 0.14	0.27 ± 0.06	219 ± 7
341	HD 2796	4701 ± 47	1.41 ± 0.15	-2.53 ± 0.07	14 ± 8
342	HD 284248	6174 ± 140	4.18 ± 0.15	-1.62 ± 0.09	-6 ± 15
343	HD 2857	7844 ± 149	2.45 ± 0.22	-1.40 ± 0.11	-6 ± 56
344	HD 28978	8708 ± 173	3.36 ± 0.21	-0.33 ± 0.09	-2 ± 4
345	HD 29391	7360 ± 146	4.07 ± 0.21	0.07 ± 0.07	86 ± 4
346	HD 29391	7383 ± 146	4.10 ± 0.21	0.10 ± 0.07	66 ± 4
347	HD 29391	7366 ± 146	4.09 ± 0.21	0.09 ± 0.07	78 ± 5
348	HD 3008	4349 ± 67	0.67 ± 0.19	-1.82 ± 0.13	13 ± 4
349	HD 30328	4737 ± 32	2.64 ± 0.14	0.07 ± 0.05	35 ± 10
350	HD 30743	6390 ± 100	4.14 ± 0.14	-0.41 ± 0.07	31 ± 9
351	HD 31421	4452 ± 30	2.27 ± 0.14	-0.26 ± 0.06	47 ± 7
352	HD 33299	4525 ± 49	0.91 ± 0.19	-0.01 ± 0.09	136 ± 13
353	HD 33793	3698 ± 59	4.81 ± 0.14	-0.59 ± 0.09	12 ± 7
354	HD 345957	5878 ± 133	3.88 ± 0.14	-1.40 ± 0.09	20 ± 10
355	HD 35179	4933 ± 34	2.30 ± 0.14	-0.61 ± 0.06	26 ± 10
356	HD 36702	4379 ± 68	0.77 ± 0.19	-2.21 ± 0.14	-5 ± 7
357	HD 37763	4498 ± 47	3.10 ± 0.14	0.17 ± 0.05	76 ± 6
358	HD 37828	4474 ± 44	1.31 ± 0.14	-1.44 ± 0.07	-28 ± 8
359	HD 37828	4477 ± 44	1.32 ± 0.14	-1.42 ± 0.07	-15 ± 6
360	HD 38145	7055 ± 140	4.02 ± 0.21	0.00 ± 0.07	97 ± 6
361	HD 38237	8042 ± 160	3.81 ± 0.21	0.03 ± 0.07	1 ± 5
362	HD 38769	6819 ± 135	3.82 ± 0.21	0.18 ± 0.07	107 ± 3
363	HD 3883	7567 ± 150	3.54 ± 0.21	0.65 ± 0.07	-15 ± 3
364	HD 39587	5906 ± 92	4.39 ± 0.14	-0.06 ± 0.06	295 ± 5
365	HD 39833	5802 ± 91	4.37 ± 0.14	0.13 ± 0.06	84 ± 11
366	HD 39949	5389 ± 46	1.13 ± 0.14	-0.09 ± 0.06	148 ± 3
367	HD 41433	5125 ± 43	2.27 ± 0.14	-0.01 ± 0.06	73 ± 5
368	HD 41661	6519 ± 129	3.79 ± 0.21	0.15 ± 0.07	164 ± 3
369	HD 41667	4644 ± 45	1.72 ± 0.14	-1.20 ± 0.07	75 ± 6
370	HD 41770	6956 ± 138	3.69 ± 0.21	0.49 ± 0.07	-18 ± 6
371	HD 42143	8681 ± 172	3.36 ± 0.21	-0.15 ± 0.07	69 ± 7
372	HD 42182	5058 ± 66	4.63 ± 0.14	0.11 ± 0.06	47 ± 8
373	HD 42256	4709 ± 32	2.47 ± 0.14	-0.31 ± 0.06	11 ± 9
374	HD 42983	4808 ± 50	3.59 ± 0.14	-0.01 ± 0.05	48 ± 19
375	HD 43021	7935 ± 157	4.20 ± 0.21	-0.71 ± 0.09	0 ± 5

Continued on next page

(Continued)

ID	Star	$T_{\rm eff}$ (K)	$\log g$	[Fe/H]	EW(He) (mÅ)
376	HD 44007	4922 ± 50	2.25 ± 0.15	-1.63 ± 0.07	36 ± 9
377	HD 44285	4263 ± 29	2.01 ± 0.14	-0.10 ± 0.05	28 ± 15
378	HD 44391	4638 ± 33	1.08 ± 0.14	-0.03 ± 0.05	52 ± 16
379	HD 44515	4130 ± 28	2.27 ± 0.14	0.06 ± 0.05	-15 ± 19
380	HD 44770	6502 ± 129	4.28 ± 0.21	-0.09 ± 0.07	130 ± 8
381	HD 45196	7229 ± 143	3.66 ± 0.21	0.16 ± 0.07	86 ± 1
382	HD 45282	5271 ± 99	3.12 ± 0.14	-1.51 ± 0.09	42 ± 9
383	HD 45507	5063 ± 43	2.45 ± 0.14	-0.09 ± 0.06	78 ± 10
384	HD 46454	4191 ± 28	1.63 ± 0.14	-0.31 ± 0.06	39 ± 12
385	HD 4813	6153 ± 96	4.25 ± 0.14	-0.14 ± 0.06	92 ± 5
386	HD 48616	6496 ± 66	1.33 ± 0.14	0.08 ± 0.06	17 ± 3
387	HD 4893	4109 ± 28	2.29 ± 0.14	0.03 ± 0.05	0 ± 23
388	HD 4906	5164 ± 67	3.77 ± 0.14	-0.70 ± 0.07	39 ± 4
389	HD 49068	4501 ± 30	1.77 ± 0.14	-0.03 ± 0.05	61 ± 7
390	HD 49739	7216 ± 143	3.95 ± 0.21	-0.12 ± 0.07	68 ± 7
391	HD 50372	4758 ± 32	1.76 ± 0.14	0.02 ± 0.05	214 ± 8
392	HD 50819	5280 ± 45	2.20 ± 0.14	0.01 ± 0.06	282 ± 3
393	HD 50877	4125 ± 44	0.16 ± 0.19	0.13 ± 0.09	-7 ± 9
394	HD 52298	6308 ± 99	4.29 ± 0.14	-0.32 ± 0.07	16 ± 5
395	HD 52973	5834 ± 59	1.05 ± 0.14	0.20 ± 0.06	51 ± 4
396	HD 53003	5799 ± 59	1.18 ± 0.14	0.06 ± 0.06	10 ± 13
397	HD 53927	4925 ± 52	4.72 ± 0.14	-0.28 ± 0.06	90 ± 12
398	HD 54828	4928 ± 34	2.43 ± 0.14	-0.69 ± 0.06	242 ± 2
399	HD 5544	4591 ± 32	2.25 ± 0.14	-0.08 ± 0.05	39 ± 5
400	HD 55583	4571 ± 31	2.64 ± 0.14	-0.03 ± 0.05	309 ± 9
401	HD 55693	5755 ± 90	4.20 ± 0.14	0.18 ± 0.06	31 ± 5
402	HD 56448	5040 ± 43	2.64 ± 0.14	-0.09 ± 0.06	31 ± 6
403	HD 57132	4082 ± 28	1.63 ± 0.14	-0.31 ± 0.06	-57 ± 7
404	HD 57707	4837 ± 51	3.19 ± 0.14	-0.03 ± 0.05	60 ± 7
405	HD 58051	4023 ± 27	2.07 ± 0.14	0.04 ± 0.05	47 ± 14
406	HD 58072	5127 ± 43	2.38 ± 0.14	0.03 ± 0.06	34 ± 5
407	HD 58455	4195 ± 29	2.08 ± 0.14	-0.03 ± 0.05	-3 ± 17
408	HD 58554	4399 ± 30	2.07 ± 0.14	-0.27 ± 0.06	56 ± 6
409	HD 5857	4631 ± 31	2.71 ± 0.14	-0.19 ± 0.05	55 ± 5
410	HD 58790	4663 ± 32	2.50 ± 0.14	-0.11 ± 0.05	62 ± 15
411	HD 59295	4634 ± 31	2.25 ± 0.14	0.00 ± 0.05	44 ± 11
412	HD 59984	5900 ± 92	3.89 ± 0.14	-0.81 ± 0.07	12 ± 3
413	HD 60319	5902 ± 92	4.01 ± 0.14	-0.90 ± 0.07	18 ± 6
414	HD 61064	6553 ± 130	3.67 ± 0.21	0.29 ± 0.07	200 ± 3
415	HD 61064	6545 ± 130	3.68 ± 0.21	0.28 ± 0.07	203 ± 3
416	HD 6229	5055 ± 64	2.12 ± 0.15	-1.21 ± 0.09	6 ± 14
417	HD 6268	4662 ± 47	1.37 ± 0.14	-2.47 ± 0.07	-15 ± 6
418	HD 62968	5132 ± 43	2.59 ± 0.14	-0.04 ± 0.06	214 ± 4
419	HD 64332	3501 ± 57	0.22 ± 0.19	-0.28 ± 0.17	-26 ± 8
420	HD 64630	7799 ± 155	3.82 ± 0.21	0.16 ± 0.07	34 ± 8
421	HD 65354	4098 ± 29	1.19 ± 0.14	-0.01 ± 0.05	-62 ± 14
422	HD 65372	7931 ± 102	2.61 ± 0.21	-0.19 ± 0.07	34 ± 8
423	HD 65583	5245 ± 69	4.46 ± 0.14	-0.78 ± 0.07	41 ± 5
424	HD 66776	4792 ± 33	2.64 ± 0.14	0.02 ± 0.05	41 ± 4
425	HD 69701	3721 ± 38	1.19 ± 0.14	-0.31 ± 0.09	-33 ± 7

Continued on next page

(Continued)

ID	Star	$T_{\rm eff}$ (K)	$\log g$	[Fe/H]	EW(He) (mÅ)
426	HD 69701	3702 ± 38	1.15 ± 0.14	-0.29 ± 0.09	-9 ± 14
427	HD 71160	4047 ± 27	1.78 ± 0.14	0.00 ± 0.05	65 ± 6
428	HD 71310	7725 ± 154	3.48 ± 0.22	-0.20 ± 0.09	54 ± 4
429	HD 71310	7760 ± 155	3.51 ± 0.22	-0.18 ± 0.07	69 ± 3
430	HD 71497	4778 ± 33	2.63 ± 0.14	0.14 ± 0.05	53 ± 8
431	HD 72968	9569 ± 190	3.67 ± 0.21	0.44 ± 0.07	-8 ± 6
432	HD 73665	4968 ± 34	2.65 ± 0.14	0.17 ± 0.05	51 ± 13
433	HD 74000	6151 ± 138	4.09 ± 0.14	-1.96 ± 0.09	19 ± 5
434	HD 74088	3945 ± 34	1.53 ± 0.15	-0.52 ± 0.09	-16 ± 7
435	HD 74166	4276 ± 29	1.83 ± 0.14	0.02 ± 0.05	75 ± 8
436	HD 74721	9571 ± 196	4.22 ± 0.21	-0.57 ± 0.09	5 ± 8
437	HD 75318	5388 ± 70	4.43 ± 0.14	-0.15 ± 0.06	60 ± 13
438	HD 7595	4334 ± 31	1.87 ± 0.15	-0.61 ± 0.06	-30 ± 9
439	HD 76780	5657 ± 88	4.27 ± 0.14	0.12 ± 0.06	89 ± 11
440	HD 76780	5664 ± 89	4.29 ± 0.14	0.13 ± 0.06	108 ± 10
441	HD 78737	6510 ± 129	4.23 ± 0.21	-0.50 ± 0.09	16 ± 6
442	HD 79349	3848 ± 32	1.67 ± 0.14	-0.02 ± 0.07	106 ± 7
443	HD 79349	3847 ± 32	1.68 ± 0.14	-0.03 ± 0.07	98 ± 9
444	HD 81797	4131 ± 28	1.59 ± 0.14	-0.04 ± 0.05	-10 ± 10
445	HD 83212	4505 ± 49	1.02 ± 0.15	-1.60 ± 0.07	9 ± 17
446	HD 83632	4138 ± 28	1.36 ± 0.14	-0.87 ± 0.06	0 ± 11
447	HD 85380	5956 ± 93	3.98 ± 0.14	0.02 ± 0.06	22 ± 8
448	HD 85773	4441 ± 69	0.84 ± 0.19	-2.35 ± 0.13	17 ± 4
449	HD 8724	4754 ± 50	1.69 ± 0.15	-1.64 ± 0.07	35 ± 9
450	HD 8724	4732 ± 48	1.62 ± 0.15	-1.68 ± 0.07	41 ± 5
451	HD 88737	6072 ± 95	3.92 ± 0.14	0.15 ± 0.06	225 ± 4
452	HD 9051	4869 ± 48	2.02 ± 0.14	-1.70 ± 0.07	45 ± 4
453	HD 9051	4873 ± 48	2.00 ± 0.14	-1.69 ± 0.07	48 ± 5
454	HD 90862	4039 ± 27	1.59 ± 0.14	-0.58 ± 0.06	-19 ± 12
455	HD 93329	8236 ± 235	3.31 ± 0.21	-1.32 ± 0.10	3 ± 6
456	HD 93487	5172 ± 63	2.23 ± 0.14	-1.18 ± 0.08	59 ± 5
457	HD 9356	6178 ± 139	3.40 ± 0.14	-1.04 ± 0.09	-11 ± 8
458	HD 9356	6666 ± 132	3.46 ± 0.21	-0.90 ± 0.09	0 ± 7
459	HD 93813	4354 ± 29	2.08 ± 0.14	-0.24 ± 0.06	-4 ± 3
460	HD 98468	4494 ± 33	2.02 ± 0.15	-0.40 ± 0.06	-3 ± 25
461	HD 98817	3780 ± 62	0.15 ± 0.19	0.08 ± 0.14	-0 ± 12
462	HD 99109	5295 ± 69	4.36 ± 0.14	0.37 ± 0.06	45 ± 13
463	HD 99329	7018 ± 139	4.04 ± 0.21	0.18 ± 0.07	147 ± 7
464	HD 99491	5412 ± 71	4.34 ± 0.14	0.31 ± 0.06	97 ± 10
465	HE 0146-1548	5092 ± 69	2.74 ± 0.17	-2.69 ± 0.09	2 ± 10
466	HE 1142-1422	6174 ± 139	3.97 ± 0.14	-2.18 ± 0.09	91 ± 8
467	HE 1204-0744	6217 ± 140	3.95 ± 0.14	-2.29 ± 0.09	35 ± 7
468	HE 1346-0427	6030 ± 136	3.84 ± 0.14	-2.42 ± 0.09	8 ± 5
469	HE 1428-1950	4838 ± 33	2.30 ± 0.14	-0.85 ± 0.06	414 ± 5
470	HIP 100047	3848 ± 50	4.62 ± 0.14	-0.12 ± 0.07	175 ± 8
471	HIP 100047	3835 ± 50	4.59 ± 0.14	-0.08 ± 0.07	149 ± 5
472	HIP 64965	4501 ± 68	4.62 ± 0.14	-1.14 ± 0.07	90 ± 7
473	HIP 66993	3706 ± 59	4.77 ± 0.14	-0.49 ± 0.09	102 ± 9
474	HIP 70472	3968 ± 52	4.63 ± 0.14	-0.17 ± 0.07	163 ± 6
475	HIP 75423	3507 ± 56	4.82 ± 0.14	0.00 ± 0.07	140 ± 6

Continued on next page

(Continued)

ID	Star	$T_{\rm eff}$ (K)	$\log g$	[Fe/H]	EW(He) (mÅ)
476	HIP 96710	3665 ± 58	4.74 ± 0.14	-0.06 ± 0.07	140 ± 9
477	HV 2255	3878 ± 52	0.17 ± 0.19	0.07 ± 0.14	-23 ± 10
478	HV 2555	3522 ± 58	0.09 ± 0.19	0.25 ± 0.14	-32 ± 9
479	IRAS 06404+0311	3890 ± 56	0.30 ± 0.21	0.04 ± 0.15	-14 ± 19
480	IRAS 06404+0311	3881 ± 54	0.28 ± 0.20	0.06 ± 0.14	44 ± 15
481	IRAS 06498-1102	4192 ± 28	1.25 ± 0.14	-0.11 ± 0.05	11 ± 10
482	ISO-MCMS J004950.3-731116	3827 ± 52	0.68 ± 0.19	-0.52 ± 0.17	-20 ± 11
483	ISO-MCMS J005059.4-731914	3806 ± 51	0.71 ± 0.19	-0.92 ± 0.17	22 ± 8
484	ISO-MCMS J005314.8-730601	3762 ± 38	1.12 ± 0.14	-0.71 ± 0.09	-18 ± 22
485	ISO-MCMS J005332.4-730501	4391 ± 32	1.05 ± 0.14	-0.58 ± 0.06	-7 ± 22
486	ISO-MCMS J005622.2-730334	3847 ± 52	0.99 ± 0.20	-0.58 ± 0.17	2 ± 20
487	LHS 1841	4704 ± 71	4.76 ± 0.14	-1.46 ± 0.07	62 ± 4
488	LHS 2463	4801 ± 72	4.60 ± 0.14	-1.79 ± 0.07	61 ± 2
489	NGC 1904 153	4182 ± 65	0.55 ± 0.19	-1.81 ± 0.13	-2 ± 5
490	NGC 1904 160	4324 ± 67	0.91 ± 0.19	-1.49 ± 0.14	6 ± 6
491	NGC 1904 223	4226 ± 65	0.69 ± 0.19	-1.42 ± 0.13	-4 ± 5
492	NGC 2682 108	4191 ± 28	2.14 ± 0.14	-0.09 ± 0.05	65 ± 9
493	NGC 2682 108	4190 ± 29	2.10 ± 0.14	-0.07 ± 0.05	36 ± 14
494	NGC 4147 230	4431 ± 69	0.99 ± 0.19	-1.78 ± 0.14	-0 ± 7
495	NGC 5139 1627	4520 ± 49	1.47 ± 0.15	-1.18 ± 0.07	-25 ± 12
496	NGC 5139 1627	4520 ± 47	1.49 ± 0.15	-1.17 ± 0.07	-47 ± 12
497	NGC 5139 3812	3593 ± 59	0.14 ± 0.19	-0.44 ± 0.17	-41 ± 10
498	NGC 5139 3812	3589 ± 59	0.06 ± 0.19	-0.45 ± 0.17	-12 ± 10
499	NGC 6838 1009	4520 ± 31	1.48 ± 0.14	-0.88 ± 0.06	-26 ± 4
500	NGC 6838 1037	4555 ± 32	2.05 ± 0.14	-0.86 ± 0.06	75 ± 8
501	NGC 6838 1037	4501 ± 32	1.98 ± 0.14	-0.90 ± 0.06	42 ± 6
502	NGC 6838 1039	4963 ± 40	2.03 ± 0.15	-0.97 ± 0.06	18 ± 8
503	NGC 6838 1039	4996 ± 39	2.13 ± 0.15	-0.94 ± 0.06	0 ± 4
504	NGC 6838 1053	4167 ± 29	1.55 ± 0.14	-0.86 ± 0.06	4 ± 9
505	NGC 6838 1063	4611 ± 33	1.64 ± 0.14	-0.85 ± 0.06	37 ± 5
506	NGC 6838 1063	4582 ± 36	1.61 ± 0.15	-0.89 ± 0.06	32 ± 12
507	NGC 6838 1066	4211 ± 30	1.62 ± 0.15	-0.90 ± 0.06	-47 ± 8
508	NGC 6838 1066	4218 ± 30	1.62 ± 0.15	-0.86 ± 0.06	-13 ± 11
509	NGC 6838 1066	4197 ± 35	1.63 ± 0.16	-0.89 ± 0.07	3 ± 9
510	NGC 6838 1071	4326 ± 30	1.79 ± 0.14	-0.90 ± 0.06	87 ± 6
511	NGC 6838 1073	4723 ± 37	2.33 ± 0.15	-0.88 ± 0.06	79 ± 5
512	NGC 6838 1073	4729 ± 36	2.31 ± 0.15	-0.88 ± 0.06	60 ± 10
513	NGC 6838 1075	4757 ± 41	2.40 ± 0.16	-0.86 ± 0.07	62 ± 7
514	NGC 6838 1075	4773 ± 39	2.48 ± 0.15	-0.84 ± 0.06	45 ± 13
515	NGC 6838 1077	3950 ± 33	1.49 ± 0.14	-0.82 ± 0.09	-13 ± 10
516	NGC 6838 1077	3940 ± 33	1.47 ± 0.14	-0.82 ± 0.09	-3 ± 6
517	NGC 6838 1078	4305 ± 30	2.02 ± 0.14	-0.18 ± 0.05	109 ± 9
518	NGC 6838 1078	4298 ± 29	2.02 ± 0.14	-0.17 ± 0.05	34 ± 15
519	NGC 7078 1079	4638 ± 53	1.35 ± 0.16	-2.35 ± 0.07	26 ± 14
520	OGLE 212654c8	4545 ± 34	2.59 ± 0.15	0.23 ± 0.05	35 ± 13
521	OGLE 6263C6	4192 ± 29	2.54 ± 0.14	0.36 ± 0.05	81 ± 28
522	OGLE-101167c8	4644 ± 100	2.34 ± 0.30	-0.31 ± 0.13	93 ± 43
523	OGLE-27350c4	4759 ± 132	2.93 ± 0.33	-0.46 ± 0.15	-11 ± 25
524	OGLE-63839	4064 ± 32	1.78 ± 0.16	-0.54 ± 0.06	-14 ± 15
525	OGLE-75382c8	4361 ± 43	2.81 ± 0.17	0.23 ± 0.06	11 ± 28

Continued on next page

(Continued)

ID	Star	$T_{\rm eff}$ (K)	$\log g$	[Fe/H]	EW(He) (mÅ)
526	OGLE-75382c8	4293 ± 38	2.56 ± 0.16	0.36 ± 0.05	22 ± 16
527	OGLEII DIA BUL-SC03 3941	3546 ± 37	1.08 ± 0.17	-0.55 ± 0.13	-22 ± 16
528	OGLEII DIA BUL-SC04 9008	3533 ± 36	1.18 ± 0.15	-0.50 ± 0.09	-29 ± 9
529	SHV 0448341-691510	3712 ± 38	1.05 ± 0.15	-0.99 ± 0.10	-49 ± 16
530	SHV 0448341-691510	3712 ± 38	1.10 ± 0.15	-0.98 ± 0.09	-21 ± 14
531	SHV 0503595-691915	3544 ± 58	0.60 ± 0.19	-0.50 ± 0.17	-26 ± 6
532	SHV 0517337-725738	4088 ± 68	0.26 ± 0.20	-1.31 ± 0.15	66 ± 11
533	SHV 0518161-683543	4078 ± 64	0.20 ± 0.19	-1.48 ± 0.14	42 ± 14
534	SHV 0520036-692817	3641 ± 37	1.05 ± 0.14	-0.61 ± 0.09	-7 ± 9
535	SHV 0520261-693826	4381 ± 30	1.12 ± 0.14	-0.20 ± 0.05	-72 ± 27
536	SHV 0522380-691255	3936 ± 53	0.24 ± 0.19	-0.43 ± 0.17	-2 ± 9
537	SHV 0523371-713351	3847 ± 33	1.22 ± 0.15	-0.64 ± 0.09	-12 ± 18
538	SHV 0525012-694829	3677 ± 60	0.79 ± 0.19	-0.46 ± 0.17	-12 ± 3
539	SHV 0526364-693639	3752 ± 61	0.67 ± 0.19	-0.28 ± 0.17	-17 ± 11
540	SHV 0527122-695006	3739 ± 61	0.51 ± 0.19	-0.21 ± 0.17	-45 ± 13
541	SHV 0529355-694037	3759 ± 62	0.87 ± 0.20	-0.38 ± 0.17	-56 ± 14
542	SHV 0529355-694037	3742 ± 61	0.89 ± 0.20	-0.36 ± 0.17	-21 ± 16
543	SHV 0529355-694037	3756 ± 39	1.10 ± 0.17	-0.38 ± 0.10	-46 ± 24
544	SHV 0531398-701050	3630 ± 59	0.53 ± 0.19	-0.19 ± 0.14	-23 ± 11
545	SHV 0534578-702532	4116 ± 46	0.22 ± 0.19	-0.87 ± 0.12	82 ± 15
546	SHV 0534578-702532	4022 ± 45	0.17 ± 0.19	-0.93 ± 0.12	57 ± 4
547	SHV 0535237-700720	3595 ± 59	0.57 ± 0.19	-0.21 ± 0.17	9 ± 5
548	SHV 0542111-683837	4098 ± 51	0.32 ± 0.21	-0.91 ± 0.13	7 ± 9
549	SHV 0542111-683837	4080 ± 67	0.47 ± 0.20	-1.06 ± 0.14	10 ± 8
550	SV* HV 11366	3558 ± 58	0.21 ± 0.19	-0.35 ± 0.17	-29 ± 2
551	SY Pav	3541 ± 36	1.28 ± 0.14	-0.81 ± 0.09	-45 ± 7
552	SY Pav	3534 ± 36	1.29 ± 0.14	-0.80 ± 0.09	-49 ± 6
553	UZ Cen	6492 ± 66	2.42 ± 0.14	0.27 ± 0.06	22 ± 8
554	[M2002] LMC 143035	3574 ± 58	0.34 ± 0.19	-0.05 ± 0.14	-69 ± 18
555	[M2002] LMC 150040	3637 ± 59	0.68 ± 0.19	-0.91 ± 0.17	-21 ± 7
556	[M2002] LMC 157533	3950 ± 53	0.27 ± 0.19	-0.05 ± 0.14	-11 ± 2
557	[M2002] LMC 159974	4052 ± 44	0.17 ± 0.19	-0.16 ± 0.09	-9 ± 5
558	[M2002] LMC 162635	3825 ± 51	0.34 ± 0.19	-0.05 ± 0.14	2 ± 9
559	[M2002] LMC 168757	3592 ± 59	0.69 ± 0.19	-0.60 ± 0.17	-25 ± 4
560	[M2002] SMC 46662	3777 ± 62	0.80 ± 0.19	-0.71 ± 0.17	-0 ± 2
561	[M2002] SMC 52334	3997 ± 54	0.21 ± 0.19	-0.22 ± 0.17	-9 ± 4
562	[M2002] SMC 83593	3607 ± 59	0.88 ± 0.19	-0.98 ± 0.17	-58 ± 9
563	[PHS2008] RGB 512	4189 ± 38	1.17 ± 0.16	-0.97 ± 0.07	-2 ± 6
564	[PHS2008] RGB 522	4118 ± 31	1.36 ± 0.15	-0.61 ± 0.06	19 ± 10
565	[PHS2008] RGB 533	4157 ± 32	1.29 ± 0.15	-0.66 ± 0.06	-6 ± 11

Table E.2: The $\log R'_{\rm HK}$ and S-index for field-XSL stars.

ID	Star	$\log R'_{\rm HK}$	S-index	ID	Star	$\log R'_{\rm HK}$	S-index
1	2MASS J17535707-2931427	-5.02	0.0241	283	HD 201626	-5.21	0.0088
2	2MASS J18033716-2954227	-5.49	0.0092	284	HD 202851	-5.42	0.0069
3	2MASS J18351799-3428093	-5.40	0.0047	285	HD 202851	-5.39	0.0071
4	2MASS J18352206-3429112	-5.29	0.0055	286	HD 204041		0.0261
5	2MASS J18352834-3444085	-5.30	0.0043	287	HD 204041		0.0257
6	2MASS J18352834-3444085	-5.36	0.0043	288	HD 204155		0.0074
7	2MASS J18355679-3434481	-5.52	0.0038	289	HD 204155		0.0075
8	BBB SMC 104	-5.49	0.0190	290	HD 204543		0.0057
9	BBB SMC 148	-5.49	0.0137	291	HD 204587	-4.89	0.0300
10	BD+01 2916	-5.09	0.0107	292	HD 204587	-4.87	0.0311
11	BD+03 2688	-5.30	0.0067	293	HD 205202	-5.47	0.0117
12	BD+04 2466		0.0067	294	HD 205202	-5.18	0.0123
13	BD+06 0648	-5.19	0.0053	295	HD 205555		0.0079
14	BD+06 2986	-4.86	0.0308	296	HD 205734		0.0118
15	BD+06 2986	-4.89	0.0300	297	HD 205734		0.0120
16	BD+09 0352	-4.89	0.0095	298	HD 205734		0.0118
17	BD+09 2190	-4.89	0.0205	299	HD 20619	-5.97	0.0093
18	BD+09 2860		0.0049	300	HD 207222		0.0260
19	BD+09 2870		0.0050	301	HD 207222		0.0260
20	BD+09 3223		0.0059	302	HD 207222		0.0262
21	BD+17 4708		0.0096	303	HD 207795	-4.69	0.0147
22	BD+17 4708		0.0096	304	HD 209290	-4.58	0.0807
23	BD+17 4708		0.0085	305	HD 209290	-4.49	0.0839
24	BD+18 2890	-5.49	0.0054	306	HD 210295	-5.11	0.0051
25	BD+20 3603	-5.49	0.0108	307	HD 211075	-5.47	0.0050
26	BD+24 1676	-5.49	0.0147	308	HD 21197	-4.80	0.0276
27	BD+25 1981		0.0134	309	HD 212516	-5.54	0.0155
28	BD+29 2091		0.0075	310	HD 213042	-4.85	0.0196
29	BD+30 2034	-5.24	0.0066	311	HD 215578	-5.25	0.0054
30	BD+30 2611	-5.01	0.0092	312	HD 215578	-5.23	0.0053
31	BD+30 2611	-5.22	0.0080	313	HD 215578	-5.29	0.0054
32	BD-01 1792	-5.89	0.0065	314	HD 216143	-5.29	0.0052

Continued on next page

(Continued)

ID	Star	$\log R'_{\rm HK}$	S-index	ID	Star	$\log R'_{\rm HK}$	S-index
33	BD-01 1792	-6.10	0.0064	315	HD 216219		0.0072
34	BD-09 5831	-5.43	0.0040	316	HD 216219		0.0071
35	BD-11 4126	-4.62	0.0205	317	HD 217357	-4.57	0.0661
36	BD-14 5890	-4.62	0.0050	318	HD 217877		0.0075
37	BD-16 1934	-5.63	0.0103	319	HD 217877		0.0075
38	BD-16 1934	-5.67	0.0116	320	HD 218502		0.0093
39	BPS CS 30336-049	-5.67	0.0170	321	HD 218566	-4.71	0.0170
40	BS 4432	-5.70	0.0104	322	HD 218566	-4.78	0.0153
41	BS 4517	-5.89	0.0098	323	HD 218857		0.0054
42	CD-24 15398		0.0206	324	HD 220662	-5.21	0.0053
43	CD-26 10417	-4.34	0.0368	325	HD 220838	-5.22	0.0062
44	CD-28 9374	-5.33	0.0067	326	HD 221149		0.0063
45	CD-30 18140		0.0093	327	HD 221170		0.0060
46	CD-49 11404	-5.35	0.0051	328	HD 222434	-5.12	0.0062
47	CD-49 11404	-5.39	0.0052	329	HD 232078	-5.22	-0.0106
48	CD-60 3621	-5.39	0.0113	330	HD 232078	-5.65	0.0111
49	CD-60 3636	-6.15	0.0167	331	HD 23924		0.0091
50	CD-62 1346		0.0074	332	HD 24616	-5.19	0.0063
51	CI Vel		0.0099	333	HD 250792		0.0080
52	CL* NGC 121 T V1		0.0121	334	HD 25329	-4.68	0.0096
53	CL* NGC 121 T V8		0.0185	335	HD 25532	-5.34	0.0072
54	CL* NGC 1978 LE 09	-4.67	0.0313	336	HD 25673	-6.09	0.0086
55	CL* NGC 1978 LE 09		0.0238	337	HD 26297	-5.20	0.0055
56	CL* NGC 1978 LE 09	-5.55	0.0020	338	HD 270110	-5.44	0.0047
57	CL* NGC 2324 BSV 10828	-5.62	0.0036	339	HD 271018	-5.44	0.0031
58	CL* NGC 288 OCH 531		0.0109	340	HD 27771	-4.35	0.0227
59	CL* NGC 288 OCH 531	-6.01	0.0110	341	HD 2796	-4.35	0.0051
60	CL* NGC 330 ROB A3	-4.41	0.0143	342	HD 284248		0.0081
61	CL* NGC 330 ROB A3	-3.80	0.0060	343	HD 2857		0.0169
62	CL* NGC 330 ROB B38		0.0102	344	HD 28978		0.0164
63	CL* NGC 371 FTW R20		0.0270	345	HD 29391	-5.05	0.0120
64	CL* NGC 419 LE 35		0.0165	346	HD 29391	-5.30	0.0118
65	CL* NGC 5139 SAW V1	-5.75	0.0030	347	HD 29391	-5.29	0.0118

Continued on next page

(Continued)

ID	Star	$\log R'_{\rm HK}$	S-index	ID	Star	$\log R'_{\rm HK}$	S-index
66	CL* NGC 5139 SAW V1	-4.40	0.0094	348	HD 3008	-5.11	0.0108
67	CL* NGC 5904 Arp III-03	-5.56	0.0122	349	HD 30328	-5.43	0.0045
68	CL* NGC 5904 Arp IV-19	-5.28	0.0116	350	HD 30743		0.0075
69	CL* NGC 6121 LEE 2303		0.0059	351	HD 31421	-5.42	0.0055
70	CL* NGC 6121 LEE 2626	-5.10	0.0047	352	HD 33299	-5.57	0.0124
71	CL* NGC 6121 LEE 2626	-4.95	0.0071	353	HD 33793	-5.14	0.0268
72	CL* NGC 6121 LEE 2626		0.0016	354	HD 345957		0.0069
73	CL* NGC 6121 LEE 4302	-5.05	0.0076	355	HD 35179	-5.34	0.0048
74	CL* NGC 6121 LEE 4302	-5.02	0.0068	356	HD 36702	-5.34	0.0076
75	CL* NGC 6121 LEE 4611	-5.91	0.0156	357	HD 37763	-5.53	0.0045
76	CL* NGC 6121 LEE 4611	-5.40	0.0149	358	HD 37828	-5.13	0.0060
77	CL* NGC 6121 LEE 4613	-5.44	0.0141	359	HD 37828	-5.14	0.0063
78	CL* NGC 6522 ARP 1021	-5.65	0.0026	360	HD 38145	-4.54	0.0134
79	CL* NGC 6522 ARP 1021	-5.64	0.0047	361	HD 38237		0.0142
80	CL* NGC 6522 ARP 1073	-5.48	0.0125	362	HD 38769	-4.66	0.0123
81	CL* NGC 6522 ARP 3190	-5.65	0.0084	363	HD 3883		0.0091
82	CL* NGC 6522 ARP 3213	-5.65	0.0063	364	HD 39587	-4.53	0.0158
83	CL* NGC 6522 ARP 4126	-5.66	0.0065	365	HD 39833	-5.30	0.0098
84	CL* NGC 6522 Arp 4329	-5.41	0.0026	366	HD 39949	-4.80	0.0096
85	CL* NGC 6838 AH A2	-5.40	0.0042	367	HD 41433	-5.82	0.0052
86	CL* NGC 6838 AH A2	-5.62	0.0040	368	HD 41661	-4.75	0.0108
87	CL* NGC 6838 AH A2	-5.38	0.0041	369	HD 41667	-5.12	0.0056
88	CL* NGC 6838 AH A9	-5.57	0.0055	370	HD 41770		0.0071
89	CL* NGC 6838 AH A9	-5.63	0.0048	371	HD 42143		0.0170
90	G012-021		0.0082	372	HD 42182	-5.41	0.0082
91	G013-035		0.0082	373	HD 42256	-5.40	0.0043
92	G013-035		0.0083	374	HD 42983	-5.28	0.0058
93	G018-039		0.0076	375	HD 43021		0.0184
94	G019-013	-4.72	0.0252	376	HD 44007	-5.18	0.0051
95	G021-024	-4.56	0.0544	377	HD 44285	-5.55	0.0064
96	G024-003		0.0078	378	HD 44391	-5.43	0.0117
97	G029-023		0.0083	379	HD 44515	-5.73	0.0064
98	G063-026		0.0079	380	HD 44770		0.0096

Continued on next page

(Continued)

ID	Star	$\log R'_{\rm HK}$	S-index	ID	Star	$\log R'_{\rm HK}$	S-index
99	G169-28		0.0074	381	HD 45196	-4.70	0.0115
100	G187-40		0.0074	382	HD 45282		0.0061
101	G188-22		0.0077	383	HD 45507	-5.47	0.0054
102	G20-15		0.0083	384	HD 46454	-5.62	0.0066
103	HD 100906	-5.27	0.0055	385	HD 4813		0.0084
104	HD 101712	-5.27	0.0272	386	HD 48616		0.0023
105	HD 102634		0.0069	387	HD 4893	-5.67	0.0068
106	HD 103877		0.0101	388	HD 4906		0.0069
107	HD 103932	-4.78	0.0268	389	HD 49068	-5.53	0.0054
108	HD 104893	-4.78	0.0067	390	HD 49739	-4.71	0.0130
109	HD 105740	-5.16	0.0053	391	HD 50372	-5.33	0.0069
110	HD 106304		0.0344	392	HD 50819	-5.03	0.0081
111	HD 108564	-4.86	0.0125	393	HD 50877	-5.03	0.0113
112	HD 108915	-5.31	0.0060	394	HD 52298		0.0074
113	HD 109307		0.0105	395	HD 52973	-4.52	0.0094
114	HD 109443		0.0110	396	HD 53003	-4.71	0.0074
115	HD 109871	-5.81	0.0082	397	HD 53927	-4.74	0.0123
116	HD 110184	-5.81	0.0071	398	HD 54828	-4.90	0.0078
117	HD 110885	-5.92	0.0068	399	HD 5544	-5.40	0.0050
118	HD 111515		0.0082	400	HD 55583	-5.02	0.0111
119	HD 111631	-4.54	0.0873	401	HD 55693		0.0074
120	HD 111721	-5.35	0.0057	402	HD 56448	-5.51	0.0048
121	HD 111786	-4.19	0.0265	403	HD 57132	-5.70	0.0090
122	HD 112374		0.0029	404	HD 57707	-5.25	0.0054
123	HD 113002	-5.43	0.0055	405	HD 58051	-5.63	0.0084
124	HD 11397		0.0085	406	HD 58072		0.0049
125	HD 114606		0.0078	407	HD 58455	-5.49	0.0062
126	HD 114960	-5.77	0.0072	408	HD 58554	-5.41	0.0059
127	HD 116114	-4.35	0.0162	409	HD 5857	-5.36	0.0051
128	HD 116544	-4.13	0.1085	410	HD 58790	-5.42	0.0048
129	HD 116745		0.0080	411	HD 59295	-5.45	0.0048
130	HD 116745		0.0076	412	HD 59984		0.0071
131	HD 117880		0.0338	413	HD 60319		0.0075

Continued on next page

(Continued)

ID	Star	$\log R'_{\rm HK}$	S-index	ID	Star	$\log R'_{\rm HK}$	S-index
132	HD 118055	-5.17	0.0074	414	HD 61064	-4.85	0.0102
133	HD 118100	-4.12	0.1402	415	HD 61064	-4.88	0.0100
134	HD 119802	-4.42	0.0332	416	HD 6229	-5.45	0.0053
135	HD 119850	-4.96	0.0401	417	HD 6268	-5.45	0.0052
136	HD 122956	-5.16	0.0054	418	HD 62968	-5.20	0.0072
137	HD 124292		0.0081	419	HD 64332	-5.20	0.0135
138	HD 126053		0.0084	420	HD 64630		0.0098
139	HD 126661		0.0079	421	HD 65354	-6.14	0.0078
140	HD 126681		0.0086	422	HD 65372		0.0142
141	HD 126778	-5.26	0.0047	423	HD 65583		0.0081
142	HD 128429	-5.10	0.0111	424	HD 66776	-5.37	0.0048
143	HD 128801		0.0369	425	HD 69701	-5.79	0.0142
144	HD 130095		0.0337	426	HD 69701	-5.78	0.0153
145	HD 130322	-5.01	0.0110	427	HD 71160	-5.75	0.0079
146	HD 13043		0.0074	428	HD 71310		0.0126
147	HD 13043		0.0076	429	HD 71310		0.0128
148	HD 134063	-5.27	0.0047	430	HD 71497	-5.37	0.0050
149	HD 134063	-5.23	0.0050	431	HD 72968		0.0343
150	HD 134439		0.0080	432	HD 73665	-5.30	0.0047
151	HD 134440	-5.01	0.0082	433	HD 74000		0.0100
152	HD 138290	-4.65	0.0144	434	HD 74088	-4.88	0.0149
153	HD 138776		0.0068	435	HD 74166	-5.73	0.0077
154	HD 138776		0.0067	436	HD 74721		0.0271
155	HD 139717		0.0028	437	HD 75318		0.0077
156	HD 140232		0.0162	438	HD 7595	-5.42	0.0050
157	HD 140283		0.0106	439	HD 76780	-6.17	0.0089
158	HD 140283		0.0106	440	HD 76780	-5.29	0.0100
159	HD 141531	-5.30	0.0063	441	HD 78737		0.0078
160	HD 141531	-5.27	0.0059	442	HD 79349	-5.90	0.0081
161	HD 141531	-5.28	0.0057	443	HD 79349	-5.57	0.0129
162	HD 141531	-5.27	0.0060	444	HD 81797	-5.66	0.0097
163	HD 142575	-6.23	0.0120	445	HD 83212	-5.13	0.0081
164	HD 142703	-4.36	0.0240	446	HD 83632	-5.34	0.0092

Continued on next page

(Continued)

ID	Star	$\log R'_{\rm HK}$	S-index	ID	Star	$\log R'_{\rm HK}$	S-index
165	HD 144172		0.0072	447	HD 85380		0.0068
166	HD 144921		0.0129	448	HD 85773		0.0063
167	HD 144921		0.0185	449	HD 8724	-5.13	0.0051
168	HD 14625	-5.42	0.0048	450	HD 8724	-5.16	0.0052
169	HD 14938	-5.07	0.0117	451	HD 88737	-4.85	0.0117
170	HD 150281	-5.42	0.0090	452	HD 9051	-5.16	0.0053
171	HD 157089		0.0071	453	HD 9051	-5.15	0.0052
172	HD 16031		0.0083	454	HD 90862	-5.68	0.0075
173	HD 160346	-4.77	0.0126	455	HD 93329		0.0214
174	HD 160365	-4.66	0.0118	456	HD 93487	-5.66	0.0057
175	HD 161149		0.0080	457	HD 9356		0.0064
176	HD 161227		0.0083	458	HD 9356		0.0074
177	HD 161370		0.0149	459	HD 93813	-5.48	0.0060
178	HD 16160	-4.92	0.0119	460	HD 98468	-5.40	0.0049
179	HD 161770		0.0069	461	HD 98817	-5.40	0.0051
180	HD 161817		0.0152	462	HD 99109		0.0070
181	HD 16232	-4.53	0.0152	463	HD 99329	-4.55	0.0130
182	HD 162652	-5.26	0.0047	464	HD 99491	-5.41	0.0096
183	HD 163346		0.0133	465	HE 0146-1548	-5.41	0.0094
184	HD 1638	-4.85	0.0054	466	HE 1142-1422	-5.41	0.0191
185	HD 1638	-5.45	0.0059	467	HE 1204-0744	-5.41	0.0213
186	HD 1638	-5.42	0.0063	468	HE 1346-0427	-5.41	0.0271
187	HD 1638	-5.45	0.0064	469	HE 1428-1950	-5.05	0.0099
188	HD 163810		0.0078	470	HIP 100047	-4.84	0.0407
189	HD 164115	-4.72	0.0119	471	HIP 100047	-4.84	0.0395
190	HD 16456		0.0178	472	HIP 64965	-4.77	0.0148
191	HD 164967		0.0236	473	HIP 66993	-5.25	0.0203
192	HD 165195		0.0063	474	HIP 70472	-4.76	0.0385
193	HD 165887		0.0113	475	HIP 75423	-4.93	0.0483
194	HD 166161	-5.99	0.0057	476	HIP 96710	-4.88	0.0441
195	HD 166283		0.0158	477	HV 2255	-4.88	0.0025
196	HD 16673	-5.10	0.0107	478	HV 2555	-4.88	0.0110
197	HD 166991		0.0234	479	IRAS 06404+0311	-4.88	0.0225

Continued on next page

(Continued)

ID	Star	$\log R'_{\rm HK}$	S-index	ID	Star	$\log R'_{\rm HK}$	S-index
198	HD 167278	-5.52	0.0099	480	IRAS 06404+0311	-4.88	0.0572
199	HD 169032		0.0147	481	IRAS 06498-1102	-5.80	0.0078
200	HD 170413	-5.41	0.0048	482	ISO-MCMS J004950.3-731116		0.0123
201	HD 17072		0.0058	483	ISO-MCMS J005059.4-731914	-5.03	-0.0055
202	HD 17072		0.0057	484	ISO-MCMS J005314.8-730601		-0.2108
203	HD 170756	-4.68	0.0095	485	ISO-MCMS J005332.4-730501	-5.61	0.0089
204	HD 170820	-5.61	0.0162	486	ISO-MCMS J005622.2-730334		0.0130
205	HD 170899	-5.14	0.0254	487	LHS 1841	-4.91	0.0110
206	HD 171234	-4.97	0.0145	488	LHS 2463	-5.24	0.0090
207	HD 171367	-5.32	0.0052	489	NGC 1904 153	-5.30	0.0114
208	HD 171496	-5.21	0.0049	490	NGC 1904 160	-5.11	0.0102
209	HD 171496	-5.26	0.0051	491	NGC 1904 223	-5.07	0.0152
210	HD 171496	-5.19	0.0052	492	NGC 2682 108	-5.57	0.0060
211	HD 172230		0.0077	493	NGC 2682 108	-5.70	0.0061
212	HD 172365	-5.96	0.0044	494	NGC 4147 230	-5.31	0.0060
213	HD 172472	-5.10	0.0111	495	NGC 5139 1627	-4.94	0.0065
214	HD 172506	-5.10	0.0107	496	NGC 5139 1627	-5.00	0.0065
215	HD 172522		0.0096	497	NGC 5139 3812	-5.00	0.0130
216	HD 173073		0.0121	498	NGC 5139 3812	-5.00	0.0084
217	HD 173158	-4.59	0.0104	499	NGC 6838 1009	-5.49	0.0042
218	HD 173369		0.0146	500	NGC 6838 1037	-5.34	0.0043
219	HD 173669		0.0220	501	NGC 6838 1037	-5.41	0.0042
220	HD 174240		0.0262	502	NGC 6838 1039	-5.53	0.0044
221	HD 174350	-5.42	0.0043	503	NGC 6838 1039		0.0028
222	HD 174512	-4.24	0.0236	504	NGC 6838 1053	-5.53	0.0053
223	HD 174866	-4.71	0.0153	505	NGC 6838 1063	-5.54	0.0038
224	HD 174966		0.0118	506	NGC 6838 1063	-5.28	0.0055
225	HD 174966	-6.11	0.0120	507	NGC 6838 1066	-5.40	0.0046
226	HD 174966	-6.09	0.0119	508	NGC 6838 1066	-5.70	0.0042
227	HD 175058		0.0081	509	NGC 6838 1066	-6.85	0.0050
228	HD 175181	-5.47	0.0049	510	NGC 6838 1071	-5.62	0.0037
229	HD 175376	-5.69	0.0052	511	NGC 6838 1073	-5.46	0.0039
230	HD 175545	-5.42	0.0054	512	NGC 6838 1073	-5.38	0.0045

Continued on next page

(Continued)

ID	Star	$\log R'_{\rm HK}$	S-index	ID	Star	$\log R'_{\rm HK}$	S-index
231	HD 175805	-5.38	0.0095	513	NGC 6838 1075	-5.24	0.0047
232	HD 175805	-5.76	0.0092	514	NGC 6838 1075	-5.33	0.0045
233	HD 175892		0.0170	515	NGC 6838 1077	-5.74	0.0071
234	HD 176698	-5.21	0.0051	516	NGC 6838 1077	-5.72	0.0063
235	HD 176851	-5.70	0.0085	517	NGC 6838 1078	-5.84	0.0034
236	HD 178287	-5.32	0.0057	518	NGC 6838 1078	-5.86	0.0039
237	HD 179315	-5.13	0.0055	519	NGC 7078 1079	-5.86	0.0051
238	HD 179870	-5.50	0.0042	520	OGLE 212654c8	-6.93	0.0024
239	HD 179870	-5.36	0.0048	521	OGLE 6263C6	-5.75	0.0053
240	HD 180086	-4.43	0.0133	522	OGLE-101167c8		0.0089
241	HD 183085	-5.31	0.0107	523	OGLE-27350c4		-0.0028
242	HD 184266		0.0086	524	OGLE-63839		0.0283
243	HD 184571	-4.80	0.0108	525	OGLE-75382c8		0.0062
244	HD 185094	-5.62	0.0104	526	OGLE-75382c8	-5.49	0.0299
245	HD 186478	-5.62	0.0044	527	OGLEII DIA BUL-SC03 3941		1.5797
246	HD 187111	-5.16	0.0060	528	OGLEII DIA BUL-SC04 9008	-7.95	0.0142
247	HD 18769		0.0182	529	SHV 0448341-691510	-5.95	0.0025
248	HD 188262	-4.58	0.0259	530	SHV 0448341-691510	-7.31	0.0100
249	HD 188262	-4.64	0.0249	531	SHV 0503595-691915	-6.78	0.0304
250	HD 188510		0.0072	532	SHV 0517337-725738	-6.78	0.0080
251	HD 18907	-6.02	0.0065	533	SHV 0518161-683543	-6.78	-0.0028
252	HD 189511	-5.23	0.0069	534	SHV 0520036-692817		-0.0206
253	HD 190073	-4.01	0.0411	535	SHV 0520261-693826	-5.50	0.0120
254	HD 19019	-5.50	0.0098	536	SHV 0522380-691255	-5.50	0.0042
255	HD 190390		0.0047	537	SHV 0523371-713351	-4.99	0.0133
256	HD 190404	-5.09	0.0081	538	SHV 0525012-694829		-0.0125
257	HD 190404	-5.16	0.0078	539	SHV 0526364-693639	-5.99	0.0195
258	HD 190404	-5.10	0.0079	540	SHV 0527122-695006	-6.13	0.0318
259	HD 191709	-5.16	0.0100	541	SHV 0529355-694037	-5.79	0.0027
260	HD 19304		0.0101	542	SHV 0529355-694037	-5.70	0.1244
261	HD 193225	-4.61	0.0134	543	SHV 0529355-694037	-6.95	-0.0173
262	HD 193281		0.0182	544	SHV 0531398-701050	-6.21	0.0159
263	HD 193281		0.0184	545	SHV 0534578-702532	-6.21	0.0703

Continued on next page

(Continued)

ID	Star	$\log R'_{\rm HK}$	S-index	ID	Star	$\log R'_{\rm HK}$	S-index
264	HD 193326		0.0057	546	SHV 0534578-702532	-6.21	0.1826
265	HD 193896		0.0052	547	SHV 0535237-700720	-5.57	0.0148
266	HD 193896	-6.67	0.0054	548	SHV 0542111-683837	-5.57	0.0175
267	HD 195729		0.0121	549	SHV 0542111-683837	-5.57	-0.0260
268	HD 196125	-4.94	0.0108	550	SV* HV 11366	-5.57	0.0117
269	HD 196218		0.0071	551	SY Pav		0.0002
270	HD 196892		0.0075	552	SY Pav	-6.72	0.0022
271	HD 196892		0.0075	553	UZ Cen		0.0033
272	HD 19787	-5.32	0.0053	554	[M2002] LMC 143035		0.0037
273	HD 200081		0.0082	555	[M2002] LMC 150040	-6.59	0.0110
274	HD 200081		0.0079	556	[M2002] LMC 157533	-6.59	0.0204
275	HD 200494	-5.55	0.0052	557	[M2002] LMC 159974	-6.59	0.0213
276	HD 200779	-4.82	0.0331	558	[M2002] LMC 162635	-6.59	0.0075
277	HD 201053	-5.25	0.0053	559	[M2002] LMC 168757	-7.62	0.0050
278	HD 201237	-4.92	0.0116	560	[M2002] SMC 46662	-6.37	0.0121
279	HD 201237	-4.93	0.0115	561	[M2002] SMC 52334	-6.37	0.0144
280	HD 201237	-4.94	0.0114	562	[M2002] SMC 83593	-6.57	0.0064
281	HD 201377	-4.65	0.0171	563	[PHS2008] RGB 512	-5.10	0.0165
282	HD 201626	-4.98	0.0107	564	[PHS2008] RGB 522	-4.67	0.0103
283	HD 201626	-5.21	0.0088	565	[PHS2008] RGB 533		-0.0011

Table E.3: The fractional X-ray luminosity measurements for the field-XSL stars.

ID	Star	$\log L_{X1}/L_{Gaia}$	$\log L_{X2}/L_{Gaia}$	$\log L_{X3}/L_{Gaia}$	$\log L_{X4}/L_{Gaia}$	$\log L_{X5}/L_{Gaia}$	$\log L_{X8}/L_{Gaia}$	$\log L_{RXS}/L_{Gaia}$
43	CD-26 10417							-3.12±0.06
48	CD-60 3621	-7.49±0.31	-6.45±0.09	-6.38±0.08	-6.86±0.22	-7.17±1.51	-5.98±0.12	
49	CD-60 3636	-8.88±0.46	-7.69±0.10	-7.62±0.10	-8.19±0.32	-8.48±1.68	-7.21±0.13	
105	HD 102634							-5.21±0.16
112	HD 108915	-7.77±0.69		-7.14±0.23	-6.98±0.42		-6.25±0.21	
119	HD 111631							-4.19±0.10
128	HD 116544							-3.04±0.04
133	HD 118100							-2.71±0.02
134	HD 119802							-4.36±0.17
142	HD 128429							-4.24±0.06
145	HD 130322	-6.24±0.07	-6.16±0.06	-7.15±0.27	-7.48±0.87		-5.78±0.09	
152	HD 138290							-4.38±0.09
169	HD 14938	-6.25±0.03	-5.28±0.01	-5.62±0.02	-6.35±0.09	-6.93±0.80	-5.15±0.02	-4.09±0.08
173	HD 160346							-4.89±0.10
181	HD 16232	-5.05±0.00	-4.42±0.00	-5.04±0.00	-6.02±0.02	-7.12±0.23	-4.24±0.00	-3.68±0.04
196	HD 16673							-4.57±0.07
204	HD 170820		-7.67±0.11	-7.63±0.12	-7.87±0.29	-7.24±0.43	-6.92±0.21	
232	HD 175805							-4.87±0.20
234	HD 176698	-7.62±0.47	-6.51±0.09	-7.14±0.26	-8.07±2.39		-6.25±0.28	
254	HD 19019							-4.75±0.13
264	HD 193326							-4.96±0.21
299	HD 20619							-5.02±0.16
304	HD 209290	-6.07±0.12	-5.91±0.11	-6.73±0.37	-7.20±1.83	-6.02±1.10	-5.42±0.29	
308	HD 21197							-4.64±0.13
321	HD 218566	-6.20±0.09	-6.19±0.09	-7.62±0.79		-6.41±1.09	-5.79±0.28	
334	HD 25329	-6.32±0.12	-6.05±0.08	-6.44±0.22	-6.64±0.60	-7.30±4.88	-5.45±0.10	
338	HD 270110	-7.59±3.70	-7.07±2.56	-6.24±0.46	-5.23±0.23	-4.93±0.91	-4.34±0.24	
340	HD 27771	-5.24±0.01	-4.88±0.01	-5.46±0.02	-7.22±0.53	-6.62±0.99	-4.65±0.01	-4.02±0.13
364	HD 39587	-5.46±0.01	-4.92±0.00	-5.51±0.01	-6.31±0.02	-7.15±0.19	-4.72±0.00	-4.16±0.02
365	HD 39833							-4.83±0.17
380	HD 44770							-4.51±0.07
385	HD 4813							-5.18±0.07

Continued on next page

(Continued)

ID	Star	$\log L_{X1}/L_{Gaia}$	$\log L_{X2}/L_{Gaia}$	$\log L_{X3}/L_{Gaia}$	$\log L_{X4}/L_{Gaia}$	$\log L_{X5}/L_{Gaia}$	$\log L_{X8}/L_{Gaia}$	$\log L_{RXS}/L_{Gaia}$
400	HD 55583							-4.90±0.23
415	HD 61064							-5.41±0.14
432	HD 73665	-8.62±0.31	-8.28±0.18	-7.73±0.09	-7.59±0.15	-7.62±0.75	-7.10±0.23	
447	HD 85380	-8.96±0.47	-8.86±0.49	-9.30±1.46		-8.71±5.85	-8.09±1.44	
463	HD 99329							-5.23±0.18
464	HD 99491	-6.16±0.02	-5.78±0.01	-6.46±0.02	-7.36±0.13	-7.38±0.43	-5.56±0.01	-4.95±0.12

Bibliography

Adibekyan V. Z., Sousa S. G., Santos N. C., Delgado Mena E., González Hernández J. I., Israelian G., Mayor M., Khachatryan G., 2012, A&A, 545, A32

Aguilera-Gómez C., Ramírez I., Chanamé J., 2018, A&A, 614, A55

Ahumada R., et al., 2020, ApJS, 249, 3

Albrow M. D., Cottrell P. L., 1996, MNRAS, 278, 337

Alonso-Santiago J., et al., 2021, A&A, 656, A149

Amarsi A. M., 2015, MNRAS, 452, 1612

Andrae R., et al., 2018, A&A, 616, A8

Andreasen D. T., Sousa S. G., Delgado Mena E., Santos N. C., Tsantaki M., Rojas-Ayala B., Neves V., 2016, A&A, 585, A143

Andretta V., Giampapa M. S., 1995, ApJ, 439, 405

Andretta V., Jones H. P., 1997, ApJ, 489, 375

Andretta V., Giampapa M. S., Covino E., Reiners A., Beeck B., 2017, ApJ, 839, 97

Arentsen A., et al., 2019, A&A, 627, A138

Asplund M., Amarsi A. M., Grevesse N., 2021, A&A, 653, A141

Athay R. G., Menzel D. H., 1956, ApJ, 123, 285

Avrett E. H., Fontenla J. M., Loeser R., 1994, in Rabin D. M., Jefferies J. T., Lindsey C., eds, Vol. 154, Infrared Solar Physics. p. 35

Bailer-Jones C. A. L., Rybizki J., Fouesneau M., Demleitner M., Andrae R., 2021, AJ, 161, 147

Ballet J., Burnett T. H., Digel S. W., Lott B., 2020, arXiv e-prints, p. arXiv:2005.11208

Baratella M., et al., 2020, A&A, 640, A123

Barnes S. A., 2003, ApJ, 586, 464

Bastian N., Lardo C., 2018, ARA&A, 56, 83

Basu S., Mazumdar A., Antia H. M., Demarque P., 2004, MNRAS, 350, 277

Bensby T., et al., 2013, A&A, 549, A147

Bertelli G., Girardi L., Marigo P., Nasi E., 2008, A&A, 484, 815

Bethe H. A., 1939, Physical Review, 55, 434

Bianchi L., Shiao B., Thilker D., 2017, ApJS, 230, 24

Bland-Hawthorn J., Gerhard O., 2016, ARA&A, 54, 529

Boller T., Freyberg M. J., Trümper J., Haberl F., Voges W., Nandra K., 2016, A&A, 588, A103

Boro Saikia S., et al., 2018, A&A, 616, A108

Brown E. L., et al., 2022, MNRAS, 514, 4300

Buder S., et al., 2021, MNRAS, 506, 150

Burbidge E. M., Burbidge G. R., Fowler W. A., Hoyle F., 1957, Reviews of Modern Physics, 29, 547

Caffau E., et al., 2019, A&A, 622, A68

Carlsson M., 1986, Uppsala Astronomical Observatory Reports, 33

Carretta E., Bragaglia A., Gratton R., Lucatello S., 2009, A&A, 505, 139

Carroll B. W., Ostlie D. A., 1996, An Introduction to Modern Astrophysics

Cayrel R., 1988, in Cayrel de Strobel G., Spite M., eds, Vol. 132, The Impact of Very High S/N Spectroscopy on Stellar Physics. p. 345

Chen Y.-P., Trager S. C., Peletier R. F., Lançon A., Vazdekis A., Prugniel P., Silva D. R., Gonneau A., 2014, A&A, 565, A117

Chertok I. M., Obridko E. I., Mogilevsky V. N., Shilova N. S., Hudson H. S., 2002, ApJ, 567, 1225

Claudi R., et al., 2017, European Physical Journal Plus, 132, 364

Clayton D. D., Fowler W. A., Hull T. E., Zimmerman B. A., 1961, Annals of Physics, 12, 331

Cosentino R., et al., 2012, in McLean I. S., Ramsay S. K., Takami H., eds, Society of Photo-Optical Instrumentation Engineers (SPIE) Conference Series Vol. 8446, Ground-based and Airborne Instrumentation for Astronomy IV. p. 84461V, doi:10.1117/12.925738

Cottaar M., et al., 2014, ApJ, 794, 125

Cuntz M., Ulmschneider P., 1994, in Caillault J.-P., ed., Astronomical Society of the Pacific Conference Series Vol. 64, Cool Stars, Stellar Systems, and the Sun. p. 368

Deng L.-C., et al., 2012, Research in Astronomy and Astrophysics, 12, 735

Dere K. P., Landi E., Young P. R., Del Zanna G., 2001, ApJS, 134, 331

Dib S., Schmeja S., Parker R. J., 2018, MNRAS, 473, 849

Dotter A., Chaboyer B., Jevremović D., Kostov V., Baron E., Ferguson J. W., 2008, ApJS, 178, 89

Dupree A. K., Avrett E. H., 2013, ApJ, 773, L28

Dupree A. K., Sasselov D. D., Lester J. B., 1992, ApJ, 387, L85

Dupree A. K., Smith G. H., Strader J., 2009, AJ, 138, 1485

Dupree A. K., Strader J., Smith G. H., 2011, ApJ, 728, 155

Dupree A., Brickhouse N., Irwin J., Kurucz R., Newton E., 2018, in 20th Cambridge Workshop on Cool Stars, Stellar Systems and the Sun. Cambridge Workshop on Cool Stars, Stellar Systems, and the Sun. p. 87 (arXiv:1811.05572), doi:10.5281/zenodo.1491756

Evans I. N., et al., 2020a, in American Astronomical Society Meeting Abstracts #235. p. 154.05

Evans P. A., et al., 2020b, ApJS, 247, 54

Fontenla J. M., Avrett E. H., Loeser R., 1990, ApJ, 355, 700

Fontenla J. M., Avrett E. H., Loeser R., 1991, ApJ, 377, 712

Fontenla J. M., Avrett E. H., Loeser R., 1993, ApJ, 406, 319

Freund S., Robrade J., Schneider P. C., Schmitt J. H. M. M., 2018, A&A, 614, A125

Fuhrmeister B., et al., 2019, A&A, 632, A24

Gaia Collaboration et al., 2018, A&A, 616, A1

Gonneau A., et al., 2020, A&A, 634, A133

Gray D. F., 2005, The Observation and Analysis of Stellar Photospheres

Gullikson K., Dodson-Robinson S., Kraus A., 2014, AJ, 148, 53

Hartkopf W. I., McAlister H. A., 1984, PASP, 96, 105

Hashimoto M.-a., Nakamura R., Thushari E. P. B. A., Arai K., 2018, Big-Bang Nucleosynthesis, doi:10.1007/978-981-13-2935-7.

Hayes C. R., et al., 2018, ApJ, 852, 49

Heiter U., Jofré P., Gustafsson B., Korn A. J., Soubiran C., Thévenin F., 2015, A&A, 582, A49

Helmi A., 2020, ARA&A, 58, 205

Hirayama T., 1971, Sol. Phys., 17, 50

Holtzman J. A., et al., 2018, AJ, 156, 125

Howell S. B., et al., 2014, PASP, 126, 398

Hoyle F., 1946, MNRAS, 106, 343

Hubeny I., Mihalas D., 2014, Theory of Stellar Atmospheres

Husser T. O., Wende-von Berg S., Dreizler S., Homeier D., Reiners A., Barman T., Hauschildt P. H., 2013, A&A, 553, A6

Ikeda Y., Kobayashi N., Kondo S., Yasui C., Motohara K., Minami A., 2006, in McLean I. S., Iye M., eds, Society of Photo-Optical Instrumentation Engineers (SPIE) Conference Series Vol. 6269, Society of Photo-Optical Instrumentation Engineers (SPIE) Conference Series. p. 62693T, doi:10.1117/12.672665

Ikeda Y., et al., 2022, PASP, 134, 015004

Isaacson H., Fischer D., 2010, ApJ, 725, 875

Jansen F., et al., 2001, A&A, 365, L1

Jian M., Gao S., Zhao H., Jiang B., 2017, AJ, 153, 5

Jian M., et al., 2020, MNRAS, 494, 1724

Jofré P., et al., 2014, A&A, 564, A133

Jofré P., Heiter U., Soubiran C., 2019, ARA&A, 57, 571

Judge P. G., Meisner R. W., 1994, in Hunt J. J., ed., ESA Special Publication Vol. 373, Solar Dynamic Phenomena and Solar Wind Consequences, the Third SOHO Workshop. p. 67

Jurić M., et al., 2008, ApJ, 673, 864

Kausch W., et al., 2015, A&A, 576, A78

Kim J. J., Lee Y.-W., 2018, ApJ, 869, 35

Kim Y. C., Yi S. K., Demarque P., 2001, in American Astronomical Society Meeting Abstracts #198. p. 43.01

Kippenhahn R., Weigert A., Weiss A., 2013, Stellar Structure and Evolution, doi:10.1007/978-3-642-30304-3.

Kobayashi C., Karakas A. I., Lugaro M., 2020, ApJ, 900, 179

Kondo S., et al., 2019, ApJ, 875, 129

Kovtyukh V. V., 2007, MNRAS, 378, 617

Kovtyukh V. V., Soubiran C., Belik S. I., Gorlova N. I., 2003, A&A, 411, 559

Kovtyukh V. V., Soubiran C., Belik S. I., 2004, A&A, 427, 933

Kovtyukh V. V., Soubiran C., Bienaymé O., Mishenina T. V., Belik S. I., 2006, MNRAS, 371, 879

Kurucz R. L., 1993, SYNTHE spectrum synthesis programs and line data

Kurucz R. L., 2005, Memorie della Societa Astronomica Italiana Supplementi, 8, 14

Lambert D. L., 1987, ApJS, 65, 255

Lee Y. W., Joo J. M., Sohn Y. J., Rey S. C., Lee H. C., Walker A. R., 1999, Nature, 402, 55

Lee J.-W., Kang Y.-W., Lee J., Lee Y.-W., 2009, Nature, 462, 480

Linsky J. L., 2017, ARA&A, 55, 159

Linsky J. L., Avrett E. H., 1970, PASP, 82, 169

Linsky J. L., Haisch B. M., 1979, ApJ, 229, L27

Luck R. E., 2017, AJ, 153, 21

Luck R. E., 2018, AJ, 155, 111

Lyubimkov L. S., Lambert D. L., Rostopchin S. I., Rachkovskaya T. M., Poklad D. B., 2010, MNRAS, 402, 1369

Mackereth J. T., Crain R. A., Schiavon R. P., Schaye J., Theuns T., Schaller M., 2018, MNRAS, 477, 5072

Maeckle R., Holweger H., Griffin R., Griffin R., 1975, A&A, 38, 239

Magain P., 1986, A&A, 163, 135

Maggio A., Vaiana G. S., Haisch B. M., Stern R. A., Bookbinder J., Harnden F. R. J., Rosner R., 1990, ApJ, 348, 253

Majewski S. R., et al., 2017, AJ, 154, 94

Marino A. F., et al., 2011, A&A, 532, A8

Matsunaga N., et al., 2020, ApJS, 246, 10

Matsunaga N., Jian M., Taniguchi D., Elgueta S. S., 2021, MNRAS, 506, 1031

Matteucci F., Brocato E., 1990, ApJ, 365, 539

Mauas P. J. D., Cacciari C., Pasquini L., 2006, A&A, 454, 609

McKeever J. M., Basu S., Corsaro E., 2019, ApJ, 874, 180

McWilliam A., 1997, ARA&A, 35, 503

Milkey R. W., Heasley J. N., Beebe H. A., 1973, ApJ, 186, 1043

Milone A. P., et al., 2018, MNRAS, 481, 5098

Mittag M., Schmitt J. H. M. M., Schröder K. P., 2013, A&A, 549, A117

Moore C. E., Merrill P. W., 1968, Partial Grotrian Diagrams of Astrophysical Interest

Navarrete C., Chanamé J., Ramírez I., Meza A., Anglada-Escudé G., Shkolnik E., 2015, ApJ, 808, 103

Noyes R. W., Hartmann L. W., Baliunas S. L., Duncan D. K., Vaughan A. H., 1984, ApJ, 279, 763

Obrien George T. J., Lambert D. L., 1986, ApJS, 62, 899

Oliva E., et al., 2006, in McLean I. S., Iye M., eds, Society of Photo-Optical Instrumentation Engineers (SPIE) Conference Series Vol. 6269, Society of Photo-Optical Instrumentation Engineers (SPIE) Conference Series. p. 626919, doi:10.1117/12.670006

Origlia L., et al., 2014, in Ramsay S. K., McLean I. S., Takami H., eds, Society of Photo-Optical Instrumentation Engineers (SPIE) Conference Series Vol. 9147, Ground-based and Airborne Instrumentation for Astronomy V. p. 91471E, doi:10.1117/12.2054743

Origlia L., et al., 2019, A&A, 629, A117

Pasquini L., 1992, A&A, 266, 347

Pasquini L., Mauas P., Käufl H. U., Cacciari C., 2011, A&A, 531, A35

Paxton B., Bildsten L., Dotter A., Herwig F., Lesaffre P., Timmes F., 2011, ApJS, 192, 3

Paxton B., et al., 2019, ApJS, 243, 10

Perdelwitz V., et al., 2021, A&A, 652, A116

Piotto G., et al., 2005, ApJ, 621, 777

Piotto G., et al., 2007, ApJ, 661, L53

Piotto G., et al., 2015, AJ, 149, 91

Pitrou C., Coc A., Uzan J.-P., Vangioni E., 2018, Phys. Rep., 754, 1

Planck Collaboration et al., 2016, A&A, 594, A13

Rainer M., et al., 2018, in Evans C. J., Simard L., Takami H., eds, Society of Photo-Optical Instrumentation Engineers (SPIE) Conference Series Vol. 10702, Ground-based and Airborne Instrumentation for Astronomy VII. p. 1070266, doi:10.1117/12.2312130

Reddy A. B. S., 2020, MNRAS, 495, 383

Reddy A. B. S., Lambert D. L., 2019, MNRAS, 485, 3623

Ricker G. R., et al., 2015, Journal of Astronomical Telescopes, Instruments, and Systems, 1, 014003

Rutten R. J., 2003, Radiative Transfer in Stellar Atmospheres

Rutten R. J., 2015, Introduction to Astrophysical radiative transfer, 4 edn. https://webspace.science.uu.nl/~rutte101/Introduction_Astrophysical.html

Ryabchikova T., Piskunov N., Kurucz R. L., Stempels H. C., Heiter U., Pakhomov Y., Barklem P. S., 2015, Phys. Scr., 90, 054005

Sameshima H., et al., 2018, PASP, 130, 074502

Sanz-Forcada J., Dupree A. K., 2008, A&A, 488, 715

Schrijver C. J., 1987, A&A, 172, 111

Seeger P. A., Fowler W. A., Clayton D. D., 1965, ApJS, 11, 121

Seifert W., et al., 2012, in McLean I. S., Ramsay S. K., Takami H., eds, Society of Photo-Optical Instrumentation Engineers (SPIE) Conference Series Vol. 8446, Ground-based and Airborne Instrumentation for Astronomy IV. p. 844633, doi:10.1117/12.927009

Smette A., et al., 2015, A&A, 576, A77

Smith M. A., 1983, AJ, 88, 1031

Smith G. H., 2016, Publ. Astron. Soc. Australia, 33, e057

Smith G. H., Dupree A. K., Strader J., 2004, PASP, 116, 819

Smith G. H., Dupree A. K., Strader J., 2012, PASP, 124, 1252

Smith G. H., Dupree A. K., Strader J., 2014, PASP, 126, 901

Sneden C., Bean J., Ivans I., Lucatello S., Sobeck J., 2012, MOOG: LTE line analysis and spectrum synthesis, Astrophysics Source Code Library, record ascl:1202.009 (ascl:1202.009)

Stock J., 1956, ApJ, 123, 258

Strader J., Dupree A. K., Smith G. H., 2015, ApJ, 808, 124

Suzuki T. K., 2007, ApJ, 659, 1592

Takeda Y., 1995, PASJ, 47, 287

Takeda Y., Takada-Hidai M., 2011, PASJ, 63, 547

Tobiska W. K., 1991, Journal of Atmospheric and Terrestrial Physics, 53, 1005

Truemper J., 1982, Advances in Space Research, 2, 241

Vacca W. D., Cushing M. C., Rayner J. T., 2003, PASP, 115, 389

Vaughan Arthur H. J., Zirin H., 1968, ApJ, 152, 123

Verma K., Raodeo K., Basu S., Silva Aguirre V., Mazumdar A., Mosumgaard J. R., Lund M. N., Ranadive P., 2019, MNRAS, 483, 4678

Vernazza J. E., Avrett E. H., Loeser R., 1981, ApJS, 45, 635

Vernet J., et al., 2011, A&A, 536, A105

Vollmann K., Eversberg T., 2006, Astronomische Nachrichten, 327, 862

Webb N. A., et al., 2020, A&A, 641, A136

Wilson O. C., 1968, ApJ, 153, 221

Wilson O. C., 1978, ApJ, 226, 379

Ye X., Zhao J., Liu J., Bird S. A., Liu C., Liang X., Zhang J., Zhao G., 2021, AJ, 161, 8

Yi S., Demarque P., Kim Y.-C., Lee Y.-W., Ree C. H., Lejeune T., Barnes S., 2001, ApJS, 136, 417

Yong D., et al., 2013, ApJ, 762, 26

Zarro D. M., Zirin H., 1986, ApJ, 304, 365

Zhang H. W., Zhao G., 2005, MNRAS, 364, 712

Zhao J. K., Oswalt T. D., Rudkin M., Zhao G., Chen Y. Q., 2011, AJ, 141, 107

Zhao J. K., Oswalt T. D., Zhao G., Lu Q. H., Luo A. L., Zhang L. Y., 2013, AJ, 145, 140

Zirin H., 1975, ApJ, 199, L63

Zirin H., 1976, ApJ, 208, 414

Zirin H., 1982, ApJ, 260, 655